
Electronic Thesis and Dissertation Repository

6-12-2018 4:30 PM

An In-Silico Assessment of Stemless Shoulder Arthroplasty: from CT to Predicted Bone Response

Jacob M. Reeves

The University of Western Ontario

Supervisor

Johnson, James A.

The University of Western Ontario Co-Supervisor

Athwal, George S.

The University of Western Ontario

Graduate Program in Mechanical and Materials Engineering

A thesis submitted in partial fulfillment of the requirements for the degree in Doctor of Philosophy

© Jacob M. Reeves 2018

Follow this and additional works at: <https://ir.lib.uwo.ca/etd>



Part of the [Biomechanical Engineering Commons](#), [Biomedical Devices and Instrumentation Commons](#), and the [Computer-Aided Engineering and Design Commons](#)

Recommended Citation

Reeves, Jacob M., "An In-Silico Assessment of Stemless Shoulder Arthroplasty: from CT to Predicted Bone Response" (2018). *Electronic Thesis and Dissertation Repository*. 5398.

<https://ir.lib.uwo.ca/etd/5398>

This Dissertation/Thesis is brought to you for free and open access by Scholarship@Western. It has been accepted for inclusion in Electronic Thesis and Dissertation Repository by an authorized administrator of Scholarship@Western. For more information, please contact wlsadmin@uwo.ca.

Abstract

Despite the emergence of stemless humeral implants that utilize short fixation features to gain purchase solely in the metaphysis, the literature contains little information regarding the morphology and mechanical properties of the humerus' proximal trabecular-canal, and how stemless implants impact bone response. The present work employs *in-silico* tools, including CT-based and Finite Element (FE) methods, to define parameters that may influence stemless implant design.

The density and morphology of the proximal humerus were assessed using CT-derived point clouds of the trabecular-canal. Bone density was found to diminish 15-20mm beneath the humeral head resection and was greater peripherally. The depth, path and bounding diameters of the proximal trabecular-canal were also quantified and established the spatial constraints in which implants should be designed.

To address the lack of consensus regarding the FE modelling of humeral trabecular-stiffness, eight (8) FE models were constructed then duplicated six different trabecular-stiffness relationships. The deviation induced in FE outcomes by stiffness relationship selection was quantified. It was determined that inhomogeneous stiffness definition is important; however, the anatomic site from which the stiffness is defined induced minor deviations in the implant-bone contact area, the change in bone stresses and the potential bone response following stemless reconstruction.

Finally, with humeral FE modelling parameters defined, a series of ten generic stemless implants were designed with fixation features that were primarily central, peripheral or boundary-crossing. A population of five (5) cadaveric humeral FE models were constructed for each implant. Tradeoffs were found, with central implants producing the least resorbing potential, and peripheral implants maintaining the most implant-bone contact. Regardless of fixation feature design, predicted bone changes were most prominent within the lateral quadrant of the humerus, directly beneath the humeral head resection.

The present work advances the understanding of stemless humeral arthroplasty. The morphological parameters defined provide a spatial definition of the region in which stemless implants function. Through the development of humeral FE models, general trends in bone response following stemless reconstruction were noted; along with tradeoffs regarding the placement of stemless fixation features. These methods can be applied in the design of future stemless implants.

Keywords: Shoulder Arthroplasty, Stemless Implants, Joint Reconstruction, Humerus Morphology, Finite Element Analysis

Co-Authorship Statement

Chapter 1

JM Reeves – Sole author

Chapter 2

JM Reeves – LabVIEW code development, study design, data collection, statistical analysis, wrote manuscript

GS Athwal – Resection plane selection, study design, reviewed manuscript

JA Johnson – Study design, reviewed manuscript

Chapter 3

JM Reeves – LabVIEW code development, study design, data collection, statistical analysis, wrote manuscript

JA Johnson – Study design, reviewed manuscript

GS Athwal – Resection plane selection, study design, reviewed manuscript

Chapter 4

JM Reeves – FE model development, study design, data collection, statistical analysis, wrote manuscript

GS Athwal – Resection plane selection, study design, reviewed manuscript

JA Johnson – Study design, reviewed manuscript

GDG Langohr – Study design, reviewed manuscript

Chapter 5

JM Reeves – FE model development, study design, data collection, statistical analysis, wrote manuscript

GDG Langohr – Study design, reviewed manuscript

GS Athwal – Resection plane selection, study design, reviewed manuscript

JA Johnson – Study design, reviewed manuscript

Chapter 6

JM Reeves: Sole author.

Appendix C

JM Reeves – FE model development, study design, data collection, statistical analysis, wrote manuscript

GS Athwal – Study design, resection plane selection, reviewed manuscript

JS Johnson – Study design, reviewed manuscript

Appendix D

JM Reeves – FE model development, study design, data collection, statistical analysis, wrote manuscript

DT Axford – Data Collection

GDG Langohr – Study design, reviewed manuscript

GS Athwal – Study design, implant insertion consulting, reviewed manuscript

JA Johnson – Study design, reviewed manuscript

Appendix E

JM Reeves – CT scanning, study design, data collection, statistical analysis, wrote manuscript

NK Knowles – Study design, CT scanning, reviewed manuscript

GS Athwal – Study design, reviewed manuscript

JA Johnson – Study design, reviewed manuscript

Dedication

To My Family

Acknowledgements

To my family, for your unfailing support in everything that I do. Your belief in me has enabled me to pursue my studies without hesitation. I attribute the development of my curiosity to the loving and supportive home in which I grew up.

To Dr. Johnson and Dr. Athwal, thank you for your ongoing support and insight throughout my doctoral work. Your leadership styles have enabled me to grow as a researcher, fostering my scientific curiosity and independence; which is something that I hope to emulate during the supervisory opportunities that I have in my career moving forward.

I would also like to acknowledge the support that I received from all of the lab-mates that I have had over the years, both at the HULC BioEngineering lab, as well as at the BTL. You have all contributed to my development as a researcher and have made the labs both enjoyable and supportive environments.

Finally, I would further like to acknowledge that funding and support for this thesis was received from NSERC, OGS and the Collaborative Musculoskeletal Health Research program at the University of Western Ontario.

Table of Contents

Abstract.....	ii
Co-Authorship Statement	iv
Dedication.....	vi
Acknowledgements.....	vii
Table of Contents.....	viii
List of Tables	xii
List of Figures.....	xiii
List of Appendices.....	xviii
Nomenclature.....	xx
Chapter 1.....	1
Introduction	1
1.1 Anatomy of the Shoulder.....	1
1.1.1 The Glenohumeral Joint	3
1.1.2 Motions of the Shoulder	3
1.1.3 Glenohumeral Soft Tissue Constructs	5
1.1.3.1 Passive Soft Tissues – Ligaments and Joint Capsule	5
1.1.3.2 Active Soft Tissues – Muscles.....	6
1.1.4 Glenohumeral Osseous Constructs	7
1.1.4.1 Bone Structure and Elastic Properties	7
1.1.4.2 The Scapula	9
1.1.4.3 The Proximal Humerus.....	11
1.2 Shoulder Arthroplasty.....	13
1.2.1 The Implants of Anatomic Shoulder Arthroplasty	14
1.2.1.1 The Glenoid Implant.....	14
1.2.1.2 The Humeral Implant.....	14
1.2.2 Indications for Shoulder Arthroplasty	16
1.2.3 Complications of Shoulder Arthroplasty	18
1.2.4 Present State of Stemless Humeral Components.....	19
1.2.4.1 Stemless Humeral Implants Currently Manufactured	19
1.2.4.2 Performance of Stemless Shoulder Implants in the Literature	20
1.3 Wolff’s Law and Stress Shielding	28

1.4 Scientific Methods for Analyzing Shoulder Arthroplasty	29
1.4.1 Radiographic Tools – Computed Tomography	29
1.4.2 The Finite Element Method	29
1.4.2.1 Finite Element Theory	31
1.4.2.2 The Finite Element Mesh.....	31
1.4.2.3 Modelling Joint Reaction Forces	34
1.4.2.4 Modelling Bone as a Material.....	37
1.4.2.5 Finite Element Outcome Variables.....	41
1.5 Thesis Rationale.....	44
1.6 Objectives and Hypotheses.....	45
1.6.1 Specific Objectives	45
1.6.2 Specific Hypotheses.....	45
1.7 Thesis Overview	46
1.8 References.....	47
Chapter 2.....	63
An Assessment of Proximal Humerus Density with Reference to Stemless Implants	63
2.1 Introduction	63
2.2 Materials and Methods	64
2.3 Results	69
2.4 Discussion.....	75
2.5 Conclusion	78
2.6 References.....	78
Chapter 3.....	83
An Analysis of Proximal Humerus Morphology with Special Interest in Stemless Shoulder Arthroplasty	83
3.1 Introduction	83
3.2 Materials and Methods	84
3.3 Results:	88
3.3.1 Canal Path:.....	88
3.3.2 Fitted Canal Diameter:.....	91
3.3.3 Resection Depth:.....	91
3.3.4 Articular Aspect Ratio:.....	97
3.4 Discussion.....	97

3.5 Conclusions	102
3.6 References.....	102
Chapter 4.....	106
The Effect of Trabecular Modulus Anatomic Site Selection on FE Outcomes for Shoulder Arthroplasty	106
4.1 Introduction	106
4.2 Materials and Methods	107
4.3 Results	112
4.3.1 Implant-Bone Contact.....	112
4.3.2 Change in Bone Stress	112
4.3.3 Potential Bone Response	117
4.3.3.1 Cortical Region.....	117
4.3.3.2 Trabecular Region	123
4.4 Discussion.....	130
4.5 Conclusions	132
4.6 References.....	132
Chapter 5.....	139
The Effect of Stemless Humeral Component Fixation-Feature Design on Bone Stress and Strain Response	139
5.1 Introduction	139
5.2 Materials and Methods	140
5.2.1 Bone Model Development:.....	140
5.2.2 Implant Designs	141
5.2.3 Finite Element Modeling	144
5.2.4 Outcome Variables	144
5.2.5 Statistical Approaches	145
5.3 Results	145
5.3.1 Implant-Bone Contact.....	145
5.3.2 Absolute Change in Bone Stress	146
5.3.2.1 Cortical Bone	146
5.3.2.2 Trabecular Bone.....	152
5.3.3 Expected Bone Response.....	157
5.3.3.1 Cortical Bone	157
5.3.3.2 Trabecular Bone.....	161

5.4 Discussion.....	165
5.5 Conclusion.....	169
5.6 References.....	169
Chapter 6.....	176
General Discussions and Concluding Thoughts.....	176
6.1 Summary.....	176
6.2 Strengths and Limitations.....	179
6.3 Future Directions.....	183
6.4 Significance.....	184
6.5 References.....	185
Appendices.....	188
Curriculum Vitae.....	305

List of Tables

Table 1.1: Features of Currently Available Stemless Implants	22
Table 1.2a: Summary of <i>In-Vivo</i> Anatomic Stemless Humeral Studies (2010-2016).....	24
Table 1.2b: Summary of <i>In-Vivo</i> Anatomic Stemless Humeral Studies (2017-2018)	25
Table 1.3: Cartesian Ratios and Resultant Joint Reaction Forces for the Glenohumeral Joint.	36
Table 1.4: Summary of several relevant density-modulus investigations.	40
Table 2.1: Mean (standard deviation) average apparent density (g/cm^3) of the trabecular-canal. .	73
Table 3.1: Mean (standard deviation) fitted canal diameters in the 13 proximal humerus slices. .	92
Table 4.1: Standard deviations attributed to inhomogeneous anatomic-site, FE population and homogeneous-inhomogeneous differences in the change in bone stress outcome measure; broken down regionally according to slice depth.	116
Table 4.2: Standard deviations attributed to inhomogeneous anatomic-site, FE population and homogeneous-inhomogeneous differences in the potential bone response outcome measure for cortical bone; broken down regionally according to slice depth.	120
Table 4.3: Standard deviations attributed to inhomogeneous anatomic-site, FE population and homogeneous-inhomogeneous differences in the potential bone response outcome measure for trabecular bone; broken down regionally according to slice depth.	129
Table C.1: Comparison of implant-bone contact pressure distribution for mesh refinement.	202
Table C.2: Comparison of the potential bone response for mesh refinement – 45° of abduction.	209
Table C.3: Comparison of the potential bone response for mesh refinement – 75° of abduction.	210
Table D.1: Regression Terms and Correlations for Intact and Reconstructed States	223
Table D.2: Error Terms for the Intact and Reconstructed States	226
Table F.1: CT settings used for all specimen and phantom-only scans.....	238
Table F.2: Density calibration equation terms derived from stepwise linear regression analysis.	242
Table F.3: 4-way repeated measures ANOVA results.....	243
Table F.4: Density calibration equation terms derived by calibrated, phantom-only and regression methods.....	245

List of Figures

Figure 1.1: Joints of the Shoulder.....	2
Figure 1.2: Basic Movements of the Shoulder	4
Figure 1.3: Cortical and Trabecular Bone	8
Figure 1.4: The Boney Anatomy of the Scapula	10
Figure 1.5: The Boney Anatomy of the Humerus	12
Figure 1.6: Forms of Shoulder Arthroplasty	15
Figure 1.7: Evolution of Shoulder Arthroplasty Humeral Components.....	17
Figure 1.8: Variation in Stemless Humeral Implants	21
Figure 1.9: Computed Tomography Scanning and Density Calibration	30
Figure 1.10: Discretized Finite Element Mesh	32
Figure 1.11: Tetrahedral and Hexahedral Elements	33
Figure 1.12: Identical Mesh Preparation	35
Figure 1.13: Finite Element Joint Reaction Force Application	38
Figure 2.1: Selection of Currently Available Stemless Implants.	65
Figure 2.2: Stemless Relevant Cartesian Coordinate System.....	66
Figure 2.3: Division of the Proximal Humerus	68
Figure 2.4: Humeral Regions-of-Interest for CT Assessment	70
Figure 2.5: Average Apparent Density Results for Male Subjects.....	71
Figure 2.6: Average Apparent Density Results for Female Subjects	72
Figure 3.1: Region-of-Interest for the Proximal Humerus	85
Figure 3.2: Landmarks and Coordinate System for the Proximal Humerus	87
Figure 3.3: Visualization of the Proximal Humerus' Canal Path Results	89
Figure 3.4: Visualization of the Proximal Humerus' Fitted Canal Diameter Results	90
Figure 3.5: Sample Linear Regression Between Canal Diameter and Subject Height (Slice 4)	93
Figure 3.6: Histogram of the Proximal Humerus' Resection Depth Results.....	94
Figure 3.7: Linear Regression Between the Proximal Humerus' Resection Depth and Resection Diameter	95
Figure 3.8: Linear Regression Between the Proximal Humerus' Resection Depth and Subject Height	96
Figure 3.9: Histogram of the Proximal Humerus' Articular Aspect Ratio Results	98
Figure 4.1: Humeral Joint Reaction Force Application.....	109
Figure 4.2: Density-Modulus Relationships Applied to the Proximal Humerus.....	111

Figure 4.3: Implant-Bone Contact Percentage Results	113
Figure 4.4: Inhomogeneous Anatomic-Site Change in Bone Stress Results (45°)	114
Figure 4.5: Inhomogeneous Anatomic-Site Change in Bone Stress Results (75°)	115
Figure 4.6: Homogeneous-Inhomogeneous Change in Bone Stress Results (45°)	118
Figure 4.7: Homogeneous-Inhomogeneous Change in Bone Stress Results (75°)	119
Figure 4.8: Inhomogeneous Anatomic-Site Potential Time-Zero Bone Response Results for Cortical Bone (45°).....	121
Figure 4.9: Inhomogeneous Anatomic-Site Potential Time-Zero Bone Response Results for Cortical Bone (75°).....	122
Figure 4.10: Homogeneous-Inhomogeneous Potential Time-Zero Bone Response Results for Cortical Bone (45°).....	124
Figure 4.11: Homogeneous-Inhomogeneous Potential Time-Zero Bone Response Results for Cortical Bone (75°).....	125
Figure 4.12: Inhomogeneous Anatomic-Site Potential Time-Zero Bone Response Results for Trabecular Bone (45°)	127
Figure 4.13: Inhomogeneous Anatomic-Site Potential Time-Zero Bone Response Results for Trabecular Bone (75°)	128
Figure 5.1: The Division and Coordinates of the Proximal Humerus	142
Figure 5.2: Stemless Implants Used for Humeral Reconstruction	143
Figure 5.3: Implant-Bone Contact Results for All Stemless Implants	147
Figure 5.4: The Percentage Change in Anterior Quadrant Cortical Bone Stress Results for All Stemless Implants	148
Figure 5.5: The Percentage Change in Posterior Quadrant Cortical Bone Stress Results for All Stemless Implants	149
Figure 5.6: The Percentage Change in Medial Quadrant Cortical Bone Stress Results for All Stemless Implants	150
Figure 5.7: The Percentage Change in Lateral Quadrant Cortical Bone Stress Results for All Stemless Implants	151
Figure 5.8: The Percentage Change in Anterior Quadrant Trabecular Bone Stress Results for All Stemless Implants	153
Figure 5.9: The Percentage Change in Posterior Quadrant Trabecular Bone Stress Results for All Stemless Implants	154

Figure 5.10: The Percentage Change in Medial Quadrant Trabecular Bone Stress Results for All Stemless Implants	155
Figure 5.11: The Percentage Change in Lateral Quadrant Trabecular Bone Stress Results for All Stemless Implants	156
Figure 5.12: The Potential Time-Zero Cortical Bone Response for All Stemless Implants (45° Abduction)	158
Figure 5.13: The Potential Time-Zero Cortical Bone Response for All Stemless Implants (75° Abduction)	159
Figure 5.14: The Potential Time-Zero Trabecular Bone Response for All Stemless Implants (45° Abduction)	162
Figure 5.15: The Potential Time-Zero Trabecular Bone Response for All Stemless Implants (75° Abduction)	163
Figure C.1: Model run time broken down according to mesh size and abduction angle.	199
Figure C.2: Implant bone contact pressure distribution for all mesh sizes, shown for loading corresponding to both 45° (A) and 75° (B) of abduction.	201
Figure C.3: Comparison of the change in bone stress outcome measure between different mesh sizes for both cortical and trabecular bone at 45° and 75° of abduction.	203
Figure C.4: Direct comparison of the difference in the change in bone stress outcome measure between 2.0mm and 1.0mm mesh sizes.....	204
Figure C.5: Time-zero potential bone response of cortical bone subject to 45° loading.	205
Figure C.6: Time-zero potential bone response of trabecular bone subject to 45° loading.....	206
Figure C.7: Time-zero potential bone response of cortical bone subject to 75° loading.	207
Figure A.C: Time-zero potential bone response of trabecular bone subject to 75° loading.....	208
Figure D.1: Experimental Specimen Orientation Apparatus	216
Figure D.2: Experimental and FE Humerus Load Application	218
Figure D.3: Strain Gauge and Node Pair Locations in Experimental and FE Models	220
Figure D.4: Linear Correlation Plots for the Intact and Reconstructed State	222
Figure D.5: Bland-Altman Plots for the Intact and Reconstructed States	224
Figure D.6: Linear Regression and Bland-Altman Plots for the Change in Strain Following Humeral Reconstruction	227
Figure F.1: Process flow diagram, outlining the sequence of events for the phantom-only, regression and standard calibration methods.	240

Figure F.2: Plots of mean \pm SD ash density percent difference (relative to proper calibration equation terms) for both phantom-only and regression calibration methods.	246
Figure F.3: Bland-Altman plots for density calibration equation slope and vertical intercept terms, comparing phantom-only and regression calibration methods.	247
Figure H.1: Additional Views of the Stemless Implant Articular Component.....	265
Figure H.2: Additional Views of the PegStraight Stemless Fixation Feature	266
Figure H.3: Additional Views of the PegAnatomic Stemless Fixation Feature	267
Figure H.4: Additional Views of the Peripheral4x5S Stemless Fixation Feature	268
Figure H.5: Additional Views of the Peripheral4x5A Stemless Fixation Feature	269
Figure H.6: Additional Views of the Peripheral4x10S Stemless Fixation Feature	270
Figure H.7: Additional Views of the Peripheral4x10A Stemless Fixation Feature	271
Figure H.8: Additional Views of the QuadFlange Stemless Fixation Feature	272
Figure H.9: Additional Views of the HexFlange Stemless Fixation Feature	273
Figure H.10: Additional Views of the QuadPeg Stemless Fixation Feature	274
Figure H.11: Additional Views of the HexPeg Stemless Fixation Feature	275
Figure I.1: Summary of Statistical Differences for the Change in Cortical Bone Stress Outcome	277
Figure I.2: Summary of Statistical Differences for the Change in Trabecular Bone Stress Outcome	278
Figure I.3: Summary of Statistical Differences for the Time-Zero Potential Resorbing Response of Cortical Bone.....	279
Figure I.4: Summary of Statistical Differences for the Time-Zero Potential Unchanged Response of Cortical Bone.....	280
Figure I.5: Summary of Statistical Differences for the Time-Zero Potential Remodeling Response of Cortical Bone.....	281
Figure I.6: Summary of Statistical Differences for the Time-Zero Potential Resorbing Response of Trabecular Bone	282
Figure I.7: Summary of Statistical Differences for the Time-Zero Potential Unchanged Response of Trabecular Bone	283
Figure I.8: Summary of Statistical Differences for the Time-Zero Potential Remodeling Response of Trabecular Bone	284
Figure J.1: von Mises Plots of Specimen 1's Cortical Shell for Loading at 45° of Abduction....	285
Figure J.2: von Mises Plots of Specimen 1's Trabecular-Canal for Loading at 45° of Abduction	286

Figure J.3: von Mises Plots of Specimen 1’s Cortical Shell for Loading at 75° of Abduction....	287
Figure J.4: von Mises Plots of Specimen 1’s Trabecular-Canal for Loading at 75° of Abduction	288
Figure J.5: von Mises Plots of Specimen 2’s Cortical Shell for Loading at 45° of Abduction....	289
Figure J.6: von Mises Plots of Specimen 2’s Trabecular-Canal for Loading at 45° of Abduction	290
Figure J.7: von Mises Plots of Specimen 2’s Cortical Shell for Loading at 75° of Abduction....	291
Figure J.8: von Mises Plots of Specimen 2’s Trabecular-Canal for Loading at 75° of Abduction	292
Figure J.9: von Mises Plots of Specimen 3’s Cortical Shell for Loading at 45° of Abduction....	293
Figure J.10: von Mises Plots of Specimen 3’s Trabecular-Canal for Loading at 45° of Abduction	294
Figure J.11: von Mises Plots of Specimen 3’s Cortical Shell for Loading at 75° of Abduction..	295
Figure J.12: von Mises Plots of Specimen 3’s Trabecular-Canal for Loading at 75° of Abduction	296
Figure J.13: von Mises Plots of Specimen 4’s Cortical Shell for Loading at 45° of Abduction..	297
Figure J.14: von Mises Plots of Specimen 4’s Trabecular-Canal for Loading at 45° of Abduction	298
Figure J.15: von Mises Plots of Specimen 4’s Cortical Shell for Loading at 75° of Abduction..	299
Figure J.16: von Mises Plots of Specimen 4’s Trabecular-Canal for Loading at 75° of Abduction	300
Figure J.17: von Mises Plots of Specimen 5’s Cortical Shell for Loading at 45° of Abduction..	301
Figure J.18: von Mises Plots of Specimen 5’s Trabecular-Canal for Loading at 45° of Abduction	302
Figure J.19: von Mises Plots of Specimen 5’s Cortical Shell for Loading at 75° of Abduction..	303
Figure J.20: von Mises Plots of Specimen 5’s Trabecular-Canal for Loading at 75° of Abduction	304

List of Appendices

Appendix A – Glossary	188
Appendix B – Copyright License for Figure 1.3	192
Appendix C – Mesh Convergence	197
C.1 Materials and Methods	197
C.2 Results	198
C.3 Discussion	200
C.4 References	211
Appendix D – Finite Element Validation	213
D.1 Introduction	213
D.2 Materials and Methods	215
D.2.1 Experimental Model	215
D.2.1.1 Specimen Preparation	215
D.2.1.2 Experimental Protocol	215
D.2.2 Computational Model	217
D.2.3 Comparative Metrics	219
D.3 Results	221
D.4 Discussion	225
D.5 Conclusions	230
D.6 References	230
Appendix E – Ethics Approval	234
Appendix F – Post-Hoc CT Calibration Methods	235
F.1 Introduction	235
F.2 Materials and Methods	236
F.3 Results	241
F.4 Discussion	244
F.5 References	250
Appendix G - Creating Masks and Solid Body Models of Bone	254
G.1 Introduction	254
G.2 Bone Masking Methods	254
G.2.1 The Proximal Humerus Mask	254
G.2.2 The Trabecular Mask	257

G.3 Solid Body Modeling in SolidWorks	259
G.4 In-Silico Humeral Head Resection and Positioning a Stemless Implant	261
G.4.2 Resection Coordinates and Stemless Implant Positioning	262
G.4.3 Stemless Implant Positioning	263
G.4.4 Cutting the Implant’s Fixation Features out of the Bone	263
Appendix H – Generic Stemless Implant Details	265
Appendix I – Supplementary Significance Tables for Stemless Implant Assessment	276
Appendix J – von Mises Stress Plots for Chapter 5 FE Models	285

Nomenclature

Δ	Change
$^{\circ}$	Degree
ρ	Density
μ	Micro
σ	Stress
ε	Strain
2D	Two-Dimensional
3D	Three-Dimensional
4D	Four-Dimensional
BMD	Bone Mineral Density
cm	Centimeter
CPRESS	Contact Pressure
CT	Computed Tomography
E	Elastic (Young's) Modulus
FE	Finite Element
g	Grams
HU	Hounsfield Units
mm	Millimeter
RoM	Range-of-Motion
U, SED	Strain Energy Density

Chapter 1

Introduction

It is often necessary to rely on collaborative knowledge to advance the understanding of complicated questions. One example of this is the application of mechanical engineering tools, such as the Finite Element (FE) method, in the field of orthopaedics. With the improvement of computational power easing the burden of analyzing complicated models, in-silico engineering methods are becoming more popular. The present investigation relies on mechanical engineering tools, including three-dimensional (3D) modelling and FE analysis, to improve the understanding of stemless implants for humeral reconstruction during shoulder arthroplasty. This chapter provides an introduction to the anatomy of the shoulder (focusing on the proximal humerus), as well as an overview of shoulder arthroplasty and the engineering tools utilized within this thesis, followed by the specific objectives and hypotheses.*

1.1 Anatomy of the Shoulder

The shoulder is a complicated assembly that is comprised of three bones, along with several ligaments and musculotendinous units, which function together to form three principle joints (*i.e.*, glenohumeral, sternoclavicular and acromioclavicular joints), as well as two lesser articulations (*i.e.*, scapulothoracic and subacromial articulations) (Figure 1.1). When acting in unison these anatomical constructs appear to function as a single joint, known more colloquially as the shoulder. The complicated motions performed by the shoulder, which can exceed the range-of-motion (RoM) of a simple ball-in-socket [1,2], are only possible through the collective action of these articulations. Together, the joints of the shoulder articulate with the support and action of soft tissues (*i.e.*, ligaments, musculotendinous units, *etc.*) to provide the greatest RoM in all three anatomic planes

* Due to the clinical and technical nature of this investigation, a glossary can be found in Appendix A.

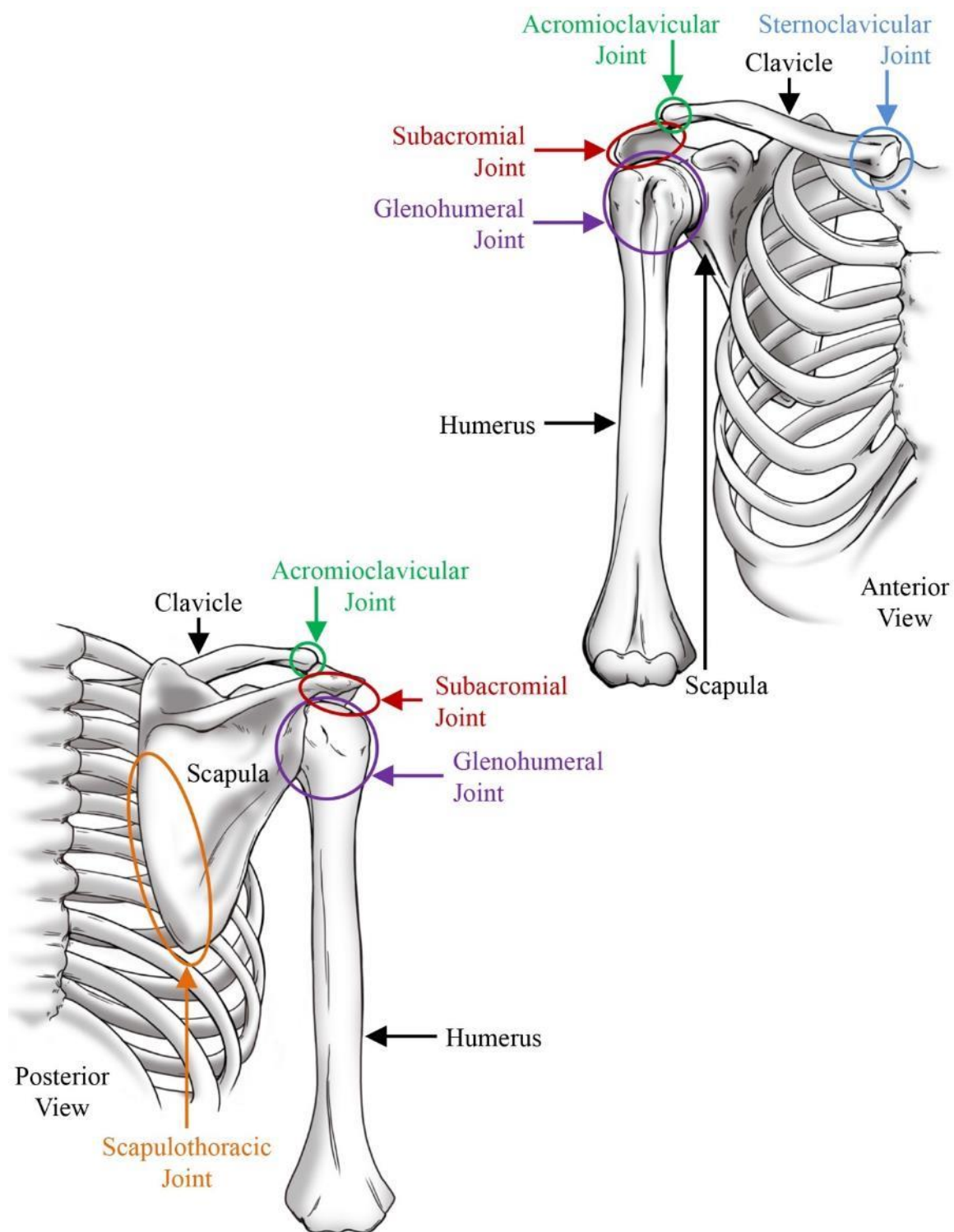


Figure 1.1: Joints of the Shoulder

The shoulder is comprised of five joints, the primary of which is the glenohumeral articulation.

(coronal, sagittal and transverse) of any articulation in the body [1,2]. Unfortunately, the function and motion of the shoulder can be negatively impacted by the injury of any of the many sub-components outlined above [3].

1.1.1 The Glenohumeral Joint

The glenohumeral joint contributes the largest RoM to the shoulder [4–8]. It is a ball-in-socket style articulation that can be categorized into its osseous constructs (*i.e.*, bones), soft tissues (*i.e.*, ligaments, musculotendinous units) and joint capsule. It is formed by the articulation between the glenoid fossa (a dish-like cartilage-coated surface extending laterally outwards from the scapula) and the humeral head (a convex hemisphere atop the humerus that is angled medially, posteriorly and superiorly) (Figure 1.1).

An understanding of the joint reaction forces that exist between the glenoid and humerus is critical to the analysis of shoulder arthroplasty. *In-vitro* analyses [9–11], along with musculoskeletal computational models [12,13], have been developed to quantify contact within the glenohumeral joint; however, due to the number of muscles that contribute to joint positioning, there exist too many unknowns to properly calculate the glenohumeral joint reaction force. Accordingly, Bergmann *et al* have developed a telemetrized shoulder implant to directly measure the *in-vivo* loads passing through the glenohumeral joint following arthroplasty [14–16]. While their findings are reflective of post-operative loads, the magnitudes and orientations of forces that they report are the most reliable source of glenohumeral joint reaction forces available in the literature; and suggest that loads within the shoulder can exceed a bodyweight, despite it not being a weight-bearing joint.

1.1.2 Motions of the Shoulder

Movement of the upper arm (*i.e.*, the humerus) relative to the axial skeleton is commonly reported *via* four motions: axial rotation, elevation, forward flexion, and horizontal flexion-extension (Figure 1.2). These gross shoulder movements are the consequence of the independent motions of both the humerus and scapula. Axial rotation refers to motion about the diaphyseal axis of the humerus and can be classified as either internal or external rotation. Elevation refers generally to lateral movement of the arm away from

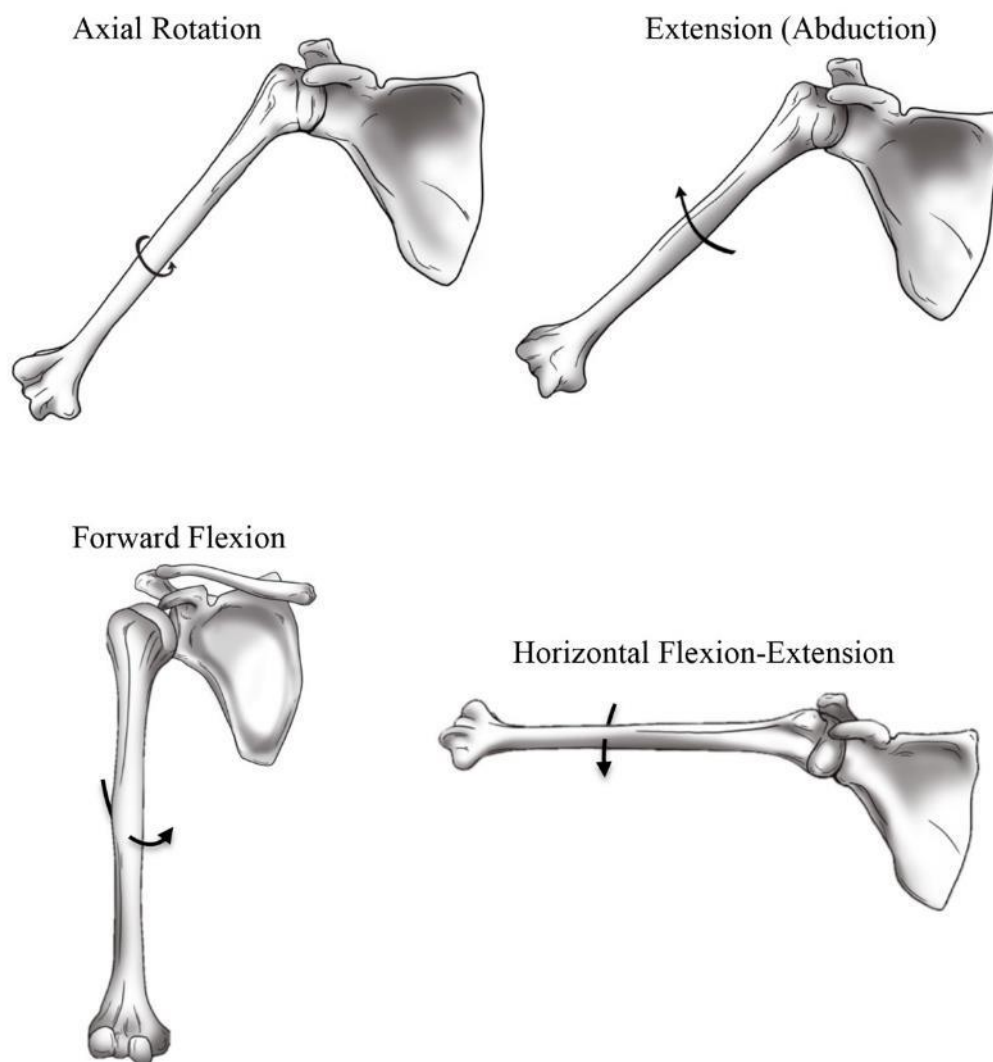


Figure 1.2: Basic Movements of the Shoulder

The complex motions performed by the shoulder can be broken down into four basic movements: axial rotation, extension (abduction), forward flexion and horizontal flexion-extension.

the body. Though elevation solely in the coronal plane is possible, from a biomechanics perspective it is often advantageous to describe elevation which takes place in the scapular plane ($\sim 30^\circ$ anterior); as this is where the deltoid and supraspinatus are better aligned to produce elevation [17,18]. For the remainder of this thesis, elevation within the scapular plane will be referred to as abduction. Abduction is typically limited to 167° for men and 171° for women, though it can exceed 180° [17]. Forward flexion is a special case of elevation in which the motion of the humerus is away from the body in the anterior direction. Finally, horizontal flexion-extension refers to the anterior-posterior movement of the humerus constrained to the horizontal plane; it is often associated with throwing motions in sports. The division between positions of horizontal flexion and extension is generally regarded as the scapular plane. In the case of a healthy shoulder, maximum glenohumeral stability can be achieved when the arm is placed in this plane and externally rotated [17]; however, the opposite is true for this position (and moving the arm further posterior) if the shoulder is compromised by anterior instability [19].

1.1.3 Glenohumeral Soft Tissue Constructs

1.1.3.1 Passive Soft Tissues – Ligaments and Joint Capsule

Stability of the glenohumeral joint is provided in-part by passive soft tissues including several ligaments, the glenoid labrum and the joint capsule, which are engaged through the relative movement of the glenoid and humerus, as opposed to contractile action. The glenoid labrum is a fibrocartilaginous tissue that surrounds the glenoid's articular dish, increasing the depth and conformity of the glenohumeral articulation without resisting motion as much as an osseous construct, while also serving as an attachment site for several glenohumeral ligaments [1,20]. Another important passive soft tissue is the joint capsule, which is a thin membrane that surrounds the glenohumeral articulation, connecting the glenoid labrum and rim medially with the articular margin of the humeral head laterally. The capsule encloses the joint and provides nutrients and synovial fluid to the articulation. For the glenohumeral joint, the capsule can become tensioned when at the extremes of the shoulder's RoM, but usually remains relatively loose [2].

Collectively, these passive soft tissues assist with stabilized joint motion in a way that

osseous constructs cannot; by resisting tensile loads while permitting compressive deformation [1,21–24].

1.1.3.2 Active Soft Tissues – Muscles

The motions observed by the glenohumeral joint are a consequence of the action of several muscles working together to orient the joint in space and assist with stability. These muscles are generally categorized using the bones between which they originate and terminate. The scapulohumeral muscles (which originate on the scapula and terminate on the humerus) include: the coracobrachialis, deltoid, infraspinatus, subscapularis, supraspinatus, teres major and teres minor. Of these, the deltoid provides up to 50% of the total abduction moment for the humerus [23], and can be divided into independently functioning anterior, middle and posterior sub-sections, based on where it originates along the acromion (of the scapula) and the clavicle. The deltoid then traverses the glenohumeral joint and terminates on the lateral aspect of the humerus' diaphysis at the deltoid tuberosity.

Another important musculotendinous construct of the shoulder is the rotator cuff, which provides some abduction and axial rotation moments [3] as well as stability during joint motion [1]. It is composed of several scapulohumeral muscles (infraspinatus, subscapularis, supraspinatus and teres minor), along with their associated tendons, and some passive stabilizers (ligaments and the joint capsule). Though individual activation of these muscles is possible, the interconnected nature of the rotator cuff can cause the passive tension of some components to be influenced by the loading of others [25].

In addition, humerothoracic muscles (originate on the thoracic cage and terminate on the humerus) of the latissimus dorsi and pectoralis major can also influence glenohumeral motion. Both muscles are associated with adductive motions, as well as internal rotation of the humerus, but the latissimus dorsi assists with extension, while the pectoralis major contributes to flexion [26,27]. Three biarticular muscles (*i.e.*, the short and long heads of the biceps brachii, and the triceps brachii) originate on the scapula, cross the glenohumeral joint, and terminate on the bones of the forearm (*i.e.*, the ulna and radius).

While these biarticular muscles primary functions pertain to elbow motion, they can provide resistance to shear forces and assist with overall glenohumeral stability [17,28].

1.1.4 Glenohumeral Osseous Constructs

1.1.4.1 Bone Structure and Elastic Properties

Bone is an integral part of the body, supporting loads and working with soft tissues to carry the mass of the body throughout a variety of motions [29,30]. The long bones of the appendicular skeleton (*i.e.*, the arms, legs, *etc.*) are composite structures that can be divided into two types: cortical and trabecular (Figure 1.3). Regionally, these bones are also segmented into three sub-sections corresponding to: the epiphysis (cortical and trabecular structures that are nearest to the articular surface of a bone), the diaphysis (cortical structure and hollow canal that forms the shaft) and the metaphysis (cortical and trabecular structures that transition between the epiphysis and diaphysis).

As a material, bone is also a composite, formed of both organic (*i.e.*, type I collagen, noncollagenous proteins, proteoglycans and phospholipids) and inorganic (*i.e.*, calcium phosphate hydroxyapatite) matter that together provide the resilience and strength necessary to support and respond to the environment in which we live [31]. The organic collagen provides the bone with viscoelastic properties, varying the strength and stiffness of the structure as a function of loading rate. It is also important to note that bone is an optimized structure that is constantly undergoing cellular destruction and restructuring to provide adequate stiffness while minimizing mass [29,32]. Cells known as osteoclasts and osteoblasts are responsible for the removal (*i.e.*, resorption) and addition (*i.e.*, remodeling) of bone tissue, respectively [33,34].

Cortical bone is a dense and macroscopically uniform material that forms the outer ‘shell’ of the bone. On a microscopic scale, cortical bone is formed by elongated cells (osteons) that typically run parallel to the bone’s diaphysis. Trabecular bone is less uniform, macroscopically appearing sponge-like, and is composed of a branching structure of individual trabeculae, which produce an anisometric and inhomogeneous layout that is aligned to accommodate the transfer and dispersion of loads through the epiphyseal and metaphyseal regions of the bone [35].

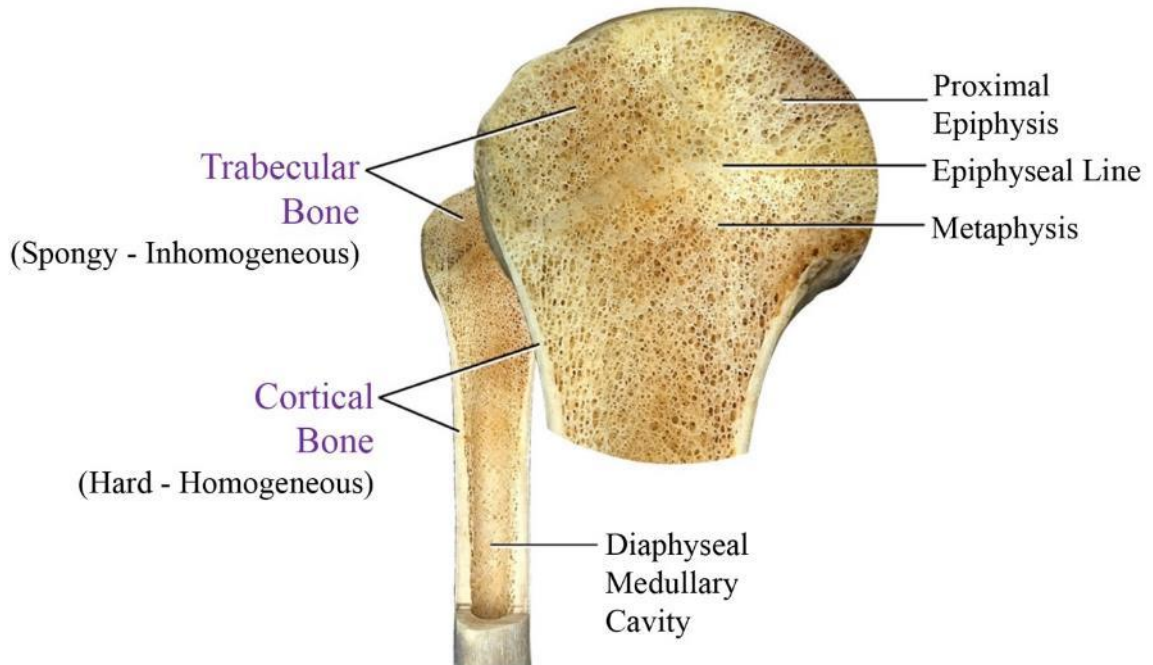


Figure 1.3: Cortical and Trabecular Bone

Bone is a composite material consisting of a hard, dense cortical shell and spongy trabecular bone. Long bones are further divided into the epiphysis, diaphysis and metaphysis. Figure adapted with permission from “Principles of Human Anatomy” 12th edition by Tortora (see Appendix B).

The compressive and tensile stiffness of a structure is defined by its elastic (*i.e.*, Young's) modulus (commonly denoted by the letter 'E'). Due to its macroscopic homogeneity, cortical bone is generally regarded as having a constant stiffness of approximately 20GPa [36–38]. Conversely, the stiffness of trabecular bone varies both by region, and the scale at which it is investigated. It can be a challenge to test the stiffness of individual trabeculae; however, regionally varying stiffness has been well correlated with changes in apparent bone density [39–42]. Accordingly, Computed Tomography (CT) imaging techniques are commonly used to quantify regional shifts in bone density, through the use of CT scans that are calibrated to convert radiation attenuation into bone density in small cubic regions known as voxels (typically on the scale of about a millimeter cubed). At this scale, correlations between trabecular bone density and elastic modulus are developed through compressive loading of small bone segments, whose elastic response is monitored under known loads [40,43–45].

1.1.4.2 The Scapula

The scapula, more commonly known as the shoulder blade, is the triangular bone that connects the upper extremity to the axial skeleton. It aids in positioning the arm in space by hosting the initiation of several ligaments and musculotendinous units that are required for shoulder motion [20]. The compressive joint reaction forces of the glenohumeral articulation are transferred to the scapula by the concave cartilage covered surface of the glenoid fossa, which extends laterally from the scapula to meet the humeral head (Figure 1.4). In addition, the scapula has two lateral protrusions, the acromion and the coracoid, which extend superior to the glenohumeral joint on the posterior and anterior sides, respectively, and serve as insertion sites for several muscles. The scapular spine is another boney protrusion that forms a ridge-like structure along the posterior and superior aspect of the scapula. The curved shape of the scapula's anterior face mates with the posterior rib-cage to form the scapulothoracic joint, which permits the scapula to slide dynamically over the ribcage during shoulder motion. This movement is commonly attributed 1/3 of the motion of total shoulder elevation, with the balancing 2/3 of elevation attributed to the glenohumeral joint [46].

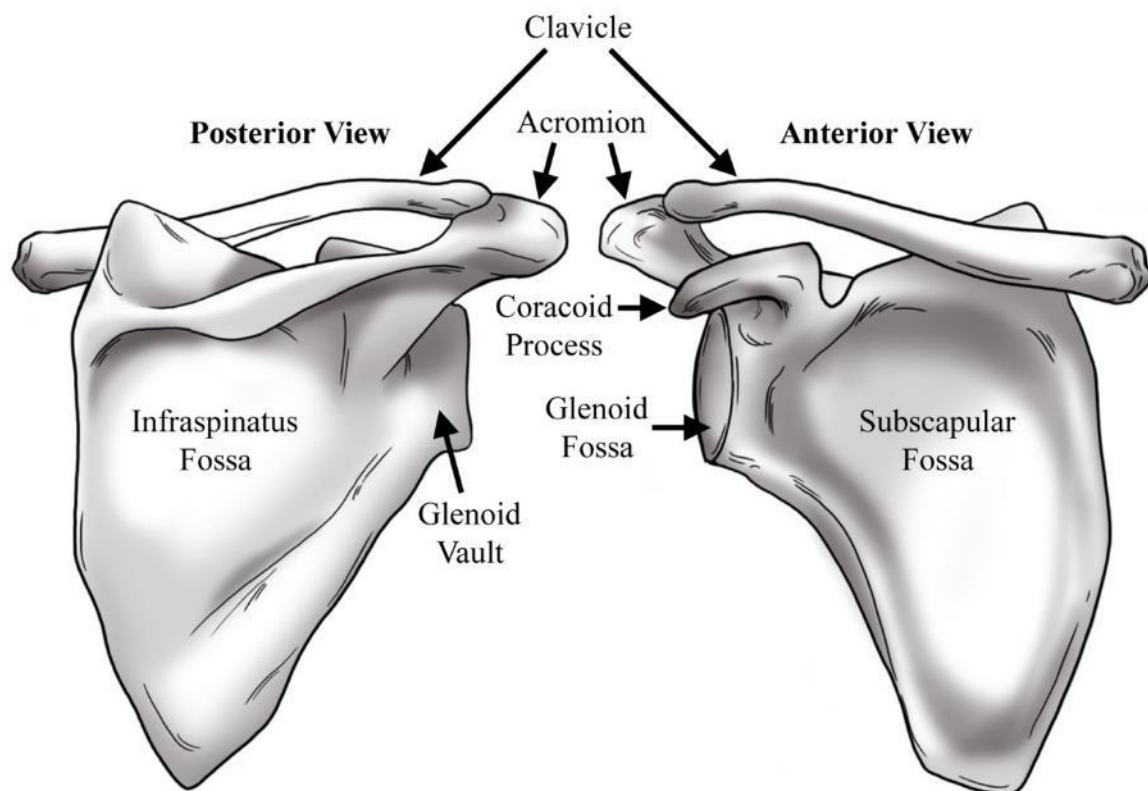


Figure 1.4: The Bony Anatomy of the Scapula

The scapula (shoulder blade) is a triangular bone that transmits shoulder loads into the axial skeleton. Of particular interest is the glenoid fossa, which supports glenohumeral articulation.

1.1.4.3 The Proximal Humerus

The humerus is the long bone of the proximal upper extremity, which connects the articulations of the shoulder and elbow. Its role is to transfer the loads of the upper extremity to the scapula, and to position the hand and arm in space. The key landmarks of the proximal humerus are the humeral head, the greater tuberosity, the lesser tuberosity and the bicipital groove (Figure 1.5). The humeral head is a hemispherical articular surface covered in cartilage (nearly uniform in thickness) [47,48], which is oriented posteriorly, superiorly and medially [20]. The bicipital groove is the trough formed between the greater and lesser tuberosities, which are lateral to the humeral head and serve as the insertion site for some of the rotator cuff muscles. In addition, the greater tuberosity provides mechanical advantage for shoulder motion by elevating supraspinatus above 30° of abduction and permitting deltoid wrapping below 60° [26,28]. Distal humeral landmarks include the deltoid tuberosity, where the deltoid inserts along the lateral side of the mid-diaphysis, and the medial and lateral epicondyles. While the distal epicondyles do not contribute to shoulder motion, they often act as landmarks that can be used to form humeral-based coordinate systems [49].

Several studies have been undertaken to quantify the gross structural morphology of the proximal humerus [50–54]. On average, the humerus is reported to be 33cm in length, with a head center offset posteriorly by 2mm and medially by 7mm from the humeral axis [50]. The humeral head is reported to have a radius of curvature ranging from 17mm to 32mm [50–54], and a thickness ranging from 12mm to 24mm [50–53]. It has been suggested by Robertson *et al* that morphological variability is an important factor that should influence implant selection and design [50]. As such, with the leading cause of shoulder arthroplasty being osteoarthritis, variation in the density and morphology of sub-articular trabecular bone should also be of interest. This is supported by studies of hip arthroplasty, which demonstrate that bone density at the time of surgery is an important factor that is inversely correlated to peri-implant bone loss following joint reconstruction [55–58].

Unfortunately, to date few studies have investigated the regional variation of trabecular bone quality in the proximal humerus, as it pertains to arthroplasty [59–62]. Some studies

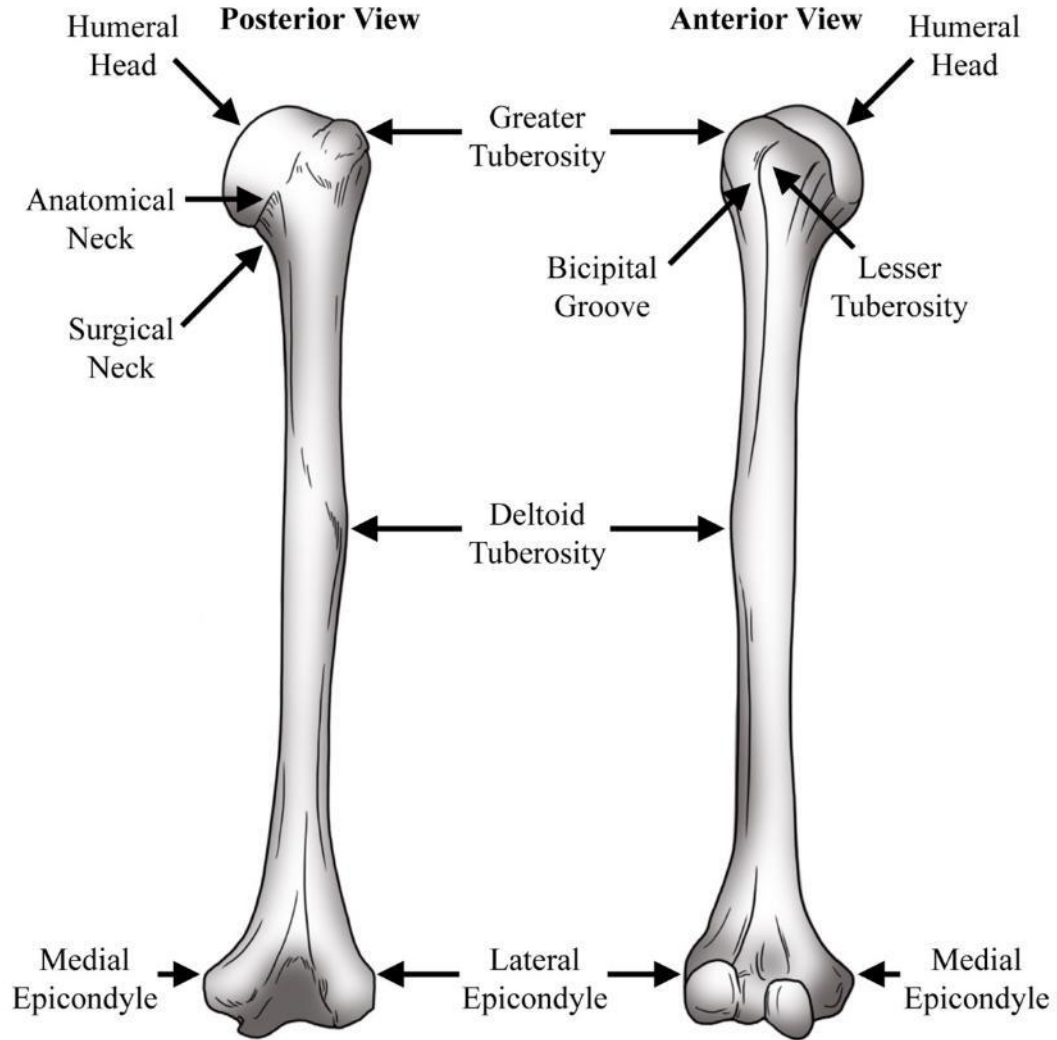


Figure 1.5: The Bony Anatomy of the Humerus

The humerus is the long bone of the upper arm, whose proximal articular surface, the humeral head, articulates with the glenoid of the scapula to form the glenohumeral joint.

have reported regional variations in subchondral bone density in the proximal humerus using CT osteoabsorbtiometry (CT-OAM), which uses intensity plots of Hounsfield Units (HU) projected onto the articular surface [60,61]. These methods have demonstrated that 71-79% of humeri exhibited bicentric density distribution patterns (with posterior and anterior maxima), and that 21-29% were classified with a monocentric (centro-posterior) maxima. Unfortunately, by projecting density data onto the articular surface of the humerus, these studies included tissue that was above the humeral head resection plane and prevented a truly 3D understanding of the density distribution.

Yamada *et al* (2007) performed an age-based assessment of bone density in the proximal humerus and found that the medial region of every bone (n = 41) consisted of more bone tissue than the lateral side; however, the coordinate system of their region of interest was aligned with the humerus' diaphyseal axis, and did not include all of the medial bone beneath a typical proximal humerus arthroplasty resection plane [62]. Similarly, Hepp *et al* found that the medial and dorsal aspects of the proximal humerus were of the greatest strength, but bone slices were again aligned with the diaphyseal axis as opposed to a coordinate system that would reflect bone tissue available post-resection of the humeral head [59]. This study also used a cadaveric population that was free of osteoarthritis and focal bone diseases. As such, the results may not be consistent with a clinical population receiving humeral arthroplasty. Only one study has investigated the distribution of humeral bone density in a 3D coordinate system that is relative to the humeral head resection plane [63]. In that 2017 investigation, Alidousti *et al* found that the humeral density increased peripherally and above the humeral epiphyseal plate, but the population size was small (n = 8), and again, they did not include osteoarthritic humeri.

Accordingly, there is a need to identify the regional variation in bone density remaining post-resection during humeral arthroplasty within a clinically relevant population; and to map out canal-based landmarks to assist with the sizing and design of humeral implants.

1.2 Shoulder Arthroplasty

Originally developed by Neer in the 1950's, shoulder arthroplasty (*i.e.*, shoulder reconstruction or replacement) is a surgical procedure used to treat severe degradation of

the shoulder joint by replacing the damaged or diseased tissue with an engineered implant [64,65]. The purpose of this procedure is to alleviate pain for the patient, while restoring more natural biomechanics and RoM. Through reconstruction of the articular surface, shoulder arthroplasty attempts to mimic the glenohumeral joint by replacing the natural anatomy with a ball-in-socket style assembly (Figure 1.6). Traditionally, this is done by replacing the glenoid surface with an open dish, while the dome of the humeral head is reconstructed by a hemispherical component [66]. This form of reconstruction is referred to as ‘anatomic’ shoulder arthroplasty. The anatomic procedure can be divided further into two forms, anatomic Total Shoulder Arthroplasty (TSA), whereby both sides of the joint (*i.e.*, the glenoid dish and humeral head) are reconstructed with implants; and hemiarthroplasty, where only one side (either the glenoid dish or the humeral head) is replaced by an implant, while the other side remains anatomically intact. In addition, to increase the utility of the deltoid muscle for abduction, the ‘Reverse’ Shoulder Arthroplasty (RSA) procedure has been introduced. This procedure is only performed as a total arthroplasty, as it reverses the natural ball-in-socket form of the glenohumeral joint by reconstructing the glenoid dish with a hemisphere and replacing the humeral head with a concave dish [66]. The focus of the present body of work pertains to the humeral component of anatomic shoulder arthroplasty.

1.2.1 The Implants of Anatomic Shoulder Arthroplasty

1.2.1.1 *The Glenoid Implant*

Briefly, the glenoid implant, if required, is used to reconstruct the natural socket of the glenohumeral joint. It can be broken down into the ‘dish component’, which is the articulating surface of the implant, and the ‘fixation component’, which is generally formed by several pegs or a keel that protrudes medially from the backside of the dish; and is responsible for stabilizing the dish component within the underlying bone [66].

1.2.1.2 *The Humeral Implant*

Similarly, the humeral component for anatomic shoulder arthroplasty can be subdivided into the ‘head (or articular) component’ and the ‘fixation component’. As above, the head component is responsible for maintaining unimpeded articulation with the glenoid, and is

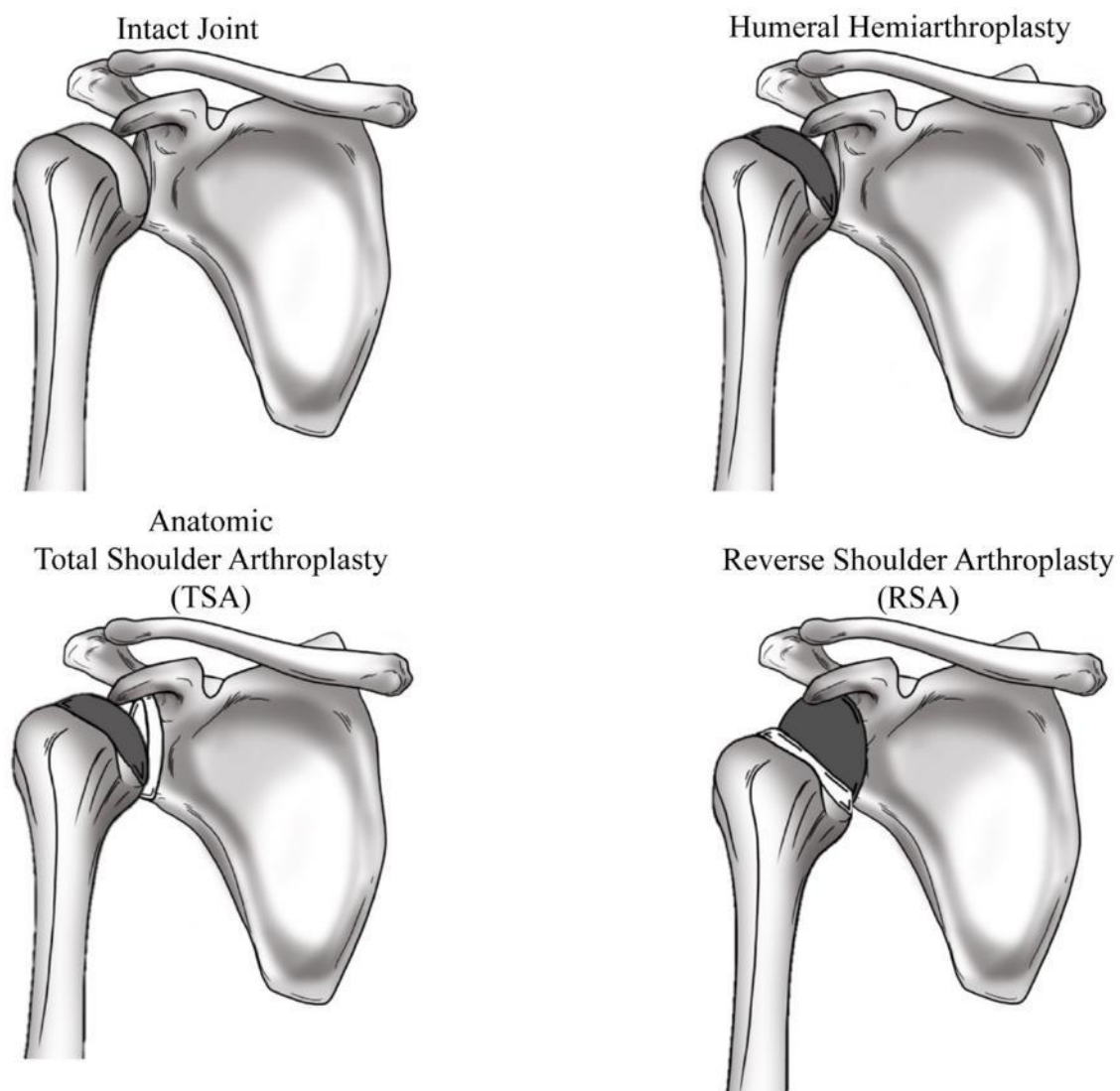


Figure 1.6: Forms of Shoulder Arthroplasty

When an intact joint is damaged, it can be reconstructed either to mimic the native anatomy (TSA, hemiarthroplasty) or to reverse the native anatomy (RSA).

generally formed by an axisymmetric hemisphere, that is usually constructed from a hard metal such as cobalt chrome [66]. While the humerus' anatomic articular surface is not axisymmetric, the head component of humeral implants maintains an axisymmetric shape to provide a more uniform contact throughout the shoulder's RoM.

The fixation component of the humeral implant has been the focus of several design iterations. The style of fixation component can be used to classify humeral implants into three general forms: standard stemmed, short stemmed and stemless (*i.e.*, metaphyseal) (Figure 1.7). Originally, humeral implants were introduced with long stems that were seated in the canal of the diaphysis [64,65], but distal cortical impingement was found to produce severe stress shielding that could lead to implant failure [67–70]. Accordingly, implant designers reduced the length of the implant stem to avoid seating the fixation component where the canal narrowed to the point of impingement. In 2004 a group of French designers introduced the first stemless humeral implant, the Total Evolutive Shoulder System (TESS; Biomet, Warsaw, IN, USA), which sought fixation exclusively in the trabecular bone of the metaphyseal region in the proximal humerus [71]. Since then, several other manufacturers have also released stemless implants for shoulder arthroplasty.

1.2.2 Indications for Shoulder Arthroplasty

Since its inception for the reconstruction of comminuted fractures to the humeral head [64], shoulder arthroplasty has become a treatment for several disorders of the shoulder including: osteoarthritis, avascular (*i.e.*, aseptic) necrosis, disorders of bursae and tendons, rheumatoid arthritis and other arthropathies of the shoulder (including rotator cuff tear) [65,72,73].

The incidence of total and hemiarthroplasty of the shoulder has been increasing in recent years [72–74]. In 2008 nearly 47,000 shoulder arthroplasty procedures were conducted in the United States (57% pooled: TSA and RSA, 43% hemiarthroplasty) [73], and as of 2011 this number exceeded 66,000 (44% TSA, 23% hemiarthroplasty, 33% RTSA) [72]. Based on Schairer *et al*'s assessments in 2011, the leading indications for TSA were osteoarthritis (93%), followed by avascular necrosis (2%), inflammatory arthritis (1%)

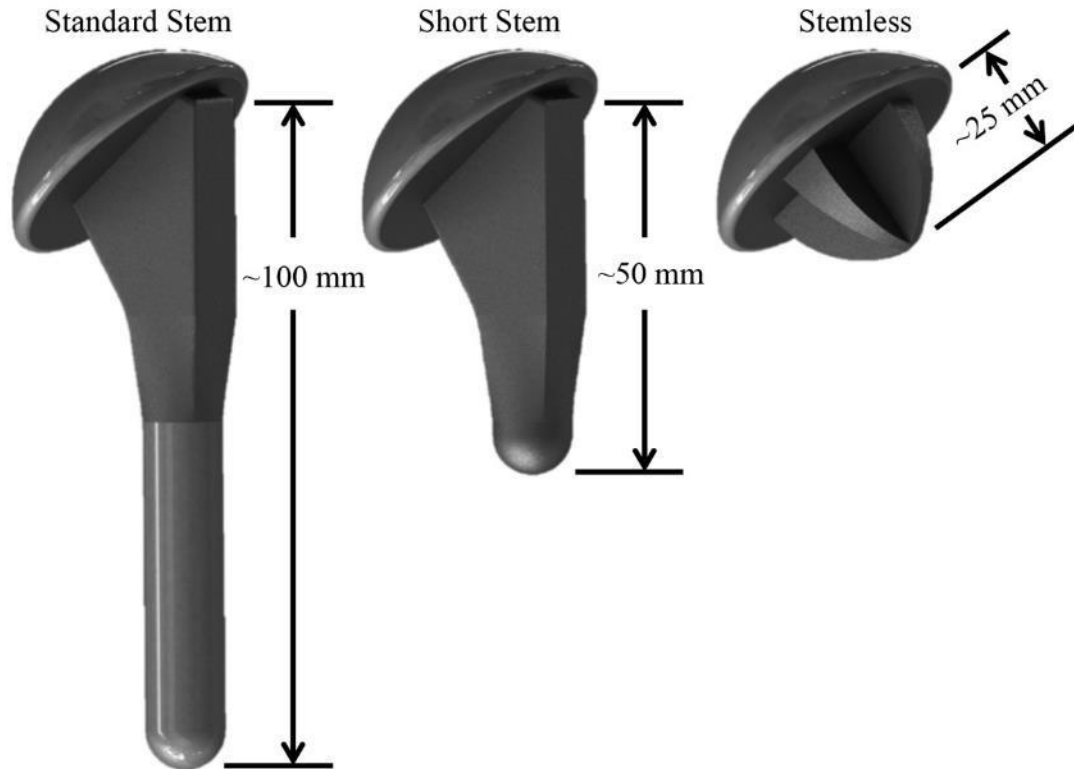


Figure 1.7: Evolution of Shoulder Arthroplasty Humeral Components

In the hopes of reducing the impact of humeral implants and to preserve more bone tissue, humeral implants have evolved from long (*i.e.*, standard) stems, to short stems, and now stemless implants that seek metaphyseal fixation without diaphyseal penetration.

and proximal humerus fractures (1%). For hemiarthroplasty, osteoarthritis was again the most prominent indication, accounting for 45% of procedures, followed by proximal humerus fractures (38%), avascular necrosis (7%), malunion/non-union (3%) and rotator cuff tear (3%). Similarly, the top indications for RSA were osteoarthritis (59%), rotator cuff tear (21%), proximal humerus fractures (10%) malunion/non-union (3%) and revision arthroplasty (3%) [72]. In a review article by van de Sande *et al* in 2006, the incidence of revision surgeries were found to be 8% overall, but were significantly higher for hemiarthroplasty (15%) compared to TSA (6%) [75]. In the United States in 2007, the average hospital charges (excluding physician fees, and in January 2009 equivalent US dollars) were found to be \$44,456 for TSA and RSA (pooled), and \$41,801 for hemiarthroplasty [74]. As such, with the prominence of these procedures growing, implant performance (*i.e.*, longevity) is an important issue that can impact future patient outcomes and health care costs.

1.2.3 Complications of Shoulder Arthroplasty

In a review by van de Sande *et al* in 2006, several common surgical complications were assessed. They found the most common perioperative (*i.e.*, during surgery) complications reported on were nerve injury (average: 0.9% of cases, range: 0-8%) and periprosthetic fractures to the glenoid and humeral shaft (average: 1.2%, range: 0-8%). Following surgery, complications of deep infection (sepsis) were uncommon (0.8%: TSA = 0.4%, hemiarthroplasty = 0.9%). However, instability was found to be one of the most common issues of shoulder arthroplasty (TSA = 5%, hemiarthroplasty = 20%). Other postoperative complications included: proximal humeral head migration (TSA = 19%, hemiarthroplasty = 31%), severe pain (TSA = 9%, hemiarthroplasty = 9%), glenoid component loosening (2% requiring revision) and humeral component loosening (3.6% prevalence, accounting for 2.5% of all revisions). Glenoid erosion is a complication unique to hemiarthroplasty, due to the mating of an implanted humeral head with the native glenoid. It has been reported with a prevalence that increases with time (mean follow-up under 60 months = 5%, greater than 60 months = 31%), with 41% of the cases of glenoid erosion eventually requiring revision surgery. Overall, van de Sande *et al* found that patients were unsatisfied in 9% of TSA cases, and 20% of hemiarthroplasty cases; and that patient

satisfaction decreased with long term follow-ups (greater than 60 months), for both TSA (83% to 67%) and hemiarthroplasty (80% to 54%) [75].

Some shoulder arthroplasty complications can be attributed, at least in part, to the design of the humeral prosthesis. In particular, long term concerns pertaining to the humeral stem include proximal bone loss arising from stress shielding, osteolysis and humeral stem loosening [67–69,75–78]. In addition, the seating of humeral stems can be a contributing factor to perioperative and post-operative humeral fractures [79,80]. Due to anatomic variation in the angle of the humerus' proximal articular surface, it can be a challenge to balance the alignment of the stem with the diaphyseal canal, while maintaining proper head alignment. This issue has led to the development of stemmed prostheses with adjustable head-neck angles. Unfortunately, even with adjustable prostheses, revision of a well-fixed humeral stem can result in the damage and loss of humeral bone stock [81–84]. This reduction in bone tissue limits the reconstructive options and the potential success of the revision surgery [81,82,84,85].

Accordingly, with these concerns in mind, implant manufacturers have gradually reduced the length and invasiveness of stemmed implants in an attempt to maintain as much of the natural loading conditions and bone tissue as possible. The most recent evolution of humeral prostheses has been the introduction of stemless implants that seek fixation in the metaphyseal bone beneath the humeral head resection plane [71,86,87]. As a consequence, their alignment relies only on the humeral head resection, not on the diaphyseal canal, simplifying the surgical procedure and leaving more bone tissue in the event that revision surgery is required. These stemless implants should not be confused with humeral resurfacing implants that preserve the majority of the humeral head, resurfacing only the articular surface, making it challenging if not impossible to expose the glenoid, thereby complicating the joint reconstruction [87]. As stemless humeral implants utilize a standard humeral neck cut, they are a more natural design evolution for humeral arthroplasty; and are the focus of this thesis.

1.2.4 Present State of Stemless Humeral Components

1.2.4.1 Stemless Humeral Implants Currently Manufactured

Several implant manufacturers (Tornier¹, Zimmer Biomet, Mathys, Arthrex, Lima and FX Solutions) have released stemless humeral implants in recent years [86,87]. While these implants all rely on fixation features that seek to establish purchase in the trabecular bone of the proximal humerus, their designs vary from simple pegs to elaborate branching structures (Figure 1.8). A certain amount of design variation is expected (for patent and other purposes); however, the diversity of fixation features in these first-generation stemless implants suggests a lack of a concise understanding regarding how they should be shaped, and where these components should be seated in the available bone to best mimic the intact bone response.

Specifically, if we classify fixation feature location into three categories: central, peripheral and boundary-crossing, the Arthrex Eclipse is centrally fixed, while the FX Solutions Easytech is fixed by a series of pegs that are independently either central or peripheral, with the remainder (Wright Medical Simpliciti, Mathys Affinis Short, Lima SMR Stemless and the Zimmer-Biomet TESS, Nano and Sidus) all relying on constructs that cross the central-peripheral boundary. There is a general consensus regarding the mode of implantation, with all of these implants (except the Eclipse) utilizing impaction (Eclipse is screwed into the bone). Additionally, they all rely on some form of surface texturing to promote implant-bone fixation (*e.g.*, Grit blast, porous coating, trabecular titanium, *etc.*). However, the geometry with which they seek fixation varies greatly, with several (Simpliciti, Sidus, SMR Stemless and Affinis Short) electing finned designs, while some rely on branching arms that curl proximally from a central peg (TESS, Nano). Others utilize a threaded central peg (Eclipse) or a combination of barbed pegs (Easytech) for implant stability. A breakdown of these implant features is presented in Table 1.1.

1.2.4.2 Performance of Stemless Shoulder Implants in the Literature

Between 2010 and 2017 there have been several *in-vivo* assessments of anatomic stemless implants in clinical populations [71,88–102]. These studies agree that stemless

¹ In March of 2015 the first stemless shoulder implant (Tornier Simpliciti, Wright Biomedical) was approved by the FDA for use in the USA (<http://investor.tornier.com/releasedetail.cfm?ReleaseID=900866>).

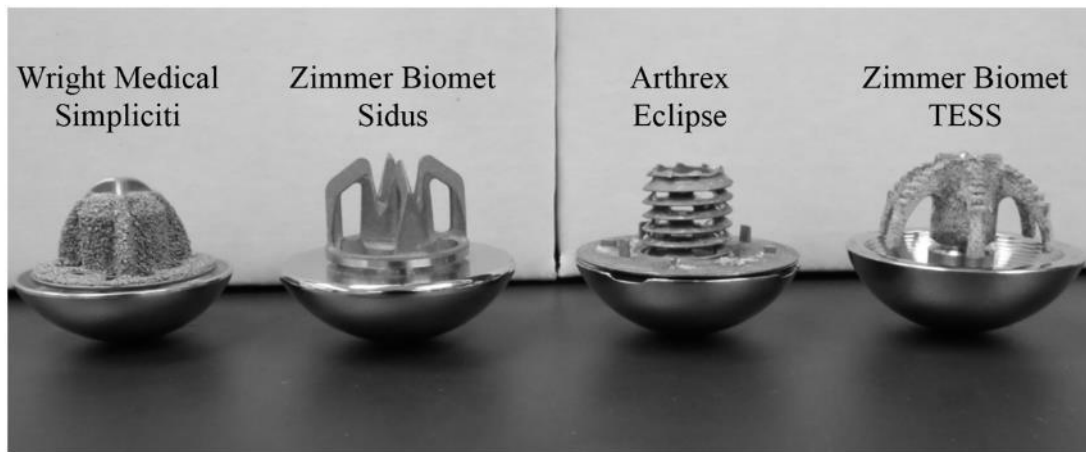


Figure 1.8: Variation in Stemless Humeral Implants

Since their introduction to the market, stemless humeral implants have utilized a wide variety of fixation features, which have taken many forms and that seek fixation in different locations within the proximal metaphysis.

Table 1.1: Features of Currently Available Stemless Implants

	Arthrex	FX Solutions	Lima SMR Stemless	Mathys Affinis Short	Wright Medical Simpliciti	Zimmer Biomet		
	Eclipse	Easytech				TESS	Nano	Sidus
Release Date	2005	2015	2015	2008	2010	2004	2013	2012
FDA Approval	No	No	No	No	Yes	No	No	Yes*
Fixation Mode	Screw-in	Impaction	Impaction	Impaction	Impaction	Impaction	Impaction	Impaction
Fixation Location	Central	Peripheral + Central	Boundary crossing	Boundary crossing	Boundary crossing	Boundary crossing	Boundary crossing	Boundary crossing
Key Features	Single hollow threaded peg	Central barbed peg + 4 barbed peripheral pegs	3 fins + Central peg + Proximal cylinder	4 hollow fins + Central peg	3 fins + Central peg	Central peg + 6 proximal branching arms	Central peg + 6 proximal branching arms	4 hollow fins
Collar	Solid	Open	None	None	Solid	None	None	Open
Surface Treatments	Grit-blast	Not specified (coated for on-growth)	Trabecular titanium design	Porous titanium	Grit-blast	Porous coating: Titanium hydroxyapatite	Titanium porous plasma spray	Rough blasted

*FDA approved, but not yet commercially sold within the US.

implants are capable of reproducing the biomechanics (*e.g.*, RoM, *etc.*) of a healthy shoulder, while offering patients pain relief. The most commonly reported clinical outcomes are the Constant score and RoM, which are summarized along with study details in Tables 1.2a/b. Several of these assessments have compared stemless to stemmed implants, and have indicated that the stemless implants perform just as well, if not better than their stemmed alternatives [89,90,92,98,102].

Stemless implants have been documented as requiring less operative time than stemmed implants [90,102], and having lower estimated surgical blood loss [90]. In addition, these implants have done well in recreating the anatomic articular geometry of the humeral head [95,96,100], though it has been suggested that special care should be given to the positioning of the humeral head resection, as there can be a tendency to implant stemless prostheses in a varus position [96].

Only one clinical investigation directly compared two stemless implants (TESS and Nano; Zimmer Biomet); indicating that the two did not present with significantly different outcomes [95], though these findings are not surprising due to the similarity between the two designs. Finally, though complication rates were low, three studies did report reduced bone mineral density or increased radiolucency with a prevalence between 29%-36% in the superior-lateral region of the trabecular bone adjacent to the implant [91,99,101]; this region was also where the highest rate of initial metabolic activity was reported by Berth *et al* in 2016 using SPECT/CT.

In addition to the *in-vivo* results outlined above, *in-silico* (*i.e.*, computer-based) FE methods can also be applied to assess the performance of stemless shoulder implants. While there have been several FE models of the shoulder construct [11,13,103–110], only two studies (by Razfar *et al* and Farve *et al*) directly assessed the performance of a stemless implant [111,112], with only one of these quantifying the bone's response [111]. In 2016, Razfar *et al* published a FE comparison of generic standard, short and stemless implants within the proximal humerus. By utilizing identical meshing techniques, they were able to normalize bone stress results to the intact state, providing strength to their analysis. This technique is unique and permits direct element-to-element comparisons between the intact and reconstructed bone around an implant to assess the bone's

Table 1.2a: Summary of *In-Vivo* Anatomic Stemless Humeral Studies (2010-2016)

Author	Implant	N	Timeline [Months]	Constant Score [Improvement] Mean(SD)	RoM [Improvement] Mean(SD)	Humeral Radiolucencies, Osteolysis, Stress Shielding
Huguet <i>et al</i> (2010)	TESS	63	36 to 51	29.6 to 75	FF: 96° to 145° ER: 20° to 40°	None
Kadum <i>et al</i> (2011)	TESS	39	9 to 24	QuickDASH and EQ-5D Improved	Not Reported	None
Berth <i>et al</i> (2013)	TESS	41	24 to 43	30.1(7.1) to 54.7(7.3)	ABD: 68°(7°) to 105°(12°) FF: 81°(7°) to 116°(10°) ER: 39°(11°) to 54°(11°)	None
Razmjou <i>et al</i> (2013)	TESS	17	24	37%(19%) to 92%(24)%	ABD: 51° (19°) to 121° (40°) FF: 69° (24°) to 135° (35°) ER: 18° (10°) to 54° (17°)	None
Habermeyer <i>et al</i> (2015)	Eclipse	96	60 to 100	45.8(13.3) to 65.0(16.3)	ABD: 74°(47°) to 130°(39°) FF: 114°(40°) to 141°(36°) ER: 25°(24°) to 44°(20°)	1.3%: incomplete radiolucent lines 3.8%: partial osteolysis under humeral cranial component 41.3%: some lowering of trabecular BMD
Maier <i>et al</i> (2015)	TESS	12	6	33.7(16.1) to 48(13.8)	ABD: 80°(34°) to 86°(21°) FF: 94°(28°) to 97°(16°)	None
Churchill <i>et al</i> (2016)	Simplificiti	149	24	44.3(13.5) to 80.7(10.5)	ABD: 103°(27°) to 147°(24°) ER: 31°(20°) to 56°(15°) IR: 64°(24°) to 74°(17°)	None
Berth <i>et al</i> (2016)	Affinis Short	28	3 to 5	29.3(6.9) to 54.8(7.2)	ABD: 69°(7°) to 105°(12°) FF: 81°(6°) to 116°(10°) ER: 38°(12°) to 55°(10°)	None
Kadum <i>et al</i> (2016)	TESS and Nano	24	12 to 50	QuickDASH and EQ-5D Improved	ABD: 60°(22°) to 130°(46°) FF: 80°(27) to 145°(38°) ER: 14°(13°) to 55°(23°) IR: 12°(12°) to 40°(26°)	None
Kadum <i>et al</i> (2016)	TESS	70	2 nd day Post-OP	N/A	Not Reported	None
Ballas <i>et al</i> (2016)	TESS	27	24 to 80	27 to 62	FF: 81° to 129° ER: 5° to 40°	3.7%: Osteolysis beneath humeral head

Note: ABD: Abduction, FF: Forward Flexion, ER: External Rotation, IR: Internal Rotation.

Table 1.2b: Summary of *In-Vivo* Anatomic Stemless Humeral Studies (2017-2018)

Author	Implant	N	Timeline [Months]	Constant Score [Improvement] Mean(SD)	RoM [Improvement] Mean(SD)	Humeral Radiolucencies, Osteolysis, Stress Shielding
Uschok <i>et al</i> (2017)	Eclipse	15	24 to 60	53.9(11.3) to 72.8(11.8)	ABD: 110°(24°) to 149°(15°) FF: 136°(31°) to 154°(9°) ER: 32°(16°) to 49°(15°)	28.6%: lowering of BMD near humeral component 36.2%:
Collin <i>et al</i> (2017)	Simpliciti	47	24 to 51	33 to 69	FF: 84° to 131° ER: 15° to 15°	radiolucent areas (primarily superior-lateral region)
von Engelhardt <i>et al</i> (2017)	TESS	21	18(9)	11%(19%) to 75%(26%)	Not Reported	None
Hawi <i>et al</i> (2017)	Eclipse	43	90 to 127	42(16) to 62(17)	ABD: 79°(50°) to 105°(43°) FF: 101°(47°) to 118°(43°) ER: 21°(27°) to 43°(19°)	29.4%: lowering of BMD in the superior-lateral region 2.3%: incomplete radiolucency ≤1mm
Heuberer <i>et al</i> (2018)	Eclipse	40	48 to 87	37.7%(15.4%) to 78.7%(16.1%)	Not Reported	11%: risk of humeral implant loosening

Note: ABD: Abduction, FF: Forward Flexion, ER: External Rotation, IR: Internal Rotation.

response to reconstruction. Their analysis determined that there was a trade-off between cortical and trabecular bone stress; where reducing implant length (from standard to short and stemless implants) resulted in cortical humeral stresses that better matched the intact state but led to an increase in the change in trabecular stress. Unfortunately, their analysis was limited to a single stemless implant design, as the focus of the study was on implant evolution; however, these methods are easily adaptable to the study of further stemless humeral implant designs.

Favre *et al* published two assessments of the Sidus stemless implant in 2016, one using *in-vitro* mechanical loading of the implant and the other a validation of an *in-silico* FE model. Their FE assessment focused on validating and quantifying stemless implant micromotion through a variety of daily activities, while their *in-vitro* assessment indicated that bone density and applied load, but not implant size, had significant effects on measured micromotion. Their *in-vitro* results indicated the importance of having adequate trabecular bone density when using a stemless prosthesis in order to reduce implant-bone micromotion [113]. These studies provide a good understanding of implant-bone motion, and assist with comprehending the type of activities that should be avoided immediately following surgery (*e.g.*, hammering a nail, lifting heavy weights, *etc.*). Their FE results indicated that 99% of the implant surface maintained micromotion levels within the threshold necessary for bone-ongrowth (*i.e.*, $<150\mu\text{m}$), suggesting that the stemless implant should maintain adequate fixation [112]; however, they did not present any information regarding the bone's response to stemless reconstruction, and they did not assess different implant designs. Furthermore, they modelled the trabecular bone as a homogeneous structure within their FE assessment, which could alter bone strains if these models were to be used to quantify bone response in the future.

In 2014 Schmidutz *et al* reported on the development of a FE model of the proximal humerus that was used to compare the geometry of two humeral resurfacing implants. Though different from stemless implants, as resurfacing implants do not resect the humeral head, this model does provide support for the use of the FE method in comparing multiple implant designs in the proximal humerus. They utilized volume-weighted compressive strains to compare the bone's response to implantation of the resurfacing

prostheses and found that load transfer became more inhomogeneous following reconstruction, but that the implant with the peripheral conical-crown design appeared to induce a more homogeneous distribution than the centrally pegged design [110]. They also indicated a substantial decrease in compressive strain beneath the implant shell, suggesting bone resorption may be an issue following reconstruction.

Though not directly comparable to stemless shoulder arthroplasty, a study by Long *et al* in 2006 used the FE method to assess the stress, strain and loading response of the femur to changes in the positioning of a stemmed articular resurfacing implant. They determined that a valgus stem orientation, while covering reamed trabecular bone, reduced the local stresses and strains associated with implant loosening [114]. Regardless of implant orientation and other variables assessed, the implants unloaded the femoral head, again demonstrating the utility of the FE method in predicting a potentially unfavorable bone remodeling response following joint reconstruction.

Though not an assessment of humeral reconstruction, Dahan *et al* validated a FE model for the intact proximal humerus, which was constructed with 2mm quadratic tetrahedral elements and an isotropic inhomogeneous trabecular stiffness using uniaxial compressive loading. They reported strong correlations between experimental and FE results (slope = 1.09; $R^2 = 0.98$), providing support for developing humeral models with these mesh and material properties [109]. Other FE models of the shoulder have also been developed to simulate overall joint biomechanics [11,13,103,107] or to specifically investigate glenoid revision [104–106,108]. While these assessments and those outlined above are less directly comparable to stemless humeral arthroplasty, they all suggest that the FE method may be a useful tool capable of assessing the bone's response to variation in parameters, such as the design of stemless humeral implants.

Though the *in-vivo* results of stemless humeral arthroplasty have been promising to date, no study has directly compared several stemless implants that rely on different fixation features head-to-head. Accordingly, an evaluation assessing the bone's response to varying stemless fixation feature geometry is warranted. The FE method is well suited to permit the direct comparison of implant designs within the same population, thereby increasing statistical power (*i.e.*, repeated measures study construct).

1.3 Wolff's Law and Stress Shielding

Wolff's Law, which states that bone resorbs and remodels in-part due to mechanical stimulus (*i.e.*, loads) [32], suggests that when the loads that act on a section of bone diminish beyond, or exceed, some threshold, the bone will respond in-kind by resorbing or remodeling. In a reconstructed joint, the implant stem or keel (introduced to provide stability to the articular head) shares some of the load that was initially born solely by the bone [115]. This reduces bone stimulus, leading to the phenomena termed stress shielding [55,116,117], which can be a cause of bone resorption and can contribute to implant loosening [55,76,118]. For the shoulder, a radiographic study by Nagels *et al* reported evidence of stress shielding surrounding humeral implants in 9% of their cases (n=70); but as they only assessed variations in cortical bone, they pose that the true incidence of stress shielding surrounding shoulder implants may be higher [67]. Others have also documented bone resorption around humeral implant stems [68–70].

One mechanical measure that has been shown to correlate well with bone adaptation is Strain Energy Density (SED) [119,120]. As an object is distorted under load, the applied force is producing 'external work' (the multiple of force by distance) on the object; this is balanced by the strain energy, or 'internal work', that is stored within the object as it distorts. This strain energy is often expressed per unit of volume, yielding the SED (Eq.1.1 and Eq.1.2).

$$SED = \frac{\sigma^2}{2E} \quad (\text{Eq.1.1})$$

For linear isotropic materials undergoing small strains, SED can be expressed as,

$$SED = \frac{1}{2}(\sigma_x \varepsilon_x + \sigma_y \varepsilon_y + \sigma_z \varepsilon_z + \sigma_{xy} \varepsilon_{xy} + \sigma_{yz} \varepsilon_{yz} + \sigma_{xz} \varepsilon_{xz}) \quad (\text{Eq.1.2})$$

With iterative computer models using SED to accurately predict the density distribution of bone in response to loads [30,119,121,122], this is a promising engineering measure that can be used to estimate the bone's potential response to arthroplasty.

1.4 Scientific Methods for Analyzing Shoulder Arthroplasty

1.4.1 Radiographic Tools – Computed Tomography

X-ray Computed Tomography (CT) is a medical imaging modality that uses radiation projected through a patient to quantify tissue attenuation (in Hounsfield Units, HU). To capture 3D attenuation data helical CT scanners rotate the radiation emitter and detector in a circular fashion while the patient moves linearly through the scanner, perpendicular to the plane of rotation (Figure 1.9) [123]. This data is then reconstructed into 3D voxels, whose attenuation is proportional to density. In orthopaedics, CT scanning has become common for quantifying the density distributions within bones, and for quantifying the geometry of bones for use in computer models of joint reconstruction [39,41,42,111,124]. CT scan attenuation is calibrated to apparent bone density through the use of calibration phantoms, which are placed alongside the patient at the time of data collection. These phantoms consist of two or more materials of known apparent density; then by measuring their attenuation in the scan, a linear relationship between apparent bone density and CT attenuation can be formed and applied to all voxels (Figure 1.9). Accordingly, CT imaging is a useful tool for non-invasively quantifying the geometry and density of bones for both medical and engineering applications.

1.4.2 The Finite Element Method

In the field of orthopaedic implant design and assessment, the use of *in-silico* computational methods such as Finite Element (FE) analysis, has become common [119,125–133]. These methods allow a variety of parameters (*e.g.*, implant material stiffness, interface friction, loading constraints, implant geometry, *etc.*) to be altered relatively easily and evaluated at reduced costs compared to traditional prototype-evaluation cycles. As these methods require discretized approximations of continuous structures, they must be constructed to resemble the geometry and properties of the true system as best as possible. Accordingly, FE analysis should be paired with *in-vitro* cadaveric testing in order to validate models.

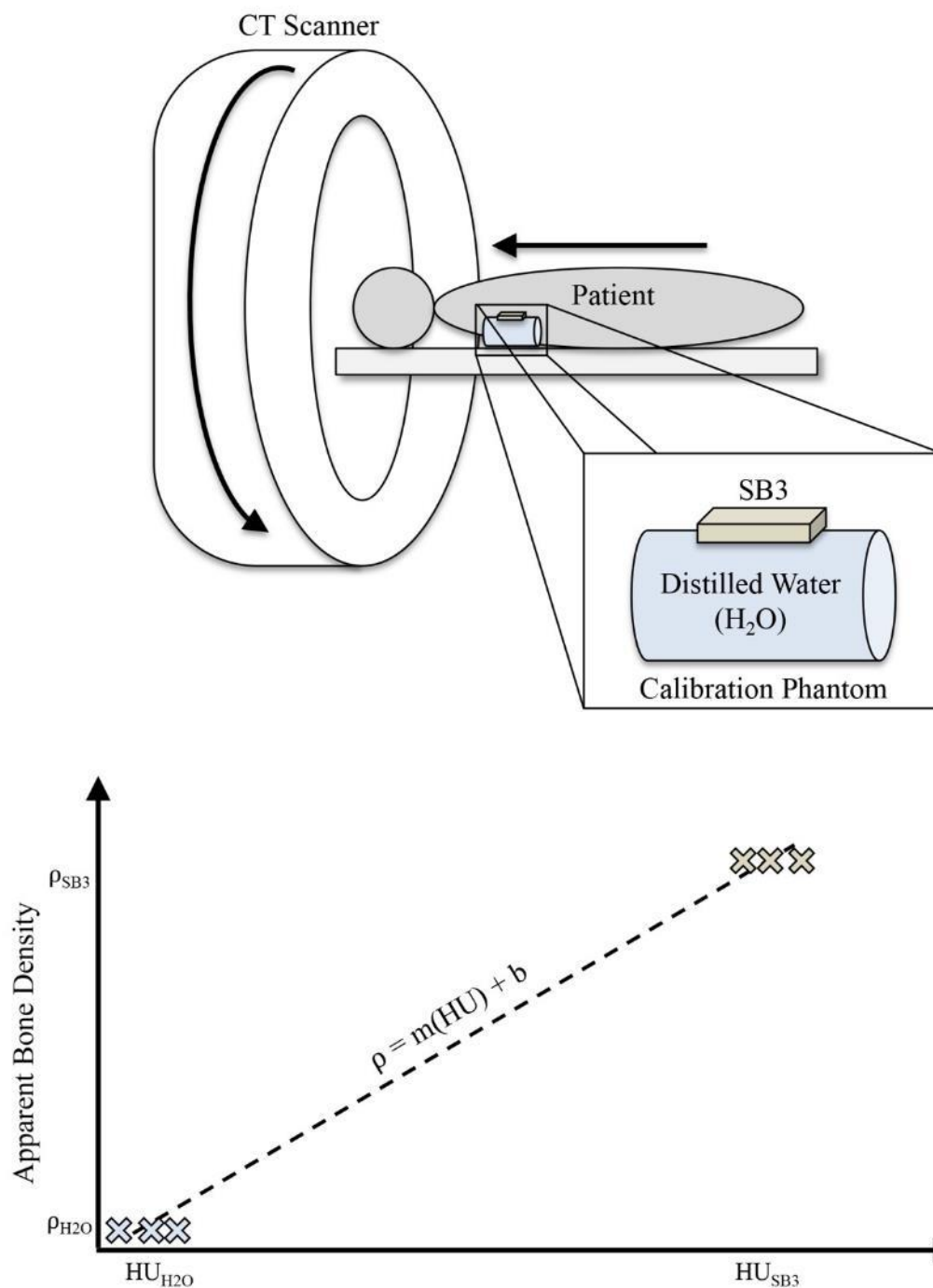


Figure 1.9: Computed Tomography Scanning and Density Calibration
 A CT scanner's emitter and detector rotate circumferentially around the patient, who is linearly slid through the scanner. Using a calibration phantom of known density, which is placed alongside the patient during the scan, CT attenuation can be calibrated to apparent bone density.

1.4.2.1 Finite Element Theory

The elastic deflection of a simple bar in response to a force can be simply calculated using Hooke's law, where deflection is equal to the applied force divided by the stiffness; however, analyzing the response of more complicated structures is not always so simple. The FE method is a numerical approach that breaks complicated geometry down into a finite number of simpler structures known as elements (hence the name 'Finite Element' method), which are connected at points called nodes, whose displacements can be individually determined from a series of algebraic expressions. Individual nodal displacements are then combined to estimate the overall response of the continuous structure at discrete locations (Figure 1.10) [134].

1.4.4.2 The Finite Element Mesh

The act of dividing the geometry of the humerus into elements is known as 'meshing', with the term 'mesh' referring to the assembly of elements as a whole. There are two main types of elements that are commonly used when developing 3D models in orthopaedics: tetrahedral and hexahedral, which are triangular and rectangular prisms, respectively (Figure 1.11). Traditionally, hexahedral elements are viewed as more favorable because they converge faster, have good accuracy, and their alternative (*i.e.*, linear tetrahedral elements) can exhibit excessive stiffness [135–137]. However, varying the configuration of the tetrahedral elements so that element edges are not linear, but quadratic (or higher order) can avoid these issues and provide results that are less susceptible to mesh refinement [135–139]. This is favorable, as it can be difficult to fit hexahedral elements to complex surface geometries, compared to tetrahedral elements. Accordingly, the quadratic tetrahedral elements are used for all FE investigations herein.

Another important concern regarding the mesh of FE models is the element size. The mesh is a discrete approximation of a continuous construct; accordingly, the smaller each element is, the better the mesh can approximate reality. If the mesh is not refined sufficiently, it can be susceptible to the formation of artificial stress concentrations which may impact results. Unfortunately, there is a trade-off; the computational time for a model to complete is inversely proportional to the number of elements within the mesh.

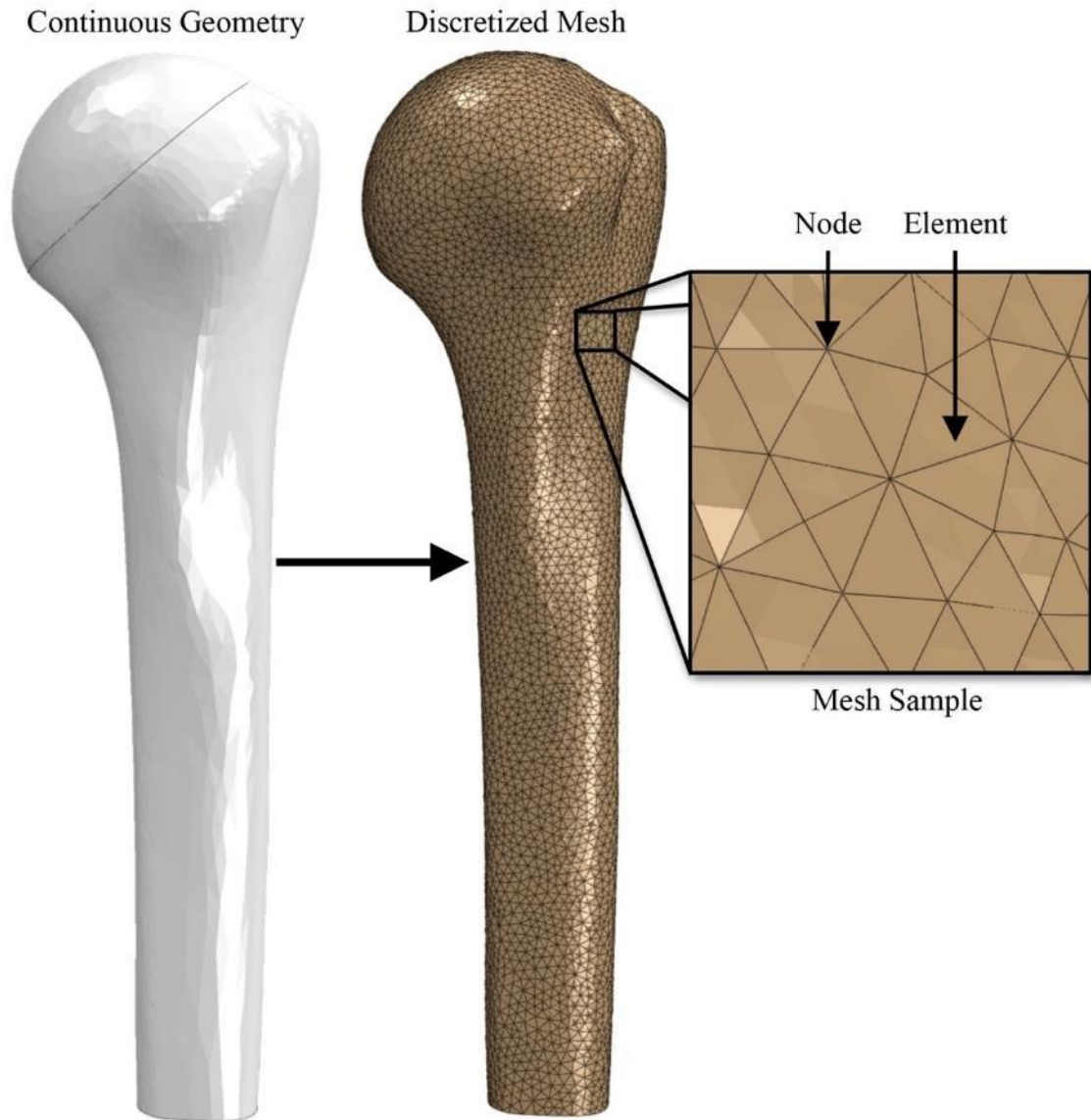


Figure 1.10: Discretized Finite Element Mesh

The FE mesh approximates a continuous structure by discretizing it into a finite number of elements, which are connected to each other via vertices known as nodes. This permits the approximation of strain throughout the structure by calculation of a discrete number of nodal displacements.

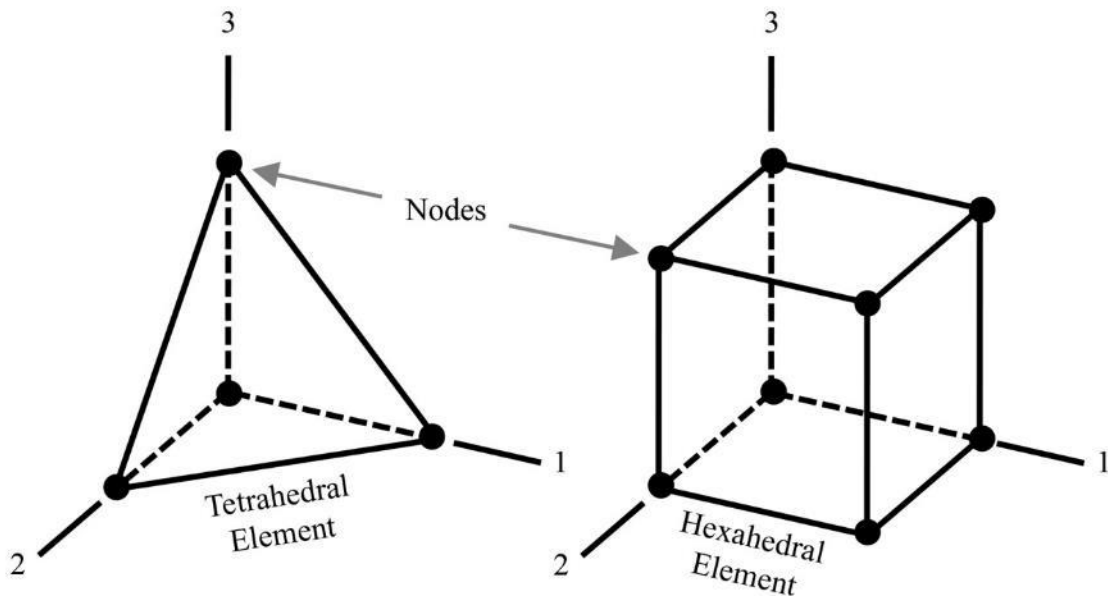


Figure 1.11: Tetrahedral and Hexahedral Elements

Elements within a 3D FE mesh are generally classified as tetrahedral or hexahedral, taking the form of a triangular or rectangular prism, respectively.

As such, it is necessary to assess how sensitive each FE outcome measure is to the mesh size by performing a mesh convergence analysis. This analysis is performed by running the model at multiple mesh sizes to determine the element size at which further refinement does not vary the results appreciably. A complete mesh convergence analysis for modelling stemless shoulder arthroplasty is provided in Appendix C; the results of which indicate that 2mm is an appropriate element edge length for modelling stemless arthroplasty in the proximal humerus.

Finally, as mentioned in Section 1.2.4.2, Razfar *et al* utilized a method for identical mesh development in their FE analysis of shoulder arthroplasty. This method retains the same bone mesh surrounding the implant in both the intact and reconstructed models. This is done by using the implant surface as a geometric boundary which divides the mesh into sub-sections, then merging nodes between the necessary mesh segments (Figure 1.12). This division and merging of basic mesh sub-sections permits the evaluation of FE outcomes on an element-to-element basis, thereby reducing the variation attributable to mesh changes when comparing the response of the two models. Accordingly, this method is adapted to each FE investigation within this thesis, and is included in the FE validation presented in Appendix D.

1.4.2.3 Modelling Joint Reaction Forces

As discussed in Section 1.1.1 the complexity of the shoulder makes the calculation of joint reaction forces an indeterminate problem. The most reliable source of joint reaction force data is the *in-vivo* telemetrized implant data reported by the OrthoLoad group in Germany (website: <https://orthoload.com>) [14–16,140,141]. They have developed several telemetrized implantable joint replacement systems that dynamically measure load within patients following surgery. From this data we can determine the breakdown of orthogonal loads (expressed as percentage of body weight) acting on the humeral head in the ISB coordinate system (Table 1.3). Since the glenohumeral joint's purpose is to support joint motion in the most efficient way possible, it is assumed that surface friction within the joint is negligible [114]. This implies that the joint reaction force must act normal to the articular surface, with a line-of-action passing through the center of the humeral head. As such, the site of load application can be reconstructed by starting at the center of

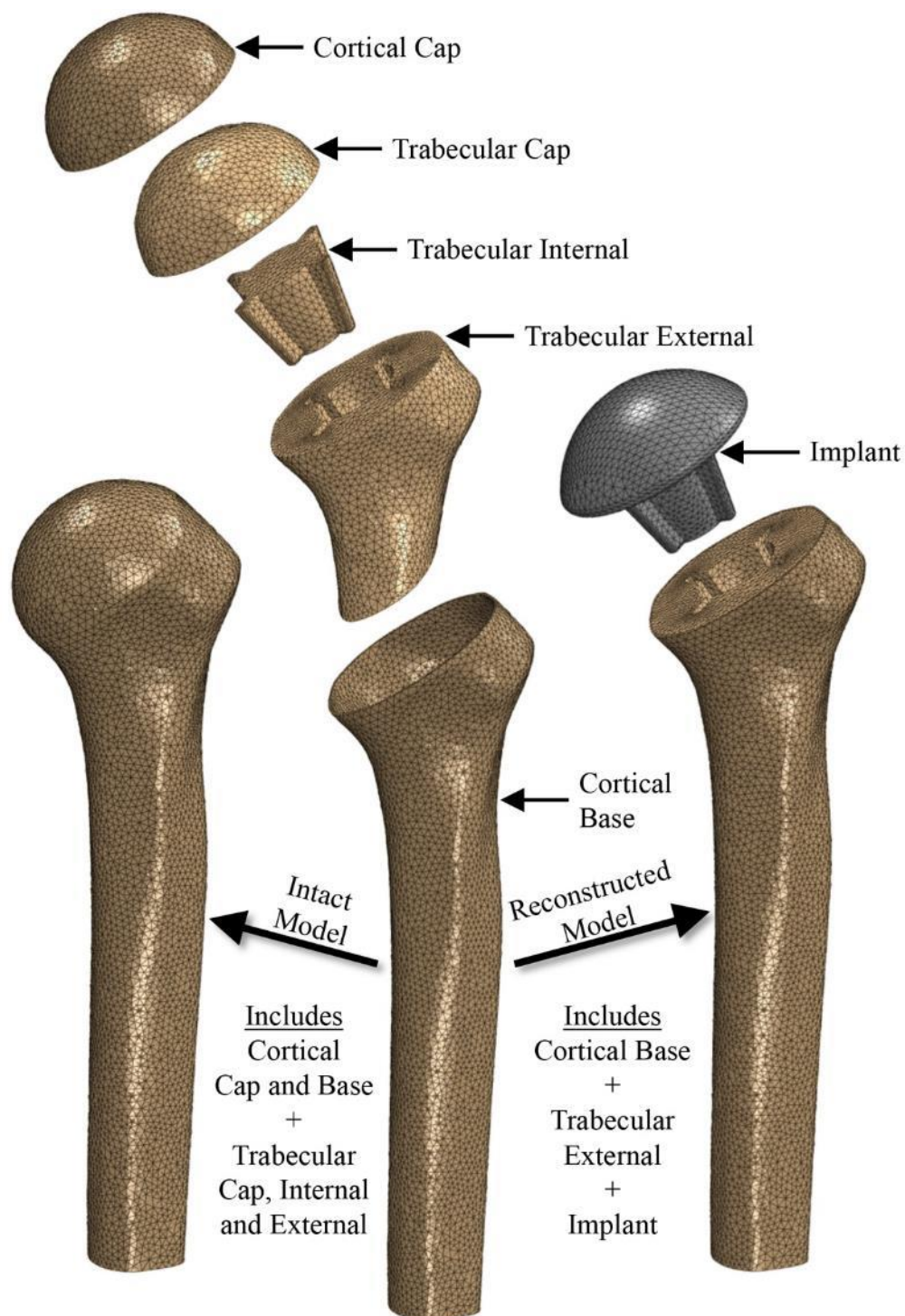


Figure 1.12: Identical Mesh Preparation

An identical bone mesh is formed for both the intact and reconstructed models of the humerus by using the implant geometry to segment the humerus; then meshing the bone and merging/deleting the necessary sub-meshes to form the two models.

Table 1.3: Cartesian Ratios and Resultant Joint Reaction Forces for the Glenohumeral Joint.

Abduction Angle	Cartesian Force Components [% Bodyweight]			Joint Reaction Force [N]
	Superior- Inferior	Posterior-Anterior	Medial- Lateral	
45°	44%	21%	16%	440
75°	74%	34%	25%	740

Note: Derived from Bergmann *et al* (2007).

the humeral head's articular hemisphere and using the orthogonal components of the reported joint reaction force to quantify a loading direction-vector in 3D space. The intersection of this direction-vector with the humeral articular surface (or in the case of a reconstructed joint, the implant's articular surface), is where the joint reaction force should be applied. The joint reaction force can then be applied at the magnitude reported by Bergmann *et al* and directed towards the center of the humeral head (Figure 1.13). Joint reaction forces change in magnitude and orientation throughout a joint's RoM. Accordingly, for each position under investigation, the orientation and magnitude of the joint reaction force can be applied as outlined above. The breakdown of joint reaction force orthogonal components for shoulder abduction angles of 45° and 75° are presented in Table 1.3. In order to convert the loads from percentage bodyweight into a physical force (measured in Newtons, N) a uniform bodyweight of 88.3kg (representing 50th percentile male weight) was assumed for all analyses in this thesis; this was done to provide consistency across all models [111].

1.4.2.4 Modelling Bone as a Material

While the material properties of implants are highly controlled, and macroscopically uniform (typically titanium or cobalt chrome alloys), the stiffness (represented by the elastic modulus [E]) of bone can vary regionally. It is generally accepted that the cortical shell of a bone can be simulated using a homogeneous modulus (approximately 20GPa) [36,38], and that trabecular bone stiffness should vary regionally as a function of the apparent density of the bone [37,38,40,44,59,106,142–145]. This is done using CT software (*e.g.*, Mimics; Materialize Inc., Plymouth, MI, USA) that can import a bone mesh and assign material stiffness to each element independently using two equations: one that linearly calibrates the CT attenuation to apparent bone density, and one that calculates elastic modulus from its exponential relationship with apparent density [39–43,111].

To date, a number of studies have been conducted to develop equations relating the elastic modulus of bone to the apparent density of CT scan data [38,40,44,106]. Some studies by Morgan *et al* and Keaveny *et al* are of particular interest to FE investigations, as they use only trabecular bone samples, and have compared equations derived from

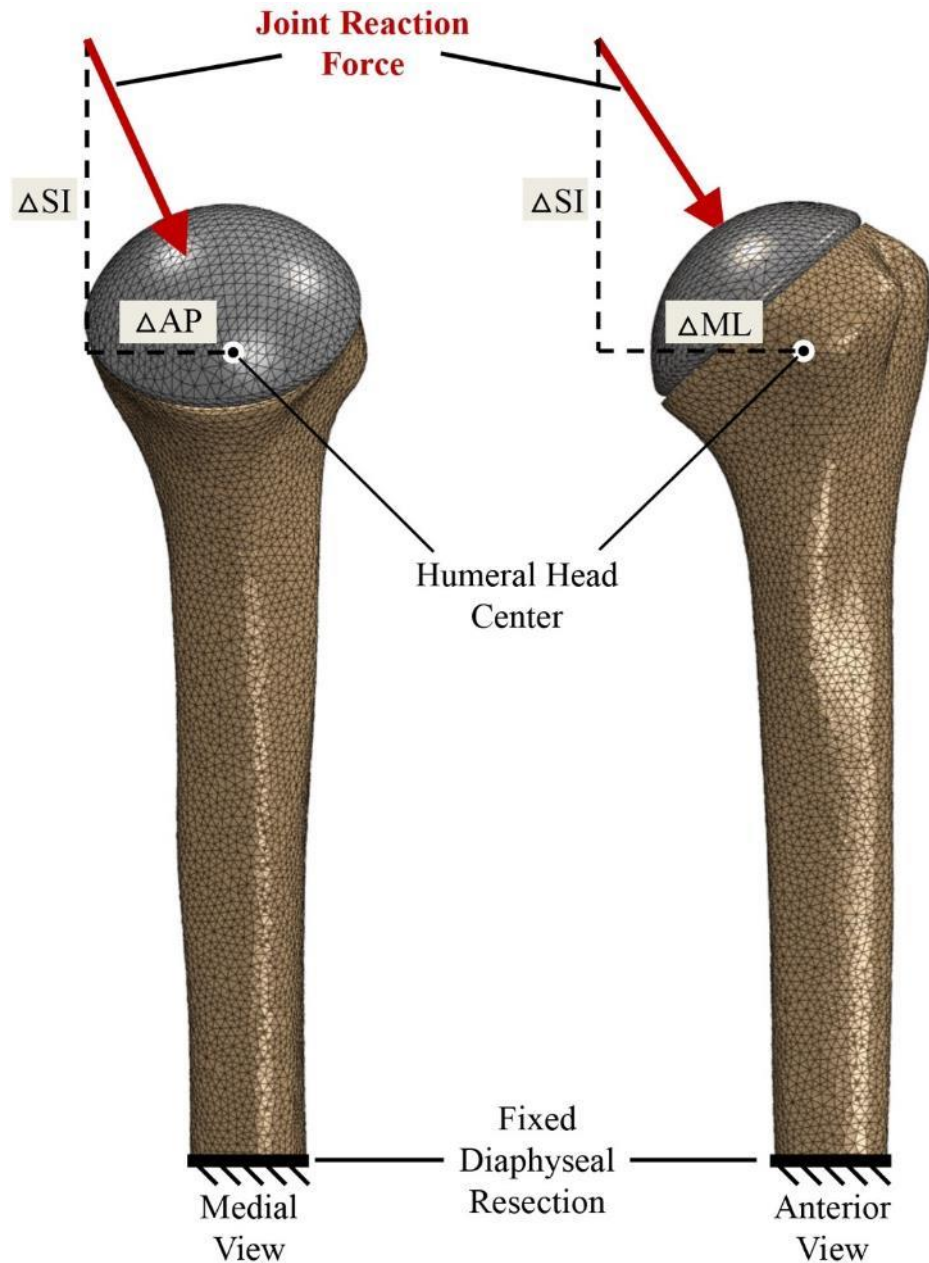


Figure 1.13: Finite Element Joint Reaction Force Application

To apply the joint reaction force to the surface of the FE model, a loading axis is formed using the Cartesian components of Bergmann *et al*'s telemetrized implant joint reaction force data. When forced to travel through the center of the humeral head, the intersection between the articular surface and the loading axis dictates the position of joint reaction force application.

several sites across the body in an attempt to better understand regional variation in trabecular bone mechanical properties [37,40,142–144]. Interestingly, these results indicate that density-modulus equations are site-specific, and should be developed for each bone separately [40,106]. As shown in Table 1.4, to-date a density-modulus equation has not been developed for the trabecular bone of the proximal humerus. Hepp *et al* (2003) performed density and strength (*i.e.*, max force [N]) assessments of the proximal humerus but did not assess the correlation between density and elastic modulus. Moreover, their indentation testing was not aligned with the trabeculae (perpendicular to the resection plane) [59]. A study by Zumstein *et al* (2012) demonstrated that subchondral mineralization (*i.e.*, attenuation [HU]) was linearly correlated to mechanical strength (*i.e.*, force [N]) in the proximal humerus ($0.35 \leq R^2 \leq 0.93$), but again, they did not develop the necessary humerus-specific density-modulus relationship required for FE investigations [145].

In the absence of a density-modulus relationship specific to the proximal humerus, the site-pooled density-modulus equation developed by Morgan *et al* in 2003 has been used to construct a FE model of humeral arthroplasty [111]. In addition, a femoral density-modulus relationship has predicted the linear elastic response of intact humeral FE models well [109]. However, as stemless implant fixation features interface with the trabecular bone of the proximal humerus, it is important to understand if the selection of the density-modulus relationship will affect the FE outcomes reported. This has not been investigated to date and is of particular interest for models that employ identical meshing techniques; as the same stiffness is applied to both intact and reconstructed models, perhaps diminishing the necessity for site-specific stiffness-relationships.

As such, before choosing a density-modulus relationship for trabecular bone when modelling stemless humeral reconstruction, the variance attributed to stiffness relationship selection should be quantified to determine if it is substantial enough to warrant the development of a density-modulus relationship specific to the proximal humerus.

Table 1.4: Summary of several relevant density-modulus investigations.

Reference	Anatomic Site	Method	N (donors)	Reported E [GPa]	$E = A\rho^B$ [GPa] Developed
Carter and Hayes (1977)	Human Trabecular (Site Unknown), Bovine Trabecular (Site Unknown)	Indentation	100 (N/A), 24 (N/A)	0.05 – 0.1	$E=3.790\rho^3$
Schaffler <i>et al</i> (1988)	Bovine Trabecular (Site Unknown)	Uniaxial Tension	20 (N/A)	14.9 – 26.2	$E=0.09\rho^{7.4}$
Ulrich <i>et al</i> (1997)	Human Femoral Head	Experiment-FEA	6 (6)	3.5 – 8.6	N/A
Rho <i>et al</i> (1997)	Human Vertebra	Nanoindentation	72 (2)	13.4 ± 2.0	N/A
Hou <i>et al</i> (1998)	Human Vertebra	Experiment-FEA	28 (28)	5.7 ± 1.6	N/A
Ladd <i>et al</i> (1998)	Human Vertebra	Experiment-FEA	5 (5)	6.6 ± 1.0	N/A
Anglin <i>et al</i> (1999)	Human Glenoid	Indentation	10 (8)	0.0067 – 0.0171	N/A
Kabel <i>et al</i> (1999)	Whale Vertebra	Experiment-FEA	29 (1)	4.49 – 7.48	N/A
Turner <i>et al</i> (1999)	Human Distal Femur	Nanoindentation, Acoustic Microscopy	30 (1), 3 (1)	18.1 ± 1.7 , 17.5 ± 1.1	N/A
Zysset <i>et al</i> (1999)	Human Femoral Neck	Nanoindentation	N/A (8)	11.4 ± 5.6	N/A
Niebur <i>et al</i> (2000)	Bovine Proximal Tibia	Experiment-FEA	7 (7)	18.7 ± 3.4	N/A
Morgan <i>et al</i> (2003)	Human Vertebra, Proximal Tibia, Greater Trochanter, Femoral Neck, Pooled	Uniaxial Mechanical Testing-FEA	61 (25), 31 (16), 23 (21), 27 (23), 142 (61)	N/A, 23 ± 4 , 24 ± 2 , 22 ± 3 , N/A	$E=4.730\rho^{1.56}$, $E=15.520\rho^{1.93}$, $E=15.010\rho^{2.18}$, $E=6.850\rho^{1.49}$, $E=8.920\rho^{1.83}$
Hepp <i>et al</i> (2003)	Human Proximal Humerus	Indentation	24 (24)	N/A	N/A
Bayraktar <i>et al</i> (2004)	Human Femoral Neck	Experiment-FEA	12 (11)	18.0 ± 2.8	N/A
Austman <i>et al</i> (2009)*	Human Ulna	Bending-FEA	8 (8)	17 - 21	$E=8.346\rho^{1.5}$
Zumstein <i>et al</i> (2012)	Human Proximal Humerus	Indentation-CT-OAM	32 (32)	N/A	N/A
Vijayakumar <i>et al</i> (2016)	Human Proximal Tibia	Indentation	113 (5)	0.042 - 1.2	N/A

*Young's modulus reported for cortical bone, not trabecular bone.

1.4.2.5 Finite Element Outcome Variables

Traditionally, FE models have been used to quantify terms such as the contact area and contact stress between two surfaces, stress at individual nodes and the strain between two nodes. However, several more elaborate FE outcomes have been developed. As outlined in Section 1.3, SED has been used to approximate the stimulus that bone uses to dictate when to resorb or remodel. Accordingly, FE models of bones have been developed that adapt to variation in SED to change the density distribution of bone through several iterations [30,119,122,146], though iterative models can be expensive, both computationally and in terms of time. Furthermore, with the advent of identical meshing techniques [111] it is possible to draw a direct comparison between stress and strains in the same element before and after joint reconstruction.

Throughout this thesis, three primary outcome measures are assessed: (1) the percentage of the implant's area that remained in contact with the surrounding bone during load application, (2) the volume-weighted absolute percentage change in bone stress, relative to the intact state [111] and (3) the time-zero potential bone response, as estimated by the percentage of bone volume that would be expected to (a) resorb, (b) remain unchanged or (c) remodel based on SED changes between the reconstructed and intact models [30,119,121,122]. Each of these outcomes is expressed as a percentage in order to permit the direct comparison of results between multiple implant geometries (as the available contact area and bone volume around the implant vary depending on the implant shape).

Implant-Bone Contact Area

Implant-bone contact area is represented as a percentage of the available contact area. To quantify this variable, the area attributed to each node (A) and the contact pressure (CPRESS) at that node is determined for the implant side of the implant-bone interface. Those nodes with CPRESS greater than zero are classified as being in contact. Then, the contact area percentage is calculated as outlined below (Eq.1.3).

$$Contact\ Area\ [\%] = \frac{A_{CPRESS > 0}}{A_{Total}} \times 100\% \quad (Eq.1.3)$$

Volume-Weighted Absolute Average Change in Bone Stress

The volume-weighted absolute average change in bone stress outcome ($\Delta\sigma$) provides a measure of the magnitude of bone stress change within a region-of-interest, relative to the intact state. The change in bone stress is calculated by directly comparing the intact and reconstructed stress state of each element within a specified bone region as follows: for each element within the region, the six stress components of the element are determined through FE analysis (*i.e.*, σ_{11} , σ_{22} , σ_{33} , σ_{12} , σ_{13} , σ_{23}). The change in each of these stress components is calculated ($\Delta\sigma_{xy}$; Eq.1.4), to account for both the magnitude and directional changes in stress. Then, the von Mises of the change in stress is calculated ($\Delta\sigma_{VM}$; Eq.1.5). To ensure that the contribution of each element to the overall stress change in a region is appropriate, the change in stress is normalized to the intact values using a volume-weighted average (Eq.1.6). Since this outcome measure is an absolute change in stress, it does not indicate whether the stress state was overall higher or lower within the reconstructed bone; rather, it reflects the overall magnitude of change from the intact state. The idealized reconstructed state would perfectly mimic the stress of the intact bone, as such, a greater change in this bone stress outcome measure should be interpreted as less favorable.

$$\Delta\sigma_{xy} = \Delta\sigma_{xy_{Reconstructed}} - \Delta\sigma_{xy_{Intact}} \quad (\text{Eq.1.4})$$

$$\Delta\sigma_{VM} = \sqrt{0.5 \times [(\Delta\sigma_{11} - \Delta\sigma_{22})^2 + (\Delta\sigma_{22} - \Delta\sigma_{33})^2 + (\Delta\sigma_{11} - \Delta\sigma_{33})^2 + 6 \times (\Delta\sigma_{12}^2 + \Delta\sigma_{23}^2 + \Delta\sigma_{31}^2)]} \quad (\text{Eq.1.5})$$

$$\Delta\sigma = \frac{\sum(\Delta\sigma_{VM_{ReconstructedElement}} \times \text{Volume}_{ReconstructedElement})}{\sum(\sigma_{VM_{IntactElement}}) \times \text{Volume}_{Region-of-Interest}} \times 100\% \quad (\text{Eq.1.6})$$

Time-Zero Potential Bone Response

While it is important to quantify the bone stress changes relative to the intact state, it is also important to understand if that change is expected to manifest as bone remodeling or bone resorption. To do this, the SED (U) of each element in a region-of-interest within the reconstructed model is compared to the SED of the identical element in the intact model. The undeformed volume of each element is also determined. If the SED of the

element is less than 45% of its intact counterpart it is classified as having resorbing potential; if it is greater than 155% of the intact SED it is classified as having remodeling potential; and if it falls between these two thresholds, it is classified as having the potential to remain unchanged (Eq.1.7). Since there have not been any SED-based adaptive models developed for the proximal humerus, the threshold value of 55% on either side of the intact SED was taken from a validated ulna model developed in 2013 [119]. To permit comparison between implants with different peri-implant bone volumes, the potential bone response is represented by the percentage of regional bone volume that falls into each of these categories.

$$\text{Resorb: } U_{\text{Implant Model}} < 0.45U_{\text{Intact Model}} \quad (\text{Eq.1.7})$$

$$\text{Remain Unchanged: } 0.45U_{\text{Intact Model}} \leq U_{\text{Implant Model}} \leq 1.55U_{\text{Intact Model}}$$

$$\text{Remodel: } U_{\text{Implant Model}} > 0.45U_{\text{Intact Model}}$$

where, $U = \text{SED of each element}$

Since the models used in this assessment are quasi-static (*i.e.*, non-iterative), classification of bone elements in this manner is only conducted for a single point in time (*i.e.*, immediate post-operative state), this outcome represents the amount of bone volume that has potential to respond according to its SED classification, and the outcome is termed ‘time-zero’. Model iteration would be required to approximate the manifestation of bone density changes, which was excluded from the present analyses due to the associated computational expense and the number of implant models under investigation.

1.5 Thesis Rationale

With the advancement of computational power, *in-silico* investigative tools are becoming more appealing for assessing complex structures numerically. One complex structure requiring assessment is the most recent evolution of shoulder arthroplasty implants: the stemless humeral component. While *in-vivo* assessments of these stemless implants have indicated promising results, the diversity present in implant fixation feature geometry suggests a lack of consensus regarding the best form for these implants. Consequently, our understanding of how these implants should be designed to best interact with the underlying bone of the proximal humerus requires advancement.

The application of computational tools such as 3D CT reconstruction and the FE method can assist with better understanding the morphology of the underlying bone of the humerus and can be used to estimate how the bone may respond to stemless reconstruction when fixation feature geometry is varied. The ability to probe within the bone in a non-invasive manner uniquely suits *in-silico* methods to further our understanding of stemless humeral reconstruction; especially considering the ethical boundaries associated with assessing implants invasively within patients. Developments within the application of clinical CT tools and the FE modelling of the reconstructed proximal humerus are presented within this work.

1.6 Objectives and Hypotheses

The overall goal of this dissertation was to develop a better understanding of the morphology of the proximal humerus, and to construct a FE model capable of simulating multiple stemless implant geometries for comparison and interpretation within that morphological understanding.

1.6.1 Specific Objectives

1. To assess the morphology of the underlying bone following proximal humerus articular reconstruction by:
 - a. Quantifying the regional changes in apparent bone density within the proximal humerus' trabecular bone in a coordinate system that is relevant to humeral head resection.
 - b. Mapping out the regional change in canal features within the proximal humerus' trabecular-canal in order to gain insight into the volume envelope that constrains the design of stemless humeral implants.
2. To understand how variation in the modelling of proximal humeral trabecular bone stiffness influences FE outcome measures when using identical meshing techniques.
3. To assess how variation in stemless implant fixation feature geometry influences the response of the post-reconstructed peri-implant bone of the proximal humerus.

1.6.2 Specific Hypotheses

1.
 - a. The apparent density of trabecular bone within the proximal humerus is non-uniform and perhaps higher peripherally near the cortical-trabecular division, as well as proximally beneath the humeral articulation, decreasing to a plateau at a quantifiable depth beneath the humeral head resection plane.

- b. The trabecular-canal of the proximal humerus follows a path whose depth, curvature and bounding diameter change in a quantifiable manner, thereby permitting pooled observations to be made regarding the volume envelope available for the design of stemless implants.
2. Changing the inhomogeneous trabecular stiffness relationship applied to proximal humerus FE models, based on several anatomic-sites throughout the body, will result in low variation (*i.e.*, standard deviations < 10%) in identical mesh-based FE outcome measures; and that these deviations will be less than those associated with transitioning to a homogeneous trabecular stiffness model.
3. Changing the fixation feature geometry of stemless implants will result in quantifiable changes in the peri-implant bone response; specifically, that implants obtaining peripheral fixation and those that follow the natural curvature of the proximal trabecular-canal will produce more favorable bone responses compared to stemless implants with central, boundary-crossing or axisymmetric designs.

1.7 Thesis Overview

Chapter 2 describes an investigation conducted to quantify the regional variation in proximal humeral bone density in a resection-based humeral coordinate system using the reconstruction of clinical CT images, as detailed in Objective 1a in Section 1.6.1. Chapter 3 then presents a study quantifying several morphological parameters of the proximal humerus' canal path, also through the application of CT-based tools, as outlined in Objective 1b. Chapter 4 describes an analysis of the response of the identical mesh-based FE outcomes, as presented in Section 1.4.2.5, to variation in the modelling of trabecular stiffness in the proximal humerus, as outlined in Objective 2. Chapter 5 then presents a FE investigation into the peri-implant humeral bone response following stemless shoulder reconstruction with a variety of fixation features whose geometry is inspired by the morphological analyses completed in Chapters 2 and 3, as outlined in Objective 3. In closing, Chapter 6 provides a discussion of the work completed within this dissertation and concluding reflections on the implications of this work as well as the future directions for this research.

1.8 References

- [1] Culham, E., and Peat, M., 1993, "Functional Anatomy of the Shoulder Complex," *J. Orthop. Sport. Phys. Ther.*, **18**(1), pp. 342–350.
- [2] Peat, M., 1986, "Functional Anatomy of the Shoulder Complex," *J. Am. Phys. Ther. Assoc.*, **66**(12), pp. 1855–1865.
- [3] Neer, C. S. I., 1990, *Shoulder Reconstruction*, W.B. Saunders Co., Philadelphia, Toronto.
- [4] An, K. N., Browne, A. O., Korinek, S., Tanaka, S., and Morrey, B. F., 1991, "Three-dimensional kinematics of glenohumeral elevation," *J. Orthop. Res.*, **9**(1), pp. 143–149.
- [5] Curl, L., and Warren, R., 1996, "Glenohumeral joint stability. Selective cutting studies on the static capsular restraints.," *Clin. Orthop. Relat. Res.*, (330), pp. 54–65.
- [6] Halder, A. M., Halder, C. G., Zhao, K. D., O'Driscoll, S. W., Morrey, B. F., and An, K. N., 2001, "Dynamic inferior stabilizers of the shoulder joint," *Clin. Biomech.*, **16**(2), pp. 138–143.
- [7] Karduna, A. R., Williams, G. R., Williams, J. L., and Iannotti, J. P., 1996, "Kinematics of the glenohumeral joint: Influences of muscle forces, ligamentous constraints, and articular geometry," *J. Orthop. Res.*, **14**(6), pp. 986–993.
- [8] Lippit, S., and Matsen, F., 1993, "Mechanisms of Glenohumeral Joint Stability," *Clin. Orthop. Relat. Res.*, (291), pp. 20–28.
- [9] Anglin, C., Wyss, U. P., and Pichora, D. R., 2000, "Glenohumeral contact forces," *Proc. Inst. Mech. Eng. Part H - J. Eng. Med.*, **214**(FEBRUARY), pp. 637–644.
- [10] Conzen, A., and Eckstein, F., 2000, "Quantitative determination of articular pressure in the human shoulder joint," *J. Shoulder Elb. Surg.*, **9**(3), pp. 196–204.
- [11] Hopkins, A. R., Hansen, U. N., Amis, A. a, Taylor, M., and Emery, R. J., 2007,

- “Glenohumeral kinematics following total shoulder arthroplasty: a finite element investigation,” *J. Orthop. Res.*, **25**(1), pp. 108–115.
- [12] Terrier, A., Ramondetti, S., Merlini, F., Pioletti, D. D., and Farron, A., 2010, “Biomechanical consequences of humeral component malpositioning after anatomical total shoulder arthroplasty,” *J. Shoulder Elb. Surg.*, **19**(8), pp. 1184–1190.
- [13] van der Helm, F. C. T., 1994, “A finite element musculoskeletal model of the shoulder mechanism,” *J. Biomech.*, **27**(5), pp. 551–569.
- [14] Bergmann, G., Graichen, F., Bender, A., Kaab, M., Rohlmann, A., and Westerhoff, P., 2007, “In vivo glenohumeral contact forces-Measurements in the first patient 7 months postoperatively,” *J. Biomech.*, **40**(10), pp. 2139–2149.
- [15] Westerhoff, P., Graichen, F., Bender, a, Halder, a, Beier, a, Rohlmann, a, and Bergmann, G., 2009, “In vivo measurement of shoulder joint loads during activities of daily living,” *J. Biomech.*, **42**(12), pp. 1840–9.
- [16] Bergmann, G., Graichen, F., Bender, a, Rohlmann, a, Halder, a, Beier, a, and Westerhoff, P., 2011, “In vivo gleno-humeral joint loads during forward flexion and abduction,” *J. Biomech.*, **44**(8), pp. 1543–52.
- [17] Itoi, E., Morrey, B. F., and An, K., 2009, “Biomechanics of the Shoulder,” *The Shoulder*, Saunders Elsevier, Philadelphia, pp. 213–266.
- [18] Poppen, N. K., and Walker, P. S., 1976, “Normal and Abnormal Motion of the Shoulder,” *J. Bone Jt. Surg.*, **58**(2), pp. 195–201.
- [19] Speer, K. P., Hannafin, J. A., Altchek, D. W., and Warren, R. F., 1994, “An Evaluation of the Shoulder Relocation Test,” *Am. J. Sports Med.*, **22**(2), pp. 177–183.
- [20] O’Brien, S. J., Voos, J. E., Neviasser, A. S., and Drakos, M. C., 2009, “Developmental anatomy of the shoulder and anatomy of the glenohumeral joint,” *The Shoulder*, Saunders Elsevier, Philadelphia, pp. 1–32.

- [21] Burkart, A. C., and Debski, R. E., 2002, "Anatomy and function of the glenohumeral ligaments in anterior shoulder instability," *Clin. Orthop. Relat. Res.*, (400), pp. 32–39.
- [22] Clark, J. M., and Harryman, D. T., 1992, "Tendons, ligaments, and capsule of the rotator cuff. Gross and microscopic anatomy," *J. Bone Jt. Surg.*, **74**(5), pp. 713–725.
- [23] Hess, S. A., 2000, "Functional stability of the glenohumeral joint," *Man. Ther.*, **5**(2), pp. 63–71.
- [24] Kask, K., Põldoja, E., Lont, T., Norit, R., Merila, M., Busch, L. C., and Kolts, I., 2010, "Anatomy of the superior glenohumeral ligament," *J. Shoulder Elb. Surg.*, **19**(6), pp. 908–916.
- [25] Soslowky, L. J., Carpenter, J. E., Bucchieri, J. S., and Flatow, E. L., 1997, "Biomechanics of the rotator cuff," *Orthop. Clin. North Am.*, **28**(1), pp. 17–30.
- [26] Ackland, D. C., Pak, P., Richardson, M., and Pandy, M. G., 2008, "Moment arms of the muscles crossing the anatomical shoulder," *J. Anat.*, **213**(4), pp. 383–390.
- [27] Ackland, D. C., and Pandy, M. G., 2011, "Moment arms of the shoulder muscles during axial rotation," *J. Orthop. Res.*, **29**(5), pp. 658–667.
- [28] Jobe, C. M., Phipatanakul, W. P., and Coen, M. J., 2009, "Gross Anatomy of the Shoulder," *The Shoulder*, Saunders Elsevier, Philadelphia, pp. 33–100.
- [29] Wolff, J., 1986, *The Law of Bone Remodelling*, Springer, Berlin.
- [30] Huiskes, R., Weinans, H., Grootenboer, H. J., Dalstra, M., Fudala, B., and Slooff, T. J., 1987, "Adaptive Bone-Remodeling Theory Applied to Prosthetic-Design Analysis," *J. Biomech.*, **20**(11), pp. 1135–1150.
- [31] Bonnucci, E., 2000, "Basic Composition and Structure of Bone," *Mechanical Testing of Bone and the Bone-Implant Interface*, Y.H. An, and R.A. Draughn, eds., CRC Press Inc., Boca Raton, pp. 3–21.

- [32] Wolff, J., 1892, “Das Gesetz der Transformation der Knochen,” *DMW-Deutsche Medizinische Wochenschrift*, **19**(47), pp. 1222–1224.
- [33] Cowin, S. C., and Hegedus, D. H., 1976, “Bone remodeling II: theory of adaptive elasticity,” *J. Elast.*, **6**(3), pp. 313–326.
- [34] Hadjidakis, D. J., and Androulakis, I. I., 2006, “Bone remodeling,” *Ann. N. Y. Acad. Sci.*, **1092**, pp. 385–396.
- [35] McKinley, M., and O’Loughlin, V. D., 2006, “Comparison of Compact and Spongy Bone,” *Human Anatomy*, K.A.W. Peterson Michelle Queck, Kristine A., ed., McGraw-Hill, New York, pp. 155–157.
- [36] Rho, J. Y., Ashman, R. B., and Turner, C. H., 1993, “Young’s modulus of trabecular and cortical bone material: Ultrasonic and microtensile measurements,” *J. Biomech.*, **26**(2), pp. 111–119.
- [37] Bayraktar, H. H., Morgan, E. F., Niebur, G. L., Morris, G. E., Wong, E. K., and Keaveny, T. M., 2004, “Comparison of the elastic and yield properties of human femoral trabecular and cortical bone tissue,” *J. Biomech.*, **37**(1), pp. 27–35.
- [38] Austman, R. L., Milner, J. S., Holdsworth, D. W., and Dunning, C. E., 2009, “Development of a customized density-modulus relationship for use in subject-specific finite element models of the ulna,” *Proc. Inst. Mech. Eng. H.*, **223**(6), pp. 787–794.
- [39] Schileo, E., Dall’Ara, E., Taddei, F., Malandrino, A., Schotkamp, T., Baleani, M., and Viceconti, M., 2008, “An accurate estimation of bone density improves the accuracy of subject-specific finite element models,” *J. Biomech.*, **41**, pp. 2483–2491.
- [40] Morgan, E. F., Bayraktar, H. H., and Keaveny, T. M., 2003, “Trabecular bone modulus-density relationships depend on anatomic site,” *J. Biomech.*, **36**, pp. 897–904.
- [41] Knowles, N. K., Reeves, J. M., and Ferreira, L. M., 2016, “Quantitative Computed

- Tomography (QCT) derived Bone Mineral Density (BMD) in finite element studies: a review of the literature,” *J. Exp. Orthop.*, **3**(36), pp. 1–16.
- [42] Taylor, W. R., Roland, E., Ploeg, H., Hertig, D., Klabunde, R., Warner, M. D., Hobatho, M. C., Rakotomanana, L., and Clift, S. E., 2002, “Determination of orthotropic bone elastic constants using FEA and modal analysis,” *J. Biomech.*, **35**(6), pp. 767–773.
- [43] Vijayakumar, V., and Quenneville, C. E., 2016, “Quantifying the regional variations in the mechanical properties of cancellous bone of the tibia using indentation testing and quantitative computed tomographic imaging,” *Proc. Inst. Mech. Eng. H.*, **230**(6), pp. 588–93.
- [44] Carter, D. R., and Hayes, W. C., 1977, “The compressive behavior of bone as a two-phase porous structure,” *J. Bone Joint Surg. Am.*, **59**(7), pp. 954–962.
- [45] Schaffler, M. B., and Burr, D. B., 1988, “Stiffness of compact bone: effects of porosity and density,” *J. Biomech.*, **21**(1), pp. 13–16.
- [46] Inman, V. T., and Abbott, L. C., 1944, “Observations on the function of the shoulder joint,” *J. Bone Jt. Surg.*, **26**(1), pp. 1–30.
- [47] Soslowky, L. J., Flatow, E. L., Bigliani, L. U., Pawluk, R. J., Ateshian, G. A., and Mow, V. C., 1992, “Quantitation of in situ contact areas at the glenohumeral joint: A biomechanical study,” *J. Orthop. Res.*, **10**(4), pp. 524–534.
- [48] Soslowky, L. J., Flatow, E. L., Bigliani, L. U., and Mow, V. C., 1992, “Articular Geometry of the Glenohumeral Joint,” *Clin. Orthop. Relat. Res.*, **285**, pp. 181–190.
- [49] Wu, G., van der Helm, F. C. T., Veeger, H. E. J. (DirkJan), Makhsous, M., Van Roy, P., Anglin, C., Nagels, J., Karduna, A. R., McQuade, K., Wang, X., Werner, F. W., and Buchholz, B., 2005, “ISB recommendation on definitions of joint coordinate systems of various joints for the reporting of human joint motion—Part II: shoulder, elbow, wrist and hand,” *J. Biomech.*, **38**(5), pp. 981–992.
- [50] Robertson, D. D., Yuan, J., Bigliani, L. U., Flatow, E. L., and Yamaguchi, K.,

- 2000, "Three-dimensional analysis of the proximal part of the humerus: relevance to arthroplasty.," *J. Bone Joint Surg. Am.*, **82**-A, pp. 1594–1602.
- [51] Roberts, S. N. J., Foley, A. P. J., Swallow, H. M., Wallace, W. A., and Coughlan, D. P., 1991, "The Geometry of the Humeral Head and the Design of Prostheses," *J. Bone Jt. Surg.*, **73**-B(4), pp. 647–650.
- [52] Iannotti, J. P., Gabriel, J. P., Schneck, S. L., Evans, B. G., and Misra, S., 1992, "The Normal Glenohumeral Relationships: An Anatomical Study of One Hundred and Forty Shoulders," *J. Bone Jt. Surg.*, **74**-A(4), pp. 491–500.
- [53] Boileau, P., and Walch, G., 1997, "The three-dimensional geometry of the proximal humerus. Implications for surgical technique and prosthetic design.," *J. Bone Jt. Surg.*, **79**-B(5), pp. 857–865.
- [54] Ballmer, F. T., Sidles, J. A., Lippitt, S. B., and Matsen, F. A., 1993, "Humeral head prosthetic arthroplasty: Surgically relevant geometric considerations," *J. Shoulder Elb. Surg.*, **2**(6), pp. 296–304.
- [55] Bauer, T. W., and Schils, J., 1999, "The pathology of total joint arthroplasty II. Mechanisms of implant failure," *Skeletal Radiol.*, **28**(9), pp. 483–497.
- [56] Engh, C., and McGovern, T., 1992, "A quantitative evaluation of periprosthetic bone-remodeling after cementless total hip arthroplasty," *J Bone Joint Surg*, **74**(7), pp.1009–1020.
- [57] Kerner, J., Huiskes, R., van Lenthe, G. ., Weinans, H., van Rietbergen, B., Engh, C. ., and Amis, a. ., 1999, "Correlation between pre-operative periprosthetic bone density and post-operative bone loss in THA can be explained by strain-adaptive remodelling," *J. Biomech.*, **32**(7), pp. 695–703.
- [58] Sychterz, C. J., and Engh, C. A., 1996, "The Influence of Clinical Factors on Periprosthetic Bone Remodeling," *Clin. Orthop. Relat. Res.*, (322), pp. 285–292.
- [59] Hepp, P., Lill, H., Bail, H., Korner, J., Niederhagen, M., Haas, N. P., Josten, C., and Duda, G. N., 2003, "Where should implants be anchored in the humeral

- head?," Clin. Orthop. Relat. Res., (415), pp. 139–147.
- [60] Zumstein, V., Kraljević, M., Huegli, R., and Muller-Gerbl, M., 2011, "Mineralisation patterns in the subchondral bone plate of the humeral head," Surg. Radiol. Anat., **33**(9), pp. 775–779.
- [61] Kraljević, M., Zumstein, V., Hügli, R., and Müller-Gerbl, M., 2013, "A comparison of subchondral bone mineralization between the glenoid cavity and the humeral head on 57 cadaverous shoulder joints," Surg. Radiol. Anat., **35**(4), pp. 295–300.
- [62] Yamada, M., Briot, J., Pedrono, A., Sans, N., Mansat, P., Mansat, M., and Swider, P., 2007, "Age- and gender-related distribution of bone tissue of osteoporotic humeral head using computed tomography," J. Shoulder Elb. Surg., **16**(5), pp. 596–602.
- [63] Alidousti, H., Giles, J. W., Emery, R. J. H., and Jeffers, J., 2017, "Spatial mapping of humeral head bone density," J. Shoulder Elb. Surg., **26**(9), pp. 1653–1661.
- [64] Neer, C. S., 1955, "Articular Replacement for the Humeral Head," J. Bone Jt. Surg., **37**(2), pp. 215–228.
- [65] Neer, C. S., 1974, "Replacement Arthroplasty for Glenohumeral Osteoarthritis," J. Bone Jt. Surg., **56**(1), pp. 1–13.
- [66] Boileau, P., Sinnerton, R. J., Chuinard, C., and Walch, G., 2006, "Arthroplasty of the shoulder," J. Bone Joint Surg. Br., **88**(5), pp. 562–75.
- [67] Nagels, J., Stokdijk, M., and Rozing, P. M., 2003, "Stress shielding and bone resorption in shoulder arthroplasty," J. Shoulder Elb. Surg., **2746**(2), pp. 35–39.
- [68] Spormann, C., Durchholz, H., Audigé, L., Flury, M., Schwyzer, H. K., Simmen, B. R., and Kolling, C., 2014, "Patterns of proximal humeral bone resorption after total shoulder arthroplasty with an uncemented rectangular stem," J. Shoulder Elb. Surg., **23**(7), pp. 1028–1035.

- [69] Inoue, K., Suenaga, N., Oizumi, N., Yamaguchi, H., Miyoshi, N., Taniguchi, N., Munemoto, M., Egawa, T., and Tanaka, Y., 2017, "Humeral bone resorption after anatomic shoulder arthroplasty using an uncemented stem," *J. Shoulder Elb. Surg.*, **26**(11), pp. 1984–1989.
- [70] Verborgt, O., El-Abiad, R., and Gazielly, D. F., 2007, "Long-term results of uncemented humeral components in shoulder arthroplasty," *J. Shoulder Elb. Surg.*, **16**(3 SUPPL.), pp. 13–18.
- [71] Huguet, D., DeClercq, G., Rio, B., Teissier, J., and Zipoli, B., 2010, "Results of a new stemless shoulder prosthesis: radiologic proof of maintained fixation and stability after a minimum of three years' follow-up.," *J. Shoulder Elbow Surg.*, **19**(6), pp. 847–52.
- [72] Schairer, W. W., Nwachukwu, B. U., Lyman, S., Craig, E. V., and Gulotta, L. V., 2015, "National utilization of reverse total shoulder arthroplasty in the United States," *J. Shoulder Elb. Surg.*, **24**(1), pp. 91–97.
- [73] Kim, S. H., Wise, B. L., Zhang, Y., and Szabo, R. M., 2011, "Increasing Incidence of Shoulder Arthroplasty in the United States," *J. Bone Jt. Surg.*, **93**, pp. 2249–2254.
- [74] Day, J. S., Lau, E., Ong, K. L., Williams, G. R., Ramsey, M. L., and Kurtz, S. M., 2010, "Prevalence and projections of total shoulder and elbow arthroplasty in the United States to 2015," *J. Shoulder Elb. Surg.*, **19**(8), pp. 1115–1120.
- [75] van de Sande, M. a J., Brand, R., and Rozing, P. M., 2006, "Indications, complications, and results of shoulder arthroplasty.," *Scand. J. Rheumatol.*, **35**(6), pp. 426–434.
- [76] Bohsali, K. I., Wirth, M. A., and Rockwood, C. A. J., 2006, "Complications of Total Shoulder Arthroplasty," *J. Bone Joint Surg. Am.*, **88**(10), pp. 2279–2292.
- [77] Wirth, M. A., and Rockwood, C. A., 1996, "Current Concepts Review - Complications of Total Shoulder-Replacement Arthroplasty*," *J. Bone Jt. Surg.*,

78(4), pp. 603–616.

- [78] Raiss, P., Edwards, T. B., Deutsch, A., Shah, A., Bruckner, T., Loew, M., Boileau, P., and Walch, G., 2014, “Radiographic Changes Around Humeral Components in Shoulder Arthroplasty,” *J. Bone Jt. Surg.*, **96**(7), p. e54(1-9).
- [79] Athwal, G. S., Sperling, J. W., Rispoli, D. M., and Cofield, R. H., 2009, “Periprosthetic humeral fractures in shoulder arthroplasty,” *J. Bone Jt. Surg.*, **91**(3), pp. 594–603.
- [80] Kumar, S., Sperling, J. W., Haidukewych, G. H., and Cofield, R. H., 2004, “Periprosthetic humeral fractures in shoulder arthroplasty,” *J. Bone Jt. Surg.*, **86**(4), pp. 680–689.
- [81] Sahota, S., Sperling, J. W., and Cofield, R. H., 2014, “Humeral windows and longitudinal splits for component removal in revision shoulder arthroplasty,” *J. Shoulder Elb. Surg.*, **23**(10), pp. 1485–1491.
- [82] Van Thiel, G. S., Halloran, J. P., Twigg, S., Romeo, A. A., and Nicholson, G. P., 2011, “The vertical humeral osteotomy for stem removal in revision shoulder arthroplasty: Results and technique,” *J. Shoulder Elb. Surg.*, **20**(8), pp. 1248–1254.
- [83] Phipatanakul, W. P., Bowen, J. M., and Jobe, C. M., 2009, “Removal of well-fixed flanged humeral prostheses may require humeral expansion,” *J. Shoulder Elb. Surg.*, **18**(5), pp. 724–727.
- [84] Johnston, P. S., Creighton, R. A., and Romeo, A. A., 2012, “Humeral component revision arthroplasty: Outcomes of a split osteotomy technique,” *J. Shoulder Elb. Surg.*, **21**(4), pp. 502–506.
- [85] Cil, A., Veillette, C. J. H., Sanchez-Sotelo, J., Sperling, J. W., Schleck, C., and Cofield, R. H., 2009, “Revision of the humeral component for aseptic loosening in arthroplasty of the shoulder,” *J. Bone Jt. Surg. - Br. Vol.*, **91-B**(1), pp. 75–81.
- [86] Churchill, R. S., 2014, “Stemless shoulder arthroplasty: current status,” *J. Shoulder Elb. Surg.*, **23**(9), pp. 1409–1414.

- [87] Churchill, R. S., and Athwal, G. S., 2016, “Stemless shoulder arthroplasty—current results and designs,” *Curr. Rev. Musculoskelet. Med.*, **9**(1), pp. 10–16.
- [88] Kadum, B., Mafi, N., Norberg, S., and Sayed-Noor, A. S., 2011, “Results of the Total Evolutive Shoulder System (TESS): A single-centre study of 56 consecutive patients,” *Arch. Orthop. Trauma Surg.*, **131**(12), pp. 1623–1629.
- [89] Razmjou, H., Holtby, R., Christakis, M., Axelrod, T., and Richards, R., 2013, “Impact of prosthetic design on clinical and radiologic outcomes of total shoulder arthroplasty: A prospective study,” *J. Shoulder Elb. Surg.*, **22**(2), pp. 206–214.
- [90] Berth, A., and Pap, G., 2013, “Stemless shoulder prosthesis versus conventional anatomic shoulder prosthesis in patients with osteoarthritis: a comparison of the functional outcome after a minimum of two years follow-up,” *J. Orthop. Traumatol.*, **14**(1), pp. 31–7.
- [91] Habermeyer, P., Lichtenberg, S., Tauber, M., and Magosch, P., 2015, “Midterm results of stemless shoulder arthroplasty: A prospective study,” *J. Shoulder Elb. Surg.*, **24**(9), pp. 1463–1472.
- [92] Maier, M. W., Lauer, S., Klotz, M. C., Bühlhoff, M., Spranz, D., and Zeifang, F., 2015, “Are there differences between stemless and conventional stemmed shoulder prostheses in the treatment of glenohumeral osteoarthritis?,” *BMC Musculoskelet. Disord.*, **16**(1), p. 275.
- [93] Churchill, R. S., Chuinard, C., Wiater, J. M., Friedman, R., Freehill, M., Jacobson, S., Spencer, E., Holloway, G. B., Wittstein, J., Lassiter, T., Smith, M., Blaine, T., and Nicholson, G. P., 2016, “Clinical and Radiographic Outcomes of the Simpliciti Canal-Sparing Shoulder Arthroplasty System: A Prospective Two-Year Multicenter Study,” *J. Bone Jt. Surg.*, **98**(7), pp. 552–560.
- [94] Berth, A., März, V., Wissel, H., Awiszus, F., Amthauer, H., and Lohmann, C. H., 2016, “SPECT/CT demonstrates the osseointegrative response of a stemless shoulder prosthesis,” *J. Shoulder Elb. Surg.*, **25**(4), pp. e96–e103.

- [95] Kadum, B., Wahlstrom, P., Khoschnau, S., Sjoden, G., and Sayed-Noor, A., 2016, "Association of lateral humeral offset with functional outcome and geometric restoration in stemless total shoulder arthroplasty," *J. Shoulder Elb. Surg.*, **25**(10), pp. e285–e294.
- [96] Kadum, B., Hassany, H., Wadsten, M., Sayed-Noor, A., and Sjoden, G., 2016, "Geometrical analysis of stemless shoulder arthroplasty: a radiological study of seventy TESS total shoulder prostheses," *Int. Orthop.*, **40**(4), pp. 751–758.
- [97] Ballas, R., Teissier, P., and Teissier, J., 2016, "Stemless shoulder prosthesis for treatment of proximal humeral malunion does not require tuberosity osteotomy," *Int. Orthop.*, **40**(7), pp. 1473–1479.
- [98] Uschok, S., Magosch, P., Moe, M., Lichtenberg, S., and Habermeyer, P., 2017, "Is the stemless humeral head replacement clinically and radiographically a secure equivalent to standard stem humeral head replacement in the long-term follow-up? A prospective randomized trial," *J. Shoulder Elb. Surg.*, **26**(2), pp. 225–232.
- [99] Collin, P., Matsukawa, T., Boileau, P., Brunner, U., and Walch, G., 2017, "Is the humeral stem useful in anatomic total shoulder arthroplasty?," *Int. Orthop.*, **41**, pp. 1035–1039.
- [100] Engelhardt, L. V. von, Manzke, M., Breil-Wirth, A., Filler, T. J., and Jerosch, J., 2017, "Restoration of the joint geometry and outcome after stemless TESS shoulder arthroplasty," *World J. Orthop.*, **8**(10), pp. 790–797.
- [101] Hawi, N., Magosch, P., Tauber, M., Lichtenberg, S., and Habermeyer, P., 2017, "Nine-year outcome after anatomic stemless shoulder prosthesis: clinical and radiologic results," *J. Shoulder Elb. Surg.*, **26**(9), pp. 1609–1615.
- [102] Heuberger, P. R., Brandl, G., Pauzenberger, L., Laky, B., Kriegleder, B., and Anderl, W., 2018, "Radiological changes do not influence clinical mid-term outcome in stemless humeral head replacements with hollow screw fixation: a prospective radiological and clinical evaluation," *BMC Musculoskelet. Disord.*, **19**(28), pp. 1–9.

- [103] Büchler, P., Ramaniraka, N. a., Rakotomanana, L. R., Iannotti, J. P., and Farron, a., 2002, “A finite element model of the shoulder: Application to the comparison of normal and osteoarthritic joints,” *Clin. Biomech.*, **17**(9–10), pp. 630–639.
- [104] Couteau, B., Mansat, P., Estivalèzes, E., Darmana, R., Mansat, M., and Egan, J., 2001, “Finite element analysis of the mechanical behavior of a scapula implanted with a glenoid prosthesis,” *Clin. Biomech.*, **16**(7), pp. 566–575.
- [105] Gupta, S., Van Der Helm, F. C. T., and Van Keulen, F., 2004, “The possibilities of uncemented glenoid component - A finite element study,” *Clin. Biomech.*, **19**(3), pp. 292–302.
- [106] Pomwenger, W., Entacher, K., Resch, H., and Schuller-Götzburg, P., 2014, “Need for CT-based bone density modelling in finite element analysis of a shoulder arthroplasty revealed through a novel method for result analysis,” *Biomed. Eng. / Biomed. Tech.*, **59**(5), pp. 421–430.
- [107] Terrier, A., Brighenti, V., Pioletti, D. P., and Farron, A., 2012, “Importance of polyethylene thickness in total shoulder arthroplasty: a finite element analysis,” *Clin. Biomech. (Bristol, Avon)*, **27**(5), pp. 443–8.
- [108] Hermida, J. C., Flores-Hernandez, C., Hoenecke, H. R., and D’Lima, D. D., 2014, “Augmented wedge-shaped glenoid component for the correction of glenoid retroversion: A finite element analysis,” *J. Shoulder Elb. Surg.*, **23**(3), pp. 347–354.
- [109] Dahan, G., Trabelsi, N., Safran, O., and Yosibash, Z., 2016, “Verified and validated finite element analyses of humeri,” *J. Biomech.*, **49**(7), pp. 1094–1102.
- [110] Schmidutz, F., Agarwal, Y., Müller, P. E., Gueorguiev, B., Richards, R. G., and Sprecher, C. M., 2014, “Stress-shielding induced bone remodeling in cementless shoulder resurfacing arthroplasty: A finite element analysis and in vivo results,” *J. Biomech.*, **47**(14), pp. 3509–3516.
- [111] Razfar, N., Reeves, J. M., Langohr, D. G., Willing, R., Athwal, G. S., and Johnson,

- J. A., 2016, "Comparison of proximal humeral bone stresses between stemless, short stem, and standard stem length: a finite element analysis," *J. Shoulder Elb. Surg.*, **25**(7), pp. 1076–83.
- [112] Favre, P., and Henderson, A. D., 2016, "Prediction of stemless humeral implant micromotion during upper limb activities," *Clin. Biomech.*, **36**, pp. 46–51.
- [113] Favre, P., Seebeck, J., Thistlethwaite, P. A. E., Obrist, M., Steffens, J. G., Hopkins, A. R., and Hulme, P. A., 2016, "In vitro initial stability of a stemless humeral implant," *Clin. Biomech.*, **32**, pp. 113–117.
- [114] Long, J. P., and Bartel, D. L., 2006, "Surgical variables affect the mechanics of a hip resurfacing system," *Clin. Orthop. Relat. Res.*, (453), pp. 115–122.
- [115] Mow, V. C., and Huiskes, R., 2005, *Basic Orthopaedic Biomechanics & Mechanobiology*, Lippincott Williams & Wilkins, Philadelphia.
- [116] Sumner, D. R., Turner, T. M., Igloria, R., Urban, R. M., and Galante, J. O., 1998, "Functional adaptation and ingrowth of bone vary as a function of hip implant stiffness," *J. Biomech.*, **31**(10), pp. 909–917.
- [117] Sumner, D. R., and Galante, J. O., 1992, "Determinants of Stress Shielding : Design Versus Materials Versus Interface," *Clin. Orthop. Relat. Res.*, **274**, pp. 202–212.
- [118] Chin, P. Y. K., Sperling, J. W., Cofield, R. H., and Schleck, C., 2006, "Complications of total shoulder arthroplasty: Are they fewer or different?," *J. Shoulder Elb. Surg.*, **15**(1), pp. 19–22.
- [119] Neuert, M. A. C., and Dunning, C. E., 2013, "Determination of remodeling parameters for a strain-adaptive finite element model of the distal ulna," *Proc. Inst. Mech. Eng. Part H - J. Eng. Med.*, **227**(9), pp. 994–1001.
- [120] Huiskes, R., Ruimerman, R., Lenthe, G. H. Van, and Janssen, J. D., 2000, "Effects of mechanical forces on maintenance and adaptation of form in trabecular bone," *Nature*, **405**(June), pp. 704–706.

- [121] Weinans, H., Huiskes, R., and Grootenboer, H. J., 1992, “The behavior of adaptive bone-remodeling simulation models,” *J. Biomech.*, **25**(12), pp. 1425–1441.
- [122] Carter, D. R., Fyhrie, D. P., and Whalen, R. T., 1987, “Trabecular bone density and loading history: Regulation of connective tissue biology by mechanical energy,” *J. Biomech.*, **20**(8).
- [123] Kalender, W. A., 2006, “X-ray computed tomography,” *Phys. Med. Biol.*, **51**(13), pp. 29–43.
- [124] Kluess, D., Souffrant, R., Mittelmeier, W., Wree, A., Schmitz, K. P., and Bader, R., 2009, “A convenient approach for finite-element-analyses of orthopaedic implants in bone contact: Modeling and experimental validation,” *Comput. Methods Programs Biomed.*, **95**(1), pp. 23–30.
- [125] Willing, R., and Kim, I. Y., 2011, “Design optimization of a total knee replacement for improved constraint and flexion kinematics,” *J. Biomech.*, **44**(6), pp. 1014–1020.
- [126] Willing, R., King, G. J. W., and Johnson, J. a, 2012, “The effect of implant design of linked total elbow arthroplasty on stability and stress: a finite element analysis,” *Comput. Methods Biomech. Biomed. Engin.*, **5842**(1248), p. 2012.
- [127] Willing, R., and Kim, I. Y., 2012, “Quantifying the competing relationship between durability and kinematics of total knee replacements using multiobjective design optimization and validated computational models,” *J. Biomech.*, **45**(1), pp. 141–147.
- [128] Willing, R., and Kim, I. Y., 2009, “Three dimensional shape optimization of total knee replacements for reduced wear,” *Struct. Multidiscip. Optim.*, **38**(4), pp. 405–414.
- [129] Willing, R., and Kim, I. Y., 2012, “The development, calibration and validation of a numerical total knee replacement kinematics simulator considering laxity and unconstrained flexion motions,” *Comput. Methods Biomech. Biomed. Engin.*,

15(6), pp. 585–593.

- [130] Lapner, M., Willing, R., Johnson, J. A., and King, G. J. W., 2014, “The effect of distal humeral hemiarthroplasty on articular contact of the elbow,” *Clin. Biomech.*, **29**(5), pp. 537–544.
- [131] Bah, M. T., Nair, P. B., and Browne, M., 2009, “Mesh morphing for finite element analysis of implant positioning in cementless total hip replacements,” *Med. Eng. Phys.*, **31**(10), pp. 1235–1243.
- [132] Fernandes, P. R., Folgado, J., Jacobs, C., and Pellegrini, V., 2002, “A contact model with ingrowth control for bone remodelling around cementless stems,” *J. Biomech.*, **35**(2), pp. 167–176.
- [133] Matsoukas, G., and Kim, I. Y., 2009, “Design optimization of a total hip prosthesis for wear reduction,” *J. Biomech. Eng.*, **131**(5), p. 51003.
- [134] Logan, D. L., 2002, “Introduction,” *A First Course in the Finite Element Method*, Brooks/Cole, Pacific Grove, pp. 1–25.
- [135] Tadepalli, S. C., Erdemir, A., and Cavanagh, P. R., 2011, “Comparison of hexahedral and tetrahedral elements in finite element analysis of the foot and footwear,” *J. Biomech.*, **44**(12), pp. 2337–2343.
- [136] Benzley, S. E., Perry, E., Merkle, K., Clark, B., and Sjaardema, G., 1995, “A Comparison of All-Hexahedral and All-Tetrahedral Finite Element Meshes for Elastic and Elasto-Plastic Analysis,” *4th Int. Meshing Roundtable*, Sandia Natl. Lab., **17**, pp. 179–191.
- [137] Cifuentes, A., and Kalbag, A., 1992, “A performance study of tetrahedral and hexahedral elements in 3-D finite element structural analysis,” *Finite Elem. Anal. Des.*, **12**(3–4), pp. 313–318.
- [138] Ramos, A., and Simões, J. A., 2006, “Tetrahedral versus hexahedral finite elements in numerical modelling of the proximal femur,” *Med. Eng. Phys.*, **28**(9), pp. 916–924.

- [139] Polgar, K., Viceconti, M., and O'Connor, J. J., 2001, "A comparison between automatically generated linear and parabolic tetrahedra when used to mesh a human femur," *Proc. Inst. Mech. Eng. Part H J. Eng. Med.*, **215**(1), pp. 85–94.
- [140] Graichen, F., Arnold, R., Rohlmann, A., and Bergmann, G., 2007, "Implantable 9-Channel Telemetry System for In Vivo Load Measurements With Orthopedic Implants," **54**(2), pp. 253–261.
- [141] Bergmann, G., Graichen, F., Rohlmann, a, Westerhoff, P., Heinlein, B., Bender, a, and Ehrig, R., 2008, "Design and calibration of load sensing orthopaedic implants.," *J. Biomech. Eng.*, **130**(April 2008), p. 21009.
- [142] Niebur, G. L., Feldstein, M. J., Yuen, J. C., Chen, T. J., and Keaveny, T. M., 2000, "High-resolution finite element models with tissue strength asymmetry accurately predict failure of trabecular bone," *J. Biomech.*, **33**(12), pp. 1575–1583.
- [143] Morgan, E. F., and Keaveny, T. M., 2001, "Dependence of yield strain of human trabecular bone on anatomic site," *J. Biomech.*, **34**(5), pp. 569–577.
- [144] Kopperdahl, D. L., and Keaveny, T. M., 1998, "Yield strain behavior of trabecular bone," *J. Biomech.*, **31**(7), pp. 601–608.
- [145] Zumstein, V., Kraljević, M., Wirz, D., Hügli, R., and Müller-Gerbl, M., 2012, "Correlation between mineralization and mechanical strength of the subchondral bone plate of the humeral head," *J. Shoulder Elb. Surg.*, **21**(7), pp. 887–893.
- [146] Huiskes, R., Weinans, H., and van Rietbergen, B., 1992, "The relationship between stress shielding and bone resorption around total hip stems and the effects of flexible materials.," *Clin. Orthop. Relat. Res.*, pp. 124–134.

Chapter 2

An Assessment of Proximal Humerus Density with Reference to Stemless Implants

A version of this chapter has been accepted for publication [1].

2.1 Introduction

Shoulder arthroplasty is an effective surgical treatment for osteoarthritis (OA), fracture, inflammatory arthritis, and cuff tear arthropathy. Implant manufacturers have recently designed shorter stem and stemless implants, which are less invasive and preserve bone, in the hopes of decreasing stress shielding and bone remodeling.

Wolff's Law states that bone is resorbed and remodeled in-part because of the loads that it is subjected to, which suggests that when the loads acting on a section of bone are diminished beyond some strain energy density threshold [2], the bone will be resorbed in response [3,4]. In a reconstructed joint, the implant stem or fins shares some of the load that was initially borne solely by the bone [5]. This load sharing can reduce bone stimulus, leading to the phenomenon termed stress shielding [6–8], which is a cause of bone resorption, and can contribute to implant loosening [6,9,10]. A radiographic study by Nagels *et al* reported evidence of stress shielding surrounding proximal humeral implants in 9% of the cases investigated (n=70); but they pose that the true incidence may be higher because they were unable to account for changes in the trabecular bone density [11].

With the concern of stress shielding in mind, implant manufacturers have gradually reduced the length of traditional stemmed implants to maintain as much of the natural loading conditions and bone as possible. Most recently, the development of ultra-short shoulder implants termed, “*stemless*” have been released by several implant manufacturers (Section 1.2.4) [12–18]. Whereas these stemless implants all seek to maintain implant fixation through establishing purchase in the trabecular bone of the

proximal humerus, their designs vary from simple pegs to elaborate branching structures (Figure 2.1). This disparity in the metaphyseal fixation features suggests that the optimal design for stemless shoulder implants (that will reduce stress shielding, while maintaining adequate implant fixation) has yet to be quantified; perhaps because there has not been a thorough investigation of the morphology of the underlying trabecular bone.

Whereas much is known about the overall structural morphology of the proximal humerus [19–32], few investigations have focused on how that morphology may have an impact on arthroplasty [19,22]. Studies suggest that morphologic variability is an important factor that should influence implant selection and design [19,33]. As such, variation in the quality of subarticular trabecular bone, in which stemless implants seek fixation, may be of interest. This is supported by studies of hip arthroplasty, which demonstrate that bone density at the time of surgery is an important factor inversely correlated to peri-implant bone loss after arthroplasty [6,34–36]. Accordingly, proximal humerus implants should seek fixation in denser regions of trabecular bone.

A few studies have investigated the regional variation of trabecular bone quality in the proximal humerus, as it pertains to arthroplasty [37–42]. Although there seems to be some consensus that the medial and dorsal regions of the proximal humerus consist of the highest density bone [37,40], only one study has begun to assess the regional variations in trabecular bone density in a three-dimensional coordinate system that is relevant to stemless shoulder arthroplasty (Figure 2.2); however, this study had a small sample size ($n = 8$) and did not include osteoarthritic humeri [42]. Accordingly, the purpose of this anatomic study was to quantify regional variations in trabecular bone apparent density (ρ_{AVG}) in a three-dimensional, stemless implant-relevant, coordinate system (Objective 1a, Section 1.6.1). To do so appropriately, gender and osteoarthritic (OA) condition were accounted for as between-subject factors.

2.2 Materials and Methods

Shoulder computed tomography (CT) scans from 98 subjects were obtained and classified into three categories per their OA condition by an experienced shoulder surgeon (GSA), using a method that has been shown to be clinically reliable [43,44].

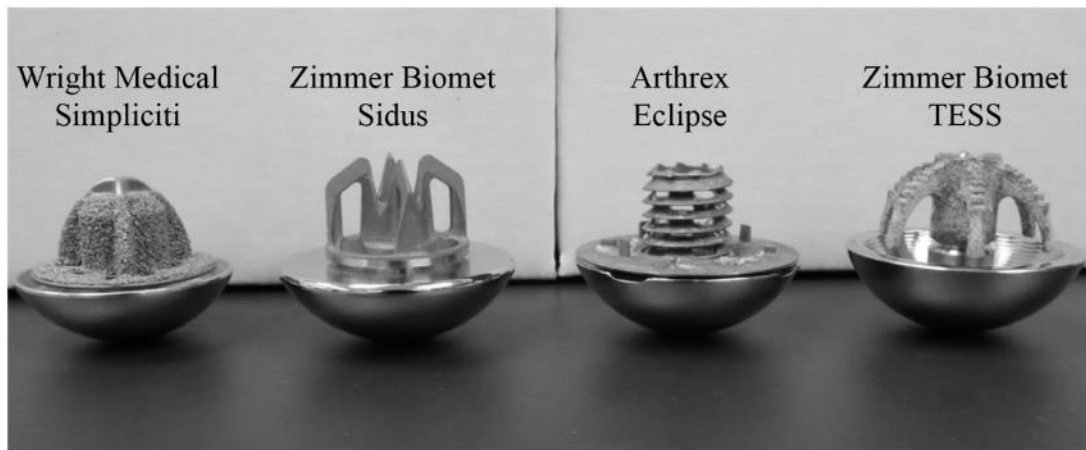


Figure 2.1: Selection of Currently Available Stemless Implants.

A selection of currently available stemless implants is shown to demonstrate the variability present in metaphyseal designs for attaining fixation in the trabecular bone of the proximal humerus.



Figure 2.2: Stemless Relevant Cartesian Coordinate System
As an example, the Tornier Simpliciti implant is presented to demonstrate that a stemless implant-relevant Cartesian coordinate system should be constructed with axes directed (A) superior-laterally, anteriorly and (B) perpendicular to the underside of the implant.

Subjects were categorized as either symmetrically (Walch Type A) osteoarthritic (15 men: 62 ± 11 years; 16 women: 69 ± 14 years), Walch B2 osteoarthritic (11 men: 64 ± 11 years; 15 women: 69 ± 7 years), or non-arthritic (25 men: 71 ± 16 years; 16 women: 70 ± 12 years). Non-arthritic subject scans were taken from a database of cadaveric shoulders, whereas the scans of the OA cohorts were obtained from patients who later underwent shoulder arthroplasty (see Appendix E for institutional ethics approval).

Using Mimics Research software (Materialise Inc., Plymouth, Michigan, USA) CT DICOM (Digital Imaging and Communications in Medicine) data were reconstructed, and voxels corresponding to the proximal humerus were manually isolated from the surrounding soft tissues using masking features available within the program. The proximal humerus masks were then further divided into two regions corresponding to (1) the cortical shell, and (2) the proximal trabecular bone and canal (hereby referred to as the trabecular-canal). A shoulder surgeon (GSA) then manually selected the location of several landmarks on the proximal humerus to define the humeral head resection plane, along with superior-lateral and inferior-medial points on the resection surface (Figure 2.3). The resection plane and points were then used to construct a proximal humerus coordinate system that was relevant to the positioning of stemless humeral implants (X : directed from inferior-medial to superior-lateral along the resection plane, Y : from posterior to anterior, Z : perpendicular to the resection plane and into the bone) (Figure 2.3).

All CT voxel information for the trabecular-canal was then exported as a 4-dimensional point cloud (*i.e.*, $[x, y, z, HU]$) and analyzed using a custom LabVIEW code (National Instruments; Austin, Texas, USA). Voxel apparent density (g/cm^3) was linearly calibrated from CT scan attenuation data (HU) (see Appendix F). The trabecular-canal was divided into 13 slices (3 above the resection plane and 10 below the resection plane), each 5mm thick, with dividing cuts parallel to the humeral head resection plane. The geometric center of each slice was used to further divide the slices into five sub-sections: a central circular section (with diameter equal to half of the canal diameter), and four peripheral quadrants corresponding to anterior, posterior, medial and lateral directions of the bone

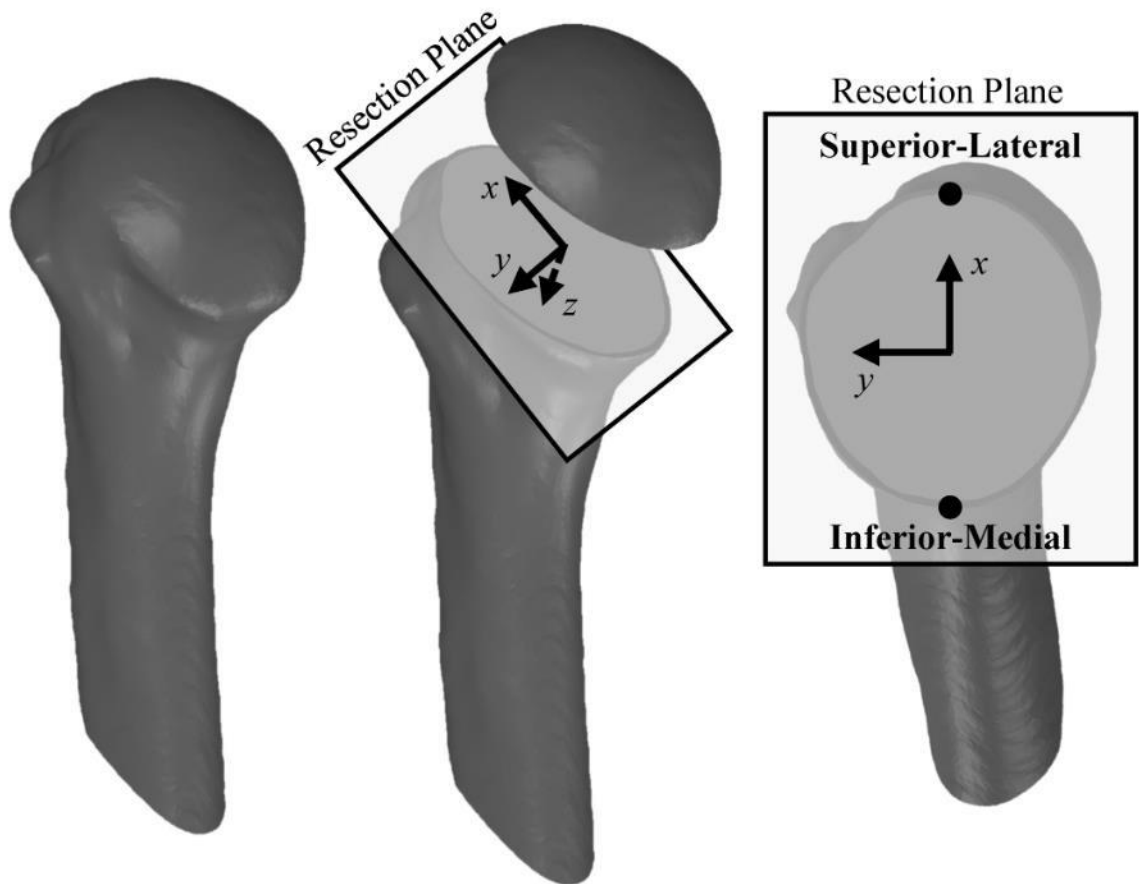


Figure 2.3: Division of the Proximal Humerus

Division of the proximal humerus into cortex and trabecular-canal sections was done manually for each subject. The humeral head surgical resection plane was used to construct a coordinate system relevant to stemless humeral implants. The x -axis points superior-laterally, the y -axis points anteriorly, and the z -axis points into the surgical resection plane.

(Figure 2.4). The average apparent density (ρ_{AVG}) was then determined in each sub-section of the trabecular-canal.

Statistical significance was assessed using SPSS (version 23, IBM; Armonk, New York, USA). A 4-way mixed repeated-measures analysis of variance was used to compare ρ_{AVG} , with the threshold for significance set at $P < 0.05$ (with an effect size $\geq 10\%$). The repeated independent variables were slice depth and slice sub-section; the between-subject factors were gender and OA classification. With a sample size of 98 statistical power was found to be ≥ 0.95 for all main effects and was ≥ 0.78 for all interactions.

2.3 Results

The average apparent density (ρ_{AVG}) was quantified in each sub-section of the proximal humerus. In general, ρ_{AVG} was found to be highest in the proximal slices and decreased distally down the canal. Slice depth was found to have a significant effect on ρ_{AVG} , with most of the proximal slices being significantly different from each other ($P < 0.001$; power = 1.00) (Figures 2.5 and 2.6). Only the most distal slices were not found to vary significantly from each other (9 vs. 10, 10 vs. 11, 10 vs. 12, 10 vs. 13, 11 vs. 12, 11 vs. 13, 12 vs. 13).

Slice sub-section was also found to have a significant effect on ρ_{AVG} , with the central sub-section having significantly lower ρ_{AVG} ($0.08 \pm 0.40 \text{g/cm}^3$) than all the peripheral (*i.e.*, endosteal edge) sections (medial: $0.15 \pm 0.49 \text{g/cm}^3$, lateral: $0.14 \pm 0.49 \text{g/cm}^3$, anterior: $0.15 \pm 0.49 \text{g/cm}^3$, posterior: $0.15 \pm 0.56 \text{g/cm}^3$; $P < 0.001$; power = 1.00) (Table 2.1, Figures 2.5 and 2.6). In addition, the medial section had significantly greater ρ_{AVG} than the lateral and posterior sub-sections ($P < 0.007$; power = 1.00). Gender was also found to cause a significant difference in trabecular-canal ρ_{AVG} , with men having significantly greater ρ_{AVG} than women (men: $0.15 \pm 0.81 \text{g/cm}^3$, women: $0.12 \pm 0.74 \text{g/cm}^3$; $P < 0.001$; power = 0.95).

Osteoarthritis (OA) condition was not found to have an independent significant impact on ρ_{AVG} ($P = 0.238$; power = 0.30); however, it did interact with slice depth and slice sub-section to produce significant differences ($P < 0.001$; power = 1.00). The slice depth-by-

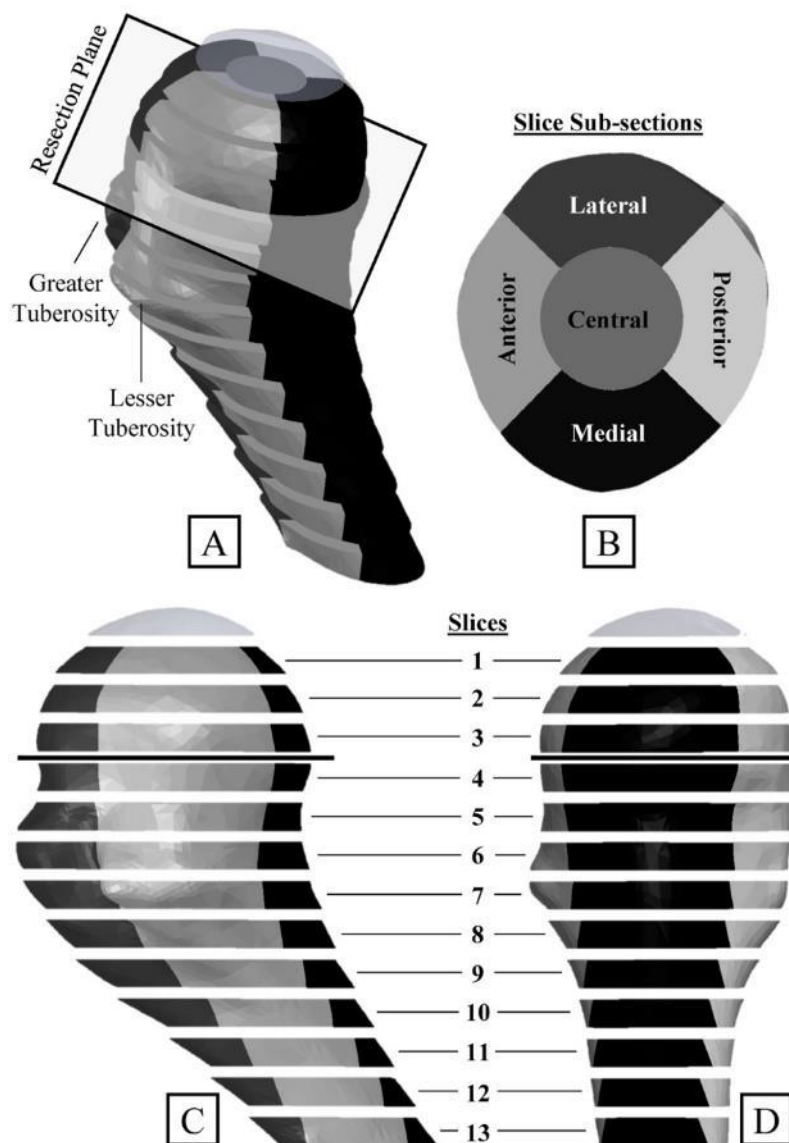


Figure 2.4: Humeral Regions-of-Interest for CT Assessment

A: Anterior-Medial view of the proximal humerus, highlighting how the trabecular-canal was divided into 13 slices, each 5mm in thickness, with dividing planes parallel to the resection plane. This is also shown in anterior (C) and medial (D) views of the proximal humerus. B: A top-view of the fourth slice (resection plane) indicates how further subdivisions were made to separate each slice into 5 sub-sections: a central circular section (with diameter half that of the canal diameter for each slice), and four peripheral sections (anterior, posterior, medial and lateral).

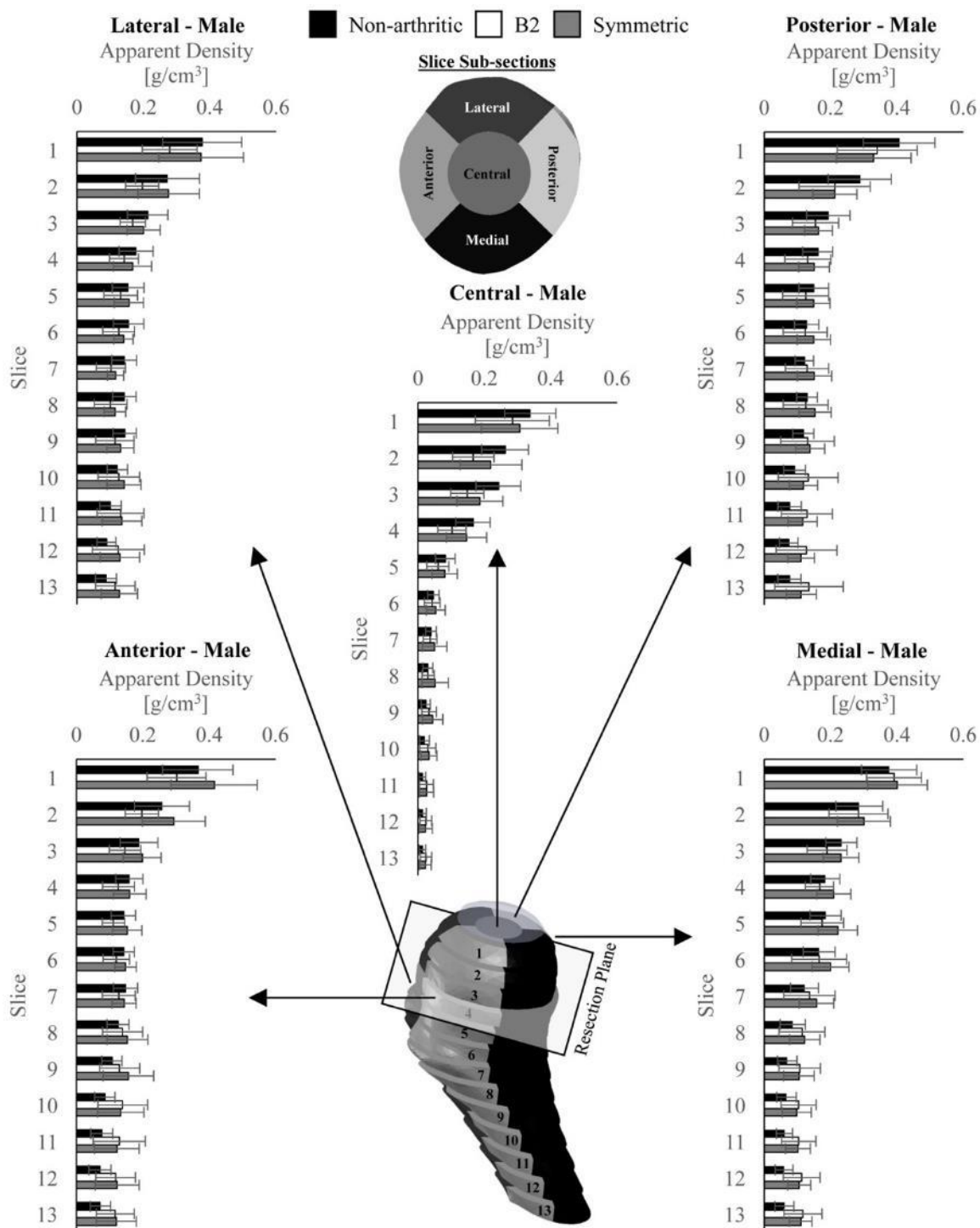


Figure 2.5: Average Apparent Density Results for Male Subjects

Results of mean±standard deviation average apparent density for male subjects. Separate graphs are provided for each sub-section of the proximal humerus' trabecular-canal (central, anterior, posterior, medial and lateral). OA classifications are indicated as different coloured bars (non-arthritic: Black, B2 OA: White, Symmetric: Grey).

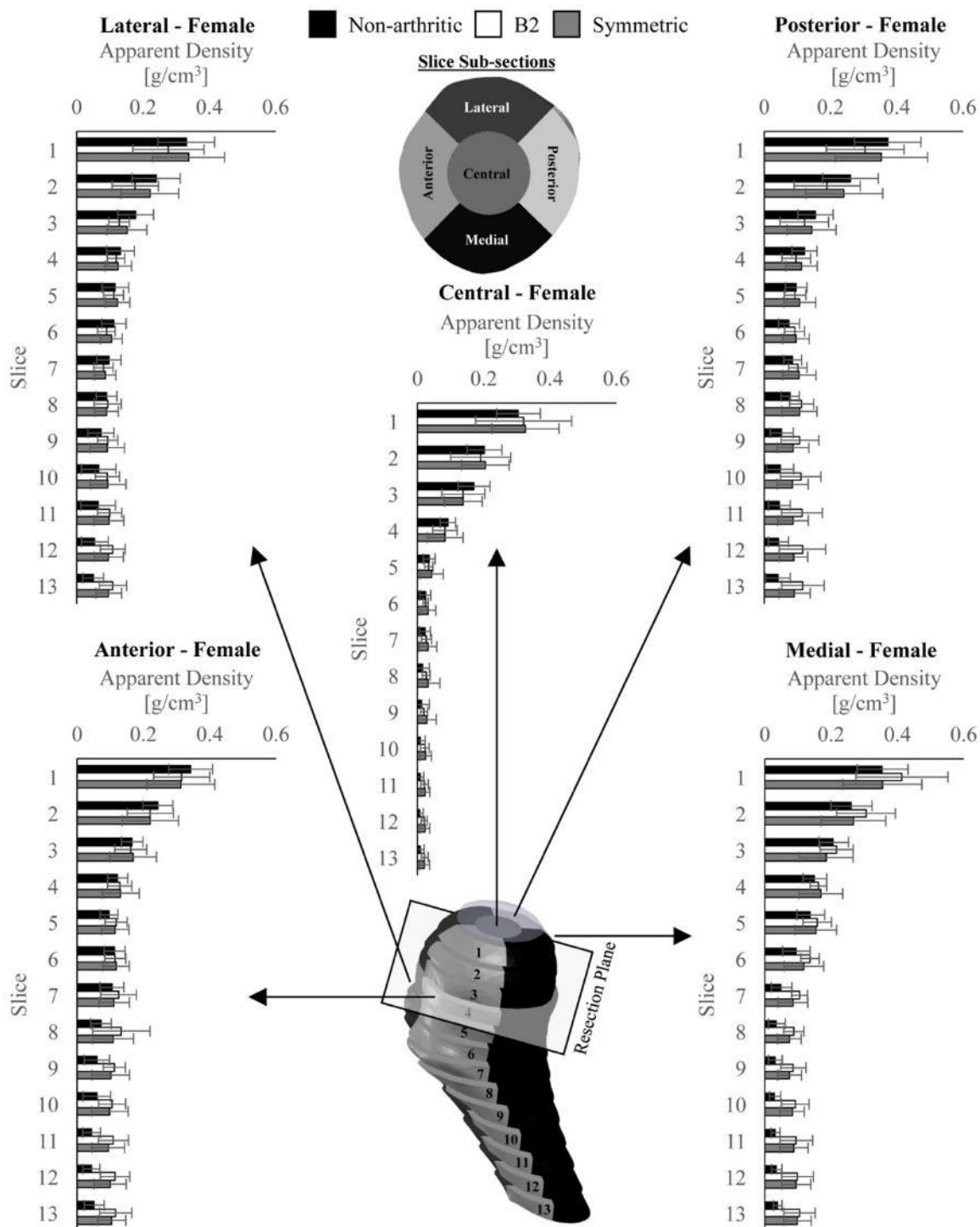


Figure 2.6: Average Apparent Density Results for Female Subjects

Results of mean±standard deviation average apparent density for female subjects. Separate graphs are provided for each sub-section of the proximal humerus' trabecular-canal (central, anterior, posterior, medial and lateral). OA classifications are indicated as different coloured bars (non-arthritic: Black, B2 OA: White, Symmetric: Grey).

Table 2.1: Mean (standard deviation) average apparent density (g/cm^3) of the trabecular-canal.

	Non-Arthritic	B2 OA	Symmetric OA	Overall
Medial	0.13 (0.22)	0.16 (0.32)	0.16 (0.30)	0.15 (0.49)
Lateral	0.15 (0.27)	0.13 (0.27)	0.15 (0.30)	0.14 (0.49)
Anterior	0.13 (0.23)	0.15 (0.29)	0.16 (0.33)	0.15 (0.49)
Posterior	0.13 (0.26)	0.14 (0.38)	0.14 (0.32)	0.14 (0.56)
Central	0.08 (0.18)	0.08 (0.25)	0.09 (0.26)	0.08 (0.40)
Males	0.14 (0.40)	0.14 (0.52)	0.16 (0.48)	0.15 (0.81)
Females	0.11 (0.34)	0.13 (0.45)	0.12 (0.48)	0.12 (0.74)

* Pooled across all slices and slice sub-sections.

OA condition interaction found that non-arthritic subjects had significantly higher ρ_{AVG} than B2 OA subjects in slices 2 and 3, but significantly lower ρ_{AVG} than B2 OA subjects in slices 9-13. Non-arthritic subjects also had significantly lower ρ_{AVG} than symmetric OA subjects in slices 8-13. No significant differences were found between B2 and symmetric OA subjects. Furthermore, the slice depth-by-OA condition interaction also found that most slice depths were significantly different from one another for non-arthritic subjects (with the exception of slices 11-13 with one another), whereas significant differences in slice depth were found only for slices 1-4 (with all slices), and slice 5 with slices 6-9. Symmetric OA subjects had significant density differences for slices 1-6 with all slices. Overall, more proximal slices were found to have higher ρ_{AVG} , with significant differences between slices persisting more distally for non-arthritic subjects compared with B2 and symmetric OA subjects.

A slice sub-section-by-OA condition interaction also presented as significant ($P < 0.001$; power = 1.00). Within the medial sub-section, non-arthritic subjects had significantly lower ρ_{AVG} ($0.13 \pm 0.22 \text{g/cm}^3$) than both B2 ($0.16 \pm 0.32 \text{g/cm}^3$) and symmetric OA subjects ($0.16 \pm 0.30 \text{g/cm}^3$); whereas in the anterior sub-section, non-arthritic subjects were only found to have significantly lower ρ_{AVG} ($0.13 \pm 0.23 \text{g/cm}^3$) than only symmetric OA subjects ($0.16 \pm 0.33 \text{g/cm}^3$). For non-arthritic subjects, the central sub-section was found to have significantly lower ρ_{AVG} ($0.08 \pm 0.18 \text{g/cm}^3$) than all other sub-sections (medial: $0.13 \pm 0.22 \text{g/cm}^3$, lateral: $0.15 \pm 0.27 \text{g/cm}^3$, anterior: $0.13 \pm 0.23 \text{g/cm}^3$, posterior: $0.13 \pm 0.26 \text{g/cm}^3$), and the lateral sub-section was found to have significantly higher ρ_{AVG} than all other sub-sections. For B2 OA subjects, the central sub-section was again found to have significantly lower ρ_{AVG} ($0.08 \pm 0.25 \text{g/cm}^3$) than all other sub-sections (medial: $0.16 \pm 0.32 \text{g/cm}^3$, lateral: $0.13 \pm 0.27 \text{g/cm}^3$, anterior: $0.15 \pm 0.29 \text{g/cm}^3$, posterior: $0.14 \pm 0.38 \text{g/cm}^3$), the medial sub-section was found to have significantly higher ρ_{AVG} than all other sub-sections, and the lateral sub-section had significantly lower ρ_{AVG} than the anterior sub-section. Finally, for symmetric OA subjects, the central subsection was also found to have a significantly lower ρ_{AVG} ($0.09 \pm 0.26 \text{g/cm}^3$) than all other sub-sections (medial: $0.16 \pm 0.30 \text{g/cm}^3$, lateral: $0.15 \pm 0.30 \text{g/cm}^3$, anterior: $0.16 \pm 0.33 \text{g/cm}^3$,

posterior: $0.14 \pm 0.32 \text{g/cm}^3$), and the medial sub-section had significantly higher ρ_{AVG} than the posterior sub-section.

The only other interaction to produce significant differences was the slice depth-by-slice sub-section interaction ($P < 0.001$; power = 1.00); however, significances did not follow a discernable trend, with most slice depths being significantly different from one another in most sub-sections, and vice versa.

2.4 Discussion

Significant differences in apparent density (ρ_{AVG}) were found within the proximal humerus because of slice depth, slice sub-section and gender main effects, along with interactions between slice depth, slice sub-section and OA condition. Overall, ρ_{AVG} within the proximal humerus is greatest in the most proximal slices (*i.e.*, closer to the articular surface), and gradually is reduced farther down the proximal canal. Figures 2.5 and 2.6 indicate that the ρ_{AVG} is highest in the slices above the resection plane (slices 1-3), and drops off by the second or third slice (~10-15mm) beneath the resection plane (slices 4-6), after which ρ_{AVG} plateaus to levels that are below those expected to contain trabecular bone ($<0.1 \text{g/cm}^3$) [45,46]. Unfortunately, this suggests that humeral head resection removes the region with the highest trabecular density, thereby forcing implants (stemless or stemmed) to seek fixation in relatively lower density bone. An equally important trend that presented in the data was that ρ_{AVG} in the central region was consistently lower than in any of the peripheral (*i.e.*, anterior, posterior, medial and lateral) regions of the trabecular-canal. This, coupled with the understanding that peri-implant bone density is inversely correlated to bone loss around an implant after arthroplasty [6,34–36], suggests that stemless implant fixation features should be designed and positioned such that they take advantage of purchase peripherally, and not just centrally. This peripheral density trend is a key finding that should be considered during the design of the next generation of stemless humeral implants. The medial sub-section of the proximal humerus' trabecular-canal also generally presented as the region with the highest apparent density, perhaps indicating a significant, but small in magnitude, ρ_{AVG} increase that could be applied to the design of stemless implant

metaphyseal features to improve fixation. These general trends were found for both men and women, but it should be noted that ρ_{AVG} was significantly lower in women compared with men, regardless of slice depth, sub-section or OA classification.

Whereas this study investigated regional variations in the proximal humerus' trabecular-canal using a unique coordinate system that is oriented with respect to stemless implants, there have been other investigations of proximal humerus density in the past. In general, the results of these studies agree well with the present findings in accounting for coordinate system orientation changes and two-dimensional limitations. Some studies have reported regional variations in subchondral bone density in the proximal humerus by CT-osteodensitometry, which uses intensity plots of Hounsfield Units (HU) projected onto the articular surface [38,39]. These methods have demonstrated that 71%-79% of humeri exhibited bicentric density distribution patterns (with posterior and anterior maxima), and that 21%-29% were classified with monocentric (centro-posterior) maxima. Unfortunately, by projecting density data onto the articular surface of the humerus, these studies did not separate bone that was above and below the humeral arthroplasty resection plane; thereby making it impossible to separate subchondral bone that would not be present after arthroplasty. Accordingly, they were unable to give a truly three-dimensional understanding of the trabecular bone distribution, and given the present study findings, it is likely that the higher subchondral bone density would overshadow variations in bone density beneath the surgical resection plane. A study by Yamada *et al* (2007) performed an age-based assessment of bone density in the proximal humerus and found that the medial region of every bone (n=41) consisted of more bone tissue than the lateral side; however, the coordinate system of the region of interest was aligned with the humerus' diaphyseal axis, and did not include all of the medial bone beneath a typical humeral head arthroplasty resection plane [40]. Similarly, Tingart *et al* also reported on the distribution of bone density in the proximal humerus in a coordinate system that was aligned with the diaphyseal axis, and found that the proximal and articular portions of the humeral head were of the greatest trabecular density [41]. Hepp *et al* also found that the medial and dorsal aspects of the proximal humerus were of the greatest strength, but bone slices were again aligned with the diaphyseal axis as opposed to a coordinate system that would reflect bone tissue available after humeral head

resection for arthroplasty [37]. Hepp *et al* also determined that strength was greatest in the cranial region and decreased caudally, which agrees with the present findings. Most recently, Alidousti *et al*, performed an assessment of proximal humerus bone density (n=8) in a coordinate system similar to the one suggested herein, and their work supports the conclusion that trabecular bone density is greatest proximally and peripherally [42].

This investigation is not without limitations. Whereas cadaveric subjects were obtained as ‘fresh-frozen’, reducing the likelihood of bone degradation post-mortem, the use of cadavers as the non-arthritic control resulted in a non-arthritic group that was of higher age than the arthritic groups. In addition, quantitative CT was chosen as the method of investigation, as it provided a non-destructive mechanism for determining ρ_{AVG} within customizable regions of the proximal humerus; however, because of the diversity of subjects included in the investigation (*i.e.* cadaveric and preoperative patients with OA), clinical CTs were used as opposed to more detailed micro-CTs. Accordingly, the voxel dimensions in which CT attenuation was quantified were larger than they could have been; however, the mean slice thickness in the present study population was $0.9\pm 0.3\text{mm}$, which is far smaller than the slice sub-sections (5mm thick) within which the ρ_{AVG} was calculated. Despite the limitations associated with using clinical CT scans, the inclusion of pre-operative patient scan data is a strength of this study, as it permitted the assessment of ρ_{AVG} within a population that would eventually receive the procedure for which stemless implants are designed. Interestingly, OA classification was not found to contribute significantly to variations in ρ_{AVG} as a main effect; however, it did interact with the other parameters to showcase some differences in ρ_{AVG} between subjects classified as non-arthritic, B2 osteoarthritic and symmetrically osteoarthritic. This finding suggests that future investigations should take a closer look at the variance of proximal humerus bone density within additional sub-classifications of OA (*e.g.*, A1, A2, B1, B2, C, *etc.*).

The findings of this investigation also have implications for computational modeling of shoulder joint reconstruction for these implant systems. The variations in bone properties noted support the use of non-homogeneous models when using the finite element method to model shoulder arthroplasty. Typically, non-homogeneous trabecular bone models are

constructed by converting CT attenuation data into density, which can then be further converted to an elastic modulus that varies regionally from element to element on the basis of CT voxel attenuation. The application of a uniform elastic modulus for all the trabecular bone of the proximal humerus would neglect the slice depth and central vs. peripheral density differences that are present within the proximal humerus, very likely altering the results obtained when assessing humeral implants with the finite element method.

2.5 Conclusion

The apparent density of the trabecular bone and canal of the proximal humerus is non-uniform. When oriented in a coordinate system relative to stemless humeral implants, apparent density is greatest above the humeral head resection plane, and decreases rapidly beneath the resection plane. Importantly, bone density also demonstrates a peripheral preference, whereby the central region of the trabecular-canal is always lower in density than the peripheral anterior, posterior, medial and lateral sub-sections. These findings have implications for the design of stemless shoulder implants, indicating that implants that seek purchase in the highest density bone should take advantage of the peripheral regions of the trabecular-canal within the first 15-20mm beneath the humeral head resection plane.

2.6 References

- [1] Reeves, J. M., Athwal, G. S., and Johnson, J. A., 2017, "An Assessment of Proximal Humerus Density with Reference to Stemless Implants," *J. Shoulder Elb. Surg.*, (**In Press**).
- [2] Neuert, M. A. C., and Dunning, C. E., 2013, "Determination of remodeling parameters for a strain-adaptive finite element model of the distal ulna," *Proc. Inst. Mech. Eng. Part H - J. Eng. Med.*, **227**(9), pp. 994–1001.
- [3] Wolff, J., 1892, "Das Gesetz der Transformation der Knochen," *DMW-Deutsche Medizinische Wochenschrift*, **19**(47), pp. 1222–1224.
- [4] Huiskes, R., Ruimerman, R., Lenthe, G. H. Van, and Janssen, J. D., 2000, "Effects of mechanical forces on maintenance and adaptation of form in trabecular bone," *Nature*, **405**(June), pp. 704–706.
- [5] Mow, V. C., and Huiskes, R., 2005, *Basic Orthopaedic Biomechanics & Mechano-*

biology, Lippincott Williams & Wilkins, Philadelphia.

- [6] Bauer, T. W., and Schils, J., 1999, "The pathology of total joint arthroplasty II. Mechanisms of implant failure," *Skeletal Radiol.*, **28**(9), pp. 483–497.
- [7] Sumner, D. R., Turner, T. M., Igloria, R., Urban, R. M., and Galante, J. O., 1998, "Functional adaptation and ingrowth of bone vary as a function of hip implant stiffness," *J. Biomech.*, **31**(10), pp. 909–917.
- [8] Sumner, D. R., and Galante, J. O., 1992, "Determinants of Stress Shielding : Design Versus Materials Versus Interface," *Clin. Orthop. Relat. Res.*, **274**, pp. 202–212.
- [9] Bohsali, K. I., Wirth, M. A., and Rockwood, C. A. J., 2006, "Complications of Total Shoulder Arthroplasty," *J. Bone Joint Surg. Am.*, **88**(10), pp. 2279–2292.
- [10] Chin, P. Y. K., Sperling, J. W., Cofield, R. H., and Schleck, C., 2006, "Complications of total shoulder arthroplasty: Are they fewer or different?," *J. Shoulder Elb. Surg.*, **15**(1), pp. 19–22.
- [11] Nagels, J., Stokdijk, M., and Rozing, P. M., 2003, "Stress shielding and bone resorption in shoulder arthroplasty," *J. Shoulder Elb. Surg.*, **2746**(2), pp. 35–39.
- [12] Razfar, N., Reeves, J. M., Langohr, D. G., Willing, R., Athwal, G. S., and Johnson, J. A., 2016, "Comparison of proximal humeral bone stresses between stemless, short stem, and standard stem length: a finite element analysis," *J. Shoulder Elb. Surg.*, **25**(7), pp. 1076–83.
- [13] Churchill, R. S., and Athwal, G. S., 2016, "Stemless shoulder arthroplasty—current results and designs," *Curr. Rev. Musculoskelet. Med.*, **9**(1), pp. 10–16.
- [14] Churchill, R. S., Chuinard, C., Wiater, J. M., Friedman, R., Freehill, M., Jacobson, S., Spencer, E., Holloway, G. B., Wittstein, J., Lassiter, T., Smith, M., Blaine, T., and Nicholson, G. P., 2016, "Clinical and Radiographic Outcomes of the Simpliciti Canal-Sparing Shoulder Arthroplasty System: A Prospective Two-Year Multicenter Study," *J. Bone Jt. Surg.*, **98**(7), pp. 552–560.
- [15] Habermeyer, P., Lichtenberg, S., Tauber, M., and Magosch, P., 2015, "Midterm results of stemless shoulder arthroplasty: A prospective study," *J. Shoulder Elb. Surg.*, **24**(9), pp. 1463–1472.
- [16] Routman, H., Becks, L., and Roche, C., 2015, *Stemless and Short Stem Humeral Components in Shoulder Arthroplasty*.
- [17] Harmer, L., Throckmorton, T., and Sperling, J. W., 2016, "Total shoulder arthroplasty: are the humeral components getting shorter?," *Curr. Rev. Musculoskelet. Med.*, **9**(1), pp. 17–22.
- [18] Huguet, D., DeClercq, G., Rio, B., Teissier, J., and Zipoli, B., 2010, "Results of a new stemless shoulder prosthesis: radiologic proof of maintained fixation and

- stability after a minimum of three years' follow-up.," *J. Shoulder Elbow Surg.*, **19**(6), pp. 847–52.
- [19] Robertson, D. D., Yuan, J., Bigliani, L. U., Flatow, E. L., and Yamaguchi, K., 2000, "Three-dimensional analysis of the proximal part of the humerus: relevance to arthroplasty.," *J. Bone Joint Surg. Am.*, **82–A**, pp. 1594–1602.
- [20] Roberts, S. N. J., Foley, A. P. J., Swallow, H. M., Wallace, W. A., and Coughlan, D. P., 1991, "The Geometry of the Humeral Head and the Design of Prostheses," *J. Bone Jt. Surg.*, **73–B**(4), pp. 647–650.
- [21] Iannotti, J. P., Gabriel, J. P., Schneck, S. L., Evans, B. G., and Misra, S., 1992, "The Normal Glenohumeral Relationships: An Anatomical Study of One Hundred and Forty Shoulders," *J. Bone Jt. Surg.*, **74–A**(4), pp. 491–500.
- [22] Boileau, P., and Walch, G., 1997, "The three-dimensional geometry of the proximal humerus. Implications for surgical technique and prosthetic design.," *J. Bone Jt. Surg.*, **79–B**(5), pp. 857–865.
- [23] Ballmer, F. T., Sidles, J. A., Lippitt, S. B., and Matsen, F. A., 1993, "Humeral head prosthetic arthroplasty: Surgically relevant geometric considerations," *J. Shoulder Elb. Surg.*, **2**(6), pp. 296–304.
- [24] DeLude, J. A., Bicknell, R. T., MacKenzie, G. A., Ferreira, L. M., Dunning, C. E., King, G. J. W., Johnson, J. A., and Drosdowech, D. S., 2007, "An anthropometric study of the bilateral anatomy of the humerus," *J. Shoulder Elb. Surg.*, **16**(4), pp. 477–483.
- [25] Hertel, R., Knothe, U., and Ballmer, F. T., 2002, "Geometry of the proximal humerus and implications for prosthetic design," *J. Shoulder Elb. Surg.*, **11**(4), pp. 331–338.
- [26] Humphrey, S. C., Sears, B. W., and Curtin, M. J., 2016, "An anthropometric analysis to derive formulae for calculating the dimensions of anatomically shaped humeral heads," *J. Shoulder Elb. Surg.*, **25**, pp. 1532–1541.
- [27] Jeong, J., and Jung, H. W., 2015, "Optimizing intramedullary entry location on the proximal humerus based on variations of neck-shaft angle," *J. Shoulder Elb. Surg.*, **24**(9), pp. 1386–1390.
- [28] Pearl, M. L., and Volk, a G., 1996, "Coronal plane geometry of the proximal humerus relevant to prosthetic arthroplasty.," *J. Shoulder Elbow Surg.*, **5**(4), pp. 320–326.
- [29] Nyffeler, R. W., Sheikh, R., Jacob, H. a C., and Gerber, C., 2004, "Influence of humeral prosthesis height on biomechanics of glenohumeral abduction. An in vitro study.," *J. Bone Joint Surg. Am.*, **86–A**(3), pp. 575–580.
- [30] Roosa, S. M. M., Hurd, A. L., Xu, H., Fuchs, R. K., and Warden, S. J., 2012, "Age-related changes in proximal humerus bone health in healthy, white males,"

Osteoporos. Int., **23**(12), pp. 2775–2783.

- [31] Zhang, L., Yuan, B., Wang, C., and Liu, Z., 2007, “Comparison of anatomical shoulder prostheses and the proximal humeri of Chinese people,” *J. Eng. Med.*, **221**(8), pp. 921–927.
- [32] Youderian, A. R., Ricchetti, E. T., Drews, M., and Iannotti, J. P., 2014, “Determination of humeral head size in anatomic shoulder replacement for glenohumeral osteoarthritis,” *J. Shoulder Elb. Surg.*, **23**(7), pp. 955–963.
- [33] Razmjou, H., Holtby, R., Christakis, M., Axelrod, T., and Richards, R., 2013, “Impact of prosthetic design on clinical and radiologic outcomes of total shoulder arthroplasty: A prospective study,” *J. Shoulder Elb. Surg.*, **22**(2), pp. 206–214.
- [34] Engh, C., and McGovern, T., 1992, “A quantitative evaluation of periprosthetic bone-remodeling after cementless total hip arthroplasty,” *J Bone Joint Surg*, **74**(7), pp.1009–1020.
- [35] Kerner, J., Huiskes, R., van Lenthe, G. ., Weinans, H., van Rietbergen, B., Engh, C. ., and Amis, a. ., 1999, “Correlation between pre-operative periprosthetic bone density and post-operative bone loss in THA can be explained by strain-adaptive remodelling,” *J. Biomech.*, **32**(7), pp. 695–703.
- [36] Sychterz, C. J., and Engh, C. A., 1996, “The Influence of Clinical Factors on Periprosthetic Bone Remodeling,” *Clin. Orthop. Relat. Res.*, (322), pp. 285–292.
- [37] Hepp, P., Lill, H., Bail, H., Korner, J., Niederhagen, M., Haas, N. P., Josten, C., and Duda, G. N., 2003, “Where should implants be anchored in the humeral head?,” *Clin. Orthop. Relat. Res.*, (415), pp. 139–147.
- [38] Zumstein, V., Kraljević, M., Huegli, R., and Muller-Gerbl, M., 2011, “Mineralisation patterns in the subchondral bone plate of the humeral head,” *Surg. Radiol. Anat.*, **33**(9), pp. 775–779.
- [39] Kraljević, M., Zumstein, V., Hügli, R., and Müller-Gerbl, M., 2013, “A comparison of subchondral bone mineralization between the glenoid cavity and the humeral head on 57 cadaverous shoulder joints,” *Surg. Radiol. Anat.*, **35**(4), pp. 295–300.
- [40] Yamada, M., Briot, J., Pedrono, A., Sans, N., Mansat, P., Mansat, M., and Swider, P., 2007, “Age- and gender-related distribution of bone tissue of osteoporotic humeral head using computed tomography,” *J. Shoulder Elb. Surg.*, **16**(5), pp. 596–602.
- [41] Tingart, M. J., Bouxsein, M. L., Zurakowski, D., Warner, J. P., and Apreleva, M., 2003, “Three-dimensional distribution of bone density in the proximal humerus,” *Calcif. Tissue Int.*, **73**(6), p. 535.
- [42] Alidousti, H., Giles, J. W., Emery, R. J. H., and Jeffers, J., 2017, “Spatial mapping of humeral head bone density,” *J. Shoulder Elb. Surg.*, **26**(9), pp. 1653–1661.

- [43] Nowak, D. D., Gardner, T. R., Bigliani, L. U., Levine, W. N., and Ahmad, C. S., 2010, "Interobserver and intraobserver reliability of the Walch classification in primary glenohumeral arthritis," *J. Shoulder Elb. Surg.*, **19**(2), pp. 180–183.
- [44] Walch, G., Badet, R., Boulahia, A., and Khoury, A., 1999, "Morphologic study of the glenoid in primary glenohumeral osteoarthritis," *J. Arthroplasty*, **14**(6), pp. 756–760.
- [45] Ashman, R. B., 1989, "Experimental Techniques," *Bone Mechanics*, S.C. Cowin, ed., CRC Press Inc., Boca Raton, p. 76.
- [46] Bonnuci, E., 2000, "Basic Composition and Structure of Bone," *Mechanical Testing of Bone and the Bone-Implant Interface*, Y.H. An, and R.A. Draughn, eds., CRC Press Inc., Boca Raton, pp. 3–21.

Chapter 3

An Analysis of Proximal Humerus Morphology with Special Interest in Stemless Shoulder Arthroplasty

A version of this chapter has been accepted for publication [1].

3.1 Introduction

Shoulder replacement, or arthroplasty, was first popularized in the 1950's by Neer, using a Vitallium implant to treat comminuted fractures of the proximal humerus [2]. For the proximal humerus, hemi-arthroplasty involves replacing the humeral head, while total arthroplasty involves replacing both the humeral head and the glenoid [3]. The incidence of shoulder arthroplasty has been increasing, in 2008 nearly 47,000 shoulder arthroplasty procedures were conducted in the United States [4], and as of 2011 this number rose above 66,000 [5]. Accordingly, with more shoulder arthroplasty procedures being performed, implant performance and longevity are becoming ever-more important issues that could have an impact on outcomes and costs.

The extra-medullary anatomy of the proximal humerus (*i.e.*, overall length, neck-shaft angle, degree of retroversion, humeral head height, radius of curvature, and head offset) is well understood [6–19]. Studies have sought to better quantify the overall shape of the humerus to comprehend structural changes that take place over time in response to activity, arm dominance, and aging. It has been suggested by Robertson *et al* that morphological variability is also an important factor that should influence implant design and selection [6]. Accordingly, the humeral morphological parameters quantified in the literature typically relate to the design of either the humeral implant stem, or the head component. For example, there has been substantial research on quantifying the neck-shaft angle of the proximal humerus [9,12,16,19] because traditional implants seek fixation by a stem press-fit into the diaphyseal portion of the humeral canal. However, with the advent of shorter implants for humeral head reconstruction, the humeral geometry of interest is expanding.

In recent years, implant manufacturers have reduced the length of traditional stemmed humeral implants [20–27]. This reduction of implant stem length is most evident in the new generation of ‘stemless’ implants, which seek fixation in the most proximal region of the post-resected humeral metaphysis (Section 1.2.4). The metaphyseal characteristic of stemless implants allows fixation and central positioning in the sub-resection region of the proximal humerus, irrespective of the neck-shaft angle, the degree of retroversion, or the location of the humeral canal [22]. Accordingly, the primary region-of-interest for the placement and fixation of stemless proximal humerus implants is the bone directly beneath the humeral head resection plane (Figure 3.1). It follows that it is important to understand the spatial limits of the region of the proximal humerus in which the implant is placed. However, the morphology of this region-of-interest has not been well quantified in the literature. Therefore, the spatial limits of this region-of-interest must be defined by measuring the shifts in the proximal canal direction, the bounding diameters along the canal, and the canal depth beneath the center of the resection plane. Accordingly, the purpose of this anatomic study was to quantify morphological parameters of interest relevant to the design of stemless implants in the proximal humerus (Objective 1b, Section 1.6.1).

3.2 Materials and Methods

Shoulder computed tomography (CT) scans were obtained with ethics approval from 98 subjects. Each was visually inspected for osteoarthritis (OA) by an experienced shoulder surgeon (GSA), and classified into one of three OA conditions: non-arthritic (25 men: 71 ± 16 years; 16 women: 70 ± 12 years), Walch type B2 OA (11 men: 64 ± 11 years; 15 women: 69 ± 7 years) or symmetric (Walch type A) OA (15 men: 62 ± 11 years; 16 women: 69 ± 14 years) using a clinically reliable method [28,29]. The non-arthritic scans were obtained from a database of cadaveric CT scans, whereas OA scans were pre-operative scans from patients who later underwent shoulder arthroplasty (see Appendix E for institutional ethics approval).

CT Digital Imaging and Communications in Medicine (DICOM) data were reconstructed using Mimics Research software (version 19; Materialise Inc., Plymouth, Michigan, USA), and the proximal humerus was manually isolated from the surrounding soft tissues

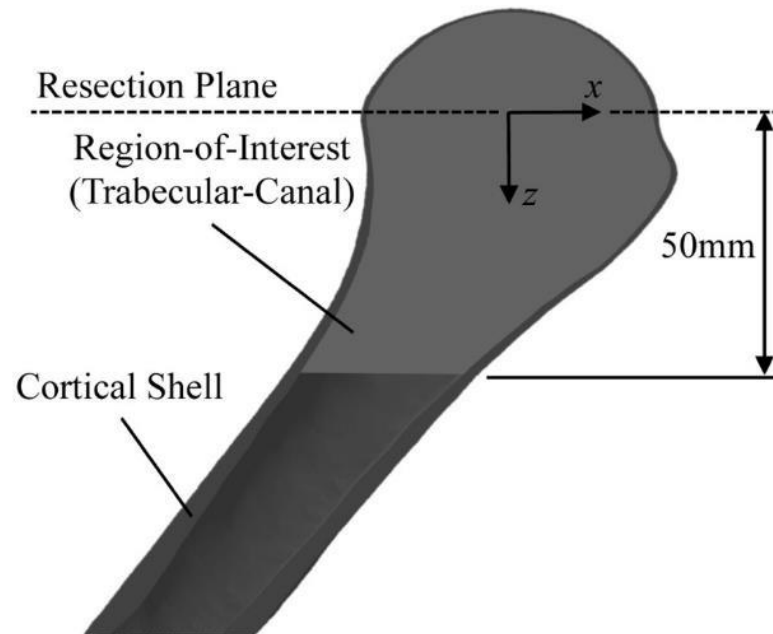


Figure 3.1: Region-of-Interest for the Proximal Humerus

The division between the cortical shell and the trabecular-canal. The region-of-interest for the proximal humerus, as it pertains to stemless implant design, is the trabecular-canal directly below the resection plane.

using masking features available within the software program (Appendix G). Each humerus was then manually divided into two regions corresponding to: (1) the cortical shell, and (2) the combination of trabecular bone and canal (*i.e.*, trabecular-canal) (Figure 3.1). The same shoulder surgeon (GSA) then identified the location for the articular resection plane, and inferior-medial and superior-lateral points on the humeral head resection plane. These points were used to construct a proximal humerus coordinate system that the authors thought would best describe the proximal humerus in a manner relevant to shoulder reconstruction with a stemless implant. The coordinate system consisted of an x -axis directed from the inferior-medial point towards the superior-lateral point along the resection plane, a y -axis directed anteriorly, and a z -axis perpendicular to the resection (positively directed into the remaining bone; $z = 0$ corresponding to the resection plane) (Figure 3.2). The use of a subject-specific anatomic resection plane, as opposed to a standard cut at 30° of retroversion, was done to highlight the independence of the stemless implant from the humeral canal.

To quantify the outcome measures of interest, the three-dimensional point cloud data for voxels corresponding to both the cortical shell and trabecular-canal were exported as text files, and were analyzed using custom LabVIEW scripts (National Instruments; Austin, Texas, USA). The trabecular-canal was divided into 13 slices (3 above the resection plane, 10 below the resection plane), each 5mm thick, with divisions parallel to the humeral head resection plane. The geometric center (x_o, y_o, z_o) of each slice was then quantified, by averaging the coordinates of all points within each slice, to determine the frontal plane (*i.e.* x - z values) and sagittal plane (*i.e.* y - z values) directional changes along the canal path. At each point along the canal path, the fitted canal diameter (\emptyset_{Canal}) was determined by positioning a circle (parallel to the resection plane) at the canal path center point, and expanding its diameter as large as possible without any part of the circle exceeding the inner canal (*i.e.*, endosteal surface).

The depth beneath the center of the resection surface ($D_{Resection}$) was determined as the average depth into the trabecular-canal that was contained within a 10mm-diameter cylinder whose central axis passed through the center of the resection plane. Furthermore, to quantify the hemispherical nature of the humeral head, the articular aspect ratio ($\emptyset: H$)

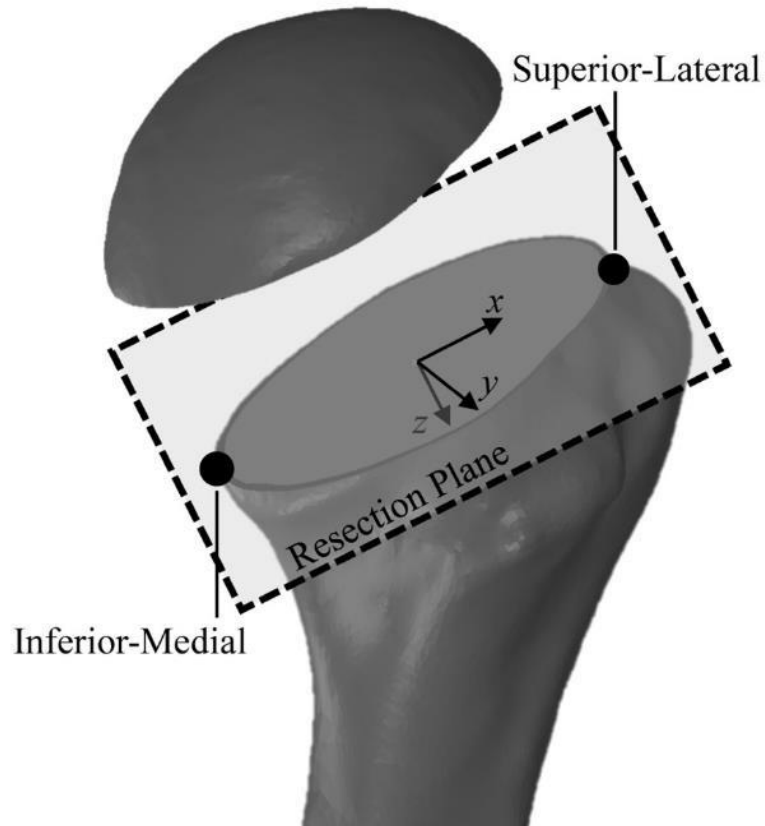


Figure 3.2: Landmarks and Coordinate System for the Proximal Humerus

Landmarks of the proximal humerus, the surgical resection plane, and the superior-lateral and inferior-medial points, were used to construct a stemless implant-relevant coordinate system. The x -axis is directed from the inferior-medial point to the superior-lateral point, the y -axis is directed from posterior to anterior, and the z -axis is directed perpendicular to the resection plane (into the sub-resection plane bone).

was determined for each subject by quantifying the approximate diameter of the resection surface ($\emptyset_{Resection}$) including the cortex, and the maximum height of the articular surface above the resection surface (H).

Statistical significance was assessed using SPSS software (version 23, IBM; Armonk, New York, USA). The canal path and fitted canal diameter variables, which repeated across slices, were evaluated using a mixed repeated-measures analysis of variance; while the resection depth and articular aspect ratio terms were evaluated using a univariate analysis of variance. The between-subject factors were OA condition and gender, while slice depth was a repeated independent variable where applicable. The threshold for significance was chosen as $P < 0.05$ (with an effect size $\geq 10\%$).

3.3 Results:

3.3.1 Canal Path:

In the x -axis or inferior-medial to superior-lateral direction, slice depth was found to have a significant impact on the canal path location ($P < 0.001$; power = 1.000). Most slice points were found to be significantly different from each other, with the exceptions of slices 1 vs. 4, 1 vs. 7 and 2 vs. 4. The first four slices (above and directly below the resection plane) remained more-or-less unchanged (*i.e.*, in-line) with one another (Figures 3.3 and 3.4). The fifth and sixth points were then located laterally, with the remaining points moving medially relative to the center of the resection plane (Figures 3.3 and 3.4). Gender was also found to significantly affect the frontal plane direction of the canal path, with female paths tending to be 2.0 ± 1.1 mm more inferior-medial than male canal paths ($P < 0.001$; power = 0.997). A slice depth-by-gender interaction demonstrated that this medialization of the female canal path was significant only in slices 6-13 (10 to 50mm below the resection plane; $P < 0.001$; power = 0.996). Within genders, frontal plane direction again tended to be significantly different between most slices ($P < 0.001$; power = 0.996).

In the y -axis or anterior-posterior (A-P) direction, the only variable that had a significant impact on the canal path direction was OA condition ($P = 0.008$; power = 0.814). It was

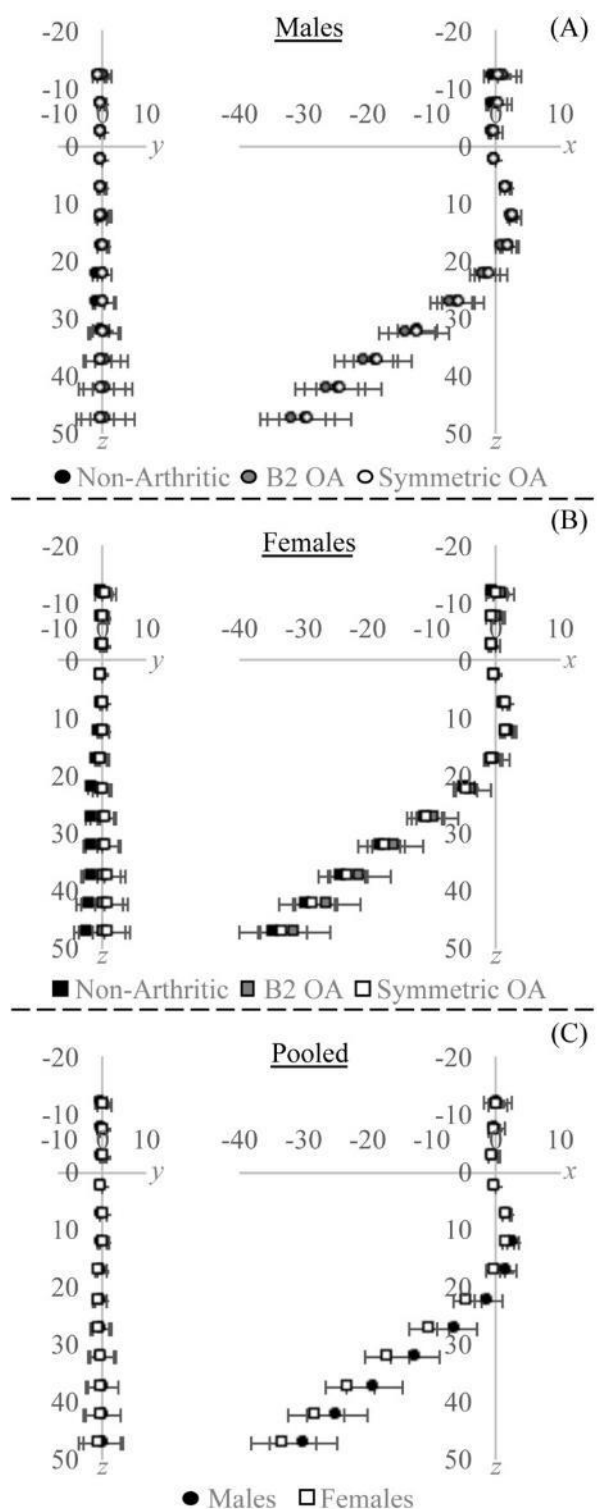


Figure 3.3: Visualization of the Proximal Humerus' Canal Path Results

Canal path results for the proximal humerus. Results are presented (A) for all male subjects, (B) for all female subjects, and (C) pooled across osteoarthritis (OA) conditions. Graphs on the left depict the sagittal plane coordinates, whereas graphs on the right depict the frontal plane coordinates. Markers are mean values, with SD error bars shown.

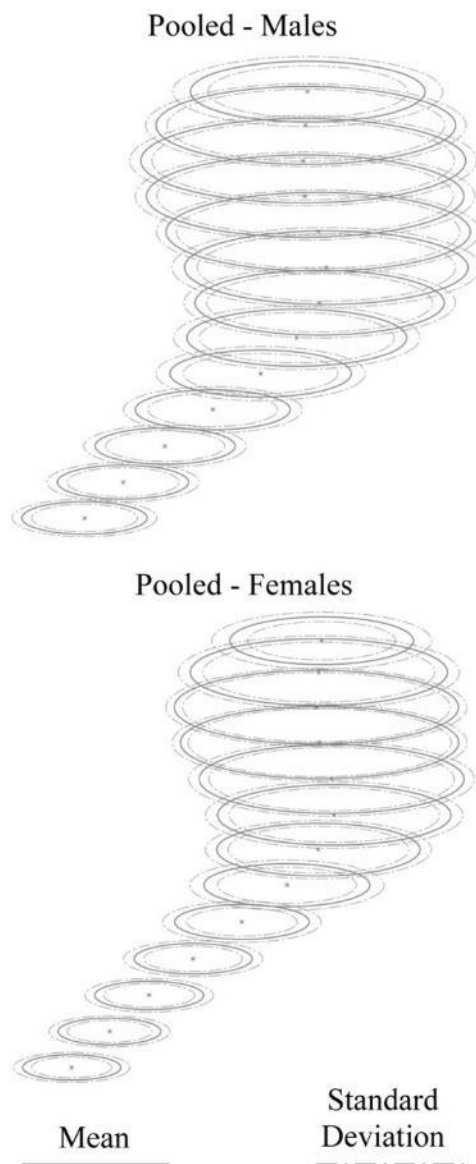


Figure 3.4: Visualization of the Proximal Humerus' Fitted Canal Diameter Results

The mean (solid lines) and one standard deviation (dashed lines) fitted canal diameters at the geometric center of each of the 13 slices of the proximal humerus. Diameter values are pooled across the osteoarthritis conditions for men and women.

determined that non-arthritic subjects had canal paths that were 0.8 ± 0.3 mm more anterior than in B2 OA subjects, and 0.3 ± 0.6 mm more posterior than in symmetric OA subjects.

3.3.2 Fitted Canal Diameter:

The fitted canal diameter varied significantly with changing slice depth ($P < 0.001$; power = 1.000). These were significantly different in each slice compared with all other slices, with the exceptions of slices 1 vs. 8 and 2 vs. 5. Overall, a pattern presented in which the slices immediately above and below the resection plane (slices 3 and 4) tended to have the largest canal diameters (Slice 3: Men $\phi_{canal} = 44\pm 3$ mm, Women $\phi_{canal} = 38\pm 2$ mm; Slice 4: Men $\phi_{canal} = 43\pm 3$ mm, Women $\phi_{canal} = 37\pm 2$ mm), with canal diameters decreasing as the distance away from the resection plane increased (Figure 3.4, Table 3.1). Gender was also found to have a significant effect on canal diameter, with men having 6 ± 1 mm significantly larger canal diameters than women ($P < 0.001$; power = 1.000). This gender difference was found to be approximately constant regardless of slice depth (Table 3.1). For each slice, canal diameter was also correlated with subject height (Figure 3.5); correlations were weak to moderate and ranged from $R^2 = 0.272$ to $R^2 = 0.498$ ($P < 0.001$).

3.3.3 Resection Depth:

The only variable that produced a significant effect in resection depth was gender. Men had a 5 ± 4 mm significantly larger resection depth than women ($P < 0.001$; power = 1.000), with the mean resection depths for men and women being 36 ± 3 mm and 31 ± 3 mm, respectively. The concentration of resection depths within the study population can be seen in Figure 3.6. A linear regression between resection depth (D) and resection plane diameter (ϕ) was also conducted (Figure 3.7) and demonstrated a moderated correlation ($R^2 = 0.472$; $P < 0.001$) between the two measures when results were pooled ($D = 0.601\phi + 5.145$). Resection depth was also found to be moderately correlated ($R^2 = 0.378$; $P < 0001$) with subject height (Figure 3.8; $D = 0.231h - 5.327$).

Table 3.1: Mean (standard deviation) fitted canal diameters in the 13 proximal humerus slices.

Fitted Canal Diameter (ϕ_{Canal}) [mm]						
	Slice	Non-Arthritic	B2 OA	Symmetric OA	Pooled	
Above Resection	1	32.0(4.1)	31.8(7.4)	31.5(3.7)	31.8(4.8)	Males
	2	39.7(2.6)	41.7(2.4)	41.0(3.3)	40.5(2.9)	
	3	42.9(2.9)	45.4(3.1)	44.7(2.6)	44.0(3.0)	
Below Resection	4	42.8(2.5)	43.8(4.0)	43.0(2.8)	43.1(2.9)	
	5	40.7(2.8)	41.8(3.1)	41.5(2.3)	41.2(2.7)	
	6	37.5(2.8)	39.8(4.1)	38.9(3.2)	38.4(3.3)	
	7	33.4(3.0)	34.4(4.4)	33.9(2.0)	33.8(3.1)	
	8	30.4(3.3)	29.4(4.9)	29.3(2.7)	29.8(3.5)	
	9	25.4(3.7)	24.0(4.1)	23.9(3.4)	24.7(3.7)	
	10	21.1(3.6)	21.4(3.5)	20.3(2.7)	20.9(3.3)	
	11	19.1(3.2)	19.6(3.4)	18.7(2.4)	19.1(3.0)	
	12	17.9(3.0)	18.4(2.7)	17.5(2.2)	17.9(2.7)	
	13	16.9(2.8)	17.5(2.6)	16.8(2.2)	17.0(2.6)	
Above Resection	1	24.3(2.8)	24.5(6.5)	24.7(4.8)	24.5(4.8)	Females
	2	33.1(2.4)	34.7(3.4)	35.1(3.7)	34.3(3.3)	
	3	36.9(1.9)	38.4(2.3)	38.7(2.1)	38.0(2.2)	
Below Resection	4	36.3(1.9)	37.8(2.2)	37.7(1.8)	37.3(2.1)	
	5	34.7(2.2)	36.6(2.2)	35.1(3.5)	35.4(2.7)	
	6	30.6(2.4)	32.0(3.4)	31.2(3.6)	31.2(3.1)	
	7	26.7(1.9)	27.5(3.0)	27.2(3.9)	27.1(3.0)	
	8	22.3(3.6)	22.2(3.7)	22.4(4.1)	22.3(3.7)	
	9	17.2(2.6)	18.6(3.8)	18.2(3.2)	18.0(3.2)	
	10	15.1(2.3)	16.3(2.9)	16.3(2.8)	15.9(2.7)	
	11	13.8(2.0)	15.0(2.7)	15.2(2.7)	14.6(2.5)	
	12	12.9(1.9)	14.3(2.7)	14.2(2.6)	13.8(2.4)	
	13	12.4(1.8)	13.5(2.5)	13.6(2.8)	13.2(2.4)	

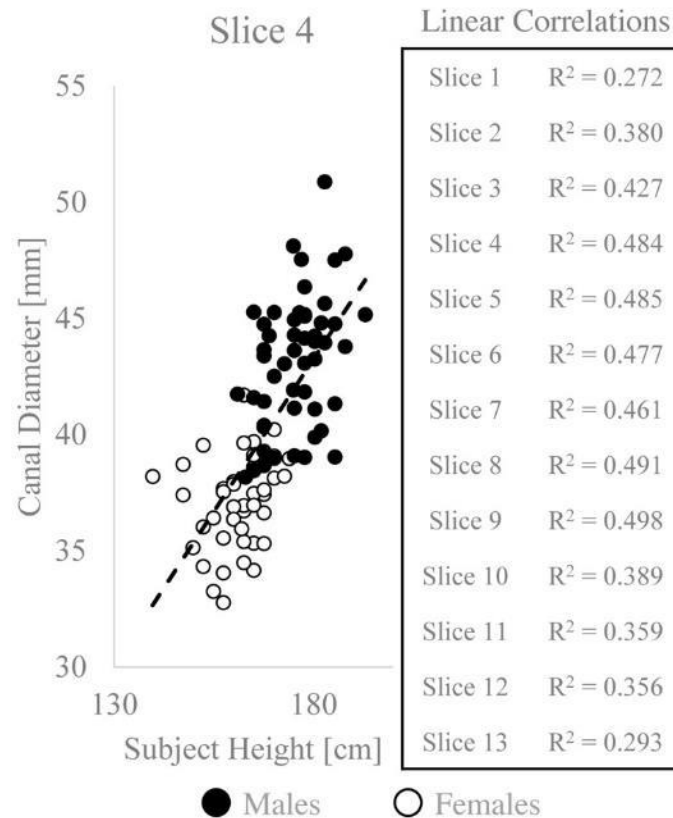


Figure 3.5: Sample Linear Regression Between Canal Diameter and Subject Height (Slice 4)

Linear regression between the canal diameters and subject height demonstrated weak to moderate ($0.272 \leq R^2 \leq 0.498$; $P < 0.001$) linear correlations. The regression for slice 4 is given as a representative sample, and R^2 -values for all slices are listed.

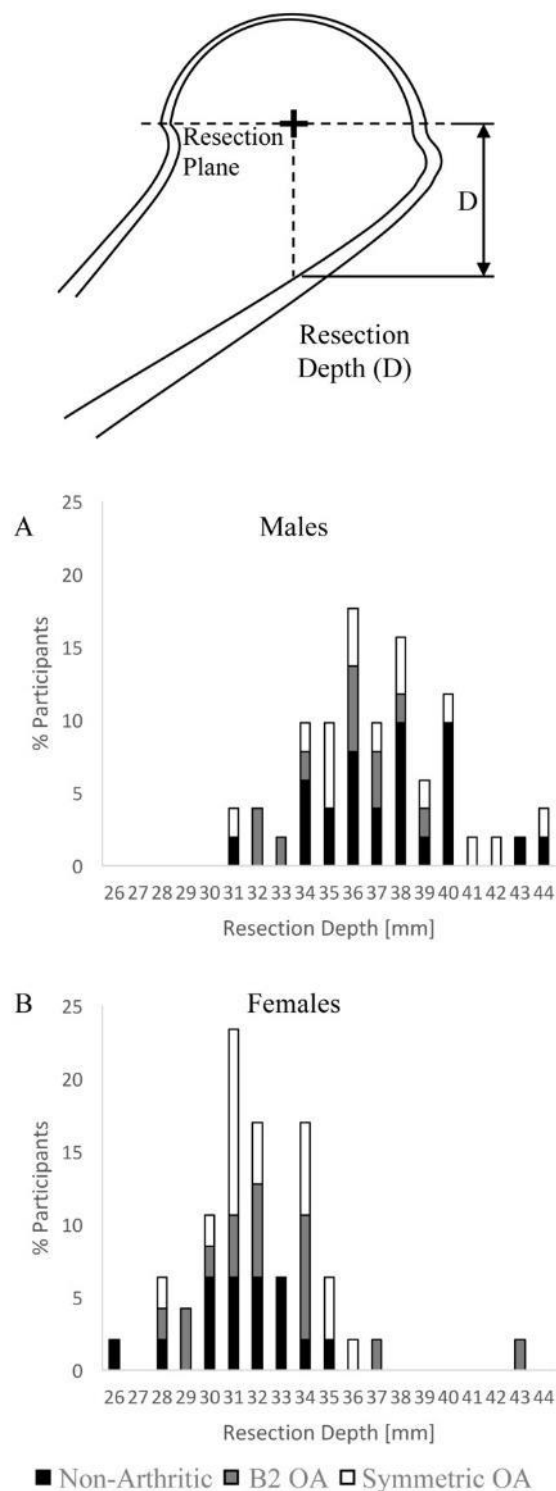


Figure 3.6: Histogram of the Proximal Humerus' Resection Depth Results

The resection depth for all (A) male and (B) female subjects (98 total) in the present study. The resection depth is measured as the maximum distance between the articular resection plane and the cortex beneath the center of the resection plane. Osteoarthritis (OA) conditions are presented as different shades in the stacked bars.

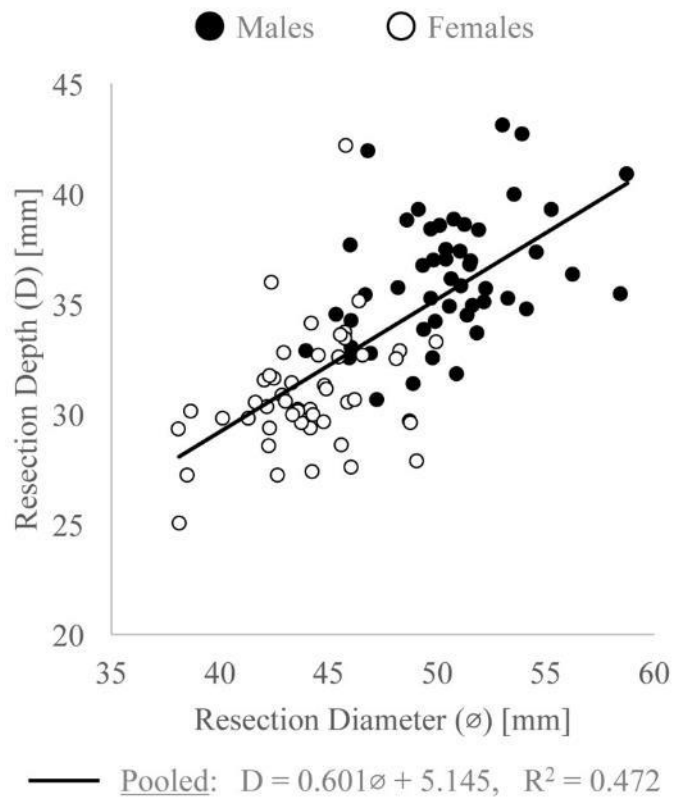


Figure 3.7: Linear Regression Between the Proximal Humerus' Resection Depth and Resection Diameter

Linear regression between the resection depth and resection diameter of the proximal humerus demonstrated a moderate ($R^2 = 0.472$; $P < 0.001$) linear correlation, perhaps suggesting that resection depth is dependent on more than scaling of the bone.

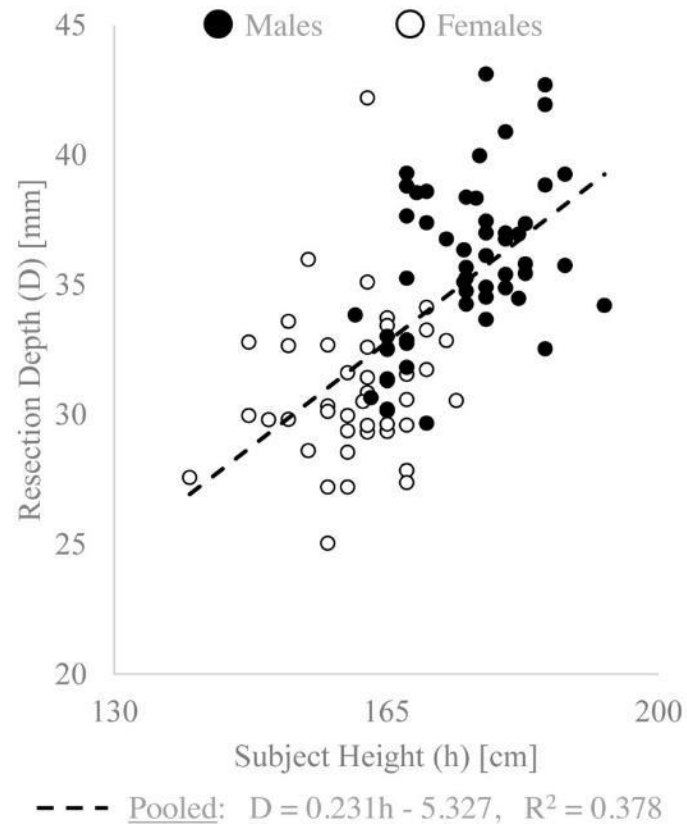


Figure 3.8: Linear Regression Between the Proximal Humerus' Resection Depth and Subject Height

Linear regression between the resection depth and subject height demonstrated a moderate ($R^2 = 0.378$; $P < 0.001$) linear correlation, perhaps suggesting that resection depth is dependent on more than subject height alone.

3.3.4 Articular Aspect Ratio:

The articular aspect ratio was found to be significantly lower in non-arthritic subjects ($2.6 \pm 0.2:1$) when compared with B2 OA ($2.7 \pm 0.3:1$) subjects ($P = 0.008$; power = 0.840) and approached significance between non-arthritic and symmetric OA ($2.7 \pm 0.3:1$) subjects ($P = 0.061$; power = 0.840). Gender did not have a significant impact on the articular aspect ratio directly; however, men did have 6 ± 4 mm significantly larger resection diameters ($P < 0.001$; power = 1.000), and 2.4 ± 2.3 mm significantly larger articular heights ($P < 0.001$; power = 1.000) compared with women. This gender bias was neutralized when expressed as a ratio ($\emptyset:H$). The significant impact of OA condition on articular aspect ratio arose because of the resection diameter, with non-arthritic subjects having significantly smaller resection diameters (46 ± 4 mm) than B2 OA subjects (48 ± 4 mm) and symmetric OA subjects (48 ± 4 mm) ($P < 0.001$; power = 1.000). The distribution of articular aspect ratios within the study population can be seen in Figure 3.9.

3.4 Discussion

This study has introduced three new morphological concepts that can be used to describe the proximal trabecular-canal of the humerus: (1) the central locations along the proximal canal path, (2) the bounding diameter of the trabecular-canal at the central locations, and (3) the canal depth beneath the center of the articular resection plane. Similar to how past quantifications of neck-shaft angle assisted with the determination of how to orient humeral articular components relative to the implant stem, it is expected that these morphological parameters can aid implant manufacturers in the design of the next generation of stemless implants for proximal humeral arthroplasty. Together, the direction and bounding limits on the proximal humerus' trabecular-canal provide a clearer understanding of the spatial envelope in which stemless metaphyseal fixation features are to be implanted.

The results indicate that the canal path of the proximal humerus remains largely straight in the sagittal plane (A-P direction) in the first 50mm beneath the articular resection plane. Whereas OA condition did have a significant effect on the canal's A-P direction,

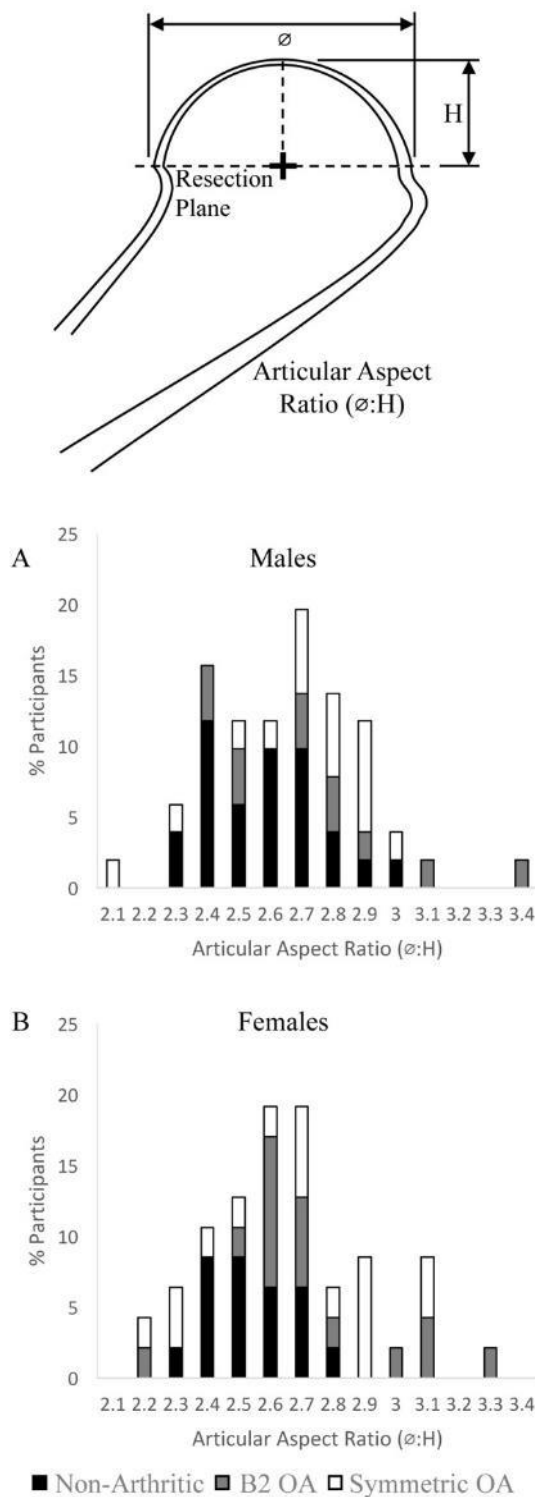


Figure 3.9: Histogram of the Proximal Humerus' Articular Aspect Ratio Results
 The articular aspect ratio for all (A) male and (B) female subjects (98 total) in the present study. The articular aspect ratio is calculated as the resection diameter divided by the humeral head height. Osteoarthritis (OA) conditions are presented as different shades in the stacked bars.

the mean differences between the non-arthritic and the two OA populations was <1 mm, which is unlikely to have any clinical impact on stemless implant design features. It is suggested that these difference in A-P canal path direction may be attributed to the orientation of the resection plane. Slight changes in the A-P tilt of this resection plane (due to poor articular geometry: articular wear and bone spurs in the CT) could account for the slight variances noted in the results. Alternatively, whereas the canal path remains relatively perpendicular to the resection above the resection plane and for the first slice beneath the resection, 5-50 mm beneath the resection plane (*i.e.*, slices 5 through 13), the trabecular-canal demonstrates significant frontal plane shifts that, when coupled with the decreasing canal diameter along these points, may have an impact on how implant fixation features should be angled (should they seek to remain directed along the center of the trabecular-canal) (Figure 3.3). Interestingly, women were found to have more inferior-medially directed canal paths in slices 6-13 than men. This is likely a consequence of the use of an absolute, not scaled, coordinate system. Because women tend to have smaller humeri than men, the same absolute depth corresponds to a greater percentage along the humeral length. Given the trend of canal path medialization with increased depth, the present gender bias is explained.

Our results from the fitted canal diameter presented with the largest diameters near the resection surface, with smaller diameters progressing away from the articular resection. The quantification of these bounding circles is important for improving the understanding of the spatial envelope available for implanting stemless features. Furthermore, the determination of an approximate 6mm difference in canal diameter between men and women at most locations in the proximal humerus should be accounted for in designing implant features that may rely on circumferential fixation. The moderate correlations ($0.272 \leq R^2 \leq 0.498$) found between canal diameters and subject height indicates a scaling relationship between subjects and canal dimensions; however, the strength of the correlation suggests that subject height alone does not account for all variance in the magnitude of the fitted canal diameters.

It was also noted that the canal depth beneath the center of the resection plane was shorter for women than for men. With the female humerus being shorter on average than the

male humerus, this was to be expected; however, quantifying the 6mm mean reduction in this length may be important for creating depth guides for centrally drilled holes that assist in boring and positioning procedures for stemless arthroplasty. Canal depth was found to be moderately correlated to subject height ($R^2 = 0.378$), which suggests that although height may be an influential factor in estimating canal depth, it cannot solely account for the variance seen within the present population. The moderate linear correlation between resection depth and resection plane diameter ($R^2 = 0.472$, $p < 0.001$) suggests that these two terms are also related, but that more affects the resection depth than just the scale of the bone (*e.g.*, resection orientation). It should also be noted that the resection depth is dependent on the placement and orientation of the resection plane, which is a subjective, not absolute, feature of the bone; however, a strength of stemless implants is their ability to be inserted at the anatomic resection plane, permitting a better match to intact articular geometry.

Finally, although not new, the articular aspect ratio terms of resection diameter and humeral head height were presented for completeness. In general, the articular aspect ratio was found to remain relatively constant (means between 2.6 and 2.7); however, the OA-classified cohorts did have higher ratios than the non-arthritic group. It is suggested that this difference arose because of the quality of the articular surfaces of the OA cohorts; and indicates some articular wear decreasing the humeral head height, thereby increasing the articular aspect ratio. Whereas more complicated non-axisymmetric terms have been developed in the literature to represent the elliptical nature of the natural humeral head [13], most implants currently manufactured use axisymmetric articular components, so the simplified axisymmetric terms were chosen for investigation. This study would be incomplete if these articular terms were not presented, at least to compare the current study population with those in the literature. The overall humeral head heights (men: 19 ± 1 mm, women: 17 ± 2 mm) and resection diameters (men: 50 ± 3 mm, women: 44 ± 3 mm) determined in this study agree well with those found in the literature (typical diameter: 36mm to 57mm, humeral head height: 12mm to 22mm) [12,13,16,19]; perhaps indicating that the new stemless morphologic parameters introduced earlier in this study

are reflective of a larger population, since Humphrey *et al* determined linear correlation between several morphological measures of the proximal humerus [13].

The morphological measures reported were obtained from a clinical CT scanner, not a micro-CT scanner. Accordingly, the precision of the scans is a limitation of the current study and is expected to influence the reported measures. However, to use pre-operative images from patients, clinical CT resolution was a necessary limitation of this study. Furthermore, the largest slice thickness in the study population was 1.5mm (mean 0.9 ± 0.3 mm), which is orders of magnitude smaller than the diameter, depth and height measurements quantified. Although the canal path positions are closer in magnitude to this uncertainty, the position is reported as an average of all voxels contained within the 5mm-thick slices, which are far larger in cross-section, and that would be equally affected by this error around the circumference of the slice. Accordingly, we are confident in the morphological terms quantified in this study. Finally, inter-surgeon and intra-surgeon reliability was not assessed for the selection of the surgical resection plane. Whereas variation in the orientation of the anatomic resection plane is not expected to have an impact on the fitted canal diameter and path, it could impact the articular aspect ratio and canal depth measures. Accordingly, reliability of the new outcome measures should be assessed in future studies. All outcome measures were quantified by custom-built LabVIEW programs to avoid user-bias; however, the manual segmentation of the humerus from the CT scans is an additional source of variability worthy of future investigation.

The inclusion of pre-operative patient scans is a strength in this study. The morphological results presented are reflective not only of a non-arthritic population, but also of B2 and symmetric OA demographics. After all, it is the OA sub-population that accounts for most shoulder arthroplasty cases performed [4]. In this manner, the present study has sought to include a clinically relevant population in the analysis of proximal humerus morphological measures specific for stemless shoulder arthroplasty. Interestingly, significant differences arising as a result of the OA condition were found only in the terms of the articular aspect ratio and the A-P direction of the canal path, the latter of which are thought to be too small to be clinically relevant.

3.5 Conclusions

Three new morphological measures have been introduced that together help to quantify the spatial limits for stemless implants in the proximal humerus. Gender was found to be the most recurrent contributor to significant differences in the proximal humerus' morphological measures, with OA condition inducing lesser variations. It is suggested that future investigations regarding stemless implants in the proximal humerus should be conducted in coordinate systems relative to the articular resection plane because this is the defining landmark of the stemless shoulder arthroplasty implant.

3.6 References

- [1] Reeves, J. M., Johnson, J. A., and Athwal, G. S., 2017, "An analysis of proximal humerus morphology with special interest in stemless shoulder arthroplasty," *J. Shoulder Elb. Surg.*, (**In Press**).
- [2] Neer, C. S., 1955, "Articular Replacement for the Humeral Head," *J. Bone Jt. Surg.*, **37**(2), pp. 215–228.
- [3] Neer, C. S., 1974, "Replacement Arthroplasty for Glenohumeral Osteoarthritis," *J. Bone Jt. Surg.*, **56**(1), pp. 1–13.
- [4] Kim, S. H., Wise, B. L., Zhang, Y., and Szabo, R. M., 2011, "Increasing Incidence of Shoulder Arthroplasty in the United States," *J. Bone Jt. Surg.*, **93**, pp. 2249–2254.
- [5] Schairer, W. W., Nwachukwu, B. U., Lyman, S., Craig, E. V., and Gulotta, L. V., 2015, "National utilization of reverse total shoulder arthroplasty in the United States," *J. Shoulder Elb. Surg.*, **24**(1), pp. 91–97.
- [6] Robertson, D. D., Yuan, J., Bigliani, L. U., Flatow, E. L., and Yamaguchi, K., 2000, "Three-dimensional analysis of the proximal part of the humerus: relevance to arthroplasty," *J. Bone Joint Surg. Am.*, **82**–A, pp. 1594–1602.
- [7] Roberts, S. N. J., Foley, A. P. J., Swallow, H. M., Wallace, W. A., and Coughlan, D. P., 1991, "The Geometry of the Humeral Head and the Design of Prostheses," *J.*

- Bone Jt. Surg., **73–B**(4), pp. 647–650.
- [8] Iannotti, J. P., Gabriel, J. P., Schneck, S. L., Evans, B. G., and Misra, S., 1992, “The Normal Glenohumeral Relationships: An Anatomical Study of One Hundred and Forty Shoulders,” *J. Bone Jt. Surg.*, **74–A**(4), pp. 491–500.
- [9] Boileau, P., and Walch, G., 1997, “The three-dimensional geometry of the proximal humerus. Implications for surgical technique and prosthetic design.,” *J. Bone Jt. Surg.*, **79–B**(5), pp. 857–865.
- [10] Ballmer, F. T., Sidles, J. A., Lippitt, S. B., and Matsen, F. A., 1993, “Humeral head prosthetic arthroplasty: Surgically relevant geometric considerations,” *J. Shoulder Elb. Surg.*, **2**(6), pp. 296–304.
- [11] DeLude, J. A., Bicknell, R. T., MacKenzie, G. A., Ferreira, L. M., Dunning, C. E., King, G. J. W., Johnson, J. A., and Drosdoweck, D. S., 2007, “An anthropometric study of the bilateral anatomy of the humerus,” *J. Shoulder Elb. Surg.*, **16**(4), pp. 477–483.
- [12] Hertel, R., Knothe, U., and Ballmer, F. T., 2002, “Geometry of the proximal humerus and implications for prosthetic design,” *J. Shoulder Elb. Surg.*, **11**(4), pp. 331–338.
- [13] Humphrey, S. C., Sears, B. W., and Curtin, M. J., 2016, “An anthropometric analysis to derive formulae for calculating the dimensions of anatomically shaped humeral heads,” *J. Shoulder Elb. Surg.*, **25**, pp. 1532–1541.
- [14] Jeong, J., and Jung, H. W., 2015, “Optimizing intramedullary entry location on the proximal humerus based on variations of neck-shaft angle,” *J. Shoulder Elb. Surg.*, **24**(9), pp. 1386–1390.
- [15] Nyffeler, R. W., Sheikh, R., Jacob, H. a C., and Gerber, C., 2004, “Influence of humeral prosthesis height on biomechanics of glenohumeral abduction. An in vitro study.,” *J. Bone Joint Surg. Am.*, **86–A**(3), pp. 575–580.
- [16] Pearl, M. L., and Volk, a G., 1996, “Coronal plane geometry of the proximal

- humerus relevant to prosthetic arthroplasty,” *J. Shoulder Elbow Surg.*, **5**(4), pp. 320–326.
- [17] Roosa, S. M. M., Hurd, A. L., Xu, H., Fuchs, R. K., and Warden, S. J., 2012, “Age-related changes in proximal humerus bone health in healthy, white males,” *Osteoporos. Int.*, **23**(12), pp. 2775–2783.
- [18] Youderian, A. R., Ricchetti, E. T., Drews, M., and Iannotti, J. P., 2014, “Determination of humeral head size in anatomic shoulder replacement for glenohumeral osteoarthritis,” *J. Shoulder Elb. Surg.*, **23**(7), pp. 955–963.
- [19] Zhang, L., Yuan, B., Wang, C., and Liu, Z., 2007, “Comparison of anatomical shoulder prostheses and the proximal humeri of Chinese people,” *J. Eng. Med.*, **221**(8), pp. 921–927.
- [20] Razfar, N., Reeves, J. M., Langohr, D. G., Willing, R., Athwal, G. S., and Johnson, J. A., 2016, “Comparison of proximal humeral bone stresses between stemless, short stem, and standard stem length: a finite element analysis,” *J. Shoulder Elb. Surg.*, **25**(7), pp. 1076–83.
- [21] Churchill, R. S., 2014, “Stemless shoulder arthroplasty: current status,” *J. Shoulder Elb. Surg.*, **23**(9), pp. 1409–1414.
- [22] Churchill, R. S., and Athwal, G. S., 2016, “Stemless shoulder arthroplasty—current results and designs,” *Curr. Rev. Musculoskelet. Med.*, **9**(1), pp. 10–16.
- [23] Harmer, L., Throckmorton, T., and Sperling, J. W., 2016, “Total shoulder arthroplasty: are the humeral components getting shorter?,” *Curr. Rev. Musculoskelet. Med.*, **9**(1), pp. 17–22.
- [24] Uschok, S., Magosch, P., Moe, M., Lichtenberg, S., and Habermeyer, P., 2017, “Is the stemless humeral head replacement clinically and radiographically a secure equivalent to standard stem humeral head replacement in the long-term follow-up? A prospective randomized trial,” *J. Shoulder Elb. Surg.*, **26**(2), pp. 225–232.
- [25] Churchill, R. S., Chuinard, C., Wiater, J. M., Friedman, R., Freehill, M., Jacobson,

- S., Spencer, E., Holloway, G. B., Wittstein, J., Lassiter, T., Smith, M., Blaine, T., and Nicholson, G. P., 2016, "Clinical and Radiographic Outcomes of the Simplicity Canal-Sparing Shoulder Arthroplasty System: A Prospective Two-Year Multicenter Study," *J. Bone Jt. Surg.*, **98**(7), pp. 552–560.
- [26] Routman, H., Becks, L., and Roche, C., 2015, Stemless and Short Stem Humeral Components in Shoulder Arthroplasty.
- [27] Habermeyer, P., Lichtenberg, S., Tauber, M., and Magosch, P., 2015, "Midterm results of stemless shoulder arthroplasty: A prospective study," *J. Shoulder Elb. Surg.*, **24**(9), pp. 1463–1472.
- [28] Nowak, D. D., Gardner, T. R., Bigliani, L. U., Levine, W. N., and Ahmad, C. S., 2010, "Interobserver and intraobserver reliability of the Walch classification in primary glenohumeral arthritis," *J. Shoulder Elb. Surg.*, **19**(2), pp. 180–183.
- [29] Walch, G., Badet, R., Boulahia, A., and Khoury, A., 1999, "Morphologic study of the glenoid in primary glenohumeral osteoarthritis," *J. Arthroplasty*, **14**(6), pp. 756–760.

Chapter 4

The Effect of Trabecular Modulus Anatomic Site Selection on FE Outcomes for Shoulder Arthroplasty

A version of this chapter has been submitted for publication [1].

4.1 Introduction

With the computational power of desktop computers increasing, the use of *in-silico* methods is becoming increasingly popular in orthopaedic research. In particular, the Finite Element (FE) method (Section 1.4.2), is commonly used to assess bone and implant strain-based outcome measures following joint arthroplasty [2–9]. FE models are well established for the joints of the lower extremity (*i.e.*, knee, hip, *etc.*) [2,5–13], and have also more recently been developed for the joints of the upper extremity [14–18]; including the shoulder [3,4,19,20]. Accordingly, when developing a FE model for shoulder arthroplasty, previous literature can guide the overall model construction (*e.g.*, frictional contact between implants and bone, *etc.*); however, model properties that are joint-specific, such as the magnitude of joint reaction forces, material properties and boundary conditions, must be applied based on evidence.

One important feature for developing realistic FE models of bone is the material stiffness (*i.e.*, elastic modulus) that is applied to the tissue. It is generally accepted that cortical bone can be modelled as a homogeneous and isometric structure, with a uniform stiffness that is independent of orientation [3,21,22]. Despite trabecular bone having anisometric stiffness, Kabel *et al* have suggested that there is little benefit realized from modelling trabecular bone as anisometric when constructing a FE model, provided that the model utilizes an inhomogeneous stiffness derived from bone density [23]. Accordingly, there has been much work in the literature indicating that trabecular stiffness should be modelled as inhomogeneous and isometric [11,24–28]. Trabecular stiffness has also been shown to vary exponentially as a function of bone density, which can be obtained using a calibrated CT scan [29,30]. Morgan *et al* have demonstrated that the regression equation

and resulting mechanical properties (*i.e.*, stiffness, yield strain, *etc.*) depend on the anatomic site from which the regression is formed [24,31]; however, the variation in FE outcomes in response to varying the regression equation based on anatomic-site has not yet been documented.

Several density-stiffness regressions have been developed for the joints of the knee, hip and spine [24,25,32,33]; however, no equation has been developed for the proximal humerus of the shoulder. As such, FE investigations of the shoulder utilize regression equations that have been developed for other anatomic-sites, or that pooled results from several sites throughout the body [3,19]. Again, the effect that this has on the outcomes of shoulder FE investigations is unknown. Furthermore, with the advent of identical meshing techniques, which can be used to partially normalize results to an intact state (subject to the same trabecular model) [3], there is the potential that the stiffness relationship of trabecular bone may have a minor impact on FE outcomes.

In light of the foregoing, the purpose of this investigation is to quantify the deviation induced in FE outcome measures for humeral arthroplasty when the trabecular stiffness relationships are changed (Objective 2, Section 1.6.1). It is hypothesized that varying the inhomogeneous trabecular stiffness based on anatomic-site (*i.e.*, anatomic-site deviation) would result in low standard deviations (less than 10%); and that these deviations would be less than those arising within the FE specimen population (*i.e.*, FE population deviation). Furthermore, it was hypothesized that the standard deviations induced from applying a homogeneous trabecular modulus, as opposed to a site-pooled inhomogeneous one (*i.e.*, homogeneous-inhomogeneous deviation), would also be greater than the inhomogeneous anatomic-site deviation.

4.2 Materials and Methods

Eight cadaveric upper extremities (left arms; mean \pm SD age = 68 \pm 6 years) were CT scanned using a GE 750HD Discovery scanner (GE Healthcare; Chicago, IL, USA), alongside a SB3-H₂O density calibration phantom (SB3 Model number 450; GAMMEX, Middleton, WI). Three axial planes were constructed along the length of the calibration phantom, dividing the SB3 bone-surrogate into quarters. In each plane, the average

attenuation (in Hounsfield Units, HU) corresponding to the distilled water and bone surrogate were determined. A linear regression was then performed between the known apparent densities (SB3: $\rho_{APP} = 1.82 \text{ g/cm}^3$; H_2O : $\rho_{APP} = 0 \text{ g/cm}^3$) and CT attenuation-values to obtain the calibration relationship between attenuation and apparent density.

In each scan, the proximal humerus was manually segmented to remove it from the surrounding soft tissues using Mimics (version 19, Materialize, Leuven, BE), and was divided into two components: (1) the cortical shell and (2) the trabecular-canal. These regions were exported into SolidWorks (Dassault Systèmes Corp, Waltham, MA, USA) where 3D solid models were formed. A shoulder surgeon then virtually selected the surgical resection plane; further dividing the cortical shell and trabecular-canal into top and bottom sections. The geometric centroid of the surgical resection plane was used to position a stemless shoulder implant (Tornier Simpliciti; Wright BioMedical, Staines-upon-Thames, Middlesex, UK) centrally, as per surgical practice. To reduce the computational demand, the proximal humeral diaphysis was resected 180mm beneath the most superior point on the surgical resection plane (Figure 4.1). In addition, the trabecular-canal was trimmed 40mm beneath the surgical resection plane.

All components were then imported into Abaqus (Dassault Systèmes Corp, Waltham, MA, USA) and were assembled to form two models: (1) an intact proximal humerus and (2) a stemless anatomic reconstruction. Identical meshing practice was followed to ensure that both models had the exact same bone mesh (quadratic tetrahedral elements with 2mm edge length, based on mesh convergence, Appendix C) for the cortical-bottom and trabecular-bottom segments [3]. For all models, the implant material was modeled as Titanium, with a stiffness of 110GPa, and Poisson's ratio of 0.3 [3,34,35]; and the implant-bone contact was divided into two frictional groups corresponding to polished ($\mu = 0.40$) [3,34] and grit blast ($\mu = 0.63$) [3,36] surface textures. Additionally, the cortical bone was considered isometric and homogeneous with an elastic modulus of 20GPa, and a Poisson's ratio of 0.3 [3,21,22]. Trabecular stiffness was modelled as isotropic but was inhomogeneously mapped to the trabecular-canal using a density-based elastic modulus regression, as outlined below.

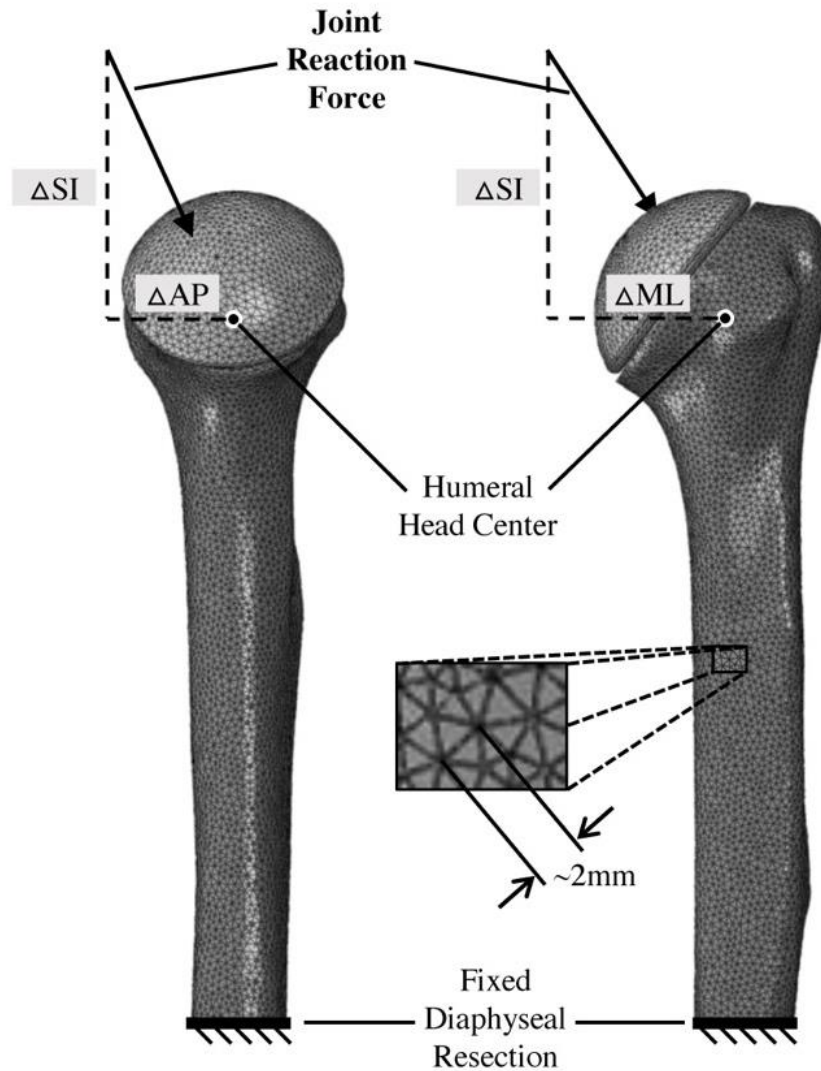


Figure 4.1: Humeral Joint Reaction Force Application

Depiction of articular load application in the FE model. Loads were oriented such that the force vector would pass through the humeral head's center of curvature and satisfy the *in-vivo* Cartesian component ratios (ΔAP : Anterior-Posterior, ΔML : Medial-Lateral, ΔSI : Superior-Inferior).

To assess the effect of changing trabecular material properties, five elastic modulus-density regression equations were independently mapped to the trabecular-canal (Figure 4.2). All relationships were derived by Morgan *et al* (2003), with four corresponding to anatomic sites throughout the body (*i.e.*, Vertebra, Proximal Tibia, Greater Trochanter and Femoral Neck), while the fifth was based on pooling results from the other sites (*i.e.*, Pooled) [24]. In addition to these material properties, a homogeneous trabecular stiffness of 155MPa (Model 3404 - 4th Generation Humerus Sawbone equivalent; Sawbones, Vashon Island, Washington, USA) was applied to assess the effect of trabecular homogeneity.

Identical joint reaction forces were applied to the articular surfaces of both the intact bone and the stemless implant, based on *in-vivo* shoulder data from Bergmann *et al* (2007). Force magnitudes were 440N and 740N representing 45° and 75° of abduction, respectively (50th-percentile male weight = 88.3kg) [3,37]. Joint loads were oriented using their Cartesian components, such that the force passed through the center of the humeral head (Figure 4.1).

The three outcome measures assessed were: (1) the percentage of the implant-bone surface area that was in contact during load application, (2) the percentage change in bone stress (relative to the intact state) and (3) the percentage of bone volume with potential to (a) resorb, (b) remodel, or (c) remain unchanged immediately following surgery. To establish which potential bone response category that an element was assigned to, the Strain Energy Density (SED) of each reconstructed bone element was compared to the exact same element in the intact bone model. The change in SED of an element has been well correlated to predicting changes in bone density [16,38–41]. In keeping with strain-adaptive FE models of the upper limb, an unchanged bone response threshold of 55% was set on either side of the intact model's SED value; if the reconstructed element's SED was below this, the element was categorized as having resorbing potential, and if the SED was above this threshold, the element was categorized as having remodeling potential [16]. To assess variation regionally, the change in stress and potential bone response were evaluated separately for cortical and trabecular bone, and in eight 5mm thick slices; parallel to and beneath the humeral head resection plane.

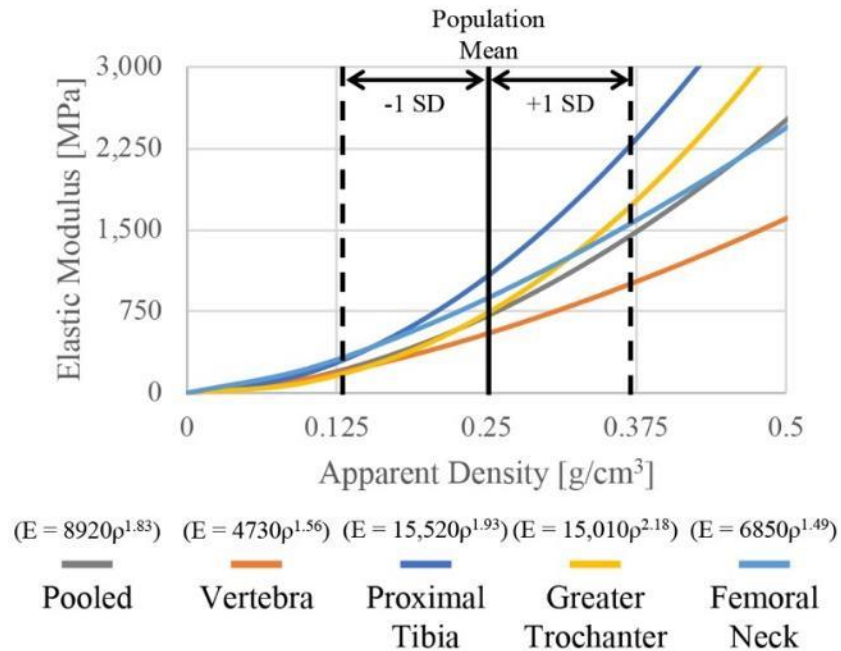


Figure 4.2: Density-Modulus Relationships Applied to the Proximal Humerus

Density-modulus relationships are presented for all inhomogeneous anatomic-sites that were utilized in the present investigation. The mean (solid vertical line) and SD (dashed vertical lines) density of the present FE population is shown for reference.

As the objective of this study was to assess the influence of trabecular stiffness selection on the deviation of these outcome measures, the comparison of the standard deviations (SD) of each outcome measure was the principle focus [42]. Standard deviations were calculated for the variance attributed to changing the inhomogeneous trabecular stiffness relationship based on anatomic-site (*i.e.*, anatomic-site deviation). In addition, as a comparative metric, the SD pertaining to differences between FE specimens (*i.e.*, FE population deviation) was also quantified. Finally, the SD comparing the site-pooled inhomogeneous results to the homogeneous trabecular results (*i.e.*, homogeneous-inhomogeneous deviation) was also determined for comparison. These deviations were quantified for each of the outcome measures outlined above; and were the primary basis for comparing trabecular relationships within this study.

4.3 Results

4.3.1 Implant-Bone Contact

The implant-bone contact percentage remained relatively constant regardless of which inhomogeneous trabecular stiffness anatomic-site equation was used; however, greater differences were found between the homogeneous and site-pooled inhomogeneous trabecular models (Figure 4.3). The SDs for inhomogeneous anatomic-site selection were found to be $0.8 \pm 0.3\%$ for 45° , and $0.7 \pm 0.2\%$ for 75° . As a comparison, the FE population deviation was $2.9 \pm 0.3\%$ for 45° , and $3.1 \pm 0.3\%$ for 75° , while the deviation associated with changing from a pooled inhomogeneous stiffness to a constant homogeneous stiffness was $6.4 \pm 2.8\%$ for 45° , and $6.9 \pm 3.0\%$ for 75° . Regardless of the loading configuration, the inhomogeneous anatomic-site SD was approximately 4-times lower than the FE population SD (45° : 3.8x less, 75° : 4.3x less), and approximately 20-times less than the homogeneous-inhomogeneous SD (45° : 20.1x less, 75° : 25.2x less).

4.3.2 Change in Bone Stress

The regional changes in cortical bone stress also remained relatively constant despite changing the inhomogeneous trabecular stiffness relationship (Figures 4.4 and 4.5). The mean SDs attributed to anatomic-site changes varied from 0.3% to 2.9% across slices (Table 4.1), with the means being $1.7 \pm 0.4\%$ for 45° , and $1.9 \pm 0.4\%$ for 75° .

Implant-Bone Contact

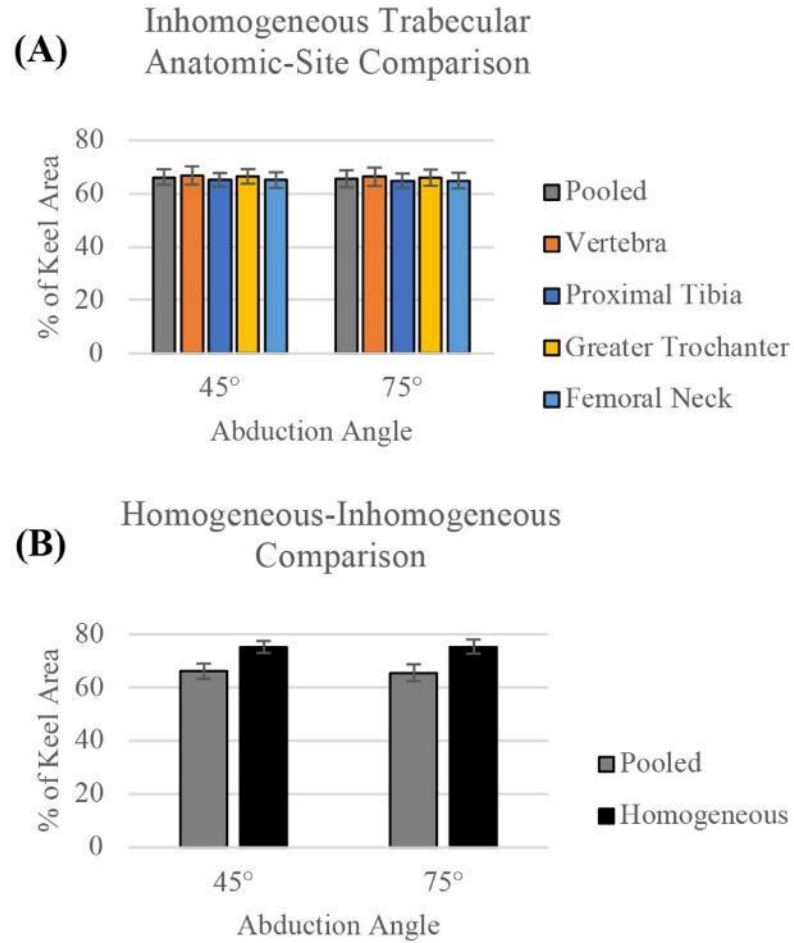


Figure 4.3: Implant-Bone Contact Percentage Results
 Mean \pm SD percentage of the implant-bone contact area that remained in contact under joint loading for (A) the inhomogeneous anatomic-site comparison and (B) the homogeneous-inhomogeneous comparison.

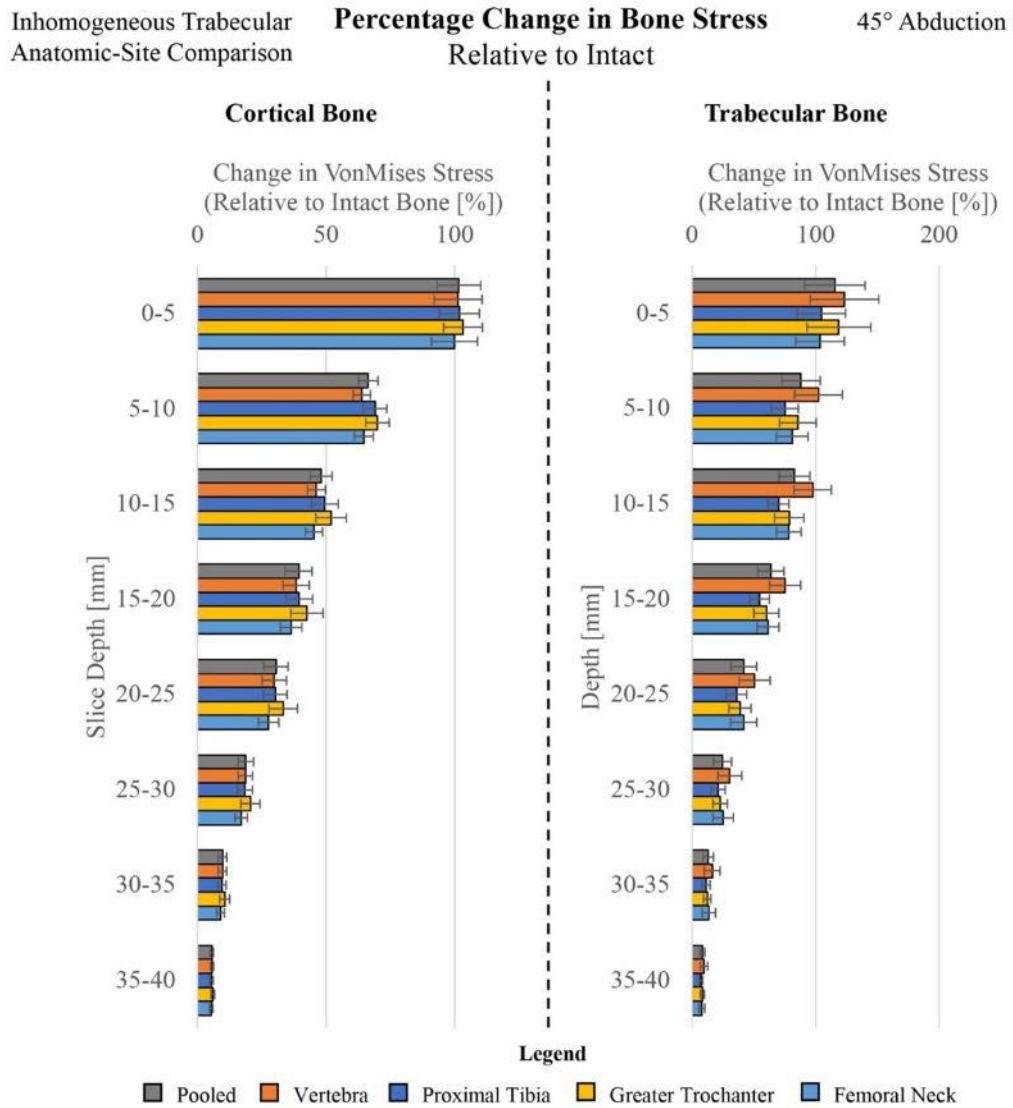


Figure 4.4: Inhomogeneous Anatomic-Site Change in Bone Stress Results (45°)

Mean ± SD percentage change in cortical and trabecular bone stress for 45° of abduction for the inhomogeneous anatomic-site comparison.

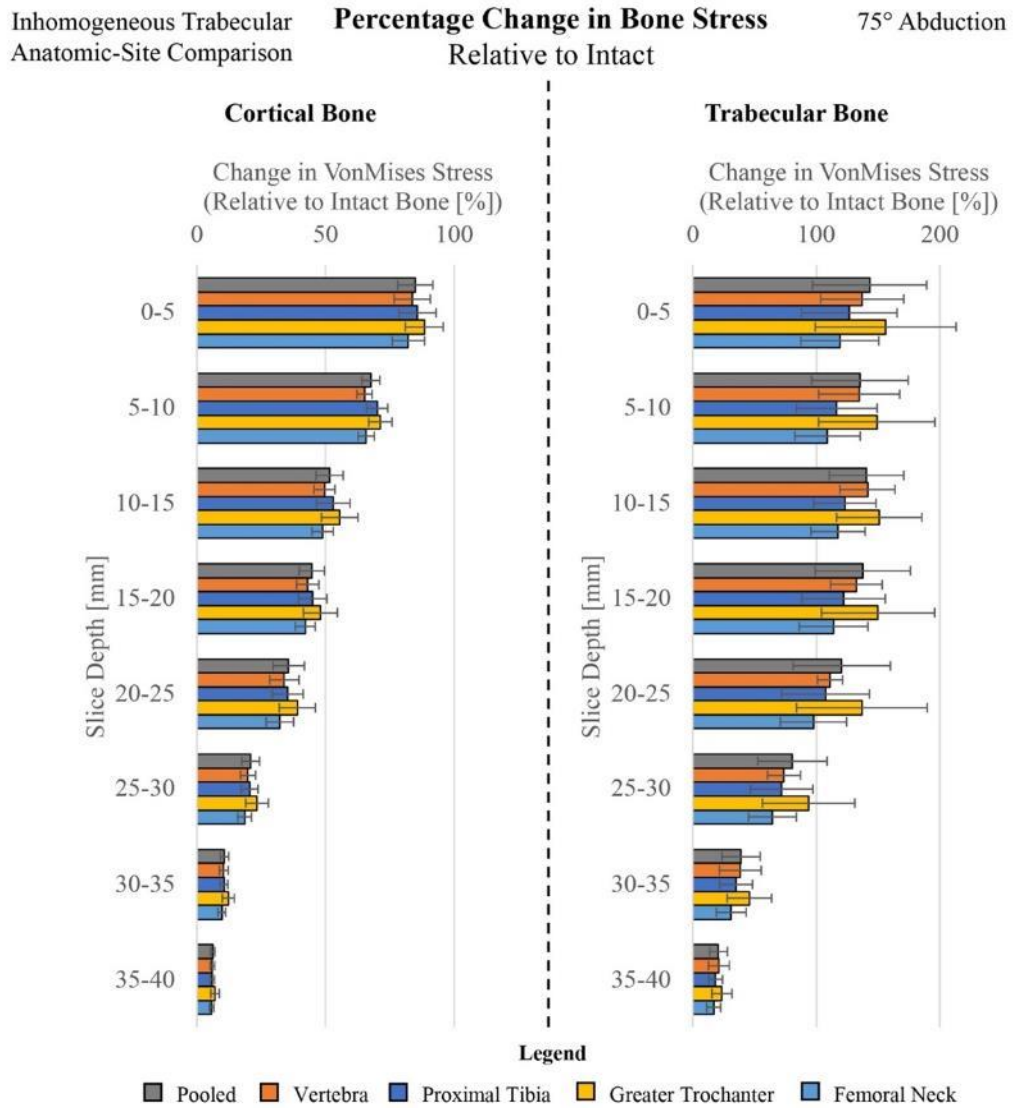


Figure 4.5: Inhomogeneous Anatomic-Site Change in Bone Stress Results (75°)

Mean ± SD percentage change in cortical and trabecular bone stress for 75° of abduction for the inhomogeneous anatomic-site comparison.

Table 4.1: Standard deviations attributed to inhomogeneous anatomic-site, FE population and homogeneous-inhomogeneous differences in the change in bone stress outcome measure; broken down regionally according to slice depth.

Slice Depth [mm]	Cortical - 45°			Trabecular - 45°		
	Inhomogeneous Anatomic-Site	FE Population	Homogeneous- Inhomogeneous	Inhomogeneous Anatomic-Site	FE Population	Homogeneous- Inhomogeneous
	Mean(SD)	Mean(SD)	Mean(SD)	Mean(SD)	Mean(SD)	Mean(SD)
0-5	1.4(0.6)	8.4(0.7)	3.5(3.2)	8.9(4.0)	23.5(3.7)	25.2(25.3)
5-10	2.7(1.4)	4.0(0.5)	4.1(3.4)	10.2(3.3)	14.7(3.2)	53.4(22.4)
10-15	2.7(1.7)	4.4(1.1)	5.1(3.3)	10.3(2.5)	11.6(2.5)	63.0(16.2)
15-20	2.4(1.3)	5.2(0.7)	3.9(2.8)	7.7(1.8)	10.0(1.8)	69.6(15.4)
20-25	2.2(1.1)	4.7(0.6)	3.6(2.4)	5.6(1.7)	10.1(1.6)	92.9(19.1)
25-30	1.4(0.7)	3.0(0.5)	4.4(1.9)	3.7(1.7)	7.4(1.7)	101.1(18.0)
30-35	0.7(0.4)	1.6(0.2)	4.0(1.3)	2.0(1.4)	4.5(1.4)	87.9(14.0)
35-40	0.3(0.2)	0.6(0.1)	2.2(1.0)	1.0(0.5)	2.1(0.6)	60.7(17.2)
Overall:	1.7(0.4)	4.0(0.2)	3.8(0.9)	6.2(0.8)	10.5(0.8)	69.2(6.6)

Slice Depth [mm]	Cortical - 75°			Trabecular - 75°		
	Inhomogeneous Anatomic-Site	FE Population	Homogeneous- Inhomogeneous	Inhomogeneous Anatomic-Site	FE Population	Homogeneous- Inhomogeneous
	Mean(SD)	Mean(SD)	Mean(SD)	Mean(SD)	Mean(SD)	Mean(SD)
0-5	1.5(0.5)	8.1(0.9)	3.8(2.7)	8.3(3.0)	22.4(2.7)	24.6(26.3)
5-10	2.7(1.4)	4.1(0.6)	4.3(3.4)	9.2(2.8)	13.3(2.7)	52.9(22.3)
10-15	2.9(1.9)	4.9(1.1)	5.1(3.4)	9.6(2.3)	10.7(1.9)	63.8(16.0)
15-20	2.5(1.4)	5.4(0.8)	4.3(2.5)	7.4(1.9)	10.1(1.9)	70.6(15.2)
20-25	2.3(1.2)	5.0(0.6)	3.7(2.5)	5.5(2.1)	10.4(2.0)	95.7(18.6)
25-30	1.6(0.8)	3.1(0.6)	4.5(2.0)	3.7(1.9)	7.9(2.1)	105.2(17.7)
30-35	0.9(0.5)	1.8(0.3)	4.0(1.1)	2.0(1.5)	5.2(1.8)	92.1(13.4)
35-40	0.6(0.5)	1.1(0.4)	2.2(1.0)	1.1(0.7)	2.4(0.7)	64.1(17.0)
Overall:	1.9(0.4)	4.2(0.2)	4.0(0.9)	5.9(0.8)	10.3(0.7)	71.1(6.6)

Comparatively, the mean FE population SDs ranged from 0.6% to 8.4% regionally, with means of $4.0 \pm 0.2\%$ for 45° , and $4.2 \pm 0.2\%$ for 75° . Accordingly, the FE population SDs were 2.5-times, and 2.3-times greater than the anatomic-site deviations for 45° and 75° , respectively. In addition, the SDs associated with changing from an inhomogeneous to homogeneous trabecular model were 3.2 and 2.5-times greater than the inhomogeneous anatomic-site SDs for 45° and 75° , respectively; with mean SDs ranging from 2.2% to 5.1% regionally (Figures 4.6 and 4.7).

The regional changes in trabecular bone stress exhibited greater SDs attributable to the selection of trabecular stiffness anatomic-site than any other outcome measure (Figures 4.4 and 4.5); with overall values of $6.2 \pm 0.8\%$ for 45° , and $5.9 \pm 0.8\%$ for 75° (means ranging from 1.0% to 10.3% regionally; Table 4.1). The regional mean anatomic-site SDs exceeded 10% for slices 2 and 3 (5-15mm beneath the resection) in 45° only, with values of $10.2 \pm 3.3\%$ and $10.3 \pm 2.5\%$, respectively. The SDs attributable to FE population and changing to a homogeneous trabecular modulus were also found to be greatest in the trabecular stress change outcome measure (Table 4.1). FE population SDs were found to be $10.5 \pm 0.8\%$ for 45° , and $10.3 \pm 0.7\%$ for 75° (means ranging from 2.1% to 23.5% regionally), corresponding to 1.8 and 1.9-times greater than the anatomic-site SDs overall, respectively. Again, the homogeneous-inhomogeneous SDs were found to be the greatest, at $69.2 \pm 6.6\%$ for 45° , and $71.1 \pm 6.6\%$ for 75° (means ranging from 24.6% to 105.2% regionally). Overall, the homogeneous-inhomogeneous SDs were 21.5 and 21.6-times greater than those attributable to inhomogeneous anatomic-site selection (Figures 4.6 and 4.7). Interestingly, the homogeneous-inhomogeneous SDs tended to be greatest in slices 4-8 (depth of 20-40mm), while the anatomic-site and FE population SDs tended to diminish in the same region (Table 4.1).

4.3.3 Potential Bone Response

4.3.3.1 Cortical Region

Standard deviations for the resorbing potential of cortical bone were small for changing the trabecular stiffness' regression based on anatomic-site (Table 4.2, Figures 4.8 and 4.9), with values of $1.3 \pm 0.4\%$ for 45° , and $1.1 \pm 0.3\%$ for 75° (Ranging from 0.0% to 3.5%

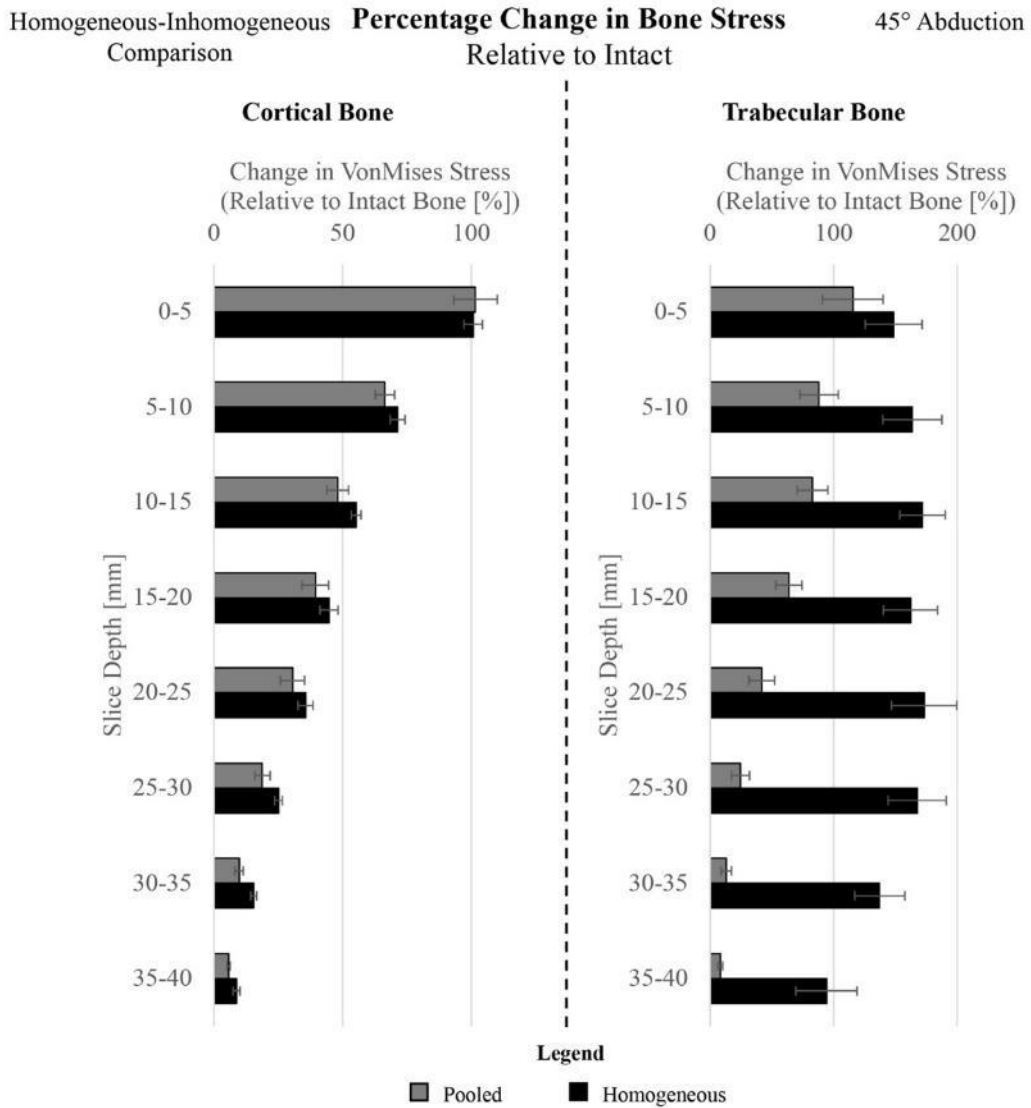


Figure 4.6: Homogeneous-Inhomogeneous Change in Bone Stress Results (45°)
 Mean ± SD percentage change in cortical and trabecular bone stress for 45° of abduction for the homogeneous-inhomogeneous comparison.

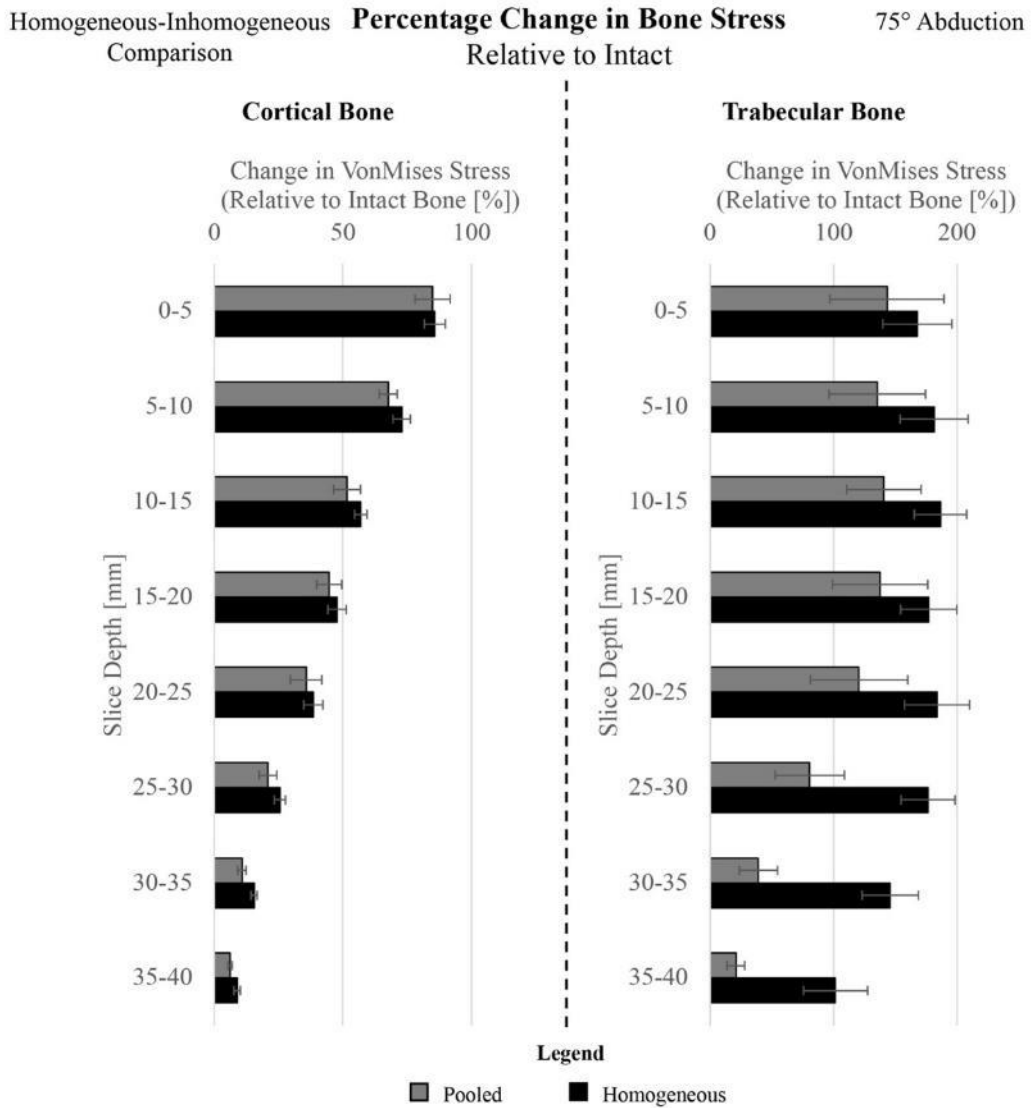


Figure 4.7: Homogeneous-Inhomogeneous Change in Bone Stress Results (75°)
 Mean ± SD percentage change in cortical and trabecular bone stress for 75° of abduction for the homogeneous-inhomogeneous comparison.

Table 4.2: Standard deviations attributed to inhomogeneous anatomic-site, FE population and homogeneous-inhomogeneous differences in the potential bone response outcome measure for cortical bone; broken down regionally according to slice depth.

Inhomogeneous Anatomic-Site Comparison						
Slice	45° Abduction			75° Abduction		
Depth [mm]	Resorbing Mean(SD)	Unchnaged Mean(SD)	Remodeling Mean(SD)	Resorbing Mean(SD)	Unchnaged Mean(SD)	Remodeling Mean(SD)
0-5	2.0(1.2)	1.3(0.6)	1.1(1.3)	1.9(1.2)	1.4(0.5)	0.9(1.3)
5-10	3.5(2.1)	2.4(1.6)	1.3(1.1)	2.9(2.1)	2.1(1.4)	1.3(1.1)
10-15	2.3(1.6)	2.7(0.8)	3.3(1.2)	1.9(0.8)	2.6(1.2)	3.3(1.6)
15-20	1.2(0.9)	3.1(1.7)	3.4(1.2)	1.0(0.6)	2.9(1.7)	3.3(1.4)
20-25	0.5(0.4)	3.6(1.5)	3.3(1.5)	0.8(0.5)	3.3(1.6)	3.3(1.5)
25-30	0.5(0.5)	1.8(0.9)	1.6(0.6)	0.5(0.7)	2.3(1.3)	2.0(1.2)
30-35	0.0(0.0)	0.1(0.1)	0.1(0.1)	0.1(0.2)	0.2(0.2)	0.1(0.2)
35-40	0.0(0.0)	0.0(0.0)	0.0(0.0)	0.0(0.0)	0.0(0.0)	0.0(0.0)
Overall:	1.3(0.4)	1.9(0.4)	1.8(0.4)	1.1(0.3)	1.9(0.4)	1.8(0.4)

FE Population Comparison						
Slice	45° Abduction			75° Abduction		
Depth [mm]	Resorbing Mean(SD)	Unchnaged Mean(SD)	Remodeling Mean(SD)	Resorbing Mean(SD)	Unchnaged Mean(SD)	Remodeling Mean(SD)
0-5	10.2(0.8)	7.1(0.4)	4.7(1.2)	10.5(0.8)	6.5(0.3)	5.4(1.3)
5-10	9.0(0.6)	8.0(0.5)	1.9(0.9)	9.1(0.7)	8.3(0.3)	2.1(0.9)
10-15	8.5(0.4)	9.1(0.9)	4.4(0.4)	9.3(0.6)	9.1(0.3)	4.0(0.5)
15-20	9.5(0.2)	12.3(0.9)	5.9(0.8)	7.9(0.7)	11.6(0.7)	7.9(0.5)
20-25	7.6(0.2)	9.1(0.6)	5.6(1.7)	5.4(0.5)	11.1(0.8)	8.6(1.4)
25-30	3.1(0.4)	3.3(0.2)	1.5(0.5)	1.1(0.6)	3.1(1.1)	2.6(1.1)
30-35	0.0(0.0)	0.1(0.1)	0.0(0.1)	0.1(0.2)	0.2(0.2)	0.1(0.2)
35-40	0.0(0.0)	0.0(0.0)	0.0(0.0)	0.0(0.0)	0.0(0.0)	0.0(0.0)
Overall:	6.0(0.1)	6.1(0.2)	3.0(0.3)	5.4(0.2)	6.2(0.2)	3.8(0.3)

Homogeneous-Inhomogeneous Comparison						
Slice	45° Abduction			75° Abduction		
Depth [mm]	Resorbing Mean(SD)	Unchnaged Mean(SD)	Remodeling Mean(SD)	Resorbing Mean(SD)	Unchnaged Mean(SD)	Remodeling Mean(SD)
0-5	10.1(7.2)	8.4(5.0)	1.9(3.0)	2.4(3.8)	9.5(7.8)	7.6(5.0)
5-10	15.6(9.6)	15.4(8.5)	1.0(1.2)	1.1(1.5)	16.2(9.8)	15.9(9.0)
10-15	23.4(11.2)	17.1(10.7)	6.6(4.0)	6.7(3.1)	23.8(10.8)	17.4(10.3)
15-20	19.1(8.6)	10.8(5.8)	9.2(3.9)	10.5(5.0)	18.7(8.6)	10.1(4.6)
20-25	9.2(5.6)	5.8(5.1)	5.0(3.5)	6.3(3.6)	9.7(5.4)	6.2(4.8)
25-30	1.3(1.6)	2.6(1.8)	1.4(0.5)	1.2(0.8)	1.7(1.3)	2.5(1.5)
30-35	0.1(0.1)	0.7(0.6)	0.6(0.5)	0.7(0.7)	0.0(0.1)	0.8(0.7)
35-40	0.0(0.0)	0.0(0.1)	0.0(0.1)	0.1(0.3)	0.0(0.0)	0.1(0.3)
Overall:	9.9(2.4)	7.6(2.1)	3.2(0.9)	3.6(1.0)	10.0(2.4)	7.6(2.0)

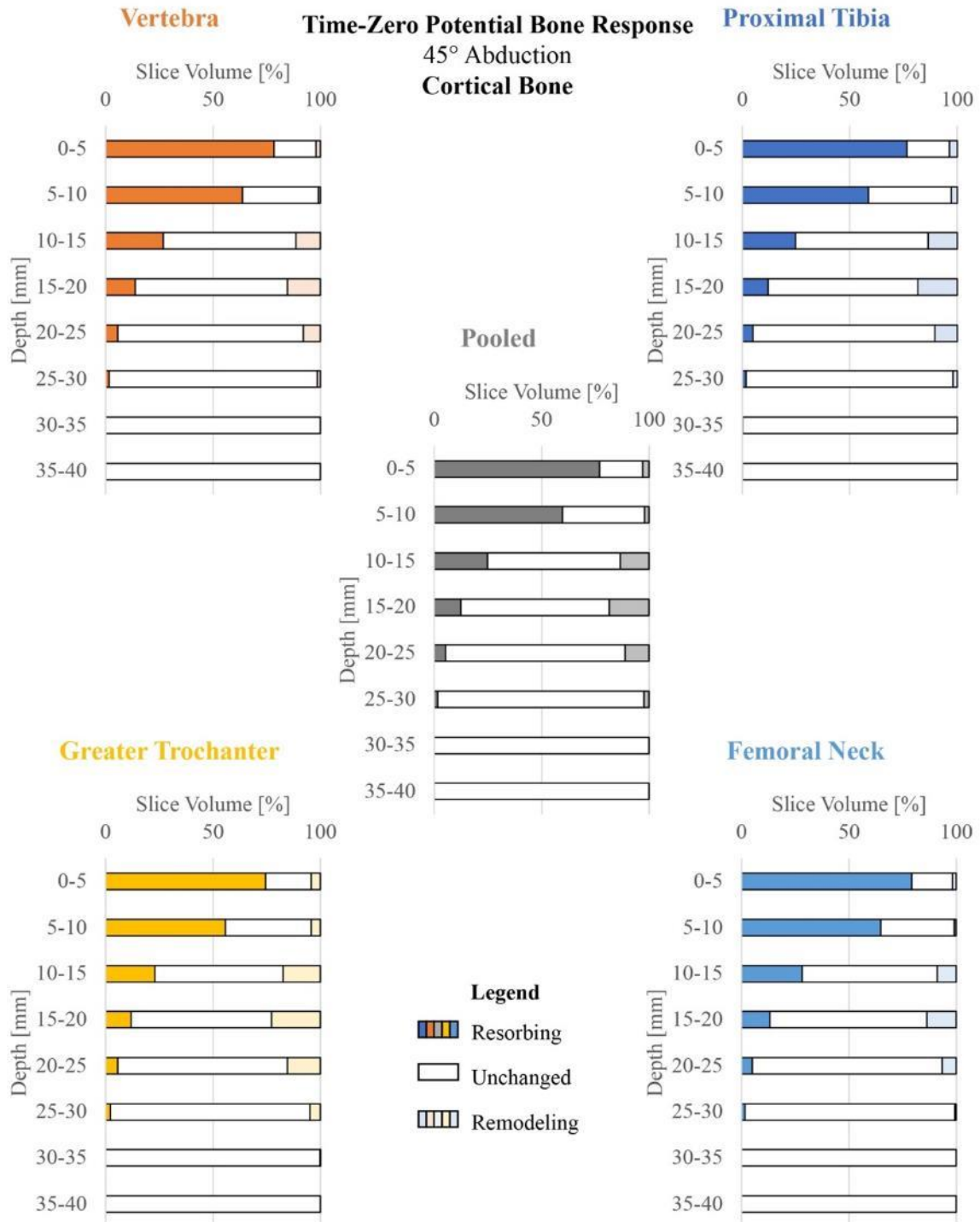


Figure 4.8: Inhomogeneous Anatomic-Site Potential Time-Zero Bone Response Results for Cortical Bone (45°)

Potential cortical bone response for 45° of abduction for the inhomogeneous anatomic-site comparison.

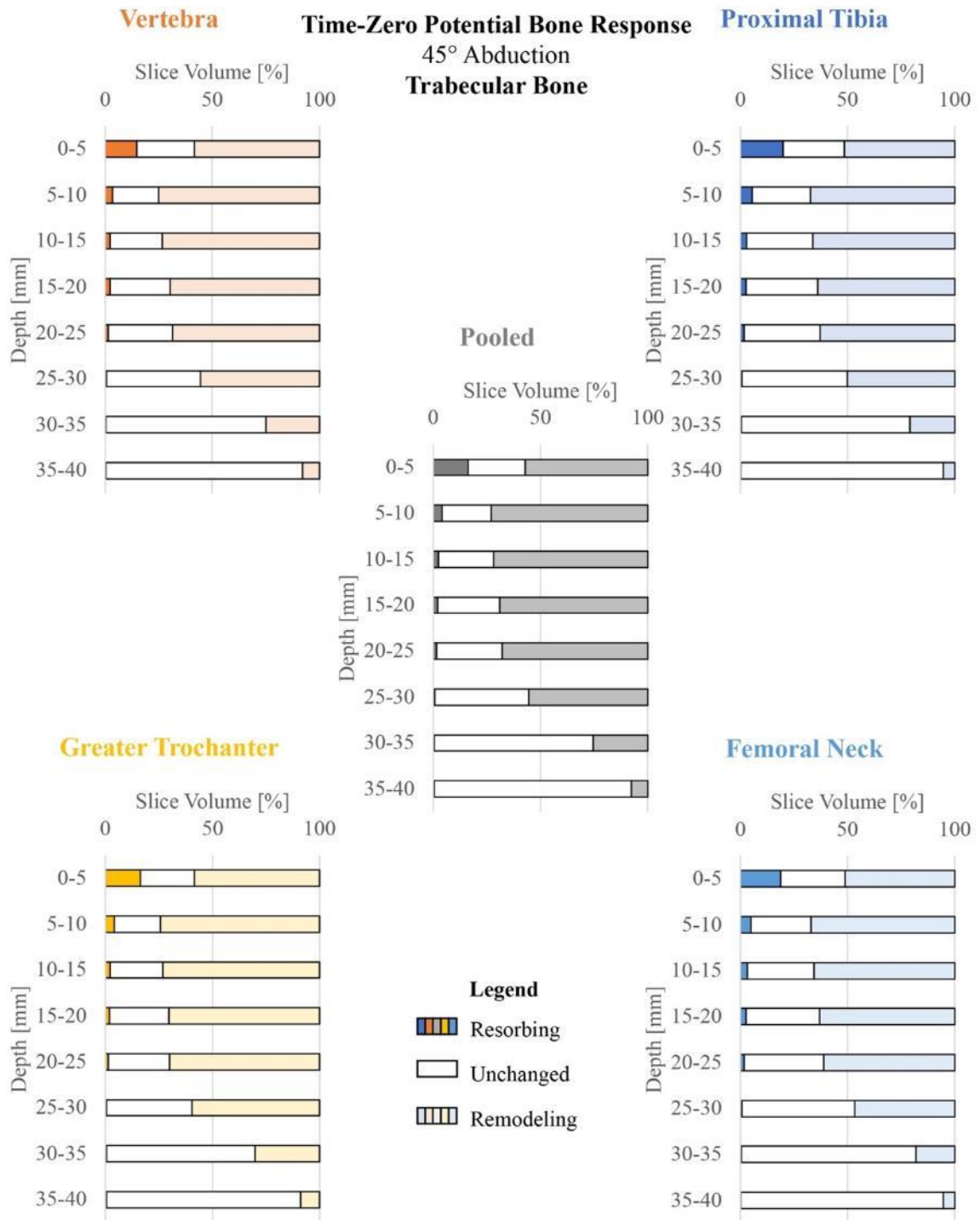


Figure 4.9: Inhomogeneous Anatomic-Site Potential Time-Zero Bone Response Results for Cortical Bone (75°)

Potential cortical bone response for 75° of abduction for the inhomogeneous anatomic-site comparison.

regionally). The overall FE population SDs were 4.8 and 4.7-times greater for 45° and 75°, respectively (45°: $6.0 \pm 0.1\%$; 75°: $5.4 \pm 0.2\%$); ranging from 0.0% to 10.5% between slices. Additionally, the cortical resorbing potential had SDs of $9.9 \pm 2.4\%$ (7.9-times greater) and $3.6 \pm 1.0\%$ (3.2-times greater), for 45° and 75°, respectively; that arose due to switching the trabecular stiffness from a pooled inhomogeneous model to a homogeneous one. Regionally, the homogeneous-inhomogeneous SDs ranged from 0.0% to 23.4% on average (Figures 4.10 and 4.11).

Similarly, the cortical bone's unchanged bone response was relatively constant despite changes to the trabecular stiffness based on anatomic-site selection (Figures 4.8 and 4.9). Overall anatomic-site SDs were $1.9 \pm 0.4\%$ for both 45° and 75° (ranging from 0.0% to 3.6% regionally; Table 4.2). In comparison, the FE population SDs ranged from 0.0% to 12.3% regionally, which were 3.2 and 3.4-times greater than the anatomic-site SDs overall, for 45° ($6.1 \pm 0.2\%$) and 75° ($6.2 \pm 0.2\%$), respectively. Similarly, the homogeneous-inhomogeneous SDs were found to be 4.0 and 5.4-times greater than the inhomogeneous anatomic-site SDs for 45° ($7.6 \pm 2.1\%$) and 75° ($10.0 \pm 2.4\%$), respectively (ranging from 0.0% to 23.8% regionally; Figures 4.10 and 4.11).

Finally, the cortical bone's remodeling potential also demonstrated minor variation attributable to changing the inhomogeneous trabecular stiffness' anatomic-site (Figures 4.8 and 4.9). The anatomic-site SDs ranged from 0.0% to 3.4% by slice depth (Table 4.2); with mean values of $1.8 \pm 0.4\%$ for both 45° and 75°. The overall SDs due to FE population variance were $3.0 \pm 0.3\%$ (1.7-times greater) and $3.8 \pm 0.3\%$ (2.1-times greater) for 45° and 75°, respectively (ranging from 0.0% to 8.6% regionally). Moreover, the homogeneous-inhomogeneous SDs were greater still, with overall values of $3.2 \pm 0.9\%$ for 45° (1.8-times greater), and $7.6 \pm 2.0\%$ for 75° (4.2-times greater). The homogeneous-inhomogeneous SDs ranged from 0.0% to 17.4% for cortical remodeling potential (Figures 4.10 and 4.11).

4.3.3.2 Trabecular Region

The trabecular bone's resorbing potential remained relatively unchanged when the inhomogeneous trabecular stiffness relationship was varied by anatomic-site

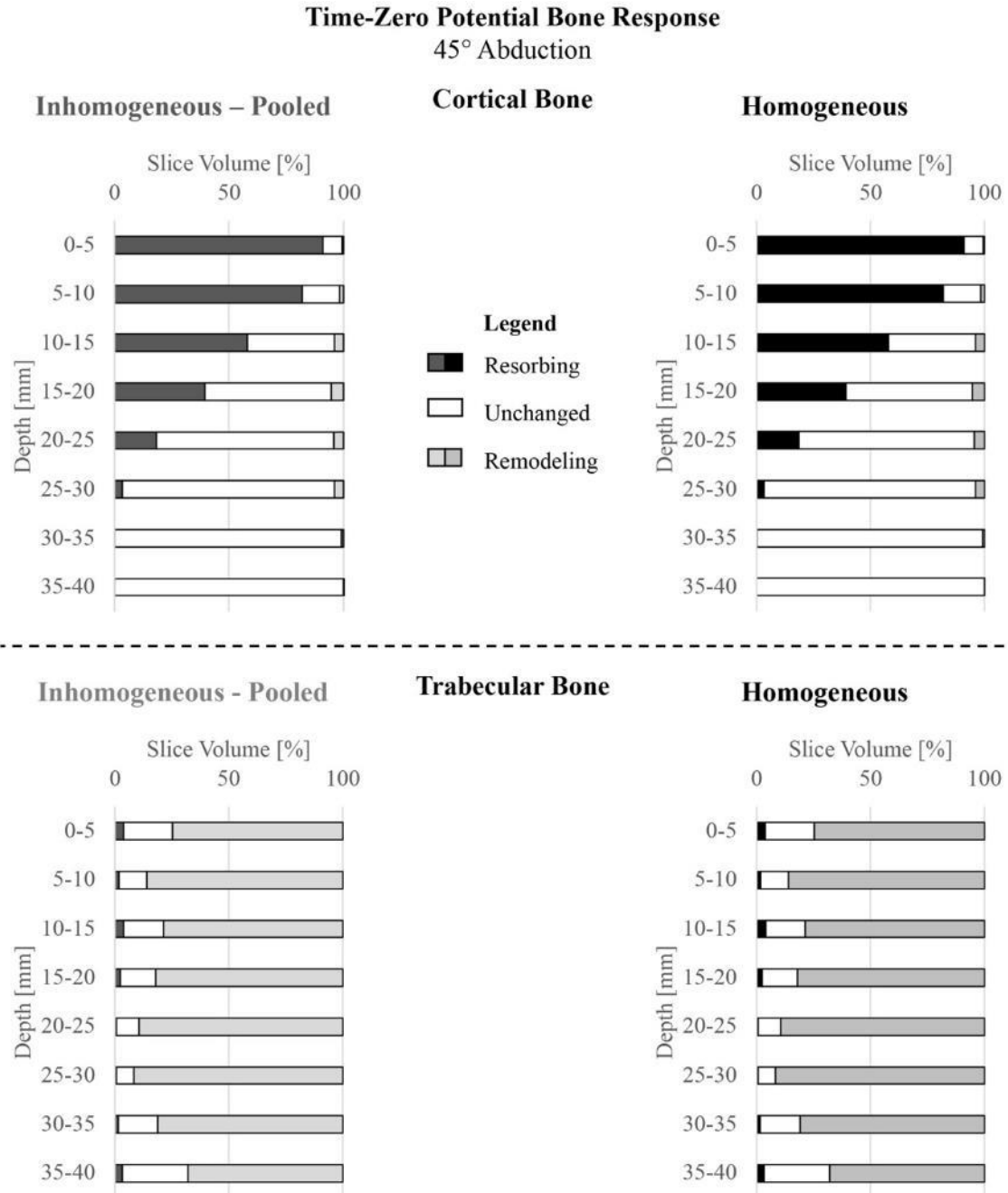


Figure 4.10: Homogeneous-Inhomogeneous Potential Time-Zero Bone Response Results for Cortical Bone (45°)

Potential cortical bone response for 45° of abduction for the inhomogeneous anatomic-site comparison.

Time-Zero Potential Bone Response
75° Abduction

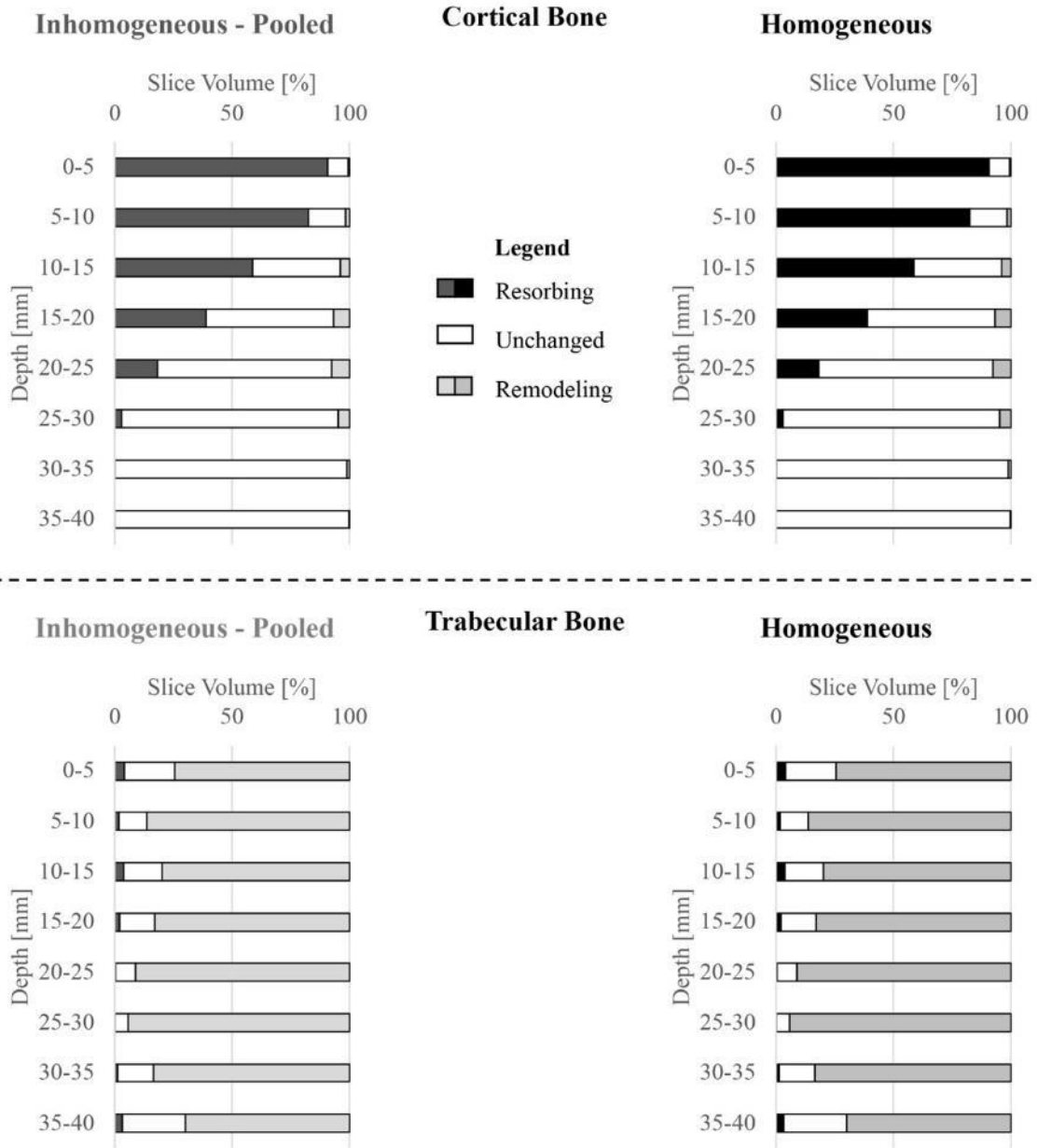


Figure 4.11: Homogeneous-Inhomogeneous Potential Time-Zero Bone Response Results for Cortical Bone (75°)

Potential cortical bone response for 75° of abduction for the inhomogeneous anatomic-site comparison.

(Figures 4.12 and 4.13). The SDs for anatomic-site changes were $0.7\pm 0.2\%$ and $0.6\pm 0.2\%$ for 45° and 75° , respectively (ranging from 0.1% to 2.5% regionally; Table 4.3). The FE population SDs were also low, though greater than the anatomic-site SDs, with mean values of $2.6\pm 0.1\%$ for 45° (3.9-times greater), and $2.2\pm 0.1\%$ for 75° (3.5-times greater). Regionally, the FE population SDs ranged from 0.4% to 6.7%. Similarly, the homogeneous-inhomogeneous SDs ranged from 0.3% to 9.2% between slices (Figures 4.10 and 4.11); with overall values that were 3.9-times greater than the inhomogeneous anatomic-site SDs, for both 45° ($2.6\pm 0.9\%$) and 75° ($2.5\pm 0.8\%$).

The trabecular bone's unchanged potential was also only minorly affected by the trabecular bone's anatomic-site stiffness relationship (Figures 4.12 and 4.13). The corresponding SDs were $3.7\pm 0.5\%$ for 45° , and $3.6\pm 0.5\%$ for 75° (ranging from 2.0% to 5.5% regionally; Table 4.3). In comparison, the FE population SDs were 2.6-times greater for both 45° and 75° , with overall values of $9.5\pm 0.4\%$ and $9.2\pm 0.4\%$, respectively (ranging from 6.9% to 14.5% regionally). The SDs attributable to homogeneous-inhomogeneous changes in trabecular stiffness were the largest (Table 4.3), with means of $19.5\pm 2.7\%$ for 45° (5.2-times greater), and $19.7\pm 2.6\%$ for 75° (5.5-times greater). Furthermore, the homogeneous-inhomogeneous SDs ranged from 6.2% to 45.7% across the slices investigated (Figures 4.10 and 4.11).

Finally, similar trends presented in the trabecular bone's remodeling potential, with low SDs attributable to changes in the trabecular stiffness' anatomic-site relationship (Figures 4.12 and 4.13). Specifically, anatomic-site SDs ranged from 2.3% to 5.5% between slices; with overall values of $4.2\pm 0.5\%$ and $4.1\pm 0.5\%$ for 45° and 75° , respectively (Table 4.3). The FE population SDs were 2.6-times greater for both 45° ($11.1\pm 0.4\%$), and 75° ($10.7\pm 0.5\%$); and ranged from 7.1% to 14.4% regionally. The homogeneous-inhomogeneous SDs were also greater than the anatomic-site deviations, with overall values of $20.3\pm 3.1\%$ for 45° (4.8-times greater), and $20.7\pm 3.1\%$ for 75° (5.1-times greater). These values ranged from 7.1% to 43.7% between slices. Interestingly, the homogeneous-inhomogeneous SDs for the trabecular bone's unchanged potential and remodeling potential exhibited the same SD increase in slices 4-8 (20-40mm deep) as were exhibited in the trabecular stress change outcome variable.

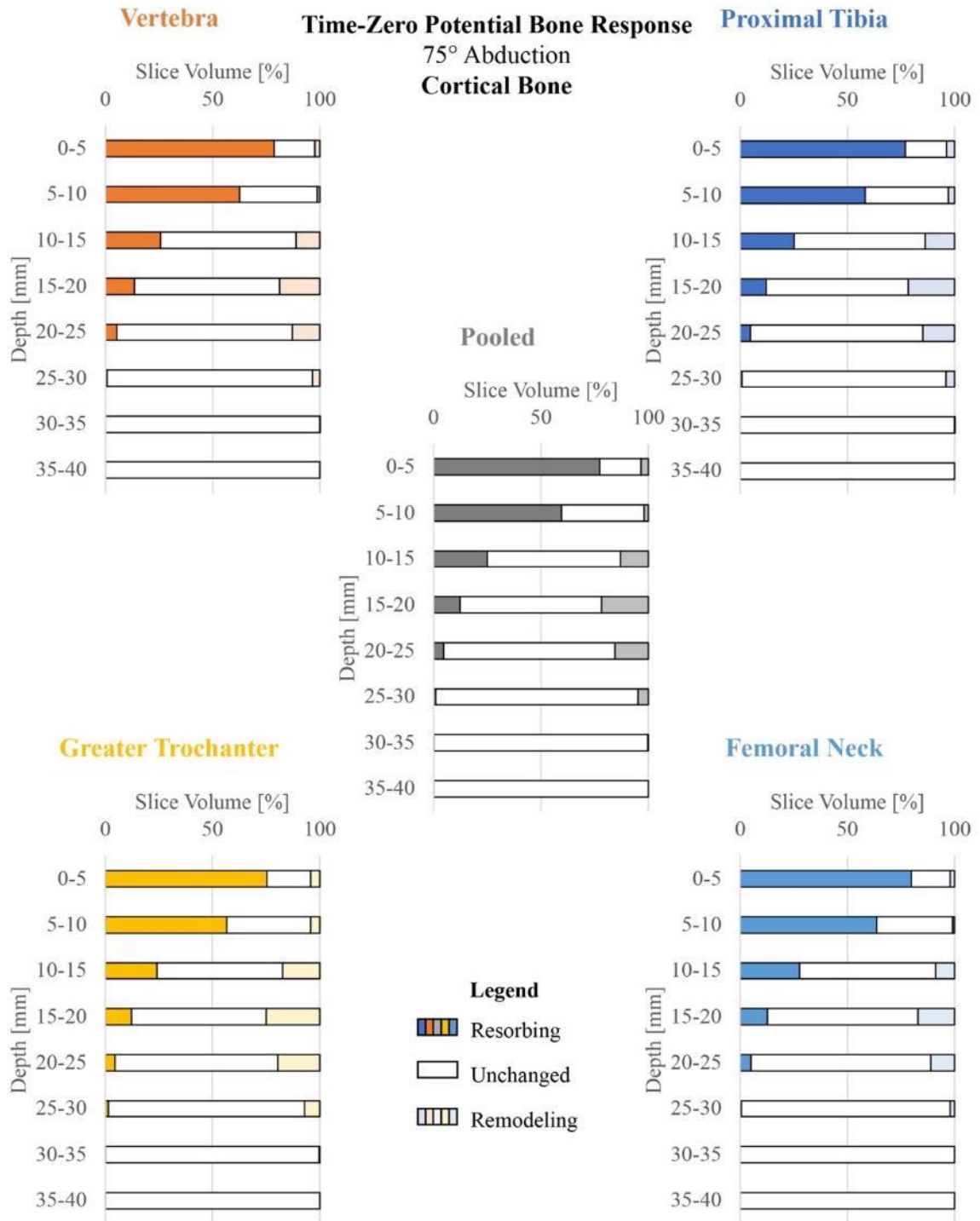


Figure 4.12: Inhomogeneous Anatomic-Site Potential Time-Zero Bone Response Results for Trabecular Bone (45°)

Potential cortical bone response for 45° of abduction for the inhomogeneous anatomic-site comparison.

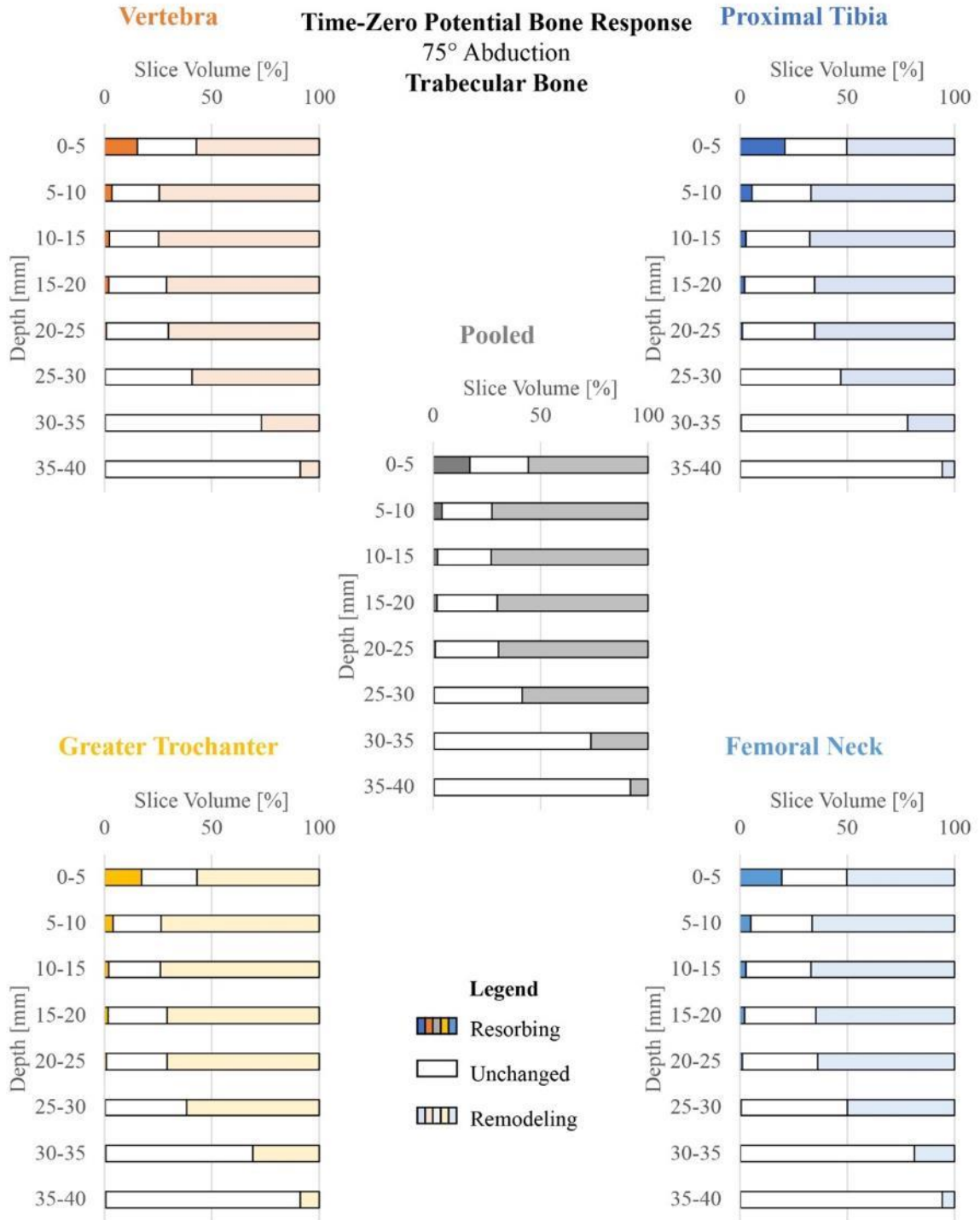


Figure 4.13: Inhomogeneous Anatomic-Site Potential Time-Zero Bone Response Results for Trabecular Bone (75°)

Potential cortical bone response for 75° of abduction for the inhomogeneous anatomic-site comparison.

Table 4.3: Standard deviations attributed to inhomogeneous anatomic-site, FE population and homogeneous-inhomogeneous differences in the potential bone response outcome measure for trabecular bone; broken down regionally according to slice depth.

Inhomogeneous Anatomic-Site Comparison						
Slice	45° Abduction			75° Abduction		
Depth [mm]	Resorbing Mean(SD)	Unchanged Mean(SD)	Remodeling Mean(SD)	Resorbing Mean(SD)	Unchanged Mean(SD)	Remodeling Mean(SD)
0-5	2.4(0.7)	2.2(0.8)	4.3(0.9)	2.5(0.8)	2.0(0.9)	4.1(0.9)
5-10	1.0(0.5)	3.3(1.3)	4.2(1.6)	1.0(0.6)	3.4(1.5)	4.3(2.0)
10-15	0.7(0.5)	3.6(1.0)	4.1(1.3)	0.5(0.4)	3.5(1.0)	4.0(1.4)
15-20	0.4(0.5)	3.5(1.0)	3.8(1.0)	0.3(0.3)	3.3(0.8)	3.6(0.9)
20-25	0.3(0.5)	4.0(1.0)	4.3(1.0)	0.2(0.3)	3.6(0.9)	3.7(0.9)
25-30	0.2(0.2)	5.5(1.0)	5.5(1.2)	0.1(0.1)	5.2(0.9)	5.2(1.0)
30-35	0.2(0.2)	5.2(2.5)	5.1(2.6)	0.1(0.1)	5.2(2.6)	5.1(2.6)
35-40	0.2(0.1)	2.6(1.9)	2.4(2.0)	0.2(0.2)	2.5(1.8)	2.3(1.8)
Overall:	0.7(0.2)	3.7(0.5)	4.2(0.5)	0.6(0.2)	3.6(0.5)	4.1(0.5)

FE Population Comparison						
Slice	45° Abduction			75° Abduction		
Depth [mm]	Resorbing Mean(SD)	Unchanged Mean(SD)	Remodeling Mean(SD)	Resorbing Mean(SD)	Unchanged Mean(SD)	Remodeling Mean(SD)
0-5	6.4(0.6)	7.4(0.6)	13.0(1.1)	6.7(0.7)	7.9(0.5)	13.6(1.0)
5-10	2.7(0.5)	9.4(1.2)	11.6(1.6)	2.8(0.6)	9.9(1.4)	12.2(1.9)
10-15	2.8(0.4)	8.6(0.7)	10.6(1.1)	2.5(0.4)	8.4(0.7)	10.5(1.1)
15-20	3.8(0.4)	10.1(0.5)	12.2(0.7)	2.6(0.3)	9.7(0.6)	11.3(0.8)
20-25	3.1(0.5)	8.2(1.0)	9.1(1.1)	1.5(0.3)	6.9(1.0)	7.4(1.1)
25-30	0.8(0.2)	11.3(0.4)	11.1(0.4)	0.3(0.1)	9.0(0.5)	8.9(0.5)
30-35	0.5(0.0)	14.1(1.8)	14.0(1.9)	0.5(0.1)	14.5(1.8)	14.4(1.8)
35-40	0.4(0.1)	7.1(1.3)	7.1(1.3)	0.5(0.2)	7.4(1.5)	7.4(1.5)
Overall:	2.6(0.1)	9.5(0.4)	11.1(0.4)	2.2(0.1)	9.2(0.4)	10.7(0.5)

Homogeneous-Inhomogeneous Comparison						
Slice	45° Abduction			75° Abduction		
Depth [mm]	Resorbing Mean(SD)	Unchanged Mean(SD)	Remodeling Mean(SD)	Resorbing Mean(SD)	Unchanged Mean(SD)	Remodeling Mean(SD)
0-5	8.8(5.1)	6.9(5.9)	13.4(11.9)	9.2(5.1)	7.3(6.0)	14.0(12.2)
5-10	2.2(2.2)	8.2(8.0)	10.0(10.1)	2.4(2.2)	9.0(8.2)	10.9(10.4)
10-15	3.1(2.1)	6.2(6.8)	7.1(7.4)	2.9(1.5)	6.2(6.7)	7.4(7.5)
15-20	1.7(2.4)	9.5(5.3)	9.3(6.0)	1.4(1.6)	9.1(5.7)	9.0(6.8)
20-25	1.0(1.7)	14.6(4.6)	15.2(4.3)	0.6(0.8)	14.8(4.9)	15.2(4.9)
25-30	0.4(0.3)	25.6(8.1)	25.6(7.8)	0.3(0.2)	25.2(6.5)	25.3(6.4)
30-35	1.1(0.9)	40.1(10.5)	39.3(10.3)	0.9(0.6)	40.7(10.5)	40.2(10.4)
35-40	2.2(1.7)	44.7(9.2)	42.6(9.2)	2.0(1.5)	45.7(9.0)	43.7(9.1)
Overall:	2.6(0.9)	19.5(2.7)	20.3(3.1)	2.5(0.8)	19.7(2.6)	20.7(3.1)

4.4 Discussion

Overall, the FE outcomes under investigation suggest that stemless humeral arthroplasty results in stress changes to both cortical and trabecular bone. These bone stress changes are greatest proximally beneath the humeral head resection plane and decrease moving further down the cortex/trabecular-canal. The SED-based bone response classification suggests that the cortical bone's resorbing potential and the trabecular bone's remodeling potential follow the same trends. These trends are largely observed, regardless of the trabecular stiffness relationship applied to the model; however, greater differences in mean values arose between homogeneous and inhomogeneous models, than between inhomogeneous models that were derived from different anatomic-sites.

The SDs attributable to changing the trabecular bone's inhomogeneous stiffness based on anatomic-site were less than those arising within the FE population, or from changing the trabecular stiffness from a pooled inhomogeneous relationship to a homogeneous one, regardless of the FE outcome measure. These findings suggest that changing the trabecular stiffness induces less variation in the outcomes investigated than would normally be found within the present population of FE specimens, provided that the trabecular-canal is modelled as inhomogeneous, not homogeneous. This supports the previous work by Kabel *et al*, who suggested that, while anisotropy may not be necessary for trabecular modelling, inhomogeneity of the trabecular-canal should be accounted for [23]. These findings further suggest that FE outcome variation remains largely dominated by population differences despite fluctuations in the trabecular bone's inhomogeneous modelling based on anatomic regression-site selection.

Overall, the cortical bone outcomes were less susceptible to variance than the trabecular bone outcomes, likely because the cortical stiffness was constant, while the trabecular stiffness varied. Changes in FE population SDs seemed to increase and decrease along with the inhomogeneous anatomic-site SDs; however, the homogeneous-inhomogeneous SDs exhibited some regional differences. Specifically, the outcomes pertaining to trabecular stress change, and trabecular unchanged and remodeling potential both presented with peaks in homogeneous-inhomogeneous differences in slices 4-8 (20-40mm beneath the resection). These differences between homogeneous and

inhomogeneous models are likely due to the morphology of the proximal humerus. It has been suggested that the apparent density of the trabecular-canal diminishes greatly beyond 20mm beneath the humeral head resection [43]. Accordingly, the homogeneous and inhomogeneous trabecular stiffness diverge in this region, with the inhomogeneous stiffness diminishing along with density, while the homogeneous stiffness remains constant. In response, the homogeneous trabecular model results predict greater changes in trabecular stress (Figures 4.6 and 4.7), and more trabecular volume within the expected remodeling classification (Figures 4.10 and 4.11). This suggests that inhomogeneity is an important factor that can influence FE outcomes.

At the onset of this assessment, it was thought that the bone response and stress change outcome measures may be less susceptible to variances attributable to anatomic-site selection, as both outcomes utilize the identical mesh between the intact and reconstructed bone models (which was subject to the same fluctuations in trabecular stiffness) to represent results relative to the intact state. This seems to agree with the present findings. Interestingly, the implant-bone contact outcome presented with low SDs attributable to inhomogeneous anatomic-site selection. This is likely because of the direct role that the implant plays in implant-bone contact. The difference between implant and trabecular-canal stiffness is far larger than the fluctuation in trabecular stiffness arising from changing the inhomogeneous anatomic-site stiffness relationship. This implant-bone stiffness difference is thought to overshadow the variations in implant-bone contact that take place because of changing the inhomogeneous trabecular stiffness. It is possible that trabecular model anatomic-site selection may have a more profound effect on implant-bone contact if the implant's stiffness were diminished and approached that of the trabecular structure.

Returning to the specific hypotheses of the present investigation; it was found that SDs attributable to inhomogeneous anatomic-site stiffness relationship selection were generally below the hypothesized 10% SD threshold, except for the trabecular stress change from 5-15mm beneath the humeral resection plane during 45° abduction. Despite the mean anatomic-site SDs of 10.2% and 10.3% in this region, all anatomic-site attributable SDs were consistently less than those arising because of FE population

differences and those of homogenous-inhomogeneous model differences. Accordingly, the hypotheses are accepted.

It is important to note that this investigation was not without limitations. Specifically, while the FE population size of 8 specimens is large compared to most FE investigations in the literature (which typically include only 1 or 2 specimens), it is expected that as the number of specimens grows, the corresponding FE population SDs would decrease. Diminishing the FE population differences could in turn result in the inhomogeneous anatomic-site changes becoming more apparent in the outcome measures. One must also consider that the strength of a FE investigation is not its ability to perfectly simulate reality, but rather, to provide insight into the trends of strain-based outcomes across complicated geometries. With this in mind, while the magnitude of the results in the present investigation did fluctuate based on the trabecular stiffness model employed, the trends in potential bone response, stress changes and implant-bone contact remained relatively constant between inhomogeneous trabecular stiffness models.

4.5 Conclusions

In conclusion, these findings reaffirm the choice of inhomogeneous trabecular models over homogeneous models for the analysis of shoulder arthroplasty; and suggest that, without a trabecular density-modulus regression specific to the proximal humerus, the best choice for modeling trabecular bone may be to continue using a site-pooled inhomogeneous regression that is based on results from several anatomic sites throughout the body.

4.6 References

- [1] Reeves, J. M., Athwal, G. S., Johnson, J. A., and Langohr, G. D. G., 2018, "The Effect of Trabecular Modulus Anatomic Site Selection on FE Outcomes for Shoulder Arthroplasty," *J. Biomech. Eng.*, p. (In Submission).
- [2] Kluess, D., Souffrant, R., Mittelmeier, W., Wree, A., Schmitz, K. P., and Bader, R., 2009, "A convenient approach for finite-element-analyses of orthopaedic implants in bone contact: Modeling and experimental validation," *Comput.*

Methods Programs Biomed., **95**(1), pp. 23–30.

- [3] Razfar, N., Reeves, J. M., Langohr, D. G., Willing, R., Athwal, G. S., and Johnson, J. A., 2016, “Comparison of proximal humeral bone stresses between stemless, short stem, and standard stem length: a finite element analysis,” *J. Shoulder Elb. Surg.*, **25**(7), pp. 1076–83.
- [4] Couteau, B., Mansat, P., Estivalèzes, E., Darmana, R., Mansat, M., and Egan, J., 2001, “Finite element analysis of the mechanical behavior of a scapula implanted with a glenoid prosthesis,” *Clin. Biomech.*, **16**(7), pp. 566–575.
- [5] Harrigan, T. P., and Harris, W. H., 1991, “A three-dimensional non-linear finite element study of the effect of cement-prosthesis debonding in cemented femoral total hip components,” *J. Biomech.*, **24**(11), pp. 1047–1058.
- [6] Huiskes, R., Weinans, H., and van Rietbergen, B., 1992, “The relationship between stress shielding and bone resorption around total hip stems and the effects of flexible materials,” *Clin. Orthop. Relat. Res.*, pp. 124–134.
- [7] Asgari, S. A., Hamouda, A. M. S., Mansor, S. B., Singh, H., and Mahdi, E., 2004, “Finite element modeling of a generic stemless hip implant design in comparison with conventional hip implants,” **40**, pp. 2027–2047.
- [8] Engh, C., and McGovern, T., 1992, “A quantitative evaluation of periprosthetic bone-remodeling after cementless total hip arthroplasty,” *J Bone Joint Surg*, **74**(7), pp.1009–1020.
- [9] Lerch, M., Kurtz, A., Stukenborg-Colsman, C., Nolte, I., Weigel, N., Bouguecha, A., and Behrens, B. A., 2012, “Bone remodeling after total hip arthroplasty with a short stemmed metaphyseal loading implant: Finite element analysis validated by a prospective DEXA investigation,” *J. Orthop. Res.*, **30**(11), pp. 1822–1829.
- [10] Abdul-Kadir, M. R., Hansen, U., Klabunde, R., Lucas, D., and Amis, A., 2008, “Finite element modelling of primary hip stem stability: The effect of interference fit,” *J. Biomech.*, **41**, pp. 587–594.

- [11] Yosibash, Z., Trabelsi, N., and Milgrom, C., 2007, “Reliable simulations of the human proximal femur by high-order finite element analysis validated by experimental observations,” *J. Biomech.*, **40**(16), pp. 3688–3699.
- [12] Kheirollahi, H., and Luo, Y., 2015, “Assessment of Hip Fracture Risk Using Cross-Section Strain Energy Determined by QCT-Based Finite Element Modeling,” *Biomed Res. Int.*, p. e413839.
- [13] Reimeringer, M., Nuño, N., Desmarais-Trépanier, C., Lavigne, M., and Vendittoli, P. a., 2012, “The influence of uncemented femoral stem length and design on its primary stability: a finite element analysis,” *Comput. Methods Biomech. Biomed. Engin.*, (June 2015), pp. 1–11.
- [14] Willing, R. T., Lalone, E. a., Shannon, H., Johnson, J. a., and King, G. J. W., 2013, “Validation of a finite element model of the human elbow for determining cartilage contact mechanics,” *J. Biomech.*, **46**(10), pp. 1767–1771.
- [15] Neuert, M. A. C., Austman, R. L., and Dunning, C. E., 2013, “The comparison of density-elastic modulus equations for the distal ulna at multiple forearm positions: A finite element study,” *Acta Bioeng. Biomech.*, **15**(3), pp. 37–43.
- [16] Neuert, M. A. C., and Dunning, C. E., 2013, “Determination of remodeling parameters for a strain-adaptive finite element model of the distal ulna,” *Proc. Inst. Mech. Eng. Part H - J. Eng. Med.*, **227**(9), pp. 994–1001.
- [17] Austman, R. L., Milner, J. S., Holdsworth, D. W., and Dunning, C. E., 2008, “The effect of the density-modulus relationship selected to apply material properties in a finite element model of long bone,” *J. Biomech.*, **41**, pp. 3171–3176.
- [18] Willing, R., King, G. J. W., and Johnson, J. a, 2012, “The effect of implant design of linked total elbow arthroplasty on stability and stress: a finite element analysis,” *Comput. Methods Biomech. Biomed. Engin.*, **5842**(1248), p. 2012.
- [19] Dahan, G., Trabelsi, N., Safran, O., and Yosibash, Z., 2016, “Verified and validated finite element analyses of humeri,” *J. Biomech.*, **49**(7), pp. 1094–1102.

- [20] Pomwenger, W., Entacher, K., Resch, H., and Schuller-Götzburg, P., 2014, “Need for CT-based bone density modelling in finite element analysis of a shoulder arthroplasty revealed through a novel method for result analysis,” *Biomed. Eng. / Biomed. Tech.*, **59**(5), pp. 421–430.
- [21] Bayraktar, H. H., Morgan, E. F., Niebur, G. L., Morris, G. E., Wong, E. K., and Keaveny, T. M., 2004, “Comparison of the elastic and yield properties of human femoral trabecular and cortical bone tissue,” *J. Biomech.*, **37**(1), pp. 27–35.
- [22] Rho, J. Y., Ashman, R. B., and Turner, C. H., 1993, “Young’s modulus of trabecular and cortical bone material: Ultrasonic and microtensile measurements,” *J. Biomech.*, **26**(2), pp. 111–119.
- [23] Kabel, J., Van Rietbergen, B., Dalstra, M., Odgaard, A., and Huiskes, R., 1999, “The role of an effective isotropic tissue modulus in the elastic properties of cancellous bone,” *J. Biomech.*, **32**(7), pp. 673–680.
- [24] Morgan, E. F., Bayraktar, H. H., and Keaveny, T. M., 2003, “Trabecular bone modulus-density relationships depend on anatomic site,” *J. Biomech.*, **36**, pp. 897–904.
- [25] Vijayakumar, V., and Quenneville, C. E., 2016, “Quantifying the regional variations in the mechanical properties of cancellous bone of the tibia using indentation testing and quantitative computed tomographic imaging,” *Proc. Inst. Mech. Eng. H.*, **230**(6), pp. 588–93.
- [26] Austman, R. L., Milner, J. S., Holdsworth, D. W., and Dunning, C. E., 2009, “Development of a customized density-modulus relationship for use in subject-specific finite element models of the ulna,” *Proc. Inst. Mech. Eng. H.*, **223**(6), pp. 787–794.
- [27] Schileo, E., Taddei, F., Malandrino, A., Cristofolini, L., and Viceconti, M., 2007, “Subject-specific finite element models can accurately predict strain levels in long bones,” *J. Biomech.*, **40**(13), pp. 2982–2989.

- [28] Peng, L., Bai, J., Zeng, X., and Zhou, Y., 2006, "Comparison of isotropic and orthotropic material property assignments on femoral finite element models under two loading conditions," *Med. Eng. Phys.*, **28**(3), pp. 227–233.
- [29] Knowles, N. K., Reeves, J. M., and Ferreira, L. M., 2016, "Quantitative Computed Tomography (QCT) derived Bone Mineral Density (BMD) in finite element studies: a review of the literature," *J. Exp. Orthop.*, **3**(36), pp. 1–16.
- [30] Taylor, W. R., Roland, E., Ploeg, H., Hertig, D., Klabunde, R., Warner, M. D., Hobatho, M. C., Rakotomanana, L., and Clift, S. E., 2002, "Determination of orthotropic bone elastic constants using FEA and modal analysis," *J. Biomech.*, **35**(6), pp. 767–773.
- [31] Morgan, E. F., and Keaveny, T. M., 2001, "Dependence of yield strain of human trabecular bone on anatomic site," *J. Biomech.*, **34**(5), pp. 569–577.
- [32] Eberle, S., Göttinger, M., and Augat, P., 2013, "Individual density-elasticity relationships improve accuracy of subject-specific finite element models of human femurs," *J. Biomech.*, **46**(13), pp. 2152–2157.
- [33] Cong, A., Buijs, J. O. Den, and Dragomir-Daescu, D., 2011, "In situ parameter identification of optimal density-elastic modulus relationships in subject-specific finite element models of the proximal femur," *Med. Eng. Phys.*, **33**(2), pp. 164–173.
- [34] Kuiper, J. H., and Huiskes, R., 1996, "Friction and stem stiffness affect dynamic interface motion in total hip replacement," *J. Orthop. Res.*, **14**(1), pp. 36–43.
- [35] Lee, Y. T., and Welsch, G., 1990, "Young's Modulus and Damping of Ti-6Al-4V Alloy as a Function of Heat Treatment and Oxygen Concentration," *Mater. Sci. Eng.*, **128**, pp. 128–77.
- [36] Grant, J. A., Bishop, N. E., Go, N., Sprecher, C., Honl, M., and Morlock, M. M., 2007, "Artificial composite bone as a model of human trabecular bone : The implant – bone interface," **40**, pp. 1158–1164.

- [37] Bergmann, G., Graichen, F., Bender, A., Kaab, M., Rohlmann, A., and Westerhoff, P., 2007, “In vivo glenohumeral contact forces-Measurements in the first patient 7 months postoperatively,” *J. Biomech.*, **40**(10), pp. 2139–2149.
- [38] Huiskes, R., Weinans, H., Grootenboer, H. J., Dalstra, M., Fudala, B., and Slooff, T. J., 1987, “Adaptive Bone-Remodeling Theory Applied to Prosthetic-Design Analysis,” *J. Biomech.*, **20**(11), pp. 1135–1150.
- [39] Huiskes, R., Ruimerman, R., Lenthe, G. H. Van, and Janssen, J. D., 2000, “Effects of mechanical forces on maintenance and adaptation of form in trabecular bone,” *Nature*, **405**(June), pp. 704–706.
- [40] Weinans, H., Huiskes, R., and Grootenboer, H. J., 1992, “The behavior of adaptive bone-remodeling simulation models,” *J. Biomech.*, **25**(12), pp. 1425–1441.
- [41] Carter, D. R., Fyhrie, D. P., and Whalen, R. T., 1987, “Trabecular bone density and loading history: Regulation of connective tissue biology by mechanical energy,” *J. Biomech.*, **20**(8).
- [42] Johnson, J. A., Rath, D. A., Dunning, C. E., Roth, S. E., and King, G. J. W., 2000, “Simulation of elbow and forearm motion in vitro using a load controlled testing apparatus,” *J. Biomech.*, **33**(5), pp. 635–639.
- [43] Reeves, J. M., Athwal, G. S., and Johnson, J. A., 2017, “An Assessment of Proximal Humerus Density with Reference to Stemless Implants,” *J. Shoulder Elb. Surg.*, **(In Press)**.

Chapter 5

The Effect of Stemless Humeral Component Fixation-Feature Design on Bone Stress and Strain Response

A version of this chapter has been accepted for publication [1].

5.1 Introduction

Since Neer first popularized shoulder arthroplasty in the 1950's [2], there have been several iterations of humeral implant design [3–8]. The focus of these iterations has been to improve the longevity of the reconstructed joint by multiple factors, one of which is reducing stress shielding in periprosthetic bone. Radiographic studies have reported regional full thickness cortical resorption with a prevalence between 4% to 18% in the proximal humerus, [9–11] which is attributed to stress shielding.

Accordingly, implant manufacturers have reduced the length of the humeral stem to maintain as much natural bone tissue as possible. In 2004, the first humeral implant with an ultra-short fixation feature, the Total Evolutive Shoulder System (TESS; Biomet Inc, Warsaw, IN, USA), was introduced [4,12]. Since then, several manufacturers have introduced similar, “stemless”, canal-sparing implants [4,5,8,12–15]; all of which seek fixation in the metaphysis of the proximal humerus (Section 1.2.4). The fixation features of these canal-sparing stemless implants vary from simple pegs to elaborate branched structures. To date, stemless shoulder implants have performed well in the *in-vivo* studies undertaken, demonstrating similar outcomes to stemmed implants, but with less operative time and blood loss [12–14,16–22].

The computer based Finite Element (FE) method (Section 1.4.2) has gained popularity in orthopaedics for its ability to estimate stress and strain changes in bone following joint replacement [5,23–29]. Specifically, strain adaptive FE models estimate changes in bone density using the amount of energy stored within bone elements [25,30–32]. These models approximate the bone's resorbing and remodeling response by measuring changes in Strain Energy Density (SED) in each element to assess if the bone's local energy

drops, or exceeds, a specified threshold. No studies to date have applied these methods to humeral reconstruction; however, for the ulna, the SED threshold has been estimated as a variance of 55% from the bone's natural SED [25].

Recently, several studies have undertaken morphological analyses of the proximal humerus in humeral head coordinate systems [33–35], making their findings of particular interest for the design of stemless implants. Specifically, based on the findings of Chapter 2, the density of the trabecular-canal dissipates approximately 20mm beneath the humeral resection plane [34], and there exists greater trabecular density peripherally [33,35]. Previous hip literature indicates that periprosthetic bone loss is inversely correlated to bone density at the time of surgery [36–39], suggesting that stemless implants may perform better with peripheral fixation features as oppose to central ones, but this has not been tested.

Accordingly, the purpose of the present investigation was to assess how variations in stemless humeral fixation feature geometry alter bone response following replacement (Objective 3, Section 1.6.1). To directly compare implant performance, the FE method was applied to humeral replacements with a variety of central, peripheral and boundary-crossing fixation features. It was hypothesized that implants that obtain peripheral fixation, and implants that follow the anatomic curvature of the humerus' trabecular-canal would produce more favorable bone responses compared to central and axisymmetric designs.

5.2 Materials and Methods

5.2.1 Bone Model Development:

Computed Tomography (CT) scans of five ($n = 5$) cadaver shoulders (Mean \pm SD age = 68 \pm 6 years) were obtained using a clinical CT scanner (GE 750HD Discovery Scanner; GE Healthcare, Chicago, IL). A calibration phantom consisting of a cortical bone surrogate (*i.e.*, SB3 model 450; GAMMEX, Middleton, WI) and distilled water, was placed alongside each arm to calibrate apparent density (g/cm^3) from CT attenuation (HU) [40]. Manual thresholding divided the proximal humerus into the cortical shell and trabecular-canal. An experienced shoulder surgeon (GSA) identified the humeral head

resection plane, along with superior-lateral and inferior-medial points of reference. These landmarks were used to construct a resection-relative coordinate system with axes directed: (A) from inferior-medial to superior-lateral along the humeral head resection plane, (B) anteriorly, and (C) perpendicular to the resection plane, positively oriented into the remaining bone [33,34] (Figure 5.1). The trabecular-canal was limited to a depth of 40mm, and the cortical diaphysis was resected 180mm from the superior-lateral resection point. This humeral division allowed for the development of ‘intact’ and ‘reconstructed’ bone models that could be identically meshed to permit element-to-element comparisons [5].

5.2.2 Implant Designs

Ten generic stemless shoulder implants were developed using SolidWorks CAD software (Dassault Systèmes Corp, Waltham, MA), each with a fixation feature having a depth of 20mm (Figure 5.2, additional details available in Appendix H). Implants were classified generally into one of three categories according to fixation feature location: (1) central, (2) peripheral, or (3) boundary-crossing. Central implants consisted of two pegged implants (*i.e.*, PegStraight and PegAnatomic), each with a diameter that varied with depth to remain half of the proximal humerus’ pooled canal-diameter [34]. PegStraight was axisymmetric and perpendicular to the implant’s humeral head back-side, while PegAnatomic followed the pooled coronal plane curvature reported in the literature [34]. The base peripheral implant (*i.e.*, Peripheral4x5S) had four rectangular pegs (width: 5mm, thickness: 3mm). Pegs were located 90° apart, and were centered at the medial, lateral, anterior and posterior sides of the implant on a circle that represented 75% of the pooled canal diameter [34] to ensure that they were predominantly peripheral. A variation of the Peripheral4x5S was formed by doubling the peg width to 10mm (*i.e.*, Peripheral4x10S). In addition, each peripheral implant also had an anatomically curved counterpart (*i.e.*, Perpiheral4x5A, and Peripheral4x10A) with pegs that followed the same curvature as PegAnatomic. The boundary-crossing implants consisted of straight 3mm thick, 17mm wide, flanged fixation features that tapered slightly inward at an angle of 14° to accommodate the tapering of the canal diameter. Either four (*i.e.*, QuadFlange) or six (*i.e.*, HexFlange) flanges protruded perpendicularly from the back-side of the implant

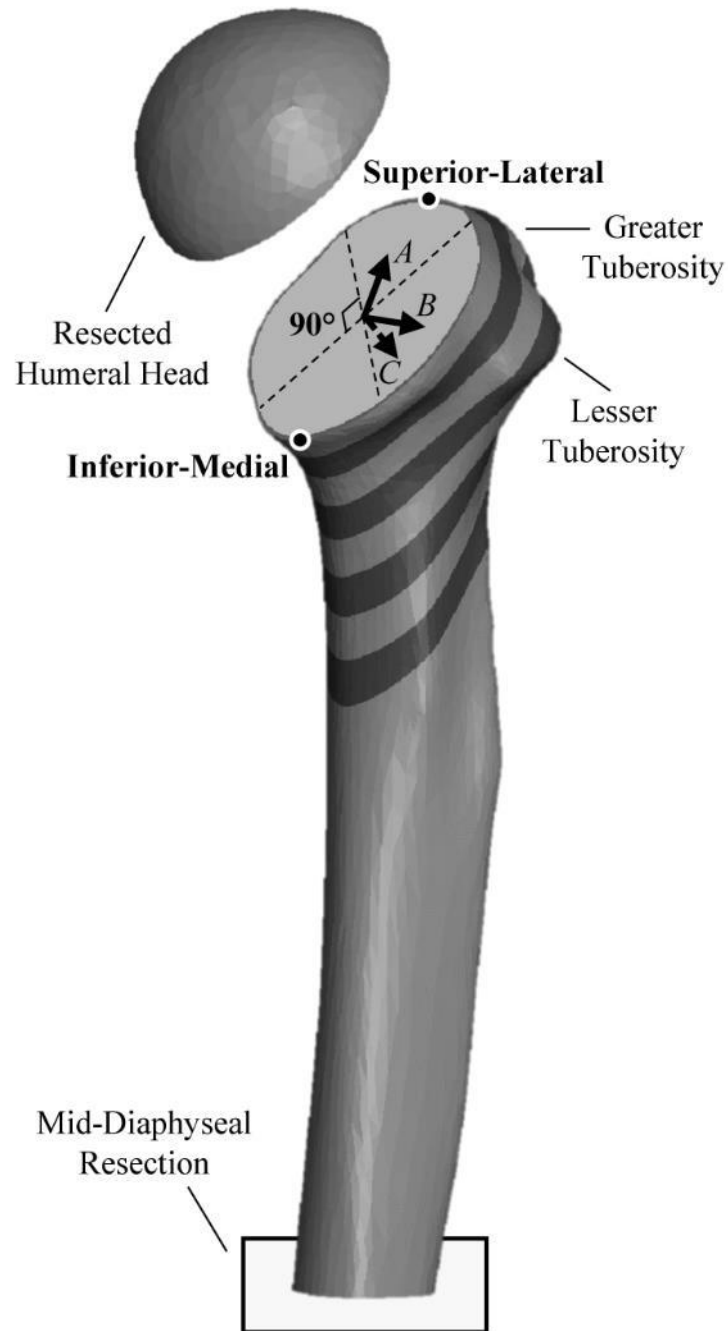


Figure 5.1: The Division and Coordinates of the Proximal Humerus

Depiction of the proximal humerus' coordinate system and sub-division into eight slices and four anatomic quadrants.

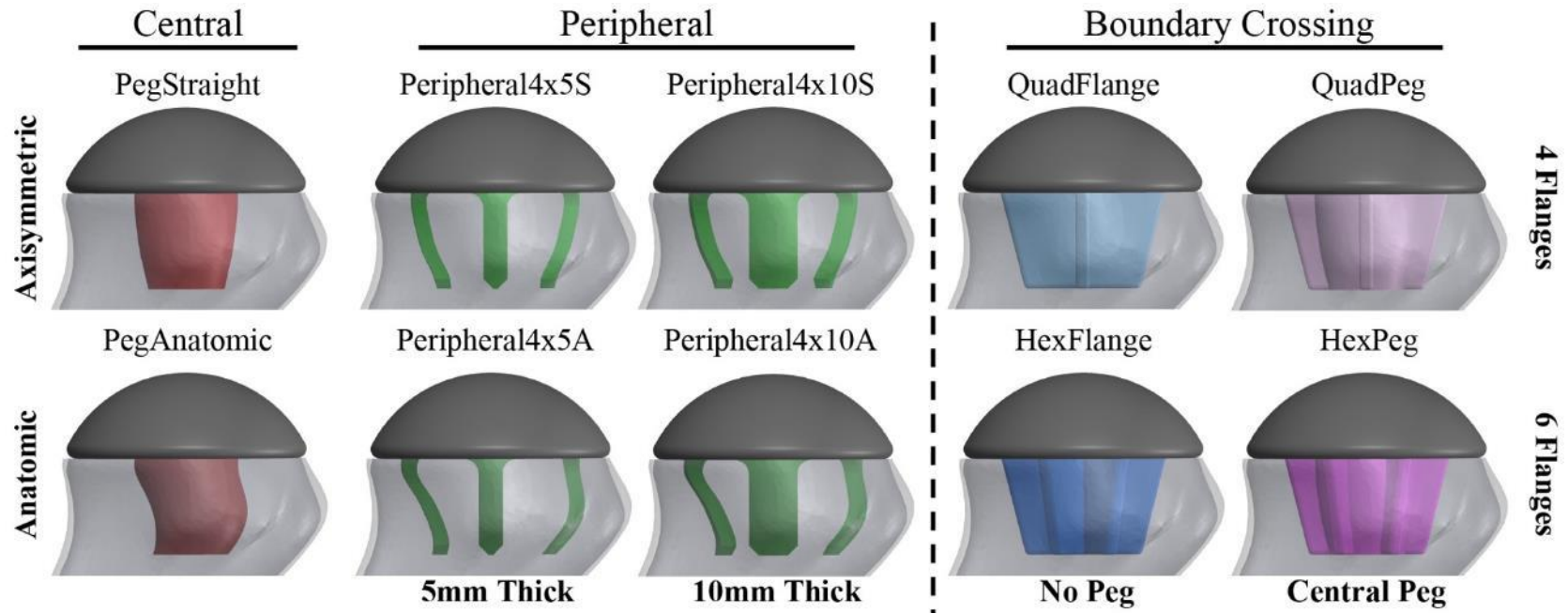


Figure 5.2: Stemless Implants Used for Humeral Reconstruction

Ten generic stemless implants were designed and categorized as having fixation features that were either: central, peripheral or boundary-crossing. Further sub-variations included: axisymmetric vs. anatomic curvature, widening peripheral pegs, and four vs. six flanged fixation features.

into the metaphyseal bone-space. These flanged implants were also hybridized with PegStraight to form two more implants (*i.e.*, QuadPeg, HexPeg) that had a core peg structure (Figure 5.2). Humeral head components were formed with an aspect ratio of 2.8:1 (diameter:height) [34], and varied by changing the articular diameter in 2mm increments to match each humerus' resection diameter; they were further fused to implant fixation features to represent a rigid Morse taper union.

5.2.3 Finite Element Modeling

FE models were developed in Abaqus (version 6.14; Dassault Systèmes Corp, Waltham, MA). All components were meshed with 2mm quadratic tetrahedral elements (based on mesh convergence, Appendix C). Cortical bone was applied a constant elastic modulus of 20GPa [5,41,42], as it is generally regarded as homogenous, while the trabecular-canal was assigned elastic moduli that varied as a function of CT density; using a site-pooled linear regression [5,43]. All implants were assigned an elastic modulus of 110GPa [44,45], representing Titanium. All materials had a Poisson's ratio of 0.3 [5]. Implant-bone contact was assumed to be grit-blast on wet-bone, and was represented as frictional ($\mu=0.63$) [5,46].

Two loading scenarios, representing 45° and 75° of shoulder abduction, were simulated by applying joint reaction forces to the articular surface [5]. The orientation and magnitude of the applied force (45°: 440N, 75°: 740N; based on 50th percentile male bodyweight of 88.3kg [5]) were taken from *in-vivo* telemetrized implant data [5,47], and were consistent for both the intact and reconstructed models. Forces passed through the center of the humeral head, such that the Cartesian components of the force matched the *in-vivo* data [5].

5.2.4 Outcome Variables

Three outcome measures were assessed: (1) the percentage of the implant's area that remained in contact with the surrounding bone during load application, (2) the volume-weighted absolute percentage change in bone stress, relative to the intact state [5] (Equation 5.1), and (3) the time-zero potential bone response, as estimated by the percentage of bone volume that would be expected to (a) resorb, (b) remain unchanged,

or (c) remodel based on SED changes between the reconstructed and intact models [25,30–32].

$$\Delta\sigma = \frac{\sum(\Delta\sigma_{VM}^{ReconstructedElement} \times Volume_{ReconstructedElement})}{\sum(\sigma_{VM}^{IntactElement}) \times Volume_{Region-of-Interest}} \times 100\% \quad (\text{Eq.5.1})$$

$$\Delta\sigma_{VM} = \sqrt{0.5 \times [(\Delta\sigma_{11} - \Delta\sigma_{22})^2 + (\Delta\sigma_{22} - \Delta\sigma_{33})^2 + (\Delta\sigma_{11} - \Delta\sigma_{33})^2 + 6 \times (\Delta\sigma_{12}^2 + \Delta\sigma_{23}^2 + \Delta\sigma_{31}^2)]}$$

$$\text{where, } \Delta\sigma_{xy} = \Delta\sigma_{xy_{IMPLANT}} - \Delta\sigma_{xy_{INTACT}}$$

The elements were categorized into the potential bone response groups as follows:

$$\text{Resorb: } U_{Implant Model} < 0.45U_{Intact Model} \quad (\text{Eq.5.2})$$

$$\text{Remain Unchanged: } 0.45U_{Intact Model} \leq U_{Implant Model} \leq 1.55U_{Intact Model}$$

$$\text{Remodel: } U_{Implant Model} > 1.55U_{Intact Model}$$

where, $U = SED$ of each element

Both the change in stress, and the potential bone response were quantified separately for the cortical shell and trabecular-canal; and were further divided into 32 subsections (Figure 5.1) corresponding to eight 5mm thick slices (parallel to the resection), and four anatomic quadrants (*i.e.*, medial, lateral, anterior, and posterior).

5.2.5 Statistical Approaches

To assess statistical significance, a 2-way RM ANOVA was conducted for the implant-contact area, and a 4-way RM ANOVA was conducted for the stress and potential bone response outcomes. All statistical analyses were completed using SPSS (version 23; IBM, Armonk, NY, USA), with the threshold for significance set as $P \leq 0.05$.

5.3 Results

5.3.1 Implant-Bone Contact

Implant-bone contact area varied significantly between implants ($P < 0.001$, power=1.000). Specifically, Peripheral4x5S and Peripheral4x5A were found to have significantly greater contact percentages than all other implants ($P \leq 0.033$), except each

other ($P=0.072$; Figure 5.3). Moreover, all peripheral implants were found to produce significantly greater contact percentages than the flanged implants and peg-flange hybrids ($P\leq 0.017$). Peripheral4x10A also produced significantly greater contact percentages than both PegAnatomic ($P=0.026$) and Peripheral4x10S ($P=0.002$), while the pegged implants had significantly higher contact percentages than QuadFlange ($P\leq 0.032$), and both peg-flange hybrids ($P\leq 0.032$). PegStraight was also significantly better than HexFlange ($P=0.020$) and PegAnatomic ($P=0.003$). QuadPeg produced significantly greater contact percentage than QuadFlange ($P=0.037$).

Changing fixation features from straight to anatomic curvature resulted in a slight decrease in pegged implant contact area, but a slight increase in peripheral implant contact area. Overall, flanged implants were found to have the lowest implant-bone contact percentages, with the hybrids falling between the peg and flange designs, and the peripheral implants producing the greatest implant-bone contact percentages.

5.3.2 Absolute Change in Bone Stress

5.3.2.1 Cortical Bone

A quadrant main effect ($P<0.001$, power=1.000) indicated higher changes in cortical stress in the lateral quadrant compared to the medial ($13.6\pm 3.4\%$ difference; $P=0.001$) and anterior ($13.5\pm 4.0\%$ difference; $P=0.002$) quadrants; as well as in the posterior quadrant compared to anterior ($5.5\pm 3.1\%$ difference; $P=0.017$) (Figures 5.4 to 5.7). Significant slice depth ($P<0.001$, power=1.000) and abduction angle ($P=0.027$, power=0.726) main effects indicated that cortical stress changes significantly varied between all slices, and were greater when loading the humerus at 45° compared to 75° abduction ($1.5\pm 1.0\%$ difference; $P=0.027$). Cortical stress differences were found to vary significantly based on the type of implant chosen ($P=0.001$, power=0.980), with PegStraight producing significantly less cortex stress change than all other implants ($P\leq 0.047$) except Peripheral4x5S ($P=0.919$) and Peripheral4x5A ($P=0.916$). Additionally, Peripheral4x5S and Peripheral4x5A were both found to induce significantly less cortex stress change than Peripheral4x10S ($P\leq 0.046$) and Peripheral4x10A ($P\leq 0.001$). HexPeg also caused significantly greater cortex changes compared to PegAnatomic ($P=0.015$),

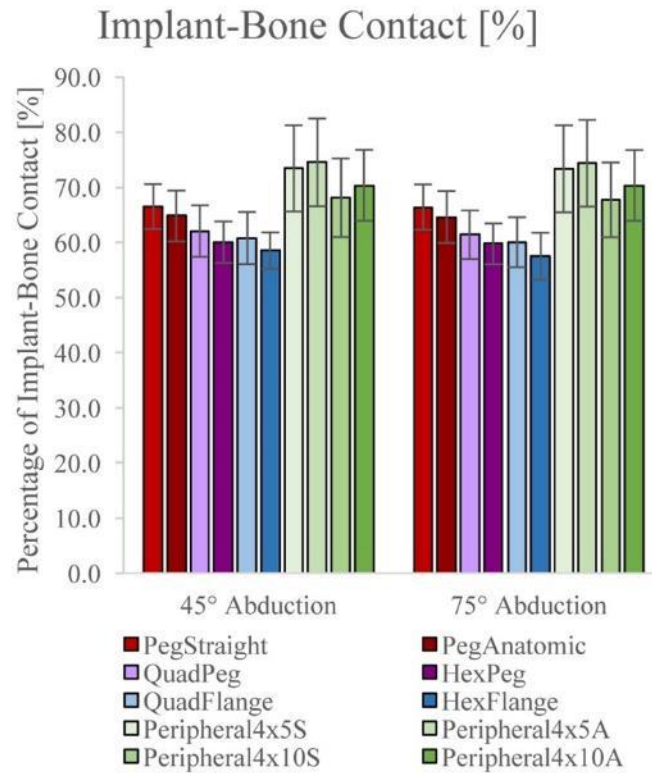


Figure 5.3: Implant-Bone Contact Results for All Stemless Implants

The mean \pm SD percentage of each implant that remained in contact with bone when loaded according to either 45° or 75° of abduction.

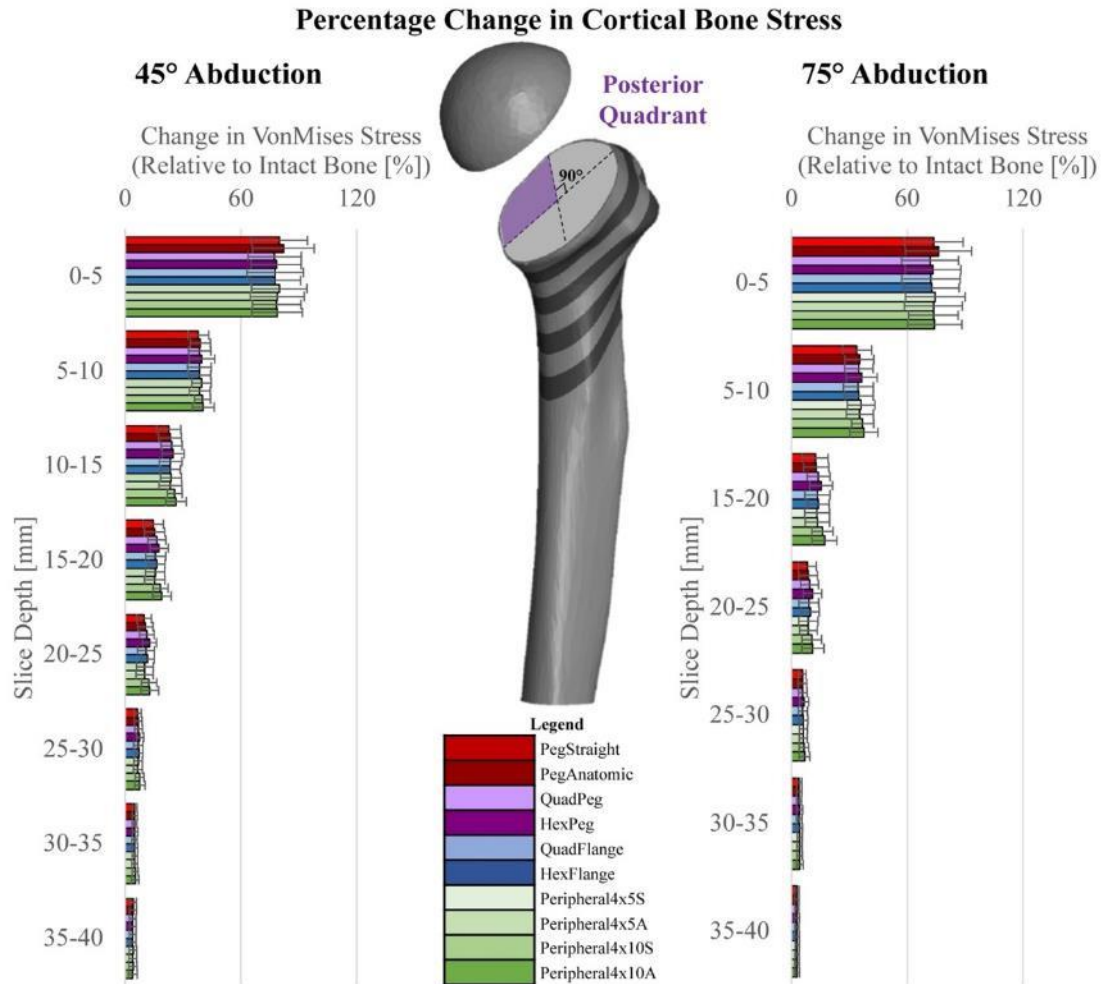


Figure 5.5: The Percentage Change in Posterior Quadrant Cortical Bone Stress Results for All Stemless Implants

The mean \pm SD percentage change in posterior quadrant cortical bone stress relative to the intact state broken down by slice depth for loading corresponding 45° and 75° of abduction.

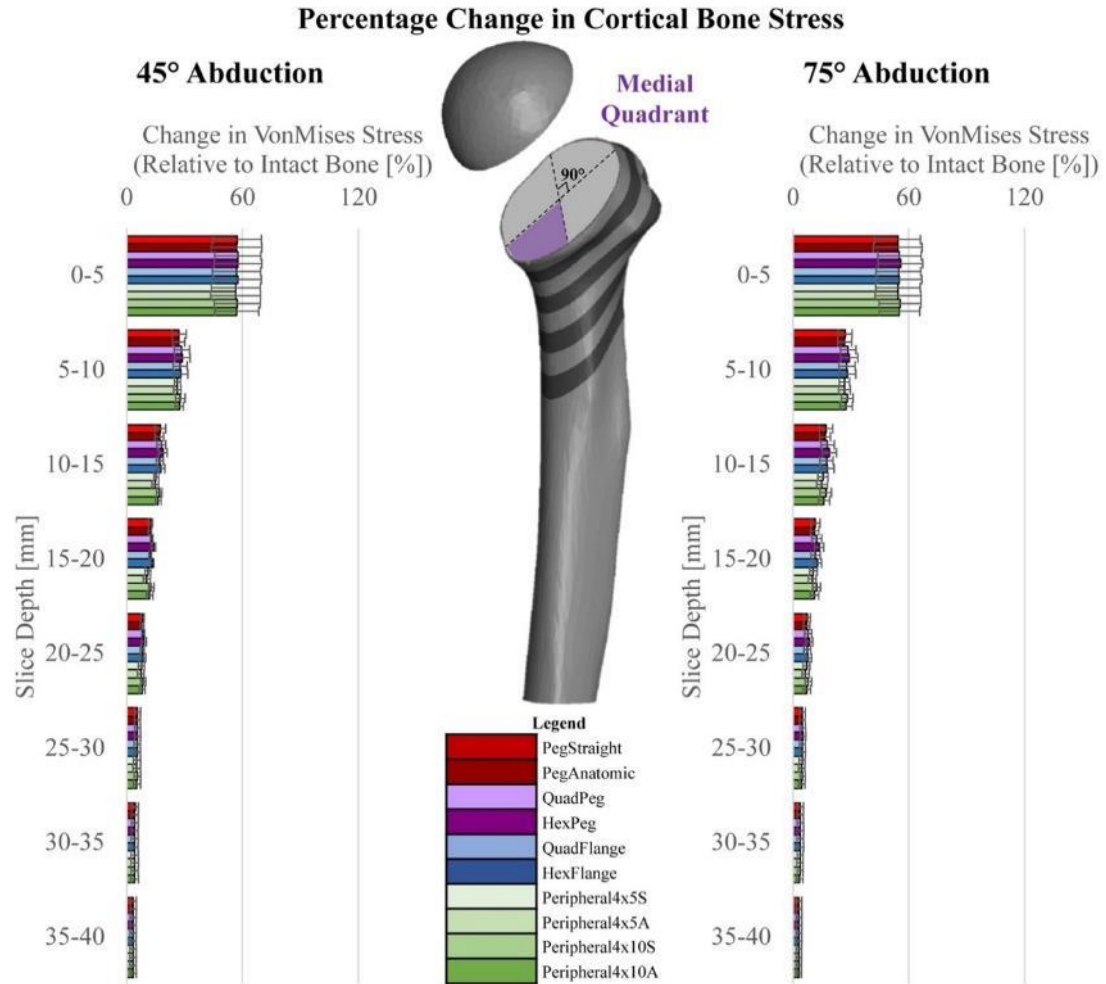


Figure 5.6: The Percentage Change in Medial Quadrant Cortical Bone Stress Results for All Stemless Implants

The mean \pm SD percentage change in medial quadrant cortical bone stress relative to the intact state broken down by slice depth for loading corresponding 45° and 75° of abduction.

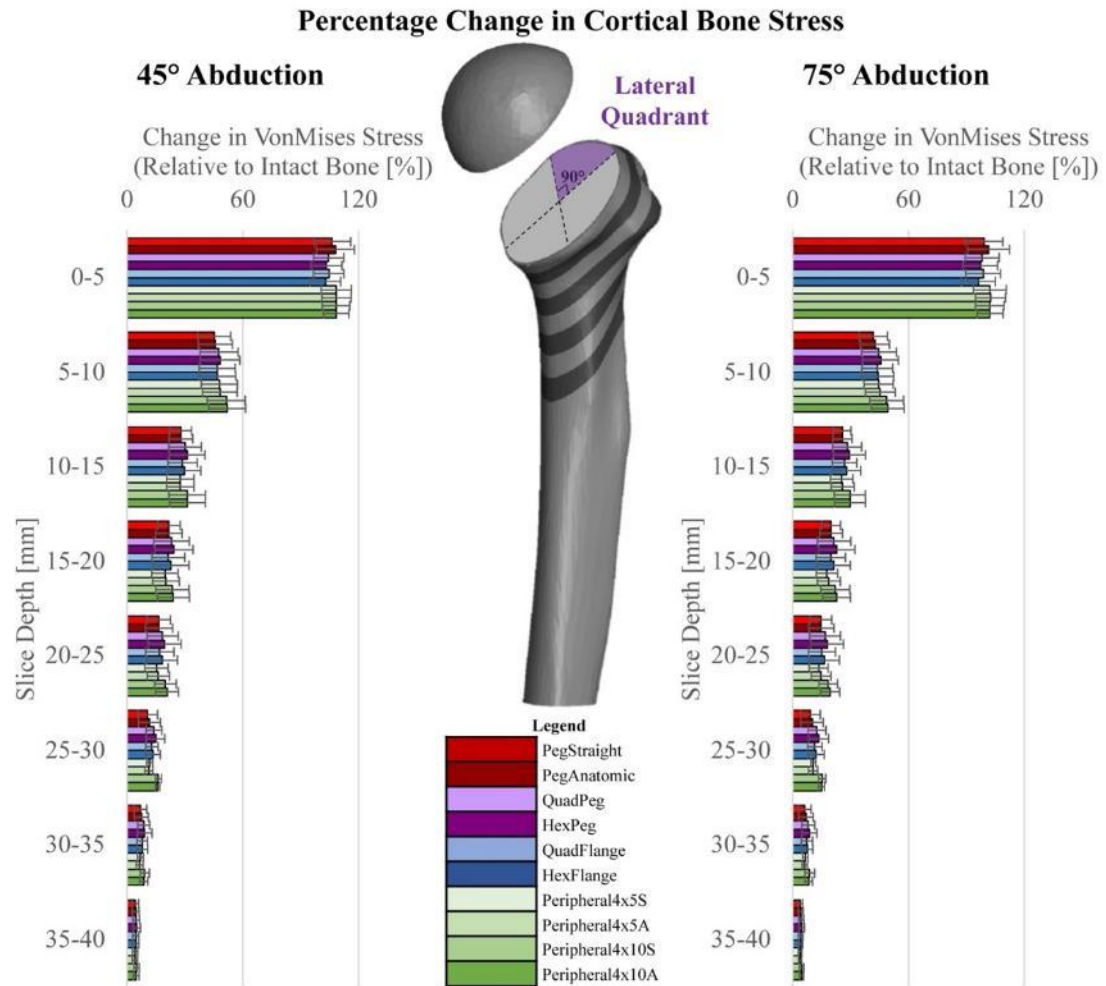


Figure 5.7: The Percentage Change in Lateral Quadrant Cortical Bone Stress Results for All Stemless Implants

The mean \pm SD percentage change in lateral quadrant cortical bone stress relative to the intact state broken down by slice depth for loading corresponding 45° and 75° of abduction.

HexFlange ($P=0.020$), QuadFlange ($P=0.010$) and QuadPeg ($P=0.004$). Furthermore, QuadFlange produced significantly less change in cortex stress than HexFlange ($P=0.010$), QuadPeg ($P=0.047$) and Peripheral4x10S ($P=0.043$; Figures 5.4 to 5.7). More specific implant comparisons, broken down by slice depth and quadrant, agree with these findings (See Appendix I). Overall, all implants elicited similar responses, with the greatest changes from the intact cortical stress occurring 0-5mm beneath the humeral resection, and tapering off down the diaphysis (Figures 5.4 to 5.7).²

5.3.2.2 Trabecular Bone

Again, a quadrant main effect ($P<0.001$, power=1.000) indicated that the change in trabecular stress was significantly greater in the lateral quadrant compared to all others (medial: $14.6\pm 6.4\%$ difference, $P=0.007$; anterior: $15.0\pm 4.4\%$ difference, $P=0.002$; posterior: $7.2\pm 3.6\%$ difference, $P=0.011$), as well as posteriorly compared to both anterior ($7.7\pm 4.4\%$ difference; $P=0.018$) and medial ($7.3\pm 4.3\%$ difference; $P=0.019$) quadrants. 45° humeral loading produced a significantly greater change in trabecular stress ($1.1\pm 0.6\%$ difference) compared to 75° humeral loading ($P=0.014$, power=0.871) (Figures 5.8 to 5.11). Again, all slice depths produced significantly different trabecular stress responses ($P<0.001$, power=1.000). Overall, an implant main effect ($P<0.001$, power=1.000) demonstrated that the pegged implants produced significantly less trabecular stress changes compared to all other implants ($P\leq 0.014$), except each other ($P=0.064$), Peripheral4x5S ($P\geq 0.073$) and Peripheral4x5A ($P\geq 0.110$). Peripheral4x10S and Peripheral4x10A were found to produce significantly greater changes in trabecular stress compared to all implants ($P\leq 0.044$), except each other ($P=0.708$) and HexPeg ($P\geq 0.679$). Finally, QuadFlange and QuadPeg both created significantly less changes in trabecular stress than HexFlange ($P\leq 0.043$) and HexPeg ($P\leq 0.005$; Figures 5.8 to 5.11). Specific implant differences according to slice depth and quadrant agree with these findings (See Appendix I).

The greatest divergence from intact trabecular stress was found 0-5mm beneath the resection (Figures 5.8 to 5.11). Trabecular stress returned closer to the intact state further

² See Appendix J for supplementary von Mises stress plot cross-sections of all specimens.

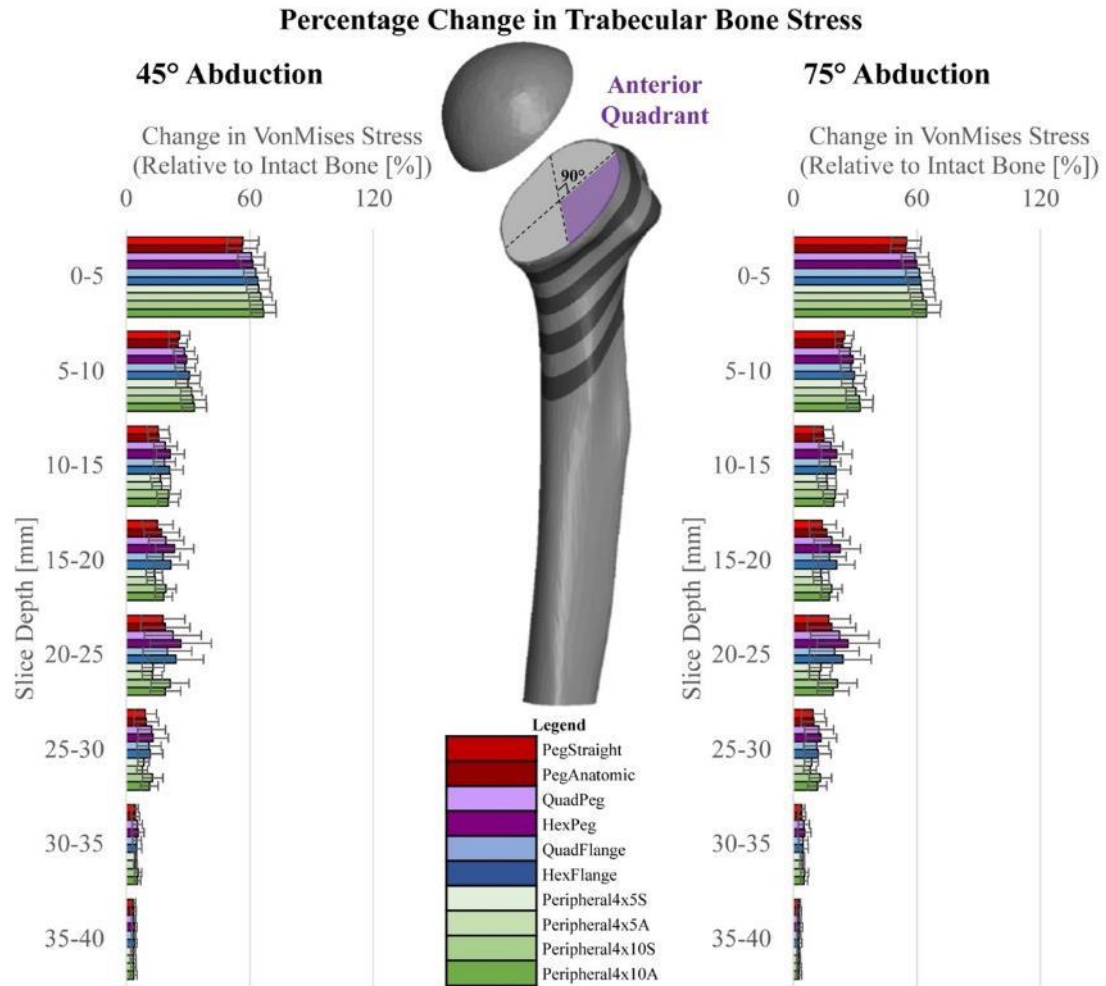


Figure 5.8: The Percentage Change in Anterior Quadrant Trabecular Bone Stress Results for All Stemless Implants

The mean \pm SD percentage change in anterior quadrant trabecular bone stress relative to the intact state broken down by slice depth for loading corresponding 45° and 75° of abduction.

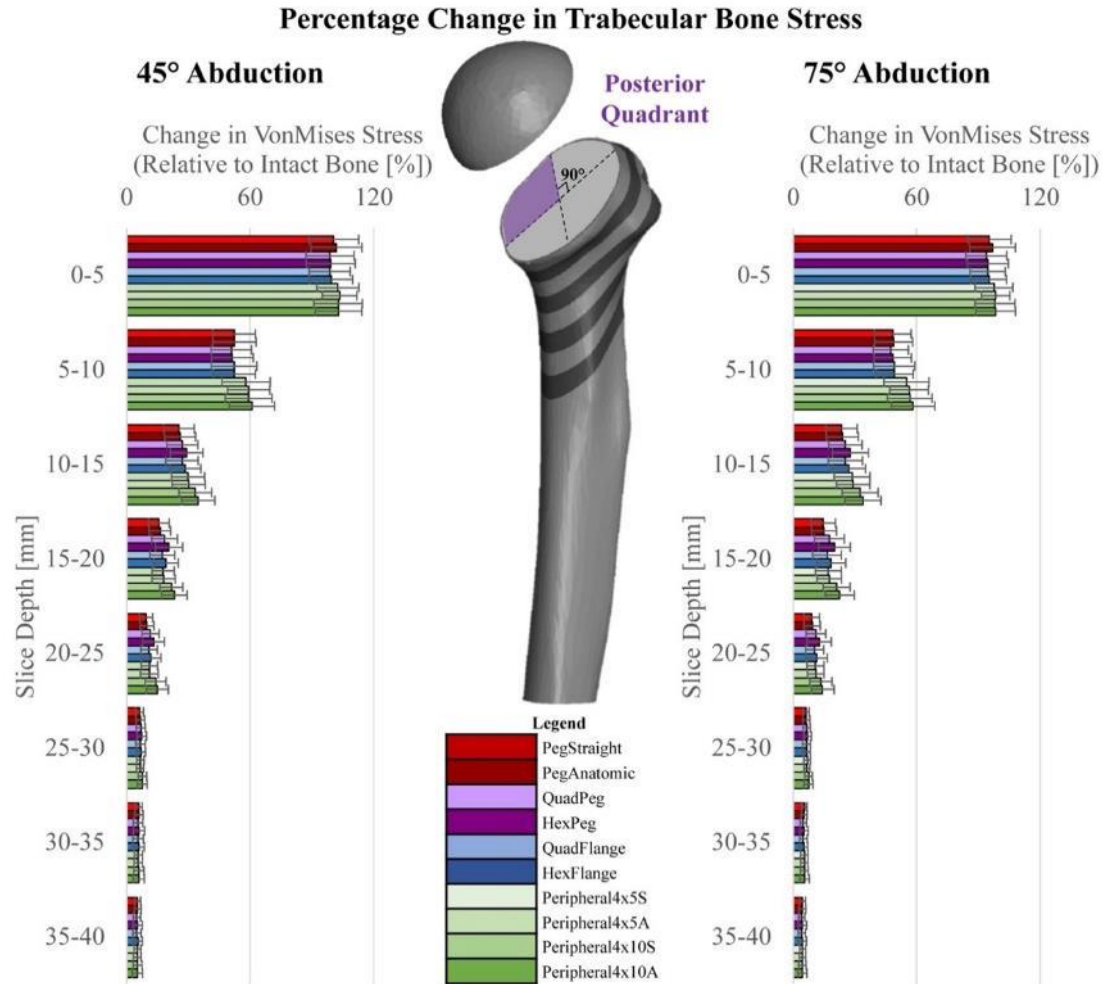


Figure 5.9: The Percentage Change in Posterior Quadrant Trabecular Bone Stress Results for All Stemless Implants

The mean \pm SD percentage change in posterior quadrant trabecular bone stress relative to the intact state broken down by slice depth for loading corresponding 45° and 75° of abduction.

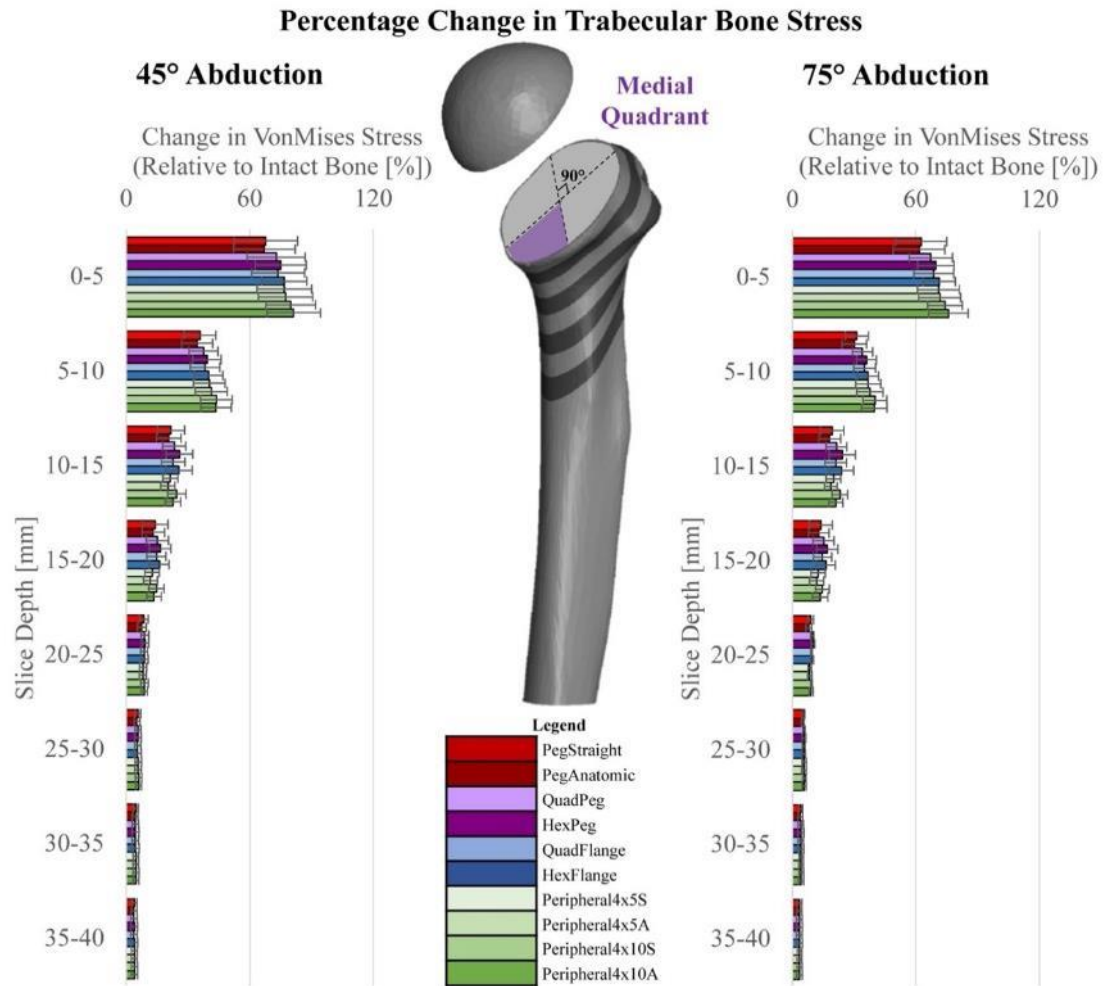


Figure 5.10: The Percentage Change in Medial Quadrant Trabecular Bone Stress Results for All Stemless Implants

The mean \pm SD percentage change in medial quadrant trabecular bone stress relative to the intact state broken down by slice depth for loading corresponding 45° and 75° of abduction.

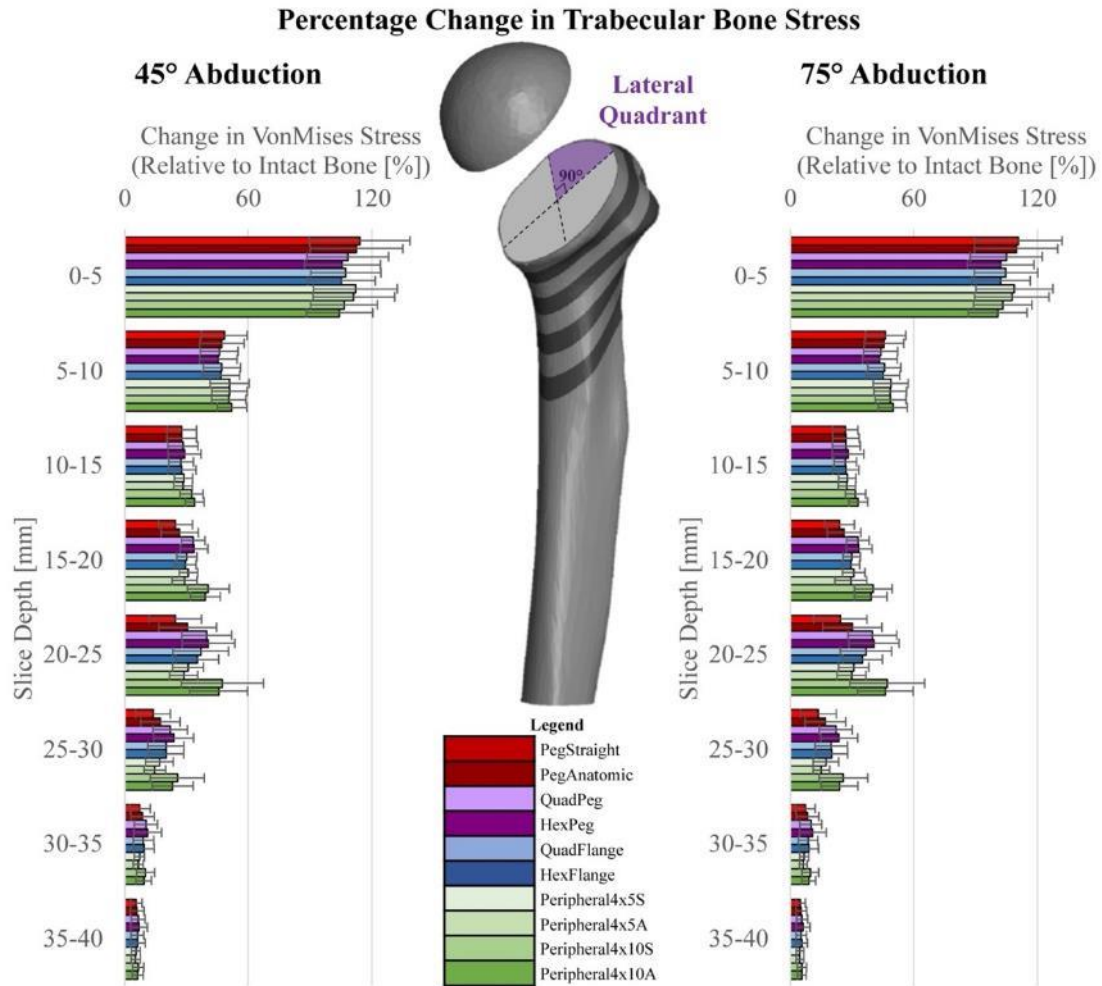


Figure 5.11: The Percentage Change in Lateral Quadrant Trabecular Bone Stress Results for All Stemless Implants

The mean \pm SD percentage change in lateral quadrant trabecular bone stress relative to the intact state broken down by slice depth for loading corresponding 45° and 75° of abduction.

down the diaphysis, except in the lateral and anterior quadrants, where there was an elevation in stress change 15-25mm beneath the resection plane. This effect was most pronounced within QuadPeg, HexPeg, Peripheral4x10S, and Peripheral4x10A (Figures 5.8 to 5.11).

5.3.3 Expected Bone Response

5.3.3.1 Cortical Bone

Below Threshold

An abduction angle main effect ($P=0.027$, power=0.729) indicated that the percentage of cortical bone volume expected to resorb was slightly higher when the humerus was loaded corresponding to 45° instead of 75° of abduction ($1.3\pm 0.9\%$ difference). Moreover, the first three slices beneath the humeral head resection plane (0-15mm) contained greater percentages of cortical bone volume with a potential to resorb compared to all other slices ($P<0.001$, power=1.000) (Figures 5.12 and 5.13). Though the bone quadrant main effect was significant ($P=0.013$, power=0.833), the pairwise comparison didn't indicate any significant differences attributable to quadrant alone. The choice of implant also presented as a significant main effect ($P<0.001$, power=1.000). Specifically, the pegged implants were found to have a lower volume percentage with resorbing potential than all other implants ($P\leq 0.015$), except Peripheral4x5S ($P\geq 0.085$) and Peripheral4x5A ($P\geq 0.185$); with PegStraight having a lower resorbing potential than PegAnatomic ($P=0.025$). HexPeg was additionally found to have a higher potential resorbing volume percentage than QuadPeg ($P=0.030$), QuadFlange ($P=0.042$), and HexFlange ($P=0.037$). The Peripheral4x5S ($P<0.001$), Peripheral4x5A ($P=0.001$) and QuadFlange ($P=0.032$) all produced significantly less expected resorbing volume percentages than Peripheral4x10A; with Peripheral4x5S ($P=0.035$) and QuadFlange ($P=0.013$) also being significantly lower than Peripheral4x10S. These results were supported by the implant comparisons broken down by slice depth and bone quadrant. Overall, the mean differences between implants were small ($\leq 3.9\%$ difference), with all eliciting similar cortical bone resorbing potentials; which were highest near the resection plane, dissipating 15-20mm beneath the resection (Figures 5.12 and 5.13). These findings

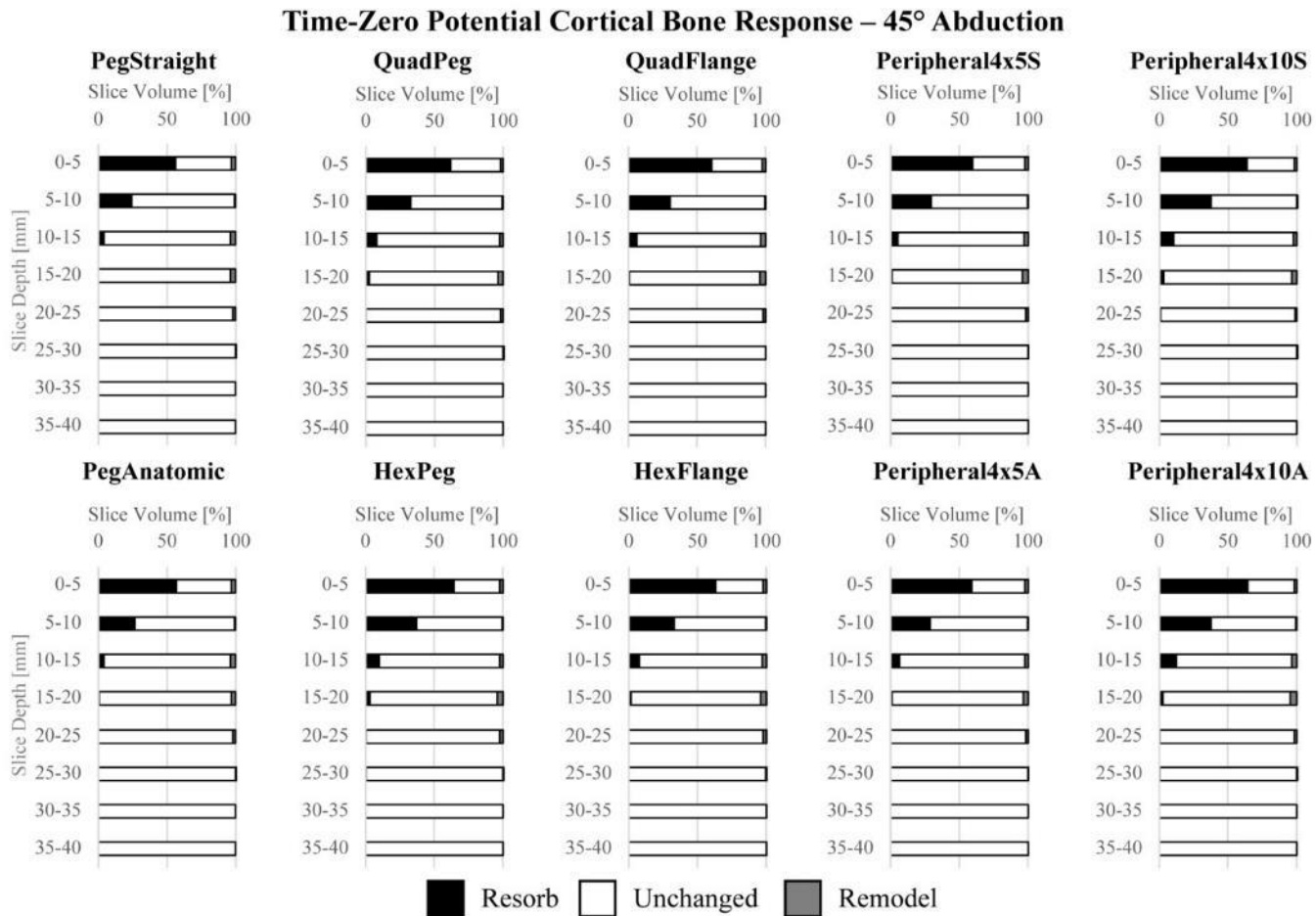


Figure 5.12: The Potential Time-Zero Cortical Bone Response for All Stemless Implants (45° Abduction)

Potential cortical bone response of all stemless implants assessed (results for 45° of abduction shown). Available bone volume in each slice (pooled across quadrants) is divided into the percentage expected to resorb (black), remain unchanged (white) and remodel (grey).

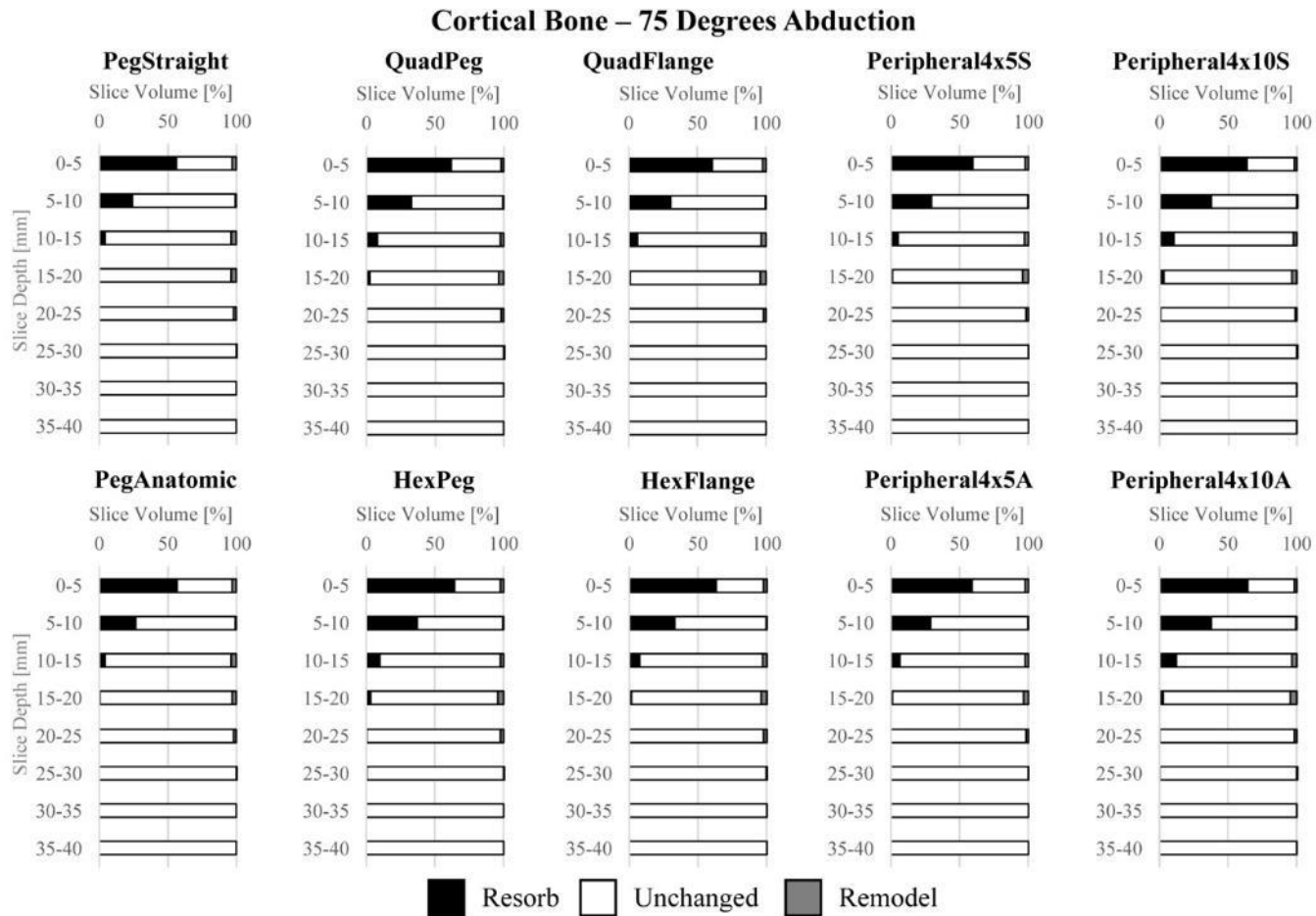


Figure 5.13: The Potential Time-Zero Cortical Bone Response for All Stemless Implants (75° Abduction)
 Potential cortical bone response of all stemless implants assessed (results for 75° of abduction shown). Available bone volume in each slice (pooled across quadrants) is divided into the percentage expected to resorb (black), remain unchanged (white) and remodel (grey).

were supported by the implant comparisons broken down by slice depth and bone quadrant (See Appendix I).

Within Threshold

Similarly, an abduction angle main effect suggested that there is a slight increase in the unchanged cortical bone volume percentage ($1.4 \pm 1.0\%$ difference; $P=0.036$, power=0.645) when the humerus is loaded at 75° abduction, compared to 45° abduction. The lateral quadrant also produced significantly less unchanged volume potential compared to the anterior quadrant ($11.1 \pm 8.8\%$ difference; $P=0.048$, power=0.781). Furthermore, the first four slices beneath the humeral head resection plane (0-20mm) retained significantly lower percentages of unchanged cortex volume compared to all other slices ($P<0.001$, power=1.000) (Figures 5.12 and 5.13). Moreover, an implant main effect ($P<0.001$, power=0.997), indicated that the pegged implants produced significantly greater volume percentages expected to remain unchanged compared to QuadPeg ($P \leq 0.029$), HexPeg ($P \leq 0.014$), HexFlange ($P \leq 0.010$), Peripheral4x10S ($P=0.008$) and Peripheral4x10A ($P=0.026$). PegAnatomic was also found to produce significantly less unchanged cortex volume percentage than QuadFlange ($P=0.049$). Peripheral4x5S also produced significantly more unchanged volume percentage than both Peripheral4x10S ($P=0.037$) and Peripheral4x10A ($P<0.001$); as did Peripheral4x5A compared to Peripheral4x10A ($P=0.001$), and QuadFlange compared to Peripheral4x10S ($P=0.028$). HexPeg further produced significantly less unchanged cortex volume percentage compared to QuadPeg ($P=0.016$), QuadFlange ($P=0.033$) and HexFlange ($P=0.029$). These differences were again supported by the implant-by-slice depth-by-bone quadrant interaction. Overall, mean differences between implant types were small ($\leq 3.5\%$ difference), suggesting that implant type has a minor effect on the percentage of unchanged cortical bone volume (Figures 5.12 and 5.13). Again, these findings were supported by the implant comparisons broken down by slice depth and bone quadrant (See Appendix I).

Above Threshold

Slice depth was the only significant main effect ($P=0.001$, power=0.986), with the percentage of cortex volume with remodeling potential being significantly greater in slice 3 (10-15mm) compared to slices 2 (5-10mm) and 4-6 (15-30mm); and significantly less in slice 4 (15-20mm) compared to slices 5-8 (20-40mm). Implant choice was not significant as a main effect ($P=0.097$, power=0.712). Overall, all implants produced similar (mean differences $\leq 0.6\%$), and small, cortical bone volume percentages within the expected remodeling threshold (Figures 5.12 and 5.13). Finally, these findings were supported by the implant comparisons broken down by slice depth and bone quadrant (See Appendix I).

5.3.3.2 Trabecular Bone

Below Threshold

Slice depth was found to have a main effect on the percentage of trabecular bone expected to resorb ($P<0.001$, power=1.000); with all slices being significantly different than each other, except slice 8 (35-40mm) compared to slices 5-7, and slice 7 (30-35mm) compared to slices 6 (25-30mm) and 8 (35-40mm) (Figures 5.14 and 5.15). Though not significant as a main effect ($P=0.085$, power=0.525), a bone quadrant pairwise comparison indicated that resorbing potential was higher in the posterior quadrant compared to the medial quadrant ($1.8\pm 1.5\%$ difference; $P=0.048$). The only other significant main effect was that of implant choice ($P<0.001$, power=1.000). All implants produced significantly different trabecular volume percentages within the resorbing potential category ($P\leq 0.047$), with the exceptions of QuadPeg compared to HexPeg ($P=0.054$), Peripheral4x5S compared to Peripheral4x5A ($P=0.971$), Peripheral4x10S compared to Peripheral4x10A ($P=0.834$), and HexFlange compared to QuadFlange ($P=0.558$) and Peripheral4x5A ($P=0.173$). The mean differences ranged from 0.2-9.6%, with the lowest resorbing potential found with pegged implants, followed by the peg-flange hybrids, flanged implants, Peripheral4x5 implants, and finally, the Peripheral4x10 implants. Neither increasing the number of flanges, nor changing the fixation feature to follow the anatomic canal path produced appreciable trends in the mean results (Figures

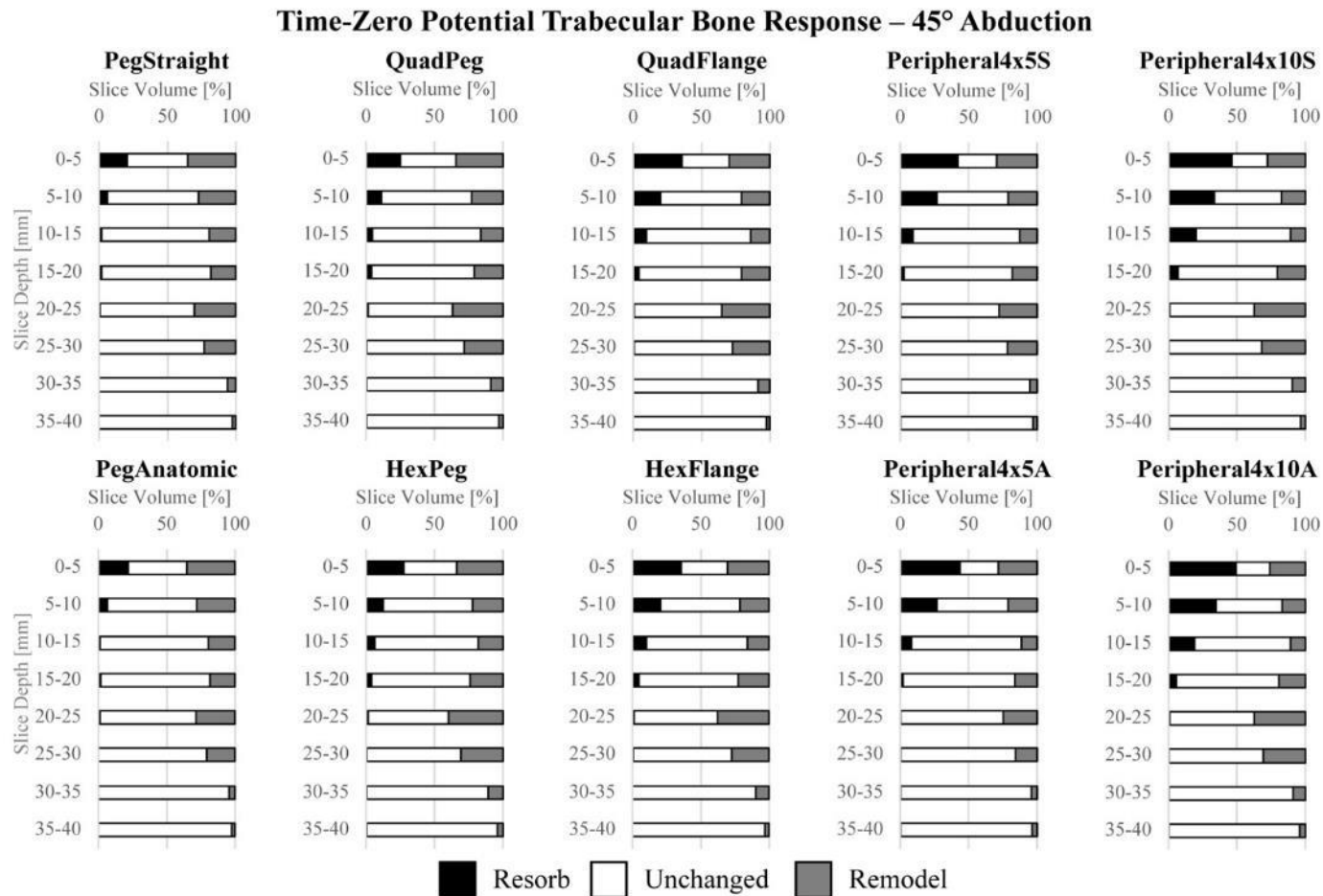


Figure 5.14: The Potential Time-Zero Trabecular Bone Response for All Stemless Implants (45° Abduction)

Potential trabecular bone response of all stemless implants assessed (results for 45° of abduction shown). Available bone volume in each slice (pooled across quadrants) is divided into the percentage expected to resorb (black), remain unchanged (white) and remodel (grey).

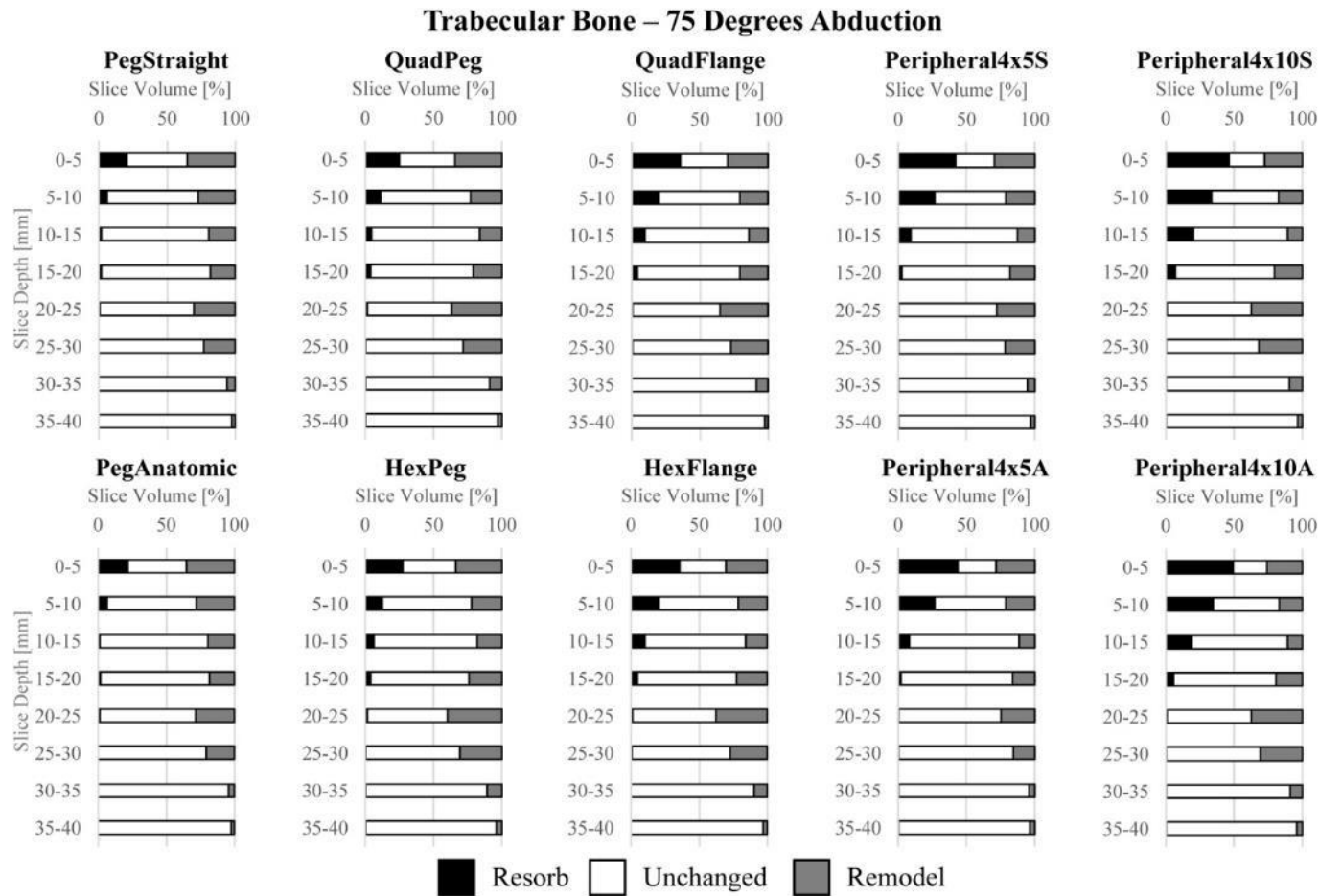


Figure 5.15: The Potential Time-Zero Trabecular Bone Response for All Stemless Implants (75° Abduction)

Potential trabecular bone response of all stemless implants assessed (results for 75° of abduction shown). Available bone volume in each slice (pooled across quadrants) is divided into the percentage expected to resorb (black), remain unchanged (white) and remodel (grey).

5.14 and 5.15). Again, these findings were supported by the implant comparisons broken down by slice depth and bone quadrant (See Appendix I).

Within Threshold

Slice depth had a main effect on the percentage of unchanged trabecular bone volume ($P < 0.001$, power=1.000), with all slices being significantly different from each other, except slices 3, 4 and 6, between which there were no significant differences. Less unchanged volume was present in the slices directly beneath the humeral head resection plane, and again at a depth of 20-30mm (Figures 5.14 and 5.15). As above, the posterior quadrant had a significantly greater percentage of unchanged trabecular volume compared to the medial quadrant ($2.8 \pm 1.9\%$ difference; $P = 0.030$), despite bone quadrant not being a significant main effect ($P = 0.354$, power=0.243). Implant choice was significant ($P < 0.001$, power=1.000); indicating that the pegged implants produced significantly more unchanged trabecular volume (by percentage) than all other implants ($P \leq 0.037$), except for each other ($P = 0.115$), Peripheral4x5S ($P \geq 0.108$) and Peripheral4x5A ($P \geq 0.541$). Similarly, QuadPeg produced significantly more unchanged trabecular volume than HexPeg ($P = 0.002$), HexFlange ($P = 0.004$), Peripheral4x10S ($P = 0.007$) and Peripheral4x10A ($P = 0.020$). HexFlange ($P \leq 0.049$), Peripheral4x10S ($P < 0.001$) and Peripheral4x10A ($P \leq 0.003$) all had significantly less unchanged potential than Peripheral4x5S and Peripheral4x5A; with QuadFlange also being significantly lower than Peripheral4x5A ($P = 0.045$). Finally, there was significantly less unchanged trabecular potential for Peripheral4x10S ($P = 0.003$) and Peripheral4x10A ($P = 0.011$) compared to QuadFlange; as well as Peripheral4x10S compared to HexPeg ($P = 0.040$). Mean differences in unchanged trabecular volume ranged from 1.9-9.1% between implants. Similar to the trabecular resorbing potential, the highest unchanged trabecular volume percentages were found for the pegged implants, followed by peg-flange hybrids, flanged implants, and peripheral implants (Figures 5.14 and 5.15). These findings were again supported by the implant comparison broken down by slice depth and bone quadrant (See Appendix I).

Above Threshold

Despite bone quadrant not being a significant main effect ($P=0.141$, $\text{power}=0.425$), the medial quadrant had significantly more trabecular remodeling potential than the posterior quadrant ($4.6\pm 2.6\%$ difference; $P=0.016$). All slices were significantly different from each other ($P<0.001$, $\text{power}=1.000$), except for slice 1 (0-5mm) compared to slices 4-6 (15-30mm), as well as slice 2 (5-10mm) compared to slices 3-6 (10-30mm), slice 3 (10-15mm) compared to slice 7 (30-35mm), and finally, slice 4 (15-20mm) compared to slice 6 (25-30mm). The choice of implant also had a significant main effect ($P<0.001$, $\text{power}=1.000$) on the trabecular remodeling potential. Peripheral4x5S and Peripheral4x5A had significantly less remodeling potential than all other implants ($P\leq 0.048$), except for PegAnatomic ($P\geq 0.059$); with Peripheral4x5A also significantly less than Peripheral4x5S ($P=0.049$). HexPeg produced significantly more trabecular remodeling potential compared to QuadPeg ($P=0.022$), QuadFlange ($P=0.015$), HexFlange ($P=0.035$) and PegAnatomic ($P=0.022$). Finally, QuadPeg had significantly greater trabecular remodeling potential compared to QuadFlange ($P=0.023$). Mean significant differences between implants ranged from 1.3-7.3%. The implant differences by slice depth and bone quadrant are presented in Appendix I. Overall, all implants elicited a high remodeling potential in the first slice (0-5mm), which reduced with depth until about 15-30mm beneath the resection plane, where the remodeling potential was again higher. These two regions of higher remodeling potential did appear to differ between implant designs, with the greatest remodeling potential in peg-flange hybrids, and the wider peripheral implants (Figures 5.14 and 5.15).

5.4 Discussion

Since stemless humeral implants were first developed, there have been several *in-vivo* assessments of their performance [12–14,16–22]; the results of which have been favorable. To the authors' knowledge there are only two published FE studies assessing a stemless humeral implant [5,48]. The first investigation, by Razfar *et al*, suggested that stemless implants may reduce stress shielding in the cortex compared to stemmed implants, but with the tradeoff of increasing changes in trabecular stress [5]; while the second study, by Favre *et al*, quantified implant-bone micromotion, and suggested that

99% of the interface was at levels that would promote bone-ongrowth [48]. The present FE investigation assessed changes in expected bone response following stemless humeral reconstruction with 10 implant designs.

The choice of implant had a significant effect on all outcome measures, though some general trends did present for all implants. One such observation was that the greatest changes in bone stress occurred directly beneath the humeral head resection plane, with changes reducing in magnitude (approaching the intact bone state) 30-40mm beneath the resection. Moreover, changes in bone stress were most prominent in the lateral quadrant, followed by the posterior, then medial and anterior. These findings agree well with radiographic assessments of stemless implants by Habermeyer *et al* and Uschok *et al*, as well as a SPECT/CT study by Berth *et al*, all of which suggested the superior-lateral region around the implant is subject to the greatest changes following stemless reconstruction [14,21,49]. Furthermore, all implants in the present investigation exhibited similar time-zero bone responses, with the greatest resorption potential 0-20mm beneath the humeral resection, and two peaks in the trabecular remodeling potential: directly beneath the resection, and near the termination of the implants (*i.e.*, 20-25mm down the trabecular-canal).

One aspect of stemless implant geometry investigated was the curvature of the pegged and peripheral implants. The change from simpler axisymmetric implants to a canal-path oriented anatomic curvature did not have any appreciable effect on bone stress changes, nor on the potential bone response; however, anatomic curvature did moderately improve the percentage of implant-bone contact for peripheral implants, while the opposite was true for the pegged implant. Given the additional surgical complexity associated with the insertion of anatomically curved implants, this moderate benefit in contact, without appreciable improvement in the expected bone stress and response, suggests that axisymmetric stemless implants may remain favorable.

Widening the pegs of the peripheral implants from 5mm to 10mm (*i.e.*, Peripheral4x5 vs. Peripheral4x10) was also assessed. Wider peripheral pegs resulted in greater changes from intact bone stress; as well as more potential for resorption, and a consequential drop in the unaltered bone response. Interestingly, the widening of peripheral implants resulted

in a marginal increase in the trabecular remodeling potential, though no effect was observed in the cortical bone. Widening peripheral pegs also resulted in a decrease in the mean implant-bone contact percentage. Accordingly, widening peripheral pegs may not be advisable; though the size of these pegs should be the subject of further investigation, as the current study was limited to only two embodiments.

The final fixation feature variation that was directly assessed was changing the number of fins on the flanged implants from 4 to 6. There were only very minor changes in magnitude associated with this increase; with slightly more stress changes presenting, as well as slightly less favorable bone responses (except for trabecular remodeling, which was found to slightly increase with 6 flanges). Moreover, there was a minor decrease in the percentage of implant-bone contact when 6 flanges were present instead of 4. These differences were small, suggesting that there is no real advantage to either embodiment.

The principle variation in implant geometry that was assessed was fixation feature positioning. Specifically, whether stemless implants should have central, peripheral or boundary-crossing fixation features. Generally, peripheral implants produced the greatest percentage of implant-bone contact. The cortical response (both change in stress and SED-based) seemed to favor centrally pegged implants and the less wide Peripheral4x5 implants, followed by flanged and hybrid implants, with the wider Peripheral4x10 implants producing the least favorable effects. The trabecular bone response was mixed, with centrally pegged implants and Peripheral4x5 implants again producing the best response, followed by peg-flange hybrids, flanged implants, except for trabecular remodeling, where hybrids seemed most advantageous; while Peripheral4x10 implants again produced the least favorable response for everything except trabecular remodeling, where Peripheral4x5 elicited less of an effect. Given the above observations, it seems that central pegged implants and Peripheral4x5 implants both have similar bone responses, that are perhaps moderately better than the boundary-crossing implants. It should be noted that the centrally pegged implants did produce less cortical and trabecular resorbing potential compared to all peripheral implants. This may be of more substantial consequence, given that bone resorption may lead to implant loosening over time; though

this should be assessed in future *in-vitro* investigations. An *in-vitro* assessment of implant stability may also be necessary for further implant differentiation.

Two loading positions (45° and 75°) were investigated and yielded only minor differences in results, with 45° producing greater stress changes and cortical resorbing potential. While statistically significant, the differences were small in magnitude, and would likely not be clinically significant. The applied load was larger for 75°; however, the orientation (derived from telemetrized implant data) was quite similar to 45°; this along with presenting results as percentage-change could explain the similarity between outcomes. Computational demand limited the number of positions assessed to two. Other orientations are suspected to yield similar results as the telemetrized load did not move substantially throughout abduction, though future investigations should assess this.

This study was not without limitations. The bone models were developed using cadaveric humeri, which may not exactly represent the bone morphology of a clinical population. While clinical CT scans could have been used, cadaveric humeri permit the use of CT settings that provide the best contrast for accurately representing the bone geometry. These settings require additional radiation exposure, which would be unethical for living subjects. In addition, the cadavers used were all males, and were slightly larger than the pooled population from which the trabecular-canal measures that were used in implant construction were derived (resection diameter: current cadavers = 51 ± 1 mm, pooled database = 47 ± 2 mm). Despite this, the authors are confident that peripheral, central and boundary-crossing implants were seated in their respective bone regions. Furthermore, the potential bone response outcome was adapted from previous *in-silico* FE models that used several iterations to adapt bone properties, while the current bone model did not iterate. Present trends in bone response make sense, and agree with previous radiographic stemmed and stemless implant literature (with the greatest changes occurring proximally and within the lateral quadrant) [10,14,21,49], though the implant differences were smaller than expected. This could be attributed to the use of non-iterative models, as it is uncertain how bone adaptations would affect further changes over time. Accordingly, the current results are representative of time-zero (*i.e.*, immediately following surgery), and should be interpreted as such; however, the authors feel that time-zero results are

important, with greater variation from the preoperative state being less favorable. Finally, the present investigation compared stemless fixation features based on only 10 generic implant designs. While there was more than one implant per category (*i.e.*, central, peripheral, and boundary-crossing), future investigations should continue to assess additional fixation feature designs, as this investigation could only begin to assess broad variations in implant geometry.

5.5 Conclusion

The design of implant fixation features impacts humeral bone response following stemless anatomic shoulder arthroplasty. Stemless implants elicited the greatest changes from the intact bone in the lateral quadrant directly beneath the humeral head resection plane. Changing the fixation feature curvature to follow the anatomic canal path did not appear to produce an appreciable benefit in outcome that would outweigh the surgical complexity necessary for implantation. Similarly, changing the number of fins in boundary-crossing implants was inconsequential; however, widening the peripheral pegs from 5mm to 10mm produced less favorable results. The use of implants with fixation features that were centrally located in the trabecular-canal produced the least potential bone resorption; however, some peripheral implants elicited similar changes in bone stress, and peripheral implants had the greatest implant-bone contact percentages.

5.6 References

- [1] Reeves, J. M., Langohr, G. D. G., Athwal, G. S., and Johnson, J. A., 2018, “The Effect of Stemless Humeral Component Fixation-Feature Design on Bone Stress and Strain Response: A Finite Element Analysis” *J. Shoulder Elb. Surg.*, p. (In Press).
- [2] Neer, C. S., 1955, “Articular Replacement for the Humeral Head,” *J. Bone Jt. Surg.*, **37**(2), pp. 215–228.
- [3] Churchill, R. S., 2014, “Stemless shoulder arthroplasty: current status,” *J. Shoulder Elb. Surg.*, **23**(9), pp. 1409–1414.
- [4] Churchill, R. S., and Athwal, G. S., 2016, “Stemless shoulder arthroplasty—

- current results and designs,” *Curr. Rev. Musculoskelet. Med.*, **9**(1), pp. 10–16.
- [5] Razfar, N., Reeves, J. M., Langohr, D. G., Willing, R., Athwal, G. S., and Johnson, J. A., 2016, “Comparison of proximal humeral bone stresses between stemless, short stem, and standard stem length: a finite element analysis,” *J. Shoulder Elb. Surg.*, **25**(7), pp. 1076–83.
- [6] Hawi, N., Tauber, M., Messina, M. J., Habermeyer, P., and Martetschläger, F., 2016, “Anatomic stemless shoulder arthroplasty and related outcomes: a systematic review,” *BMC Musculoskelet. Disord.*, **17**(1), p. 376.
- [7] Petriccioli, D., Bertone, C., and Marchi, G., 2015, “Stemless shoulder arthroplasty: a literature review,” *Joints*, **3**(1), pp. 38–41.
- [8] Harmer, L., Throckmorton, T., and Sperling, J. W., 2016, “Total shoulder arthroplasty: are the humeral components getting shorter?,” *Curr. Rev. Musculoskelet. Med.*, **9**(1), pp. 17–22.
- [9] Nagels, J., Stokdijk, M., and Rozing, P. M., 2003, “Stress shielding and bone resorption in shoulder arthroplasty,” *J. Shoulder Elb. Surg.*, **2746**(2), pp. 35–39.
- [10] Inoue, K., Suenaga, N., Oizumi, N., Yamaguchi, H., Miyoshi, N., Taniguchi, N., Munemoto, M., Egawa, T., and Tanaka, Y., 2017, “Humeral bone resorption after anatomic shoulder arthroplasty using an uncemented stem,” *J. Shoulder Elb. Surg.*, **26**(11), pp. 1984–1989.
- [11] Spormann, C., Durchholz, H., Audigé, L., Flury, M., Schwyzer, H. K., Simmen, B. R., and Kolling, C., 2014, “Patterns of proximal humeral bone resorption after total shoulder arthroplasty with an uncemented rectangular stem,” *J. Shoulder Elb. Surg.*, **23**(7), pp. 1028–1035.
- [12] Huguet, D., DeClercq, G., Rio, B., Teissier, J., and Zipoli, B., 2010, “Results of a new stemless shoulder prosthesis: radiologic proof of maintained fixation and stability after a minimum of three years’ follow-up,” *J. Shoulder Elbow Surg.*, **19**(6), pp. 847–52.

- [13] Churchill, R. S., Chuinard, C., Wiater, J. M., Friedman, R., Freehill, M., Jacobson, S., Spencer, E., Holloway, G. B., Wittstein, J., Lassiter, T., Smith, M., Blaine, T., and Nicholson, G. P., 2016, “Clinical and Radiographic Outcomes of the Simpliciti Canal-Sparing Shoulder Arthroplasty System: A Prospective Two-Year Multicenter Study,” *J. Bone Jt. Surg.*, **98**(7), pp. 552–560.
- [14] Habermeyer, P., Lichtenberg, S., Tauber, M., and Magosch, P., 2015, “Midterm results of stemless shoulder arthroplasty: A prospective study,” *J. Shoulder Elb. Surg.*, **24**(9), pp. 1463–1472.
- [15] Routman, H., Becks, L., and Roche, C., 2015, Stemless and Short Stem Humeral Components in Shoulder Arthroplasty.
- [16] Geurts, G. F., van Riet, R. P., Jansen, N., and Declercq, G., 2010, “Placement of the stemless humeral component in the Total Evolutive Shoulder System (TESS).,” *Tech. Hand Up. Extrem. Surg.*, **14**(4), pp. 214–7.
- [17] Kadum, B., Mafi, N., Norberg, S., and Sayed-Noor, A. S., 2011, “Results of the Total Evolutive Shoulder System (TESS): A single-centre study of 56 consecutive patients,” *Arch. Orthop. Trauma Surg.*, **131**(12), pp. 1623–1629.
- [18] Kadum, B., Hassany, H., Wadsten, M., Sayed-Noor, A., and Sjoden, G., 2016, “Geometrical analysis of stemless shoulder arthroplasty: a radiological study of seventy TESS total shoulder prostheses,” *Int. Orthop.*, **40**(4), pp. 751–758.
- [19] Razmjou, H., Holtby, R., Christakis, M., Axelrod, T., and Richards, R., 2013, “Impact of prosthetic design on clinical and radiologic outcomes of total shoulder arthroplasty: A prospective study,” *J. Shoulder Elb. Surg.*, **22**(2), pp. 206–214.
- [20] Maier, M. W., Lauer, S., Klotz, M. C., Bühlhoff, M., Spranz, D., and Zeifang, F., 2015, “Are there differences between stemless and conventional stemmed shoulder prostheses in the treatment of glenohumeral osteoarthritis?,” *BMC Musculoskelet. Disord.*, **16**(1), p. 275.
- [21] Uschok, S., Magosch, P., Moe, M., Lichtenberg, S., and Habermeyer, P., 2017, “Is

the stemless humeral head replacement clinically and radiographically a secure equivalent to standard stem humeral head replacement in the long-term follow-up? A prospective randomized trial,” *J. Shoulder Elb. Surg.*, **26**(2), pp. 225–232.

- [22] Berth, A., and Pap, G., 2013, “Stemless shoulder prosthesis versus conventional anatomic shoulder prosthesis in patients with osteoarthritis: a comparison of the functional outcome after a minimum of two years follow-up,” *J. Orthop. Traumatol.*, **14**(1), pp. 31–7.
- [23] Terrier, A., Brighenti, V., Pioletti, D. P., and Farron, A., 2012, “Importance of polyethylene thickness in total shoulder arthroplasty: a finite element analysis,” *Clin. Biomech. (Bristol, Avon)*, **27**(5), pp. 443–8.
- [24] Hopkins, A. R., Hansen, U. N., Amis, A. a, Taylor, M., and Emery, R. J., 2007, “Glenohumeral kinematics following total shoulder arthroplasty: a finite element investigation,” *J. Orthop. Res.*, **25**(1), pp. 108–115.
- [25] Neuert, M. A. C., and Dunning, C. E., 2013, “Determination of remodeling parameters for a strain-adaptive finite element model of the distal ulna,” *Proc. Inst. Mech. Eng. Part H - J. Eng. Med.*, **227**(9), pp. 994–1001.
- [26] Keyak, J. H., Sigurdsson, S., Karlsdottir, G. S., Oskarsdottir, D., Sigmarsdottir, A., Kornak, J., Harris, T. B., Sigurdsson, G., Jonsson, B. Y., Siggeirsdottir, K., Eiriksdottir, G., Gudnason, V., and Lang, T. F., 2013, “Effect of finite element model loading condition on fracture risk assessment in men and women: The AGES-Reykjavik study,” *Bone*, **57**(1), pp. 18–29.
- [27] Yosibash, Z., Trabelsi, N., and Milgrom, C., 2007, “Reliable simulations of the human proximal femur by high-order finite element analysis validated by experimental observations,” *J. Biomech.*, **40**(16), pp. 3688–3699.
- [28] Austman, R. L., Milner, J. S., Holdsworth, D. W., and Dunning, C. E., 2008, “The effect of the density-modulus relationship selected to apply material properties in a finite element model of long bone,” *J. Biomech.*, **41**, pp. 3171–3176.

- [29] Willing, R., King, G. J. W., and Johnson, J. a, 2012, “The effect of implant design of linked total elbow arthroplasty on stability and stress: a finite element analysis.,” *Comput. Methods Biomech. Biomed. Engin.*, **5842**(1248), p. 2012.
- [30] Weinans, H., Huiskes, R., and Grootenboer, H. J., 1992, “The behavior of adaptive bone-remodeling simulation models,” *J. Biomech.*, **25**(12), pp. 1425–1441.
- [31] Huiskes, R., Weinans, H., Grootenboer, H. J., Dalstra, M., Fudala, B., and Slooff, T. J., 1987, “Adaptive Bone-Remodeling Theory Applied to Prosthetic-Design Analysis,” *J. Biomech.*, **20**(11), pp. 1135–1150.
- [32] Carter, D. R., Fyhrie, D. P., and Whalen, R. T., 1987, “Trabecular bone density and loading history: Regulation of connective tissue biology by mechanical energy,” *J. Biomech.*, **20**(8).
- [33] Reeves, J. M., Athwal, G. S., and Johnson, J. A., 2017, “An Assessment of Proximal Humerus Density with Reference to Stemless Implants,” *J. Shoulder Elb. Surg.*, (**In Press**).
- [34] Reeves, J. M., Johnson, J. A., and Athwal, G. S., 2017, “An analysis of proximal humerus morphology with special interest in stemless shoulder arthroplasty,” *J. Shoulder Elb. Surg.*, (**In Press**).
- [35] Alidousti, H., Giles, J. W., Emery, R. J. H., and Jeffers, J., 2017, “Spatial mapping of humeral head bone density,” *J. Shoulder Elb. Surg.*, **26**(9), pp. 1653–1661.
- [36] Bauer, T. W., and Schils, J., 1999, “The pathology of total joint arthroplasty II. Mechanisms of implant failure,” *Skeletal Radiol.*, **28**(9), pp. 483–497.
- [37] Engh, C., and McGovern, T., 1992, “A quantitative evaluation of periprosthetic bone-remodeling after cementless total hip arthroplasty,” *J Bone Joint Surg*, **74**(7), pp.1009–1020.
- [38] Sychterz, C. J., and Engh, C. A., 1996, “The Influence of Clinical Factors on Periprosthetic Bone Remodeling,” *Clin. Orthop. Relat. Res.*, (322), pp. 285–292.

- [39] Kerner, J., Huiskes, R., van Lenthe, G. ., Weinans, H., van Rietbergen, B., Engh, C. ., and Amis, a. ., 1999, “Correlation between pre-operative periprosthetic bone density and post-operative bone loss in THA can be explained by strain-adaptive remodelling,” *J. Biomech.*, **32**(7), pp. 695–703.
- [40] Knowles, N. K., Reeves, J. M., and Ferreira, L. M., 2016, “Quantitative Computed Tomography (QCT) derived Bone Mineral Density (BMD) in finite element studies: a review of the literature,” *J. Exp. Orthop.*, **3**(36), pp. 1–16.
- [41] Bayraktar, H. H., Morgan, E. F., Niebur, G. L., Morris, G. E., Wong, E. K., and Keaveny, T. M., 2004, “Comparison of the elastic and yield properties of human femoral trabecular and cortical bone tissue,” *J. Biomech.*, **37**(1), pp. 27–35.
- [42] Rho, J. Y., Ashman, R. B., and Turner, C. H., 1993, “Young’s modulus of trabecular and cortical bone material: Ultrasonic and microtensile measurements,” *J. Biomech.*, **26**(2), pp. 111–119.
- [43] Morgan, E. F., Bayraktar, H. H., and Keaveny, T. M., 2003, “Trabecular bone modulus-density relationships depend on anatomic site,” *J. Biomech.*, **36**, pp. 897–904.
- [44] Kuiper, J. H., and Huiskes, R., 1996, “Friction and stem stiffness affect dynamic interface motion in total hip replacement.,” *J. Orthop. Res.*, **14**(1), pp. 36–43.
- [45] Lee, Y. T., and Welsch, G., 1990, “Young’s Modulus and Damping of Ti-6Al-4V Alloy as a Function of Heat Treatment and Oxygen Concentration,” *Mater. Sci. Eng.*, **128**, pp. 128–77.
- [46] Grant, J. A., Bishop, N. E., Go, N., Sprecher, C., Honl, M., and Morlock, M. M., 2007, “Artificial composite bone as a model of human trabecular bone : The implant – bone interface,” **40**, pp. 1158–1164.
- [47] Bergmann, G., Graichen, F., Bender, A., Kaab, M., Rohlmann, A., and Westerhoff, P., 2007, “In vivo glenohumeral contact forces-Measurements in the first patient 7 months postoperatively,” *J. Biomech.*, **40**(10), pp. 2139–2149.

- [48] Favre, P., and Henderson, A. D., 2016, "Prediction of stemless humeral implant micromotion during upper limb activities," *Clin. Biomech.*, **36**, pp. 46–51.
- [49] Berth, A., März, V., Wissel, H., Awiszus, F., Amthauer, H., and Lohmann, C. H., 2016, "SPECT/CT demonstrates the osseointegrative response of a stemless shoulder prosthesis," *J. Shoulder Elb. Surg.*, **25**(4), pp. e96–e103.

Chapter 6

General Discussions and Concluding Thoughts

This chapter provides concluding thoughts regarding this thesis as a whole. Each of the objectives and hypotheses that were outlined in Chapter 1, Section 1.6 are reviewed in the context of the corresponding investigations; followed by a discussion of some of the overall strengths and limitations of this body of work. Finally, the future directions for this research are proposed, and the significance is addressed.

6.1 Summary

As medical treatments and technology advance, it is important that our understanding of the implications of these treatments grows as well. The questions posed by modern shoulder arthroplasty are well suited for collaborative exploration through the application of mechanical engineering tools. Given the recent advancements in shoulder arthroplasty leading to the advent of a diverse line of stemless (humeral) implants, an investigation into the effect of stemless prosthesis geometry and the underlying morphology of the proximal humerus was warranted. To date the *in-vivo* studies following patients with stemless reconstructions, while early, have indicated promising results that suggest that these less invasive implants perform well compared to their stemmed counterparts [1–5]; even indicating less operative time and blood loss [1,2]. However, the limited time has resulted in few *in-vitro* and *in-silico* investigations applying engineering methods to assess stemless implant performance [6–8]. The Finite Element (FE) method is particularly well suited to assessing joint reconstruction, as it permits a direct comparison between several implant geometries in the same bone; thereby increasing the statistical power of any findings.

The two stemless shoulder FE investigations in the literature (Razfar *et al* and Favre *et al*) have indicated that the stemless implants assessed provide adequate fixation throughout a range of shoulder loading scenarios [7] and point to potential trabecular and cortical bone stress trade-offs associated with transitioning to a stemless design [6], but

neither directly compared multiple stemless implant geometries. Accordingly, this research was undertaken to develop a greater understanding of the proximal humerus' morphology in the context of stemless implant design, and to determine how variation in stemless fixation feature design can impact the response of the underlying bone.

The first phase of this research addressed the morphology of the proximal humerus (Objectives 1a and 1b) through the analysis of 98 CT scans from non-arthritic and pre-operative arthritic populations of both men and women. Two investigations were undertaken (Chapters 2 and 3), the first regarding the regional trabecular density distribution of the proximal humerus (Objective 1a; Chapter 2), and the second to introduce new morphological parameters that could aid in mapping out the canal features of the proximal humerus (Objective 1b; Chapter 3). The goal of Objective 1a was achieved by first developing a new humeral coordinate system that was based on the articular resection plane; thereby ensuring that reported results would be relevant to stemless shoulder arthroplasty. Then, by quantifying bone density in central and peripheral sub-sections following the division of the proximal trabecular-canal into 13 slices parallel to the resection plane. As such, regional density variations were found indicating that the central region of the trabecular-canal was significantly less dense than the peripheral regions (central: $0.08 \pm 0.40 \text{ g/cm}^3$, medial: $0.15 \pm 0.49 \text{ g/cm}^3$, lateral: $0.14 \pm 0.49 \text{ g/cm}^3$, anterior: $0.15 \pm 0.49 \text{ g/cm}^3$, posterior: $0.15 \pm 0.56 \text{ g/cm}^3$), and that density decreased quickly beneath the humeral head resection plane. Consequently, Hypothesis 1a was accepted, as non-uniform density was noted within the proximal humerus, following the expected trends, decreasing to a quantifiable plateau approximately 10-15mm beneath the articular resection. Following this, Objective 1b was achieved by quantifying three new parameters of the proximal humerus: (1) the regional shifts in the path of the trabecular-canal, (2) the bounding canal diameters and (3) the depth of the canal beneath the humeral resection. As hypothesized, these trabecular-canal features were quantifiable, and presented with trends that could be pooled across the study population to create a spatial envelope that can be used in the design of stemless shoulder implants. Specifically, the canal path was found to remain largely unchanged in the anterior-posterior directions; however significant shifts in the medial-lateral directions were noted progressing down the canal, which could have implications for the orientation

of stemless implant fixation features. Moreover, gender-based differences were found to be more prevalent than differences between non-arthritic and arthritic populations. These findings could be beneficial when sizing implants for men and women, and in preliminary cadaveric assessments of novel implant designs. Together the investigations undertaken to satisfy the first objective provide a clearer understanding of the morphology of the proximal humerus.

The second phase of this research (Objective 2; Chapter 4) addressed the lack of understanding regarding the influence of trabecular stiffness modeling on FE models for shoulder arthroplasty. In order to develop an appropriate FE model of stemless shoulder arthroplasty, several assumptions are necessary to approximate reality. While many inhomogeneous density-modulus relationships have been developed for other joints throughout the body, none exist for the proximal humerus. Hence, humeral models to date have employed trabecular stiffness relationships based on other joints [6,9], but have not quantified how this may influence results. As such, by developing identical FE models of stemless humeral reconstruction that varied only in the trabecular stiffness relationship employed, the investigation in Chapter 4 was able to quantify this effect for the first time. The findings indicated that varying the anatomic-site from which the trabecular stiffness was derived consistently produced lower outcome deviations than those attributable to subject differences within the FE population, or those that arose from using a homogeneous stiffness in place of a site-pooled inhomogeneous one. This was true for implant-bone contact, the change in cortical and trabecular stress, as well as the time-zero potential bone response. The deviation between homogenous and inhomogeneous trabecular models was highlighted well by the divergence of trabecular outcomes 20-40mm beneath the humeral resection plane, where bone density and corresponding stiffness diminish; indicating the importance of using an inhomogeneous stiffness when constructing humeral FE models. Overall inhomogeneous anatomic-site deviations were very low, only exceeding 10% in two sub-sections of the trabecular stress change at 45° of abduction (mean values of 10.2% and 10.3%). Moreover, changing the anatomic-site from which the stiffness relationship was derived did not influence the trends in the investigated stemless arthroplasty outcomes, provided an inhomogeneous relationship was used. Accordingly, given the unaltered trends and overall low deviations

in outcome measures, Hypothesis 2 was confirmed, and the site-pooled inhomogeneous relationship was deemed acceptable for use in the construction of a FE model for stemless shoulder arthroplasty.

In the third and final phase of this research (Objective 3; Chapter 5) the humeral response to reconstruction with a variety of stemless implants was assessed. Using the bone morphology data from Chapters 2 and 3, ten generic stemless implants were designed with fixation features that were principally either central, peripheral, or crossing the central-peripheral boundary of the proximal humerus. Additional design alterations, such as fixation features that followed the canal path (quantified in Chapter 3) as opposed to tapering off axisymmetrically, were included as well. These designs were assessed using the FE method and outcome variables that were introduced for stemless humeral reconstruction in Chapter 4. The design of stemless implants influenced the humeral bone response. Whereas the cortical response was largely insensitive to changes in the stemless implant fixation feature geometry (<4.0% change across categories of the time-zero potential bone response) the trabecular response was more directly affected (potential bone response category changes $\leq 9.6\%$). Accordingly, Hypothesis 3 was partially accepted, as significant and quantifiable changes in humeral response were detected in all outcome measures; however, little benefit was realized from changing the implant fixation features to follow the canal path, and there were tradeoffs between central, peripheral and boundary-crossing implants. Specifically, central implants elicited the least potential bone resorbing responses; however, some central and peripheral implants produced similar bone stress changes, and peripheral implants had the greatest percentage of implant-bone contact area.

6.2 Strengths and Limitations

At the time of undertaking this research, Chapters 1 and 2 were the only morphological analyses of the proximal humerus that were conducted in a resection-based coordinate system. Since that time, a study by Alidousti *et al* was published analyzing density variations in a similar manner, and with similar conclusions as those found in Chapter 2 [10]; however, their investigation consisted of only four pairs of humeri, all of which were cadaveric. With this in mind, the sample size of 98 subjects and the inclusion of pre-

operative patient scans, as well as male and female subjects are, in the author's view, major strengths of the morphological analysis of Chapters 2 and 3. Moreover, presenting the density and geometric measures relative to a resection-based coordinate system makes the interpretation of results far more impactful in the design of stemless humeral implants. This presentation permitted the first quantifications of the spatial envelope that defines the geometric limits for stemless fixation features. The morphological analyses were further strengthened by the automation of measurements (using custom LabVIEW code). By analyzing data in this manner, the 4D point-cloud was assessed independent of user bias; however, repeatability of masking techniques for the selection of the region-of-interest was not directly assessed. Another limitation of the morphological analysis was the use of clinical CT scans as opposed to higher resolution micro-CT. Clinical CT resolution precluded the quantification of micro-architectural outcomes such as trabecular orientation; however, this level of detail was not necessary for the outcome measures that were quantified and would have limited the use of patient data due to ethical limits regarding radiation exposure. Partial volume effects are also an issue with clinical CT resolution, and could have contributed to some variation in the selection of the trabecular-canal boundary; however, partial volume effects are not expected to have influenced the density-values reported in Chapter 2, as these were expressed as an average of each region-of-interest, and further refinement of the voxel size should not change the average value. With this in mind, the resolution of the clinical CT scans obtained was sufficient to quantify the dimensional variations of the proximal humerus. It is difficult to say if improved resolution would be of benefit for the morphological studies of Chapters 2 and 3, as geometric variances quantified to the sub-millimeter level would likely not improve the clinical use of the data. Finally, neither of the morphological assessments presented directly quantified the degree to which some subjects may have had osteoporosis; however, the results presented do reflect a clinical population, as the OA dataset was derived from a clinical database. Though the apparent density values would likely change in cohorts with different levels of osteoporosis, the regional trends regarding higher bone density peripherally, *etc.* are expected to remain similar.

The trabecular stiffness assessment undertaken in Chapter 4 was the first of its kind to directly quantify the deviation in arthroplasty FE outcomes attributable to changing the

trabecular material model based on the anatomic-site from which the stiffness was derived. While past studies have quantified the change in material properties that can be expected between stiffness equations from different anatomic-sites [11], the influence this has on FE outcomes has been missing in the literature. A strength of this analysis was the use of 5 inhomogeneous stiffness equations from different anatomical locations, but that were all derived by a single author using identical methods [11]. Moreover, quantifying the FE population deviation, and including a homogeneous trabecular model provided additional context regarding the level of deviations that would typically be found within a FE analysis of this manner; and helped to confirm that inhomogeneity is an important property to model in trabecular bone. It is also important to remember that the deviations and conclusions regarding the use of site-pooled inhomogeneous trabecular models, are limited to the outcome measures assessed within Chapter 4. Future investigations pertaining to other outcome measures (*e.g.*, implant-bone micro-motion) should also assess how changes to the trabecular material model may affect results. Moreover, the sample size for this investigation ($n = 8$) could generally be regarded as small; however, the inclusion of eight subjects is far greater than the vast majority of FE investigations of joint arthroplasty, as many groups often publish results of single-subject models, and hence are not able to draw statistically-backed conclusions.

Similarly, the investigation of stemless implant geometry in Chapter 5 was the first FE assessment to directly compare more than one stemless humeral implant. To date only one *in-vivo* investigation directly compared the performance of two stemless implants in their patient population [12], and these two implants were very similar in design (TESS and Nano by Zimmer Biomet). Consequently, to assess additional designs, the FE method was chosen for its ability to directly compare multiple implants within the same bone. By applying identical meshing techniques, results were normalized to the intact state on an element-to-element basis for each change in implant fixation feature geometry [6]. Unfortunately, the time required to construct and analyze each FE model limited the sample size ($n = 5$) and the number of stemless implant fixation feature variations that were assessed. In total, Chapter 5 presents the results from 200 FE models (10 implants x 2 models: intact and reconstructed x 2 abduction angles x 5 specimens). Though 10 stemless implant geometries were analyzed, infinitely more variations can be assessed in

future studies; however, this investigation was interested in the comparison of central, peripheral and boundary-crossing fixation features; and implants were designed with this in mind. It should also be noted that the surface area and replaced bone volume was variable between implants. As a consequence, all results were presented as percentages to permit statistical assessment. Another limitation of this work was that the FE models were not strain adaptive. The implementation of an adaptive model could provide a more detailed understanding of how bone density may be expected to change following joint reconstruction; however, the addition of approximately 100 iterations (as per Neuert 2013) in order to simulate progressive density changes would have further limited the number of specimens and implants that were assessed. Accordingly, the SED-based bone response outcome measure used in Chapters 1, 4 and 5 was presented as a ‘potential’ for change based on time-zero (*i.e.*, immediately post-operative) response. As such, these outcomes were offered as the percentage of regional volume with resorbing, unchanged or remodeling potential, rather than the physical density change of each individual bone element, which would have required further iteration to obtain. These time-zero potential bone responses are still meaningful though, as they provide a head-to-head comparison between implants at an instance in time, with less potential for resorbing and remodeling indicating a state more aligned with the intact state, and therefore more favorable.

Finally, it must be noted that the FE method is limited as an approximation of reality, and future work should further complement arthroplasty FE investigations with prospective *in-vivo* radiographic assessments. While FE studies can provide key insights that would otherwise be challenging to obtain via *in-vivo* or *in-vitro* methods, their true strength lies not in the model’s ability to perfectly quantify individual stress and strain values, but rather in the model’s capacity to isolate a single variable (such as an implant geometry change) and conduct parametric assessments as were done herein. This is achieved by constructing multiple FE models, then assessing the difference in outcome variable trends that arise because of these changes. As such, FE outcomes should inform, not dictate implant design.

6.3 Future Directions

While this body of work has presented several new results that have implications for the design of stemless shoulder arthroplasty, there are many more aspects requiring further investigation. The morphological terms quantified in Chapter 3 define a general spatial envelope of the proximal humerus' trabecular-canal. These terms can be refined in the future to include non-symmetric canal dimensions, to expand the bounding diameters presented in Chapter 3. Such measures would provide additional understanding of how the medial-lateral vs. anterior-posterior aspect ratio changes progressing down the canal. In addition, future morphological analyses should increase the patient population investigated to include additional osteoarthritic classifications (*e.g.*, Walch type A1, A2, B1, B2, B3, C, *etc.*). Future morphological work could also assess patients with ranging levels of osteoporosis to determine if these morphological terms vary with age and disease progression.

As suggested above, in Section 6.2, additional stemless shoulder FE investigations are warranted to further assess fixation feature designs. If the geometric variations of a specific investigation can be limited to a few embodiments, then strain adaptive methods can be employed to provide more detail regarding regional density changes following reconstruction. Such a model would be particularly useful for implant manufacturers during the implant design process if it were developed using pre-operative patient CT scans, then validated by a paired *in-vivo* radiographic study following the same patients post-operatively. Should a study of this manner be undertaken it may be advisable to develop a density-modulus relationship specific to the proximal humerus and compare this to the site-pooled relationship employed in this work, as the corresponding deviation in adaptive response may be greater than that of the FE outcomes noted in Chapter 4.

To further develop the FE models from Chapter 5 it is advisable that future studies focus on quantifying outcome measures pertaining to implant stability (*i.e.*, implant-bone micro-motion, gross implant translations, *etc.*). The current FE models focused on the stress and strain response of bone to quantify differences in fixation feature designs. These were chosen as the outcomes of interest since stemless implants have been introduced to the market in part to address concerns regarding stress shielding around

stemless implants [13–16]. While there were some differences noted between central, peripheral and boundary-crossing implants, the cortical response was largely similar for all stemless implants. A retrospective analysis of the models used for mesh convergence in this work suggests that a finer mesh (~1mm element edge-length) may be necessary for quantifying implant-bone motion. Future use of the SED-based time-zero potential bone response should be continued to assess differences between implants; however, without the implementation of an adaptive model, this outcome must always be clearly presented as only reflecting the immediate post-operative state.

6.4 Significance

In-silico radiographic and FE investigations of the proximal humerus are important tools for the design of new shoulder implants. Together, these methods assist with understanding the spatial limits imposed on implant design and the potential response of bone following joint reconstruction. Although FE modeling cannot fully replicate the *in-vivo* condition of humeral arthroplasty, it permits the quantification of invasive measures of bone stress and strain that would be unethical, if not impossible, to obtain in living patients. Though not as important in regulating the use of implants as prospective clinical trials, these *in-silico* methods benefit from their ability to assess several variables that can be easily adapted. Moreover, *in-silico* results can help to guide implant design in the early stages of product development. As such, their application to the relatively young field of stemless shoulder reconstruction is warranted.

Accordingly, with the current offering of stemless implants varying greatly in fixation feature design, the overall goal of this research was to improve the utility of *in-silico* methods in developing new understanding with regards to the morphology of the proximal humerus and the performance of stemless implants. As discussed above, the specific goals set out in Chapter 1 have been achieved. The morphological analyses undertaken have helped to define a better understanding of the distribution of bone density within the proximal humerus, as well as a spatial envelope that quantifies previously assumed boundaries for stemless implant design. It is worth noting that Chapters 2 and 3 are the first morphological analyses of the proximal humerus using a pre-operative clinical population that targeted morphological parameters of interest for

the design of stemless implants. The results of these studies have significant implications regarding implant design, as the population pooled averages can be directly applied when shaping and sizing a fleet of implants to suit a clinically relevant population.

The FE models developed in Chapters 4 and 5 have provided evidence-based decisions regarding the modelling of trabecular bone for stemless shoulder analyses; and have begun to assess the differences in bone response that can be expected when changing the fixation feature geometry of stemless implants. These models have and will continue to assist in quantifying the differences between stemless fixation features as further design iterations are made; and provide a strong foundation for future FE models of stemless shoulder arthroplasty. The time-zero trade-offs noted regarding bone response when switching between central and peripheral fixation features may have been smaller than originally anticipated, but none the less could provide meaningful insight should one form of stemless design be found to outlast others in future long-term clinical trials. Moreover, the consistency of trends in cortical and trabecular bone response across all ten implant designs assessed may suggest that these responses are reflective of stemless shoulder arthroplasty as a whole.

With this in mind, the greatest significance of this work pertains to the evidence these *in-silico* tools have provided for stemless implants in general. Chapters 2 and 3 have demonstrated that radiographic reconstruction can be a useful tool for quantifying bone morphology, which can inform decisions made regarding the design of new stemless implants (*i.e.*, where bone is most dense, how deep should implants be made, how must they curve to remain within the canal, *etc*). The consistency of cortical and trabecular bone responses following stemless reconstruction suggest that postoperative changes are most likely to occur in bone directly beneath the humeral resection plane, in particular within the lateral quadrant. Accordingly, these regions may play a key role in the early identification of implant success or failure following stemless shoulder reconstruction; and should be monitored closely in future prospective clinical trials.

6.5 References

- [1] Berth, A., and Pap, G., 2013, “Stemless shoulder prosthesis versus conventional

anatomic shoulder prosthesis in patients with osteoarthritis: a comparison of the functional outcome after a minimum of two years follow-up.," *J. Orthop. Traumatol.*, **14**(1), pp. 31–7.

- [2] Heuberer, P. R., Brandl, G., Pauzenberger, L., Laky, B., Kriegleder, B., and Anderl, W., 2018, "Radiological changes do not influence clinical mid-term outcome in stemless humeral head replacements with hollow screw fixation: a prospective radiological and clinical evaluation," *BMC Musculoskelet. Disord.*, **19**(28), pp. 1–9.
- [3] Razmjou, H., Holtby, R., Christakis, M., Axelrod, T., and Richards, R., 2013, "Impact of prosthetic design on clinical and radiologic outcomes of total shoulder arthroplasty: A prospective study," *J. Shoulder Elb. Surg.*, **22**(2), pp. 206–214.
- [4] Maier, M. W., Lauer, S., Klotz, M. C., Bühlhoff, M., Spranz, D., and Zeifang, F., 2015, "Are there differences between stemless and conventional stemmed shoulder prostheses in the treatment of glenohumeral osteoarthritis?," *BMC Musculoskelet. Disord.*, **16**(1), p. 275.
- [5] Uschok, S., Magosch, P., Moe, M., Lichtenberg, S., and Habermeyer, P., 2017, "Is the stemless humeral head replacement clinically and radiographically a secure equivalent to standard stem humeral head replacement in the long-term follow-up? A prospective randomized trial," *J. Shoulder Elb. Surg.*, **26**(2), pp. 225–232.
- [6] Razfar, N., Reeves, J. M., Langohr, D. G., Willing, R., Athwal, G. S., and Johnson, J. A., 2016, "Comparison of proximal humeral bone stresses between stemless, short stem, and standard stem length: a finite element analysis," *J. Shoulder Elb. Surg.*, **25**(7), pp. 1076–83.
- [7] Favre, P., and Henderson, A. D., 2016, "Prediction of stemless humeral implant micromotion during upper limb activities," *Clin. Biomech.*, **36**, pp. 46–51.
- [8] Favre, P., Seebeck, J., Thistlethwaite, P. A. E., Obrist, M., Steffens, J. G., Hopkins, A. R., and Hulme, P. A., 2016, "In vitro initial stability of a stemless humeral implant," *Clin. Biomech.*, **32**, pp. 113–117.

- [9] Dahan, G., Trabelsi, N., Safran, O., and Yosibash, Z., 2016, “Verified and validated finite element analyses of humeri,” *J. Biomech.*, **49**(7), pp. 1094–1102.
- [10] Alidousti, H., Giles, J. W., Emery, R. J. H., and Jeffers, J., 2017, “Spatial mapping of humeral head bone density,” *J. Shoulder Elb. Surg.*, (**In Press**).
- [11] Morgan, E. F., Bayraktar, H. H., and Keaveny, T. M., 2003, “Trabecular bone modulus-density relationships depend on anatomic site,” *J. Biomech.*, **36**, pp. 897–904.
- [12] Kadum, B., Wahlstrom, P., Khoschnau, S., Sjoden, G., and Sayed-Noor, A., 2016, “Association of lateral humeral offset with functional outcome and geometric restoration in stemless total shoulder arthroplasty,” *J. Shoulder Elb. Surg.*, **25**(10), pp. e285–e294.
- [13] Nagels, J., Stokdijk, M., and Rozing, P. M., 2003, “Stress shielding and bone resorption in shoulder arthroplasty,” *J. Shoulder Elb. Surg.*, **2746**(2), pp. 35–39.
- [14] Spormann, C., Durchholz, H., Audigé, L., Flury, M., Schwyzer, H. K., Simmen, B. R., and Kolling, C., 2014, “Patterns of proximal humeral bone resorption after total shoulder arthroplasty with an uncemented rectangular stem,” *J. Shoulder Elb. Surg.*, **23**(7), pp. 1028–1035.
- [15] Inoue, K., Suenaga, N., Oizumi, N., Yamaguchi, H., Miyoshi, N., Taniguchi, N., Munemoto, M., Egawa, T., and Tanaka, Y., 2017, “Humeral bone resorption after anatomic shoulder arthroplasty using an uncemented stem,” *J. Shoulder Elb. Surg.*, **26**(11), pp. 1984–1989.
- [16] Verborgt, O., El-Abiad, R., and Gazielly, D. F., 2007, “Long-term results of uncemented humeral components in shoulder arthroplasty,” *J. Shoulder Elb. Surg.*, **16**(3 SUPPL.), pp. 13–18.

Appendices

Appendix A – Glossary

Abduction	The act or state of being drawn away from a position that is nearer or more parallel to the centerline of the body.
Adduction	The act or state of being drawn closer to a position that is nearer or more parallel to the centerline of the body.
Anterior	Situated near the front of the body.
Arthropathy	Refers to a disease of a joint.
Arthroplasty	The surgical replacement or reconstruction of a joint.
Articulation	Synonym for a joint.
Circumduction	Limb movement, such that the distal end traverses a circular motion when the proximal end is fixed.
Comminuted	Term used to describe a severe fracture, where the object of concern has been reduced to several small parts.
Computed Tomography	A procedure commonly used in the medical field, where several X-ray scans are taken in succession and compiled together to provide 3-dimensional images based on radiation attenuation.
Coronal Plane	Imaginary plane that divides the body perpendicular to the anterior-posterior axis.
Distal	Situated further from the center of the body, or further from the point of attachment.

Elastic Modulus	Mechanical property referring to the stiffness of an object; calculated as the force exerted upon the object divided by the resulting deformation.
Epiphysis	The section of a long bone that is located closest to the articular surface.
Diaphysis	The shaft or central section of a long bone.
Glenohumeral Joint	The primary joint of the shoulder, responsible for the greatest range-of-motion. It is formed by the articulation between the glenoid of the scapula and the head of the proximal humerus.
Glenoid	The dish-like surface of the scapula that supports glenohumeral articulation.
Hemi-Arthroplasty	A surgical procedure wherein only one side of the articulation is replaced/reconstructed.
Hooke's Law	Physical relationship governing the extension of elastic objects; indicates that the force applied is equal to the stiffness of the object multiplied by its extension under that force; alternatively expressed as the stress experienced being equal to the elastic modulus multiplied by the strain observed.
Hounsfield Units	A unit used to measure radiation attenuation within CT scans.
Humerus	The long bone of the upper arm, which is responsible for bearing the loads transferred between the shoulder and elbow.
Inferior	Situated below.

Lateral	Situated to one side of the body.
Medial	Situated near the middle of the body.
Metaphysis	Narrow portion of a long bone that is located between the epiphysis and diaphysis, which hosts the growth plate.
Orthopaedics	The branch of medicine concerned with the correction of deformities to the musculoskeletal system (<i>i.e.</i> , bones, muscles, tendons, ligaments, <i>etc</i>).
Osteoarthritis	Degeneration of joint cartilage and the underlying bone; which can lead to joint pain and stiffness.
Osteonecrosis	Refers to the death of bone tissue.
Osteotomy	The surgical procedure of cutting or removing bone.
Poisson's Ratio	Mechanical property referring to the ratio of proportional decrease in the lateral length of an object to its axial elongation.
Posterior	Situated near the back of the body.
Proximal	Situated nearer to the center of the body, or nearer to the point of attachment.
Sagittal Plane	Imaginary plane that divides the body perpendicular to the medial-lateral axis.
Sepsis	Complication arising due to infection; chemicals released into the bloodstream to fight infection trigger inflammatory responses throughout the body, which can damage multiple organ systems.
Strain	Measure of deformation; calculated as the change in length divided by the length of the object that is deformed.

Strain Energy Density	Measure of the internal work/energy per unit volume that is stored within an object as it is distorted.
Stress	Measure of the pressure exerted upon an object; calculated as the force exerted divided by the area over which it is applied. Alternatively calculated from the strain that the object experiences under the applied load using Hooke's law.
Superior	Situated above.
Total Arthroplasty	A surgical procedure wherein both sides of the articulation are replaced/reconstructed.
Transverse Plane	Imaginary plane that divides the body perpendicular to the inferior-superior axis.
Wolff's Law	Bone resorbs and remodels in response to the forces/loads that it is subjected to.

Appendix B – Copyright License for Figure 1.3


RightsLink Printable License

2018-02-18, 11:44 AM

JOHN WILEY AND SONS LICENSE TERMS AND CONDITIONS

Feb 18, 2018

This Agreement between Mr. Jacob Reeves ("You") and John Wiley and Sons ("John Wiley and Sons") consists of your license details and the terms and conditions provided by John Wiley and Sons and Copyright Clearance Center.

License Number	4291990494025
License date	Feb 18, 2018
Licensed Content Publisher	John Wiley and Sons
Licensed Content Publication	Wiley Books
Licensed Content Title	Principles of Human Anatomy, 13th Edition
Licensed Content Author	Gerard J. Tortora Mark Nielsen
Licensed Content Date	Oct 1, 2013
Licensed Content Pages	1
Type of use	Dissertation/Thesis
Requestor type	University/Academic
Format	Print and electronic
Portion	Figure/table
Number of figures/tables	1
Original Wiley figure/table number(s)	pha12e_fig_06_02b - From Principles of Human Anatomy 12th-edition
Will you be translating?	No
Title of your thesis / dissertation	Tools for Assessing Stemless Shoulder Arthroplasty
Expected completion date	Aug 2018
Expected size (number of pages)	250
Requestor Location	Mr. Jacob Reeves 
Publisher Tax ID	EU826007151
Total	0.00 USD
Terms and Conditions	

TERMS AND CONDITIONS

This copyrighted material is owned by or exclusively licensed to John Wiley & Sons, Inc. or one of its group companies (each a "Wiley Company") or handled on behalf of a society with which a Wiley Company has exclusive publishing rights in relation to a particular work (collectively "WILEY"). By clicking "accept" in connection with completing this licensing transaction, you agree that the following terms and conditions apply to this transaction (along with the billing and payment terms and conditions established by the Copyright Clearance Center Inc., ("CCC's Billing and Payment terms and conditions"), at the time that you opened your RightsLink account (these are available at any time at <http://myaccount.copyright.com>).

Terms and Conditions

- The materials you have requested permission to reproduce or reuse (the "Wiley Materials") are protected by copyright.
- You are hereby granted a personal, non-exclusive, non-sub licensable (on a stand-alone basis), non-transferable, worldwide, limited license to reproduce the Wiley Materials for the purpose specified in the licensing process. This license, **and any CONTENT (PDF or image file) purchased as part of your order**, is for a one-time use only and limited to any maximum distribution number specified in the license. The first instance of republication or reuse granted by this license must be completed within two years of the date of the grant of this license (although copies prepared before the end date may be distributed thereafter). The Wiley Materials shall not be used in any other manner or for any other purpose, beyond what is granted in the license. Permission is granted subject to an appropriate acknowledgement given to the author, title of the material/book/journal and the publisher. You shall also duplicate the copyright notice that appears in the Wiley publication in your use of the Wiley Material. Permission is also granted on the understanding that nowhere in the text is a previously published source acknowledged for all or part of this Wiley Material. Any third party content is expressly excluded from this permission.
- With respect to the Wiley Materials, all rights are reserved. Except as expressly granted by the terms of the license, no part of the Wiley Materials may be copied, modified, adapted (except for minor reformatting required by the new Publication), translated, reproduced, transferred or distributed, in any form or by any means, and no derivative works may be made based on the Wiley Materials without the prior permission of the respective copyright owner. **For STM Signatory Publishers clearing permission under the terms of the [STM Permissions Guidelines](#) only, the terms of the license are extended to include subsequent editions and for editions in other languages, provided such editions are for the work as a whole in situ and does not involve the separate exploitation of the permitted figures or extracts**, You may not alter, remove or suppress in any manner any copyright, trademark or other notices displayed by the Wiley Materials. You may not license, rent, sell, loan, lease, pledge, offer as security, transfer or assign the Wiley Materials on a stand-alone basis, or any of the rights granted to you hereunder to any other person.

- The Wiley Materials and all of the intellectual property rights therein shall at all times remain the exclusive property of John Wiley & Sons Inc, the Wiley Companies, or their respective licensors, and your interest therein is only that of having possession of and the right to reproduce the Wiley Materials pursuant to Section 2 herein during the continuance of this Agreement. You agree that you own no right, title or interest in or to the Wiley Materials or any of the intellectual property rights therein. You shall have no rights hereunder other than the license as provided for above in Section 2. No right, license or interest to any trademark, trade name, service mark or other branding ("Marks") of WILEY or its licensors is granted hereunder, and you agree that you shall not assert any such right, license or interest with respect thereto
- NEITHER WILEY NOR ITS LICENSORS MAKES ANY WARRANTY OR REPRESENTATION OF ANY KIND TO YOU OR ANY THIRD PARTY, EXPRESS, IMPLIED OR STATUTORY, WITH RESPECT TO THE MATERIALS OR THE ACCURACY OF ANY INFORMATION CONTAINED IN THE MATERIALS, INCLUDING, WITHOUT LIMITATION, ANY IMPLIED WARRANTY OF MERCHANTABILITY, ACCURACY, SATISFACTORY QUALITY, FITNESS FOR A PARTICULAR PURPOSE, USABILITY, INTEGRATION OR NON-INFRINGEMENT AND ALL SUCH WARRANTIES ARE HEREBY EXCLUDED BY WILEY AND ITS LICENSORS AND WAIVED BY YOU.
- WILEY shall have the right to terminate this Agreement immediately upon breach of this Agreement by you.
- You shall indemnify, defend and hold harmless WILEY, its Licensors and their respective directors, officers, agents and employees, from and against any actual or threatened claims, demands, causes of action or proceedings arising from any breach of this Agreement by you.
- IN NO EVENT SHALL WILEY OR ITS LICENSORS BE LIABLE TO YOU OR ANY OTHER PARTY OR ANY OTHER PERSON OR ENTITY FOR ANY SPECIAL, CONSEQUENTIAL, INCIDENTAL, INDIRECT, EXEMPLARY OR PUNITIVE DAMAGES, HOWEVER CAUSED, ARISING OUT OF OR IN CONNECTION WITH THE DOWNLOADING, PROVISIONING, VIEWING OR USE OF THE MATERIALS REGARDLESS OF THE FORM OF ACTION, WHETHER FOR BREACH OF CONTRACT, BREACH OF WARRANTY, TORT, NEGLIGENCE, INFRINGEMENT OR OTHERWISE (INCLUDING, WITHOUT LIMITATION, DAMAGES BASED ON LOSS OF PROFITS, DATA, FILES, USE, BUSINESS OPPORTUNITY OR CLAIMS OF THIRD PARTIES), AND WHETHER OR NOT THE PARTY HAS BEEN ADVISED OF THE POSSIBILITY OF SUCH DAMAGES. THIS LIMITATION SHALL APPLY NOTWITHSTANDING ANY FAILURE OF ESSENTIAL PURPOSE OF ANY LIMITED REMEDY PROVIDED HEREIN.
- Should any provision of this Agreement be held by a court of competent jurisdiction to be illegal, invalid, or unenforceable, that provision shall be deemed amended to

achieve as nearly as possible the same economic effect as the original provision, and the legality, validity and enforceability of the remaining provisions of this Agreement shall not be affected or impaired thereby.

- The failure of either party to enforce any term or condition of this Agreement shall not constitute a waiver of either party's right to enforce each and every term and condition of this Agreement. No breach under this agreement shall be deemed waived or excused by either party unless such waiver or consent is in writing signed by the party granting such waiver or consent. The waiver by or consent of a party to a breach of any provision of this Agreement shall not operate or be construed as a waiver of or consent to any other or subsequent breach by such other party.
- This Agreement may not be assigned (including by operation of law or otherwise) by you without WILEY's prior written consent.
- Any fee required for this permission shall be non-refundable after thirty (30) days from receipt by the CCC.
- These terms and conditions together with CCC's Billing and Payment terms and conditions (which are incorporated herein) form the entire agreement between you and WILEY concerning this licensing transaction and (in the absence of fraud) supersedes all prior agreements and representations of the parties, oral or written. This Agreement may not be amended except in writing signed by both parties. This Agreement shall be binding upon and inure to the benefit of the parties' successors, legal representatives, and authorized assigns.
- In the event of any conflict between your obligations established by these terms and conditions and those established by CCC's Billing and Payment terms and conditions, these terms and conditions shall prevail.
- WILEY expressly reserves all rights not specifically granted in the combination of (i) the license details provided by you and accepted in the course of this licensing transaction, (ii) these terms and conditions and (iii) CCC's Billing and Payment terms and conditions.
- This Agreement will be void if the Type of Use, Format, Circulation, or Requestor Type was misrepresented during the licensing process.
- This Agreement shall be governed by and construed in accordance with the laws of the State of New York, USA, without regards to such state's conflict of law rules. Any legal action, suit or proceeding arising out of or relating to these Terms and Conditions or the breach thereof shall be instituted in a court of competent jurisdiction in New York County in the State of New York in the United States of America and each party hereby consents and submits to the personal jurisdiction of such court, waives any objection to venue in such court and consents to service of process by registered or certified mail, return receipt requested, at the last known address of such party.

WILEY OPEN ACCESS TERMS AND CONDITIONS

Wiley Publishes Open Access Articles in fully Open Access Journals and in Subscription journals offering Online Open. Although most of the fully Open Access journals publish open access articles under the terms of the Creative Commons Attribution (CC BY) License only, the subscription journals and a few of the Open Access Journals offer a choice of Creative Commons Licenses. The license type is clearly identified on the article.

The Creative Commons Attribution License

The [Creative Commons Attribution License \(CC-BY\)](#) allows users to copy, distribute and transmit an article, adapt the article and make commercial use of the article. The CC-BY license permits commercial and non-

Creative Commons Attribution Non-Commercial License

The [Creative Commons Attribution Non-Commercial \(CC-BY-NC\) License](#) permits use, distribution and reproduction in any medium, provided the original work is properly cited and is not used for commercial purposes.(see below)

Creative Commons Attribution-Non-Commercial-NoDerivs License

The [Creative Commons Attribution Non-Commercial-NoDerivs License \(CC-BY-NC-ND\)](#) permits use, distribution and reproduction in any medium, provided the original work is properly cited, is not used for commercial purposes and no modifications or adaptations are made. (see below)

Use by commercial "for-profit" organizations

Use of Wiley Open Access articles for commercial, promotional, or marketing purposes requires further explicit permission from Wiley and will be subject to a fee.

Further details can be found on Wiley Online Library

<http://olabout.wiley.com/WileyCDA/Section/id-410895.html>

Other Terms and Conditions:

v1.10 Last updated September 2015

Questions? [REDACTED] **(toll free in the US) or**
[REDACTED]

Appendix C – Mesh Convergence

C.1 Materials and Methods

To assess the sensitivity of the finite element model to mesh size, one cadaveric humerus was reconstructed *in-silico* using the Simpliciti stemless shoulder implant (Tornier Simpliciti; Wright BioMedical, Staines-upon-Thames, Middlesex, UK). Four Finite Element (FE) models were developed for the reconstruction, with the only variable between models being the mesh size. Based on previous FE studies of the proximal humerus, a 2mm average element edge length was chosen as the reference mesh size [1,2]. This mesh size corresponded to 152,449 elements within the cortical and trabecular bone that remained following joint reconstruction. In addition to the 2mm mesh, 1.4mm, 1.2mm, and 1.0mm models were also created, which corresponded to approximately doubling (320,751 elements), tripling (449,878 elements), and quadrupling (577,388 elements) the number of bone elements within the reconstructed models, respectively. Larger mesh sizes were not considered, as the intricacies of the stemless implant could not be accurately approximated with coarser elements. In addition to the reconstructed bone models, intact bone models were also developed with identical bone meshes to permit the evaluation of outcome measures that utilize element-to-element comparisons [1].

The FE model parameters used for mesh convergence assessment are the same as those described in Chapters 4 and 5 but are summarized here. All FE models were meshed using quadratic tetrahedral elements. The elements corresponding to the cortical bone were assigned a homogenous and isotropic elastic modulus of 20GPa, with a Poisson's ratio of 0.3 [1,3,4]; while the trabecular elements were inhomogeneous, and isotropically mapped using Morgan *et al*'s site-pooled density-modulus regression and were again assigned a Poisson's ratio of 0.3 [5]. Bone density was linearly calibrated from CT attenuation data (in Hounsfield Units, HU), using a SB3-H2O calibration phantom of known apparent densities (1.82g/cm^3 and 0g/cm^3 , respectively) that was scanned alongside the cadaver [6].

All FE models were fixed at the mid-diaphysis (180mm from the superior-most resection plane point) and were loaded with joint reaction forces derived from *in-vivo* telemetrized implant data [7]. Two loading configurations were considered for each model: 45° abduction (440N), and 75° abduction (740N) [1,7]. Joint reaction forces were oriented using the telemetrized force vectors and were based on a 50th percentile male body weight of 88.3kg [1].

FE model sensitivity to mesh size was assessed for outcome measures of: implant-bone contact pressure distribution, the absolute percentage change in von Mises stress for bone, and the potential time-zero bone response (SED-based). Implant-bone contact pressure distribution quantifies what percentage of the available implant-bone contact area fall within a distribution of contact pressures (from 0-2+ MPa). The change in bone stress outcome calculates the von Mises stress from the difference between each reconstructed and intact model element, then presents this as a percentage change relative to the intact stress. Finally, the potential bone response categorizes the bone volume into three groups corresponding to elements that have potential to resorb, remodel, or remain unchanged according to how their Strain Energy Density (SED) varies in the reconstructed model compared to the intact model (resorbing potential if: reconstructed SED < 0.45x intact SED; unchanged if: 0.45x intact SED ≤ reconstructed SED ≤ 1.55x intact SED; remodeling potential if: reconstructed SED > 1.55x intact SED). Both changes in bone stress and the potential bone response were quantified separately for cortical and trabecular bone, which were sub-divided into eight 5mm thick slices beneath and parallel to the humeral head resection plane. Mesh sensitivity was further assessed by quantifying the amount of time required to run the FE analysis.

All models were run using Abaqus (version 6.14; Dassault Systèmes Corp, Waltham, MA, USA) on the same computer. The computer specifications were as follows: 48GB of ram, socket 2011 dual threaded hex-core Intel i7-4930k CPU (3.40GHz).

C.2 Results

The model run time differed depending on mesh size, with run time increasing greatly as mesh size decreased (Figure C.1). Doubling, tripling and quadrupling the number of bone

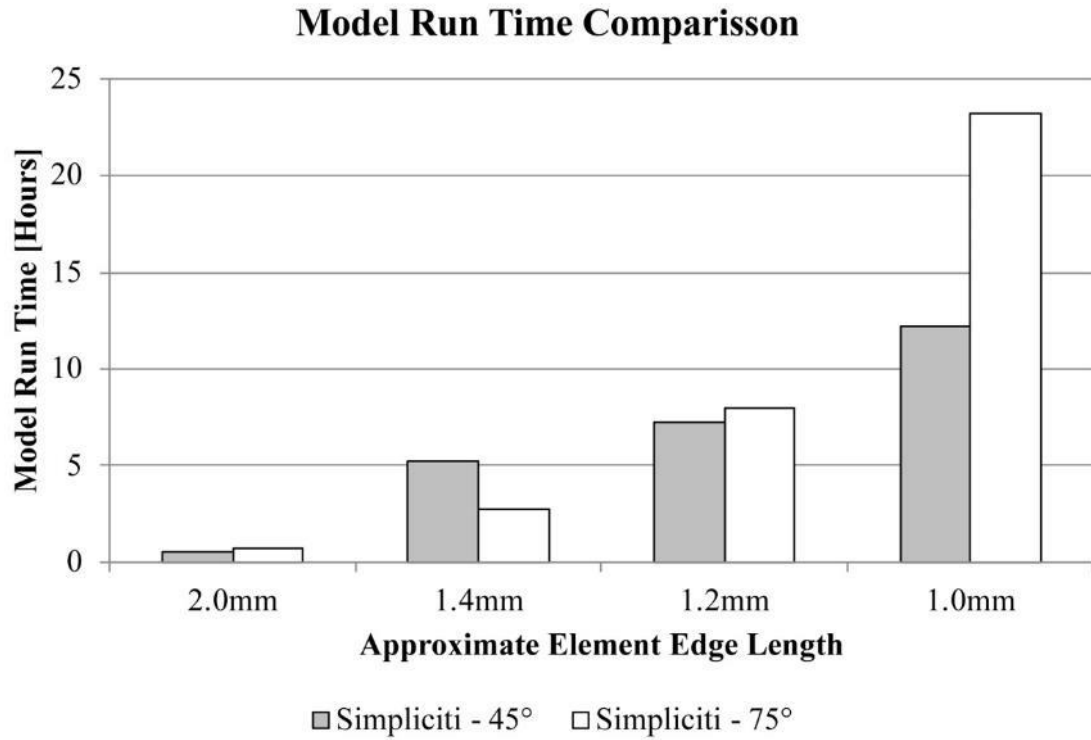


Figure C.1: Model run time broken down according to mesh size and abduction angle.

elements resulted in 6x, 12x and 28x increases in model run time compared to the 2.0mm mesh size.

The implant-bone contact pressure remained relatively constant despite mesh refinement, with the most evident changes presenting in the no contact (0MPa) group (Figure C.2), where the 2.0mm mesh produced approximately 2% less contact overall than the 1.0mm mesh (Table C.1). Overall, the distribution of contact area across different contact pressures demonstrated the same trend regardless of mesh size.

The change in bone stress following joint reconstruction, expressed as an absolute percentage change also presented with few variations attributable to mesh size (Figure C.3). The changes in cortical bone stress were particularly steady despite mesh refinement, regardless of abduction angle and slice depth. The trabecular bone stress changes did fluctuate somewhat with mesh refinement. This was most pronounced 0-5mm beneath the humeral head resection for 45° of abduction (Figure C.3). The trend within this region was for the stress changes to increase with denser meshes, before returning closer to the 2.0mm results when a 1.0mm mesh size was used. Despite this, quadrupling the mesh size resulted in minor changes compared to the 2.0mm mesh, with differences less than 4% for trabecular bone and 3% for cortical bone, regardless of slice depth and abduction angle (Figure C.4). Overall, the 2.0mm mesh resulted in slightly lower reported changes in bone stress compare to the finest 1.0mm mesh.

The potential time-zero bone responses also presented with minor differences attributable to mesh size variations, as is demonstrated by the consistency of Figures C.5 - C.8. The breakdown of changes in potential bone response according to slice depth is presented in Tables C.2 and C.3. Overall, changing from a 2.0mm mesh to a 1.0mm mesh resulted in mean differences (pooled across all slice depths) that ranged from $-2.6 \pm 3.4\%$ to $2.0 \pm 1.5\%$ for cortical bone, and from $-1.5 \pm 1.8\%$ to $2.1 \pm 1.3\%$ for trabecular bone.

C.3 Discussion

The results of mesh sensitivity analysis suggest that there are only minor differences in the implant-bone contact distribution, change in bone stress, and potential time-zero bone response outcome measures that can be attributed to refining the FE mesh size beyond

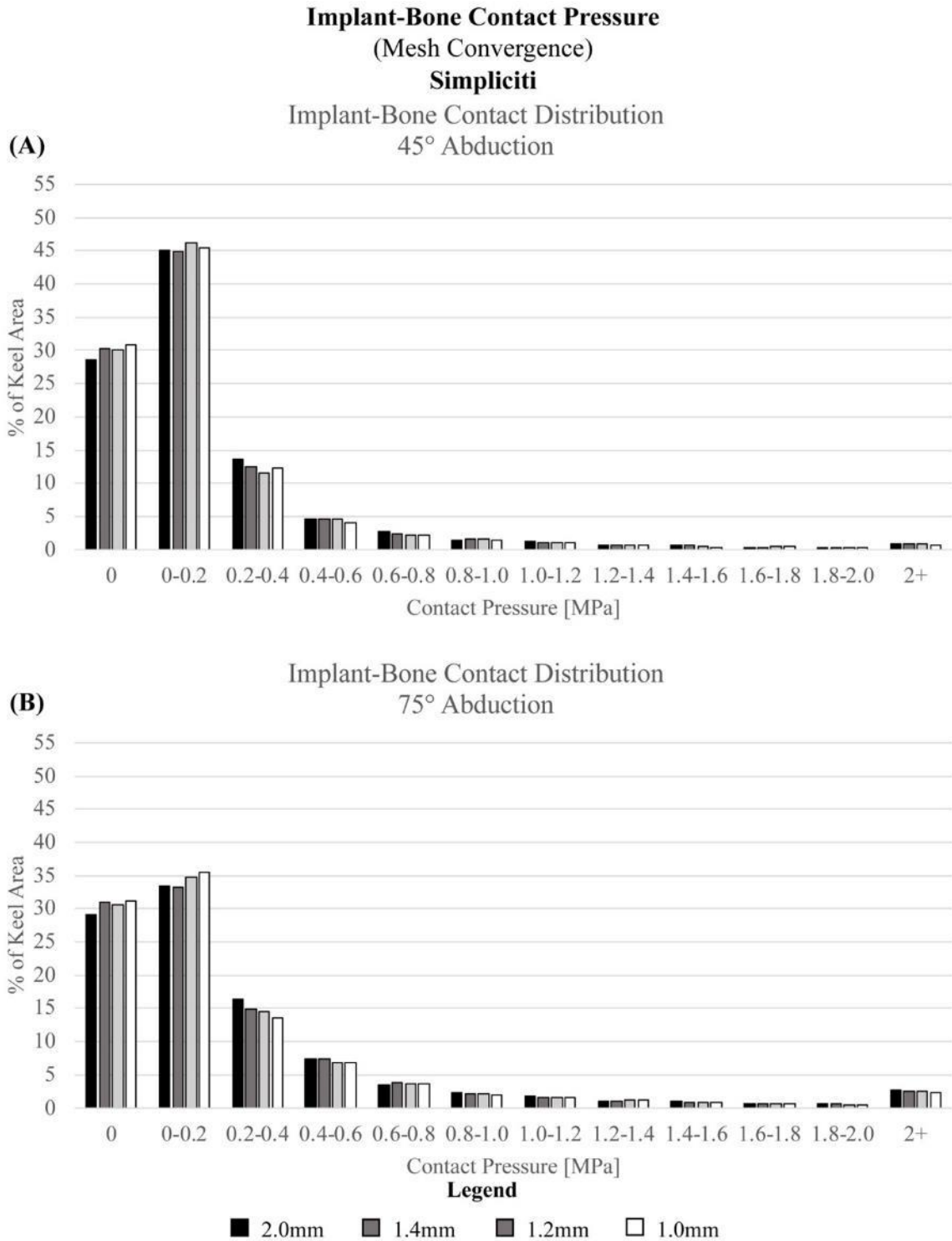


Figure C.2: Implant bone contact pressure distribution for all mesh sizes, shown for loading corresponding to both 45° (A) and 75° (B) of abduction.

Table C.1: Comparison of implant-bone contact pressure distribution for mesh refinement.

Implant-Bone Contact Pressure			
(Mesh Convergence)			
Simpliciti			
Change in Implant-Bone Contact Area [%]			
Contact Pressure	45° Abduction		
Group [MPa]	(1.4mm)-(2.0mm)	(1.2mm)-(2.0mm)	(1.0mm)-(2.0mm)
0	1.7	1.6	2.3
0-0.2	-0.2	1.1	0.4
0.2-0.4	-1.0	-2.0	-1.1
0.4-0.6	0.0	0.0	-0.5
0.6-0.8	-0.4	-0.6	-0.6
0.8-1.0	0.1	0.1	0.0
1.0-1.2	-0.2	-0.2	-0.2
1.2-1.4	0.0	0.0	0.1
1.4-1.6	0.0	-0.2	-0.2
1.6-1.8	-0.1	0.1	0.1
1.8-2.0	-0.1	-0.1	-0.1
2+	0.1	0.0	-0.2
Contact Pressure	75° Abduction		
Group [MPa]	(1.4mm)-(2.0mm)	(1.2mm)-(2.0mm)	(1.0mm)-(2.0mm)
0	1.8	1.4	2.0
0-0.2	-0.1	1.4	2.1
0.2-0.4	-1.4	-1.7	-2.7
0.4-0.6	0.1	-0.5	-0.6
0.6-0.8	0.4	0.1	0.2
0.8-1.0	-0.3	-0.3	-0.3
1.0-1.2	-0.1	-0.2	-0.2
1.2-1.4	0.0	0.2	0.0
1.4-1.6	-0.1	-0.2	-0.1
1.6-1.8	0.0	0.0	0.0
1.8-2.0	0.0	-0.1	-0.1
2+	-0.2	-0.2	-0.4

Change in Bone Stress [%] (Mesh Convergence)

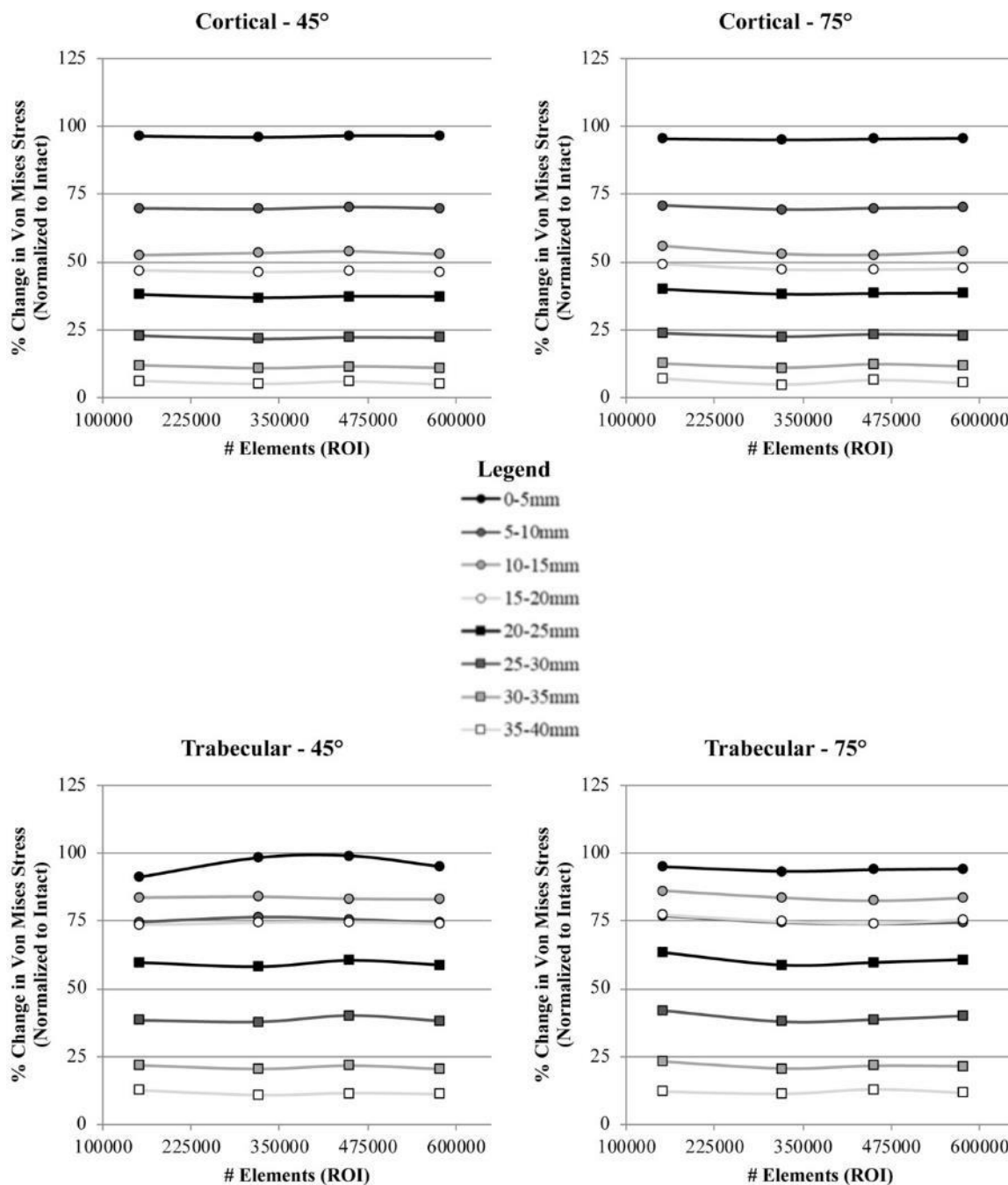


Figure C.3: Comparison of the change in bone stress outcome measure between different mesh sizes for both cortical and trabecular bone at 45° and 75° of abduction.

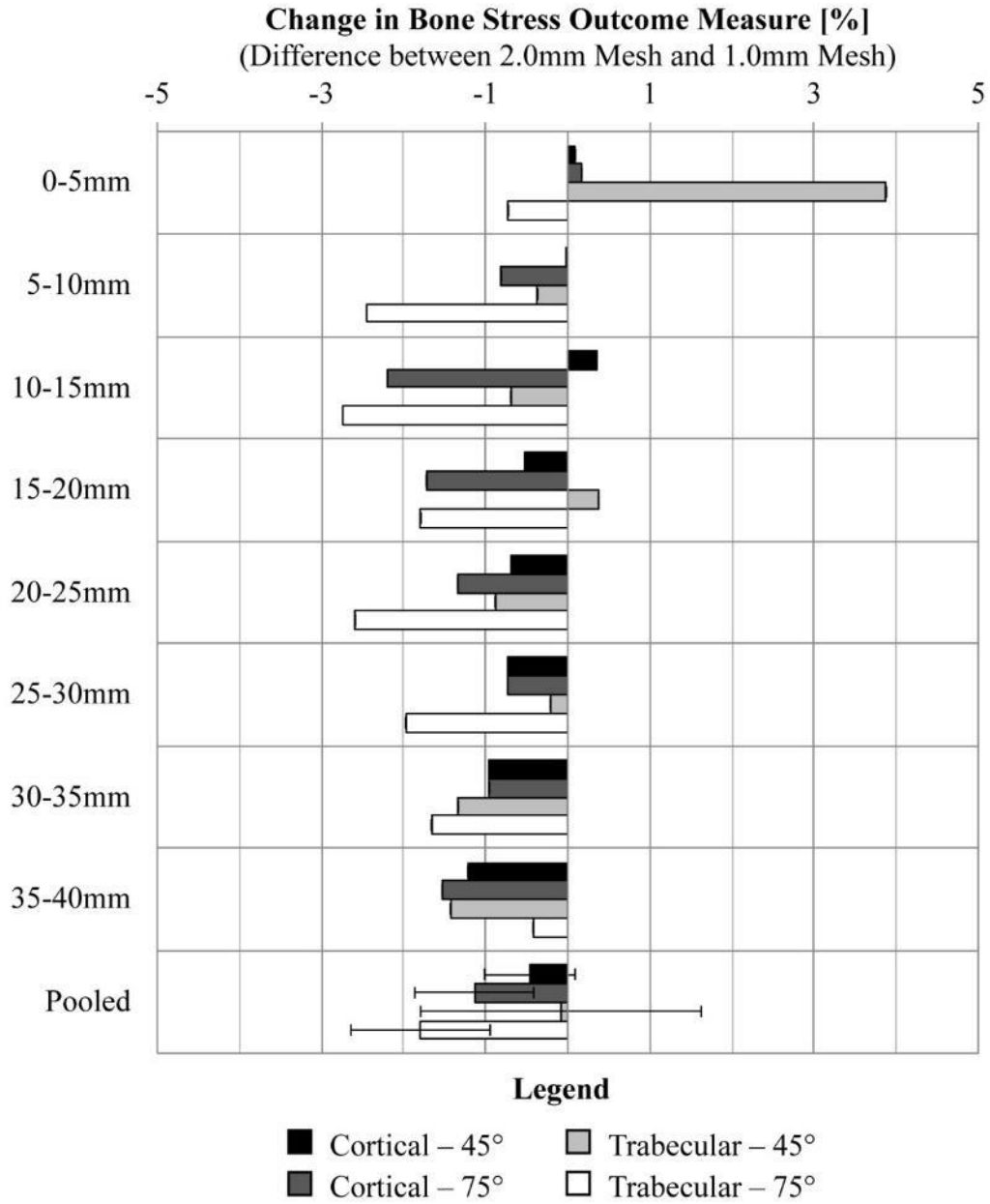


Figure C.4: Direct comparison of the difference in the change in bone stress outcome measure between 2.0mm and 1.0mm mesh sizes.

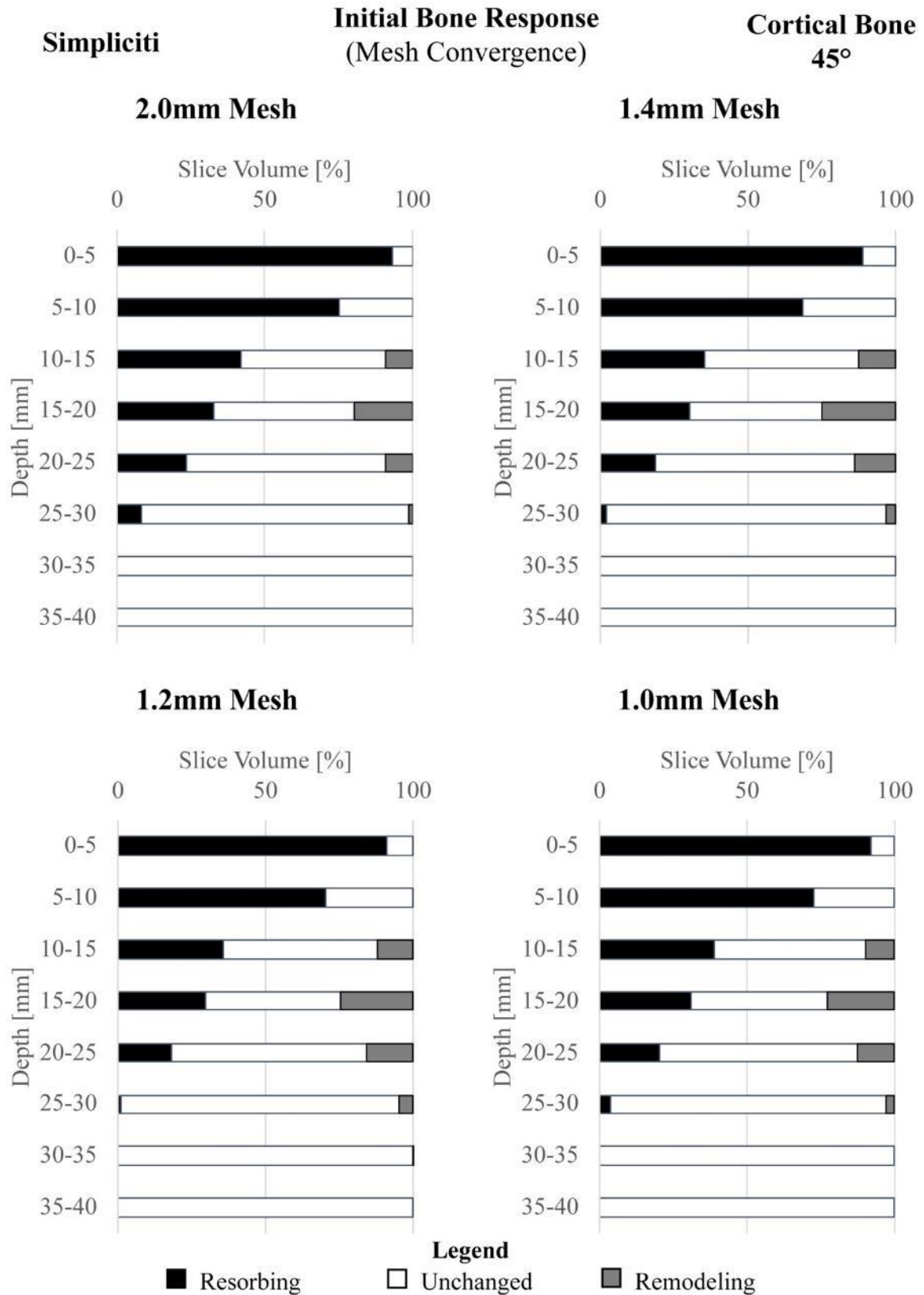


Figure C.5: Time-zero potential bone response of cortical bone subject to 45° loading.

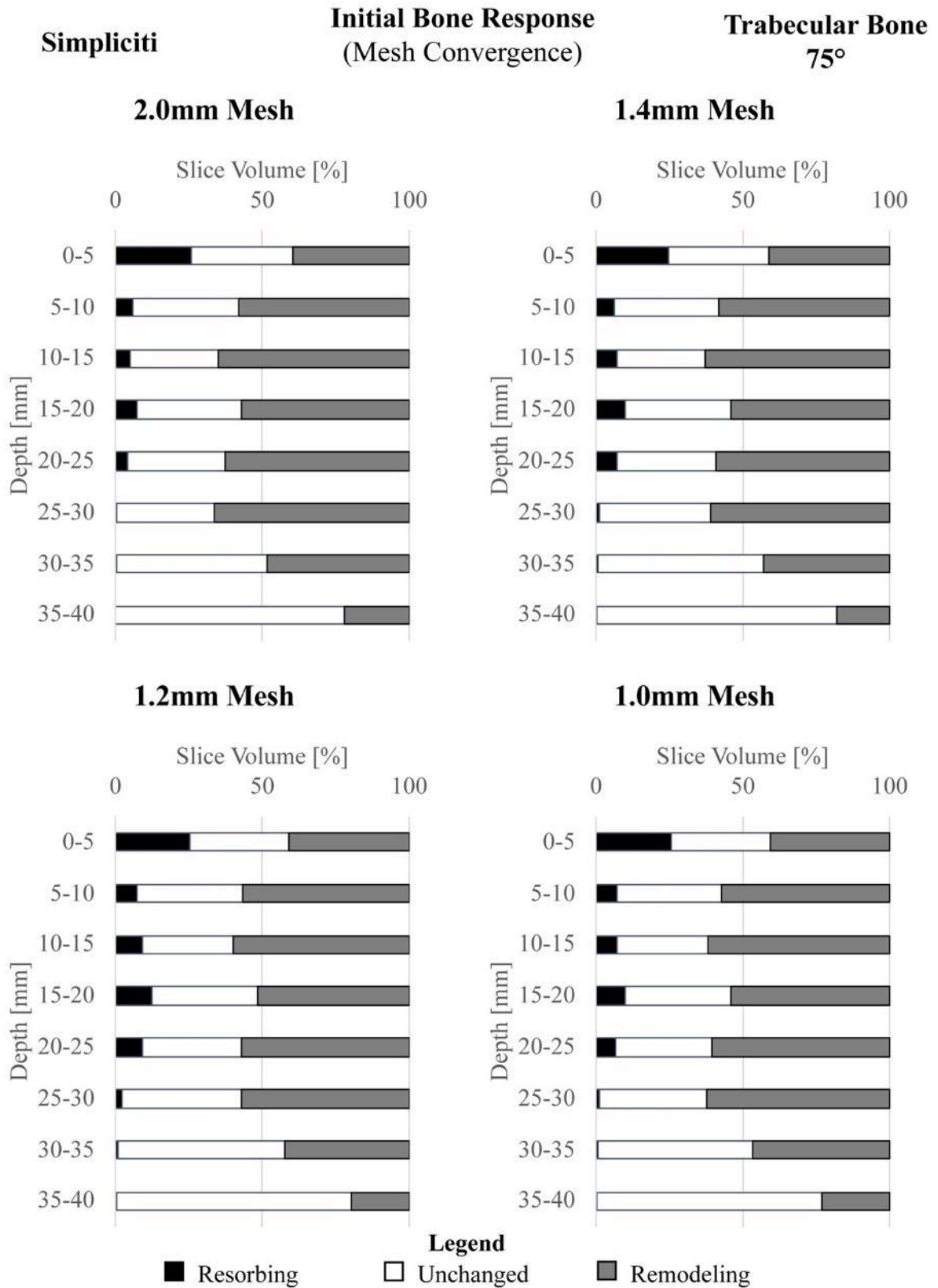


Figure A.C: Time-zero potential bone response of trabecular bone subject to 75° loading.

Table C.2: Comparison of the potential bone response for mesh refinement – 45° of abduction.

Change in Volume [%]									
Cortical Bone - 45° Loading									
Depth [mm]	(1.4mm) - (2.0mm)			(1.2mm) - (2.0mm)			(1.0mm) - (2.0mm)		
	Resorbing	Unchanged	Remodeling	Resorbing	Unchanged	Remodeling	Resorbing	Unchanged	Remodeling
0-5	-4.3	4.3	0.0	-2.3	2.3	0.0	-1.6	1.6	0.0
5-10	-6.3	6.3	0.0	-4.6	4.6	0.0	-2.4	2.4	0.0
10-15	-6.5	3.0	3.5	-6.1	2.9	3.2	-3.0	2.2	0.9
15-20	-2.9	-2.0	4.9	-3.4	-1.5	4.9	-1.7	-1.1	2.9
20-25	-4.6	-0.2	4.9	-5.2	-1.9	7.0	-3.0	-0.6	3.6
25-30	-6.3	4.2	2.1	-7.2	3.9	3.3	-4.6	3.1	1.5
30-35	0.0	0.0	0.0	0.0	0.0	0.0	0.0	0.0	0.0
35-40	0.0	0.0	0.0	0.0	0.0	0.0	0.0	0.0	0.0
Pooled	-3.9	2.0	1.9	-3.6	1.3	2.3	-2.1	1.0	1.1
SD	(2.7)	(2.9)	(2.2)	(2.7)	(2.5)	(2.7)	(1.6)	(1.6)	(1.4)
Trabecular Bone - 45° Loading									
Depth [mm]	(1.4mm) - (2.0mm)			(1.2mm) - (2.0mm)			(1.0mm) - (2.0mm)		
	Resorbing	Unchanged	Remodeling	Resorbing	Unchanged	Remodeling	Resorbing	Unchanged	Remodeling
0-5	-1.2	0.0	1.2	-0.1	-1.2	1.3	-0.4	-0.5	1.0
5-10	-0.1	-0.6	0.7	0.7	-0.7	0.0	0.4	-0.4	-0.1
10-15	-2.1	-1.4	3.5	-2.3	-0.1	2.4	-1.0	-0.8	1.7
15-20	-2.6	-1.1	3.7	-3.2	-0.2	3.4	-1.4	-0.4	1.8
20-25	-3.1	0.9	2.2	-3.9	0.7	3.2	-2.2	0.4	1.7
25-30	-1.3	-3.3	4.6	-1.5	-4.3	5.8	-0.9	-2.2	3.1
30-35	0.1	-3.0	2.9	0.1	-5.8	5.7	0.2	-3.9	3.6
35-40	0.0	-1.7	1.7	0.1	-6.5	6.4	0.2	-3.9	3.8
Pooled	-1.3	-1.3	2.6	-1.3	-2.3	3.5	-0.6	-1.4	2.1
SD	(1.2)	(1.4)	(1.3)	(1.7)	(2.8)	(2.3)	(0.9)	(1.7)	(1.3)

Table C.3: Comparison of the potential bone response for mesh refinement – 75° of abduction.

Change in Volume [%]									
Cortical Bone - 75° Loading									
Depth [mm]	(1.4mm) - (2.0mm)			(1.2mm) - (2.0mm)			(1.0mm) - (2.0mm)		
	Resorbing	Unchanged	Remodeling	Resorbing	Unchanged	Remodeling	Resorbing	Unchanged	Remodeling
0-5	0.3	-0.3	0.0	1.8	-1.8	0.0	1.5	-1.5	0.0
5-10	2.5	-2.5	0.0	5.6	-5.6	0.0	3.7	-3.7	0.0
10-15	1.7	0.7	-2.4	4.7	-1.3	-3.4	2.0	0.2	-2.2
15-20	2.1	3.4	-5.5	3.7	6.3	-10.1	1.9	3.6	-5.5
20-25	4.7	6.5	-11.3	7.4	8.0	-15.4	4.0	5.5	-9.5
25-30	3.9	0.3	-4.3	8.3	-2.3	-5.9	2.8	0.4	-3.2
30-35	0.0	0.4	-0.4	0.0	0.4	-0.4	0.0	0.3	-0.3
35-40	0.0	0.0	0.0	0.0	0.0	0.0	0.0	0.0	0.0
Pooled	1.9	1.1	-3.0	3.9	0.5	-4.4	2.0	0.6	-2.6
SD	(1.8)	(2.7)	(4.0)	(3.1)	(4.5)	(5.7)	(1.5)	(2.8)	(3.4)
Trabecular Bone - 75° Loading									
Depth [mm]	(1.4mm) - (2.0mm)			(1.2mm) - (2.0mm)			(1.0mm) - (2.0mm)		
	Resorbing	Unchanged	Remodeling	Resorbing	Unchanged	Remodeling	Resorbing	Unchanged	Remodeling
0-5	-1.2	0.1	1.1	-0.5	-0.4	0.9	-0.3	-0.5	0.8
5-10	0.4	-0.8	0.4	1.5	0.0	-1.5	1.2	-0.5	-0.7
10-15	2.0	0.3	-2.3	4.1	1.1	-5.2	2.1	0.9	-2.9
15-20	2.7	0.2	-2.9	5.0	0.5	-5.5	2.4	0.5	-3.0
20-25	3.1	0.3	-3.4	5.0	0.5	-5.5	2.3	-0.1	-2.2
25-30	0.8	4.3	-5.1	1.6	7.4	-9.0	0.6	3.3	-4.0
30-35	0.3	4.7	-5.0	0.4	5.6	-6.1	0.3	1.2	-1.5
35-40	0.1	3.6	-3.7	0.2	2.1	-2.3	0.2	-1.2	1.0
Pooled	1.0	1.6	-2.6	2.2	2.1	-4.3	1.1	0.5	-1.5
SD	(1.5)	(2.2)	(2.3)	(2.2)	(2.9)	(3.1)	(1.1)	(1.4)	(1.8)

2.0mm. Unfortunately, the intricacies of the stemless implant's fixation features prevented the use of mesh sizes that were coarser than 2.0mm, which made further comparisons impossible.

The computational time required to analyze reconstructed models greatly increased with increasing mesh density. When using FE models to compare different implants, it is beneficial to use multiple cadavers and assess several designs within the same investigation; accordingly, reducing computational demand can be a great benefit, permitting the assessment of additional implants within the same time constraints.

The present investigation was limited to assessing mesh sensitivity within a single cadaveric specimen. While further specimens could be beneficial, the consistency of the outcome measures regardless of mesh refinement suggests that the 2.0mm mesh size may be acceptable for the modeling the humeral side of an anatomic stemless shoulder reconstruction. These findings agree with previous humeral reconstruction and fracture analyses by Razfar et al and Dahan et al, respectively; who also used 2.0mm quadratic tetrahedral meshes for their assessments.

C.4 References

- [1] Razfar, N., Reeves, J. M., Langohr, D. G., Willing, R., Athwal, G. S., and Johnson, J. A., 2016, "Comparison of proximal humeral bone stresses between stemless, short stem, and standard stem length: a finite element analysis," *J. Shoulder Elb. Surg.*, **25**(7), pp. 1076–83.
- [2] Dahan, G., Trabelsi, N., Safran, O., and Yosibash, Z., 2016, "Verified and validated finite element analyses of humeri," *J. Biomech.*, **49**(7), pp. 1094–1102.
- [3] Bayraktar, H. H., Morgan, E. F., Niebur, G. L., Morris, G. E., Wong, E. K., and Keaveny, T. M., 2004, "Comparison of the elastic and yield properties of human femoral trabecular and cortical bone tissue," *J. Biomech.*, **37**(1), pp. 27–35.
- [4] Rho, J. Y., Ashman, R. B., and Turner, C. H., 1993, "Young's modulus of trabecular and cortical bone material: Ultrasonic and microtensile measurements," *J. Biomech.*, **26**(2), pp. 111–119.

- [5] Morgan, E. F., Bayraktar, H. H., and Keaveny, T. M., 2003, “Trabecular bone modulus-density relationships depend on anatomic site,” *J. Biomech.*, **36**, pp. 897–904.
- [6] Knowles, N. K., Reeves, J. M., and Ferreira, L. M., 2016, “Quantitative Computed Tomography (QCT) derived Bone Mineral Density (BMD) in finite element studies: a review of the literature,” *J. Exp. Orthop.*, **3**(1), p. 36.
- [7] Bergmann, G., Graichen, F., Bender, A., Kaab, M., Rohlmann, A., and Westerhoff, P., 2007, “In vivo glenohumeral contact forces-Measurements in the first patient 7 months postoperatively,” *J. Biomech.*, **40**(10), pp. 2139–2149.

Appendix D – Finite Element Validation

D.1 Introduction

The Finite Element (FE) method has become a common *in-silico* tool for assessing implant performance following joint reconstruction. This computational method permits the probing of stress and strain within an implant-bone construct non-invasively by discretizing the continuous structure into a finite number of volume regions, termed ‘elements’. When paired, models of the intact and reconstructed joint state can provide insight into the bone’s response to arthroplasty [1]; which is of particular help when assessing the phenomena of stress shielding that is observed *in-vivo* [2–5]. While FE models are useful for their parametric ability to assess several different variations within a controlled environment, they rely on numerous assumptions to mimic reality. Some common approximations associated with the construction of FE models of bone include: (i) the load application, (ii) the stiffness (*viz.* modulus) applied to cortical and trabecular bone, (iii) the interface conditions between the implant and bone, and (iv) the mesh type and density.

Several FE models have been developed for the proximal humerus [1,6–13]. These range from assessments focused on fractures of the native humerus [6], to investigations of the stress shielding response of bone following arthroplasty [1]. The loads applied to the proximal humerus during daily activities are well documented by *in-vivo* telemetrized implant studies [14–16]. With respect to material properties, there is a general consensus that bone can be modelled with isotropic stiffness to save computational resources [17]. Additionally, cortical bone is usually considered to be homogeneous, with a stiffness of approximately 20GPa [18,19]. When modelling the humerus for the purpose of assessing the stress and strain response of bone, the trabecular region is usually considered to have a stiffness that is inhomogeneous, varying as a function of density (quantified via a CT scan) [1,6]. These inhomogeneous relationships that map trabecular stiffness have been shown to vary based on the anatomic-site from which they are derived [20]. However, in the absence of a relationship specific to the proximal humerus, the results of Chapter 4 suggest that the site-pooled relationship developed by Morgan *et al*, and used in the

humeral FE models developed by Razfar *et al*, may be appropriate for FE models of humeral reconstruction.

Considering the number of aforementioned approximations that go into developing a FE model of the humerus, it is important to ensure that the response of the developed computational model mimics reality well. However, only four of the humeral models reported in the literature have directly sought to validate their methods by comparing their results to controlled *in-vitro* experiments [6,10]. Dahan *et al* validated their FE model of the humerus by denuding two humeri, applying uniaxial strain gauges to the cortex and subjecting the bone to known loads in three orientations via a flat plate. They were able to correlate experimental and FE results well, with an R^2 -value of 0.982 and a linear regression that approached the idealized unit scalar relationship [6]. Varghese *et al* developed FE models of the intact humerus that were validated based on 3-point bending ($R^2 = 0.99$) and torsion ($0.064 \leq R^2 \leq 0.97$) experiments; however, these tests did not subject the bone to anatomical boundary conditions, which are important for the analysis of humeral arthroplasty. Similarly, Maldonado *et al* used simplified axial compression and torsion loading to validate the stiffness of their humeral defect FE model, prior to assessing more physiologic loads *in-silico*. Finally, Favre *et al* developed and validated a FE model for measuring implant-bone interface stability following stemless humeral reconstruction. However, their analysis was limited to assessments of implant-bone micromotion, and the humeral strain response was not assessed or validated.

To date no strain (stress)-based validations have been published for humeral FE models of shoulder reconstruction. As the strain change between the intact and reconstructed bone response is often of principle concern in the design of shoulder implants, it is important to verify the validity of FE parameters for both the intact and reconstructed humeral models. With this in mind, the purpose of the present investigation was twofold: (1) to assess the correlation between experimental and FE strains for the proximal humerus for both the intact state and following stemless reconstruction, and (2) to assess how well the change in strain following reconstruction can be approximated using the FE method.

D.2 Materials and Methods

D.2.1 Experimental Model

D.2.1.1 Specimen Preparation

A cadaveric humerus (left arm, male 74 years, 142lbs) was denuded of all soft tissues using a scalpel; and was extracted from the upper arm. Upon isolation, the articular crown (which defines the outermost edge of the proximal articular surface) was identified for each specimen by a shoulder surgeon (G.S.A), and a permanent marker was used to trace an approximate humeral head (HH) resection plane. The humerus was then resected perpendicular to the diaphysis approximately 190mm from the most superior-lateral (SL) point of the HH resection plane. Four 1.5” screws were drilled into the bone in a 40mm-region from the distal resection, which acted as anchors to secure the bone. Following this, each specimen was potted in a 60mm length of PVC tubing using dental cement (Denstone Golden, Heraeus Dental; South Bend, IN, USA) such that the diaphyseal axis was concentric with the PVC cylinder and the top surface of the cement was 150mm from the SL resection point (Figure D.1). Four 6mm uniaxial strain gauges (KFH-6-350-C1-11L3M3R; Omega Spectris Canada, Laval, QC, Canada) were affixed to the proximal humerus beneath the HH resection plane. Two were placed laterally: one as high as possible on the lateral side of the greater tuberosity, the other 10mm distal to the termination of the first gauge. The remaining two gauges were each placed 10mm beneath the HH resection plane on the anterior and posterior sides of the medial divide, respectively (Figure D.1). All strain gauges were oriented so that the gauge axis ran from proximal to distal; and were secured through a series of successive degreasing and adhesive operations to ensure proper gauge adherence to bone [21,22].

D.2.1.2 Experimental Protocol

The potted specimen was secured within an arc that permitted the humerus to be rotated and fixed within a single plane. Specimens were oriented such that the HH resection plane was horizontal, which was confirmed visually using orthographic assessments with a level; this was termed the ‘neutral’ position (*i.e.*, 0°). The orientation arc was

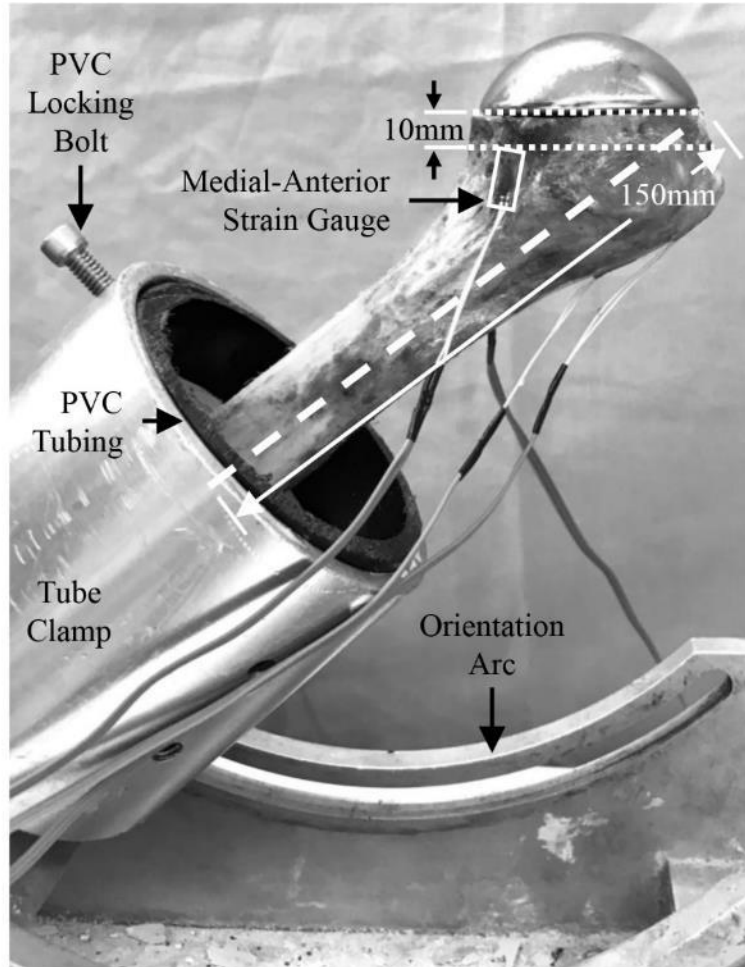


Figure D.1: Experimental Specimen Orientation Apparatus

positioned within a uniaxial pneumatic loading apparatus that was controlled by a custom LabVIEW script written to apply a desired load to the articular surface of the humerus via a flat steel plate [6] attached to the pneumatic actuator (Figure D.2).

Once the specimen was oriented with the load application point centered beneath the actuator, pre-conditioning forces cycled 5 times between 5N and 50N were applied. The loading plate was then lifted off the specimen and the strain gauge readings were zeroed to reflect the unloaded state. Articular forces were then ramped to the desired load of 250N in 50N increments at a rate of approximately 25N/s. The strain readings were recorded for 10s at a rate of 1kHz once the desired load was reached, and the average strain was calculated ($\epsilon_{\text{Experimental}}$). This process was repeated 5-times, then reiterated for an articular load of 500N. Following this, the specimen was rotated by $\pm 30^\circ$ in the plane defining the medial-lateral arc on the humeral head and testing was repeated at each new orientation ($+30^\circ$ = greater abduction, -30° = greater adduction) to represent a reasonable range of anatomic joint reaction force orientations.

Once the intact humerus was tested, a shoulder surgeon (G.S.A.) resected the humeral head and reconstructed the articular surface using a Simpliciti stemless shoulder implant (Size 3, 52x19mm articular component; Wright Medical, Memphis, TN, USA). Care was taken to ensure that the strain gauges remained unaffected by the surgical tooling during the implantation process. Testing was then repeated with the reconstructed humerus.

D.2.2 Computational Model

The humeral specimen was scanned prior to experimental testing using a helical multi-slice GE 750HD Discovery Computed Tomography (CT) scanner (GE Healthcare; Pollards Wood, Buckinghamshire, United Kingdom). The cortical shell and trabecular-canal of each bone were identified using a combination of automated and manual masking features (Appendix E) within Mimics (version 19; Materialize, Leuven, BE) and were reconstructed into 3D bone models within SolidWorks (Dassault Systèmes; Waltham, MA, USA). The same shoulder surgeon (G.S.A.) virtually identified the HH resection plane, which was used to further divide the cortical bone and trabecular-canal

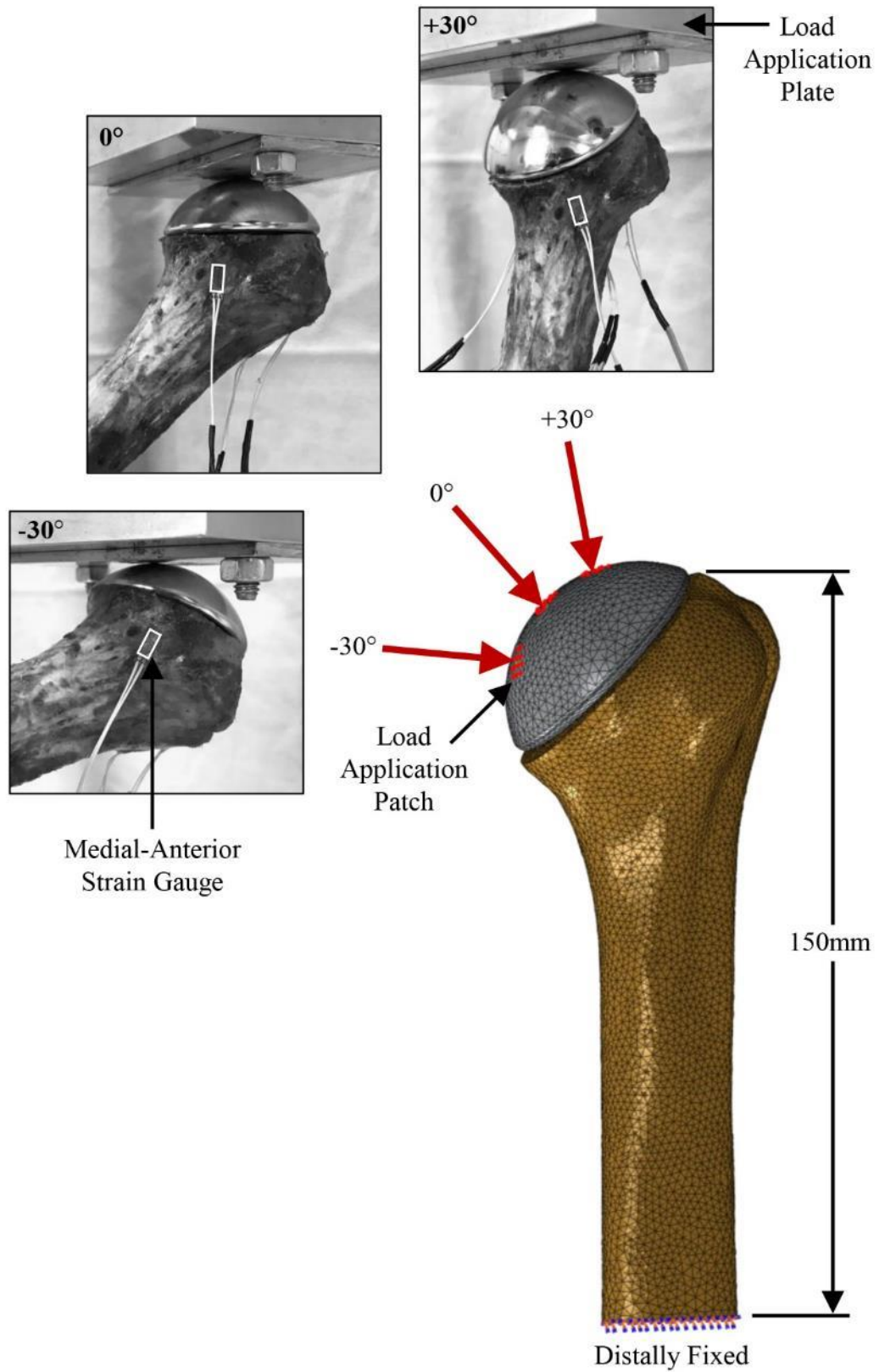


Figure D.2: Experimental and FE Humerus Load Application

into top and bottom segments. CAD files for the Simpliciti implant were obtained from the manufacturer and were used to create a reconstructed bone model, with the implant centered on the HH resection plane. Following successive Boolean operations, all bone components and the implant were imported into Abaqus (Dassault Systèmes; Waltham, MA, USA) where they were meshed using 2mm quadratic tetrahedral elements (based on mesh convergence, see Appendix C) and combined to form intact and reconstructed humerus models using identical meshing techniques [1]. In total, the intact bone model consisted of 258,373 elements, and the reconstructed model had 257,715 elements (Bone: 204,572; Implant: 53,143). All models were resected 150mm from the most SL point on the HH resection plane, and the trabecular-canal was limited to a depth of 40mm beneath the HH resection.

The Simpliciti was assigned material properties representing Titanium ($E = 110\text{GPa}$, Poisson's ratio of 0.3), as well as smooth ($\mu = 0.4$) [23] and porous ($\mu = 0.88$) [24] frictional contact with bone as necessary. The implant's articular-nucleus junction was rigidly fused together to represent a secure Morse taper connection. For the cadaveric bone, the cortical shell was modelled as isometric and homogenous, with an elastic modulus of 20GPa based on previous work [18,19], whereas the trabecular-canal was isometric and inhomogeneous, with elastic properties that were dictated by the site-pooled regression developed by Morgan *et al* (as per the conclusions of Chapter 4) [20].

All models were fixed at the distal cortical resection, and articular loads of 250N and 500N were independently applied to the articular surfaces to mimic the experimental setup (0° , $+30^\circ$ and -30° ; Figure D.2). The location of each of the four strain gauges were identified on the 3D bone models in Abaqus using measured images of the experimental gauge placement, and two nodes were selected on the cortical mesh to represent each strain gauge (Figure D.3). *In-silico* strain was calculated from the change in length of each node-pair (ϵ_{FE}).

D.2.3 Comparative Metrics

The experimental and finite element strains were compared using a standard linear regression for both the intact and reconstructed states separately. As such, a unit slope,

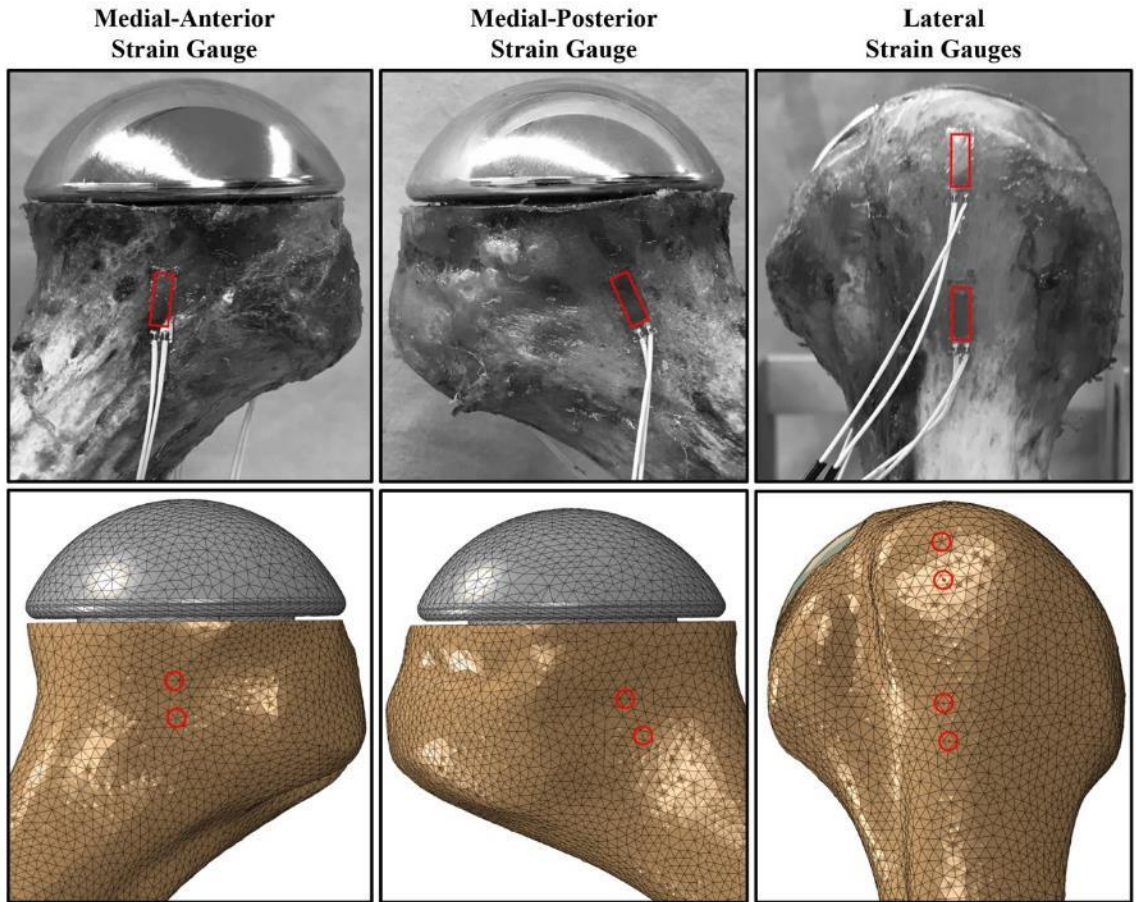


Figure D.3: Strain Gauge and Node Pair Locations in Experimental and FE Models

zero vertical-intercept, and unit correlation coefficient (R^2) would represent a perfect correlation. Results were also presented with a Bland-Altman error plot [$(\epsilon_{\text{Experimental}} - \epsilon_{\text{FE}})$, $(\epsilon_{\text{Experimental}} + \epsilon_{\text{FE}})/2$]. Furthermore, the error between experimental and FE measured strains were quantified by the root mean square error (RMSE) and the mean percentage error, which were calculated according to Eq.D.1 and Eq.D.2, respectively.

$$RMSE = \sqrt{\frac{1}{N} \sum_{i=1}^N (\epsilon_{\text{Experimental},i} - \epsilon_{\text{FE},i})^2} \text{ [}\mu\epsilon\text{]} \quad (\text{Eq.D.1})$$

$$\text{Mean Error} = \frac{100\%}{N} \sum_{i=1}^N \frac{(\epsilon_{\text{Experimental},i} - \epsilon_{\text{FE},i})}{\epsilon_{\text{Experimental},i}} \text{ [%]} \quad (\text{Eq.D.2})$$

Finally, the change in strain from intact to reconstruction was calculated both for the experimental and FE models to investigate how differences in each model may impact the changes reported following joint reconstruction. These changes were calculated as the reconstructed strain minus the intact strain and were again compared using a linear regression and a Bland-Altman error plot.

D.3 Results

The experimental strain values were consistent across the five *in-vitro* samples taken at each loading configuration for both the intact and reconstructed states. The variation in experimental strain readings was quantified using the coefficient of variation and remained low for all gauge locations (medial-anterior: $-2.9 \pm 2.4\%$; medial-posterior: $2.4 \pm 11.07\%$; lateral-top: $-4.7 \pm 5.4\%$; lateral-bottom: $-2.8 \pm 2.8\%$).

Strain values were found to linearly correlate very well between the experimental and FE models ($P < 0.001$) (Figure D.4), with R^2 -values of 0.975 and 0.926 for the intact and reconstructed states, respectively (Table D.1). The intact regression for experimental strain as a function of FE strain was defined by a slope of 1.172 and a vertical intercept of $-9.677\mu\epsilon$. Similarly, the reconstructed regression was defined by a slope of 1.127 and a vertical intercept of $-20.428\mu\epsilon$. Bland-Altman plots comparing the experimental and FE strains are presented in Figure D.5.

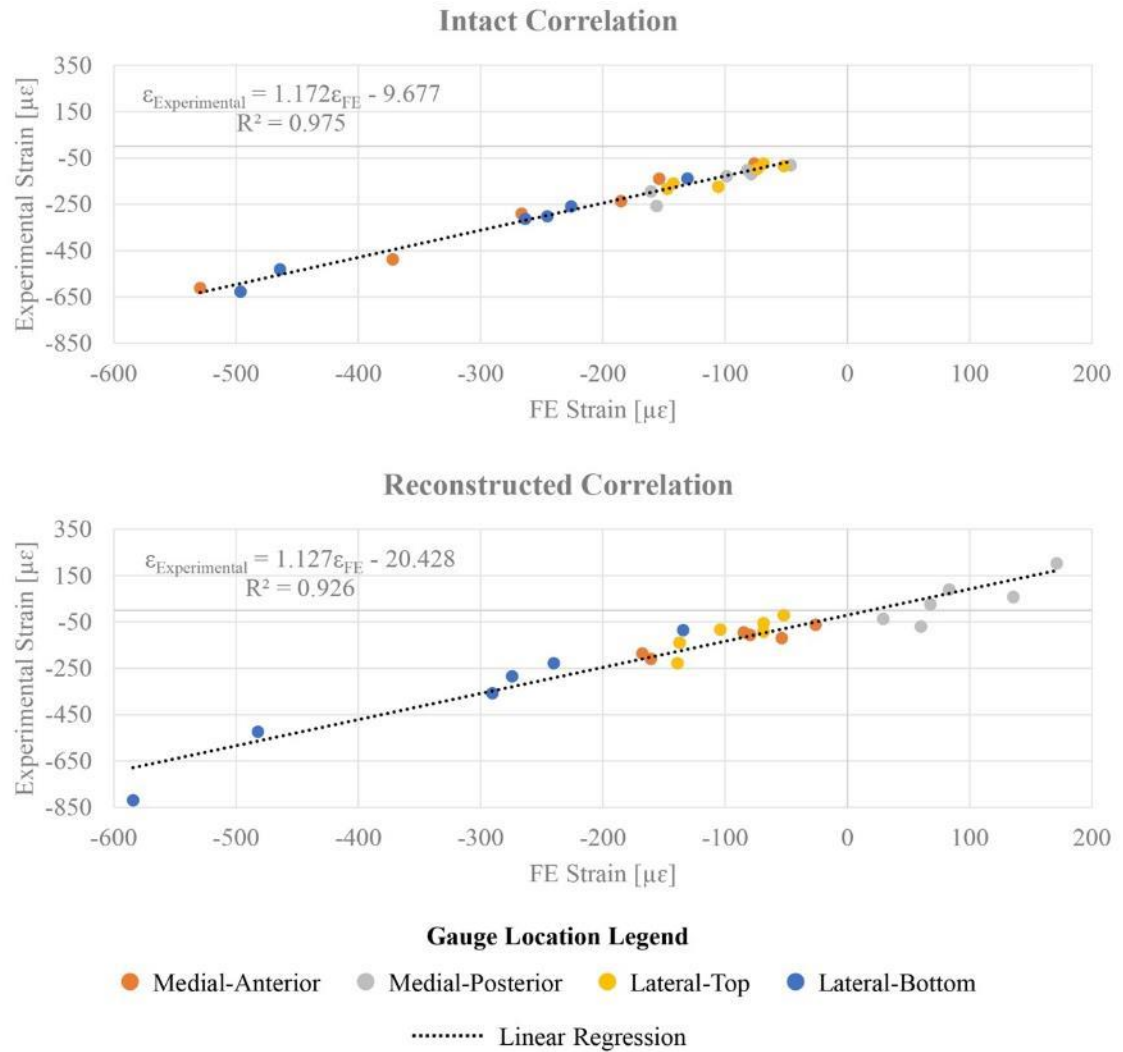


Figure D.4: Linear Correlation Plots for the Intact and Reconstructed State

Table D.1: Regression Terms and Correlations for Intact and Reconstructed States

Regression Terms			
$\varepsilon_{\text{Experimental}} = \mathbf{m} \times \varepsilon_{\text{FE}} + \mathbf{b}$			
	m	b	R²
Intact State	1.172	-9.677	0.975
Reconstructed State	1.127	-20.428	0.926

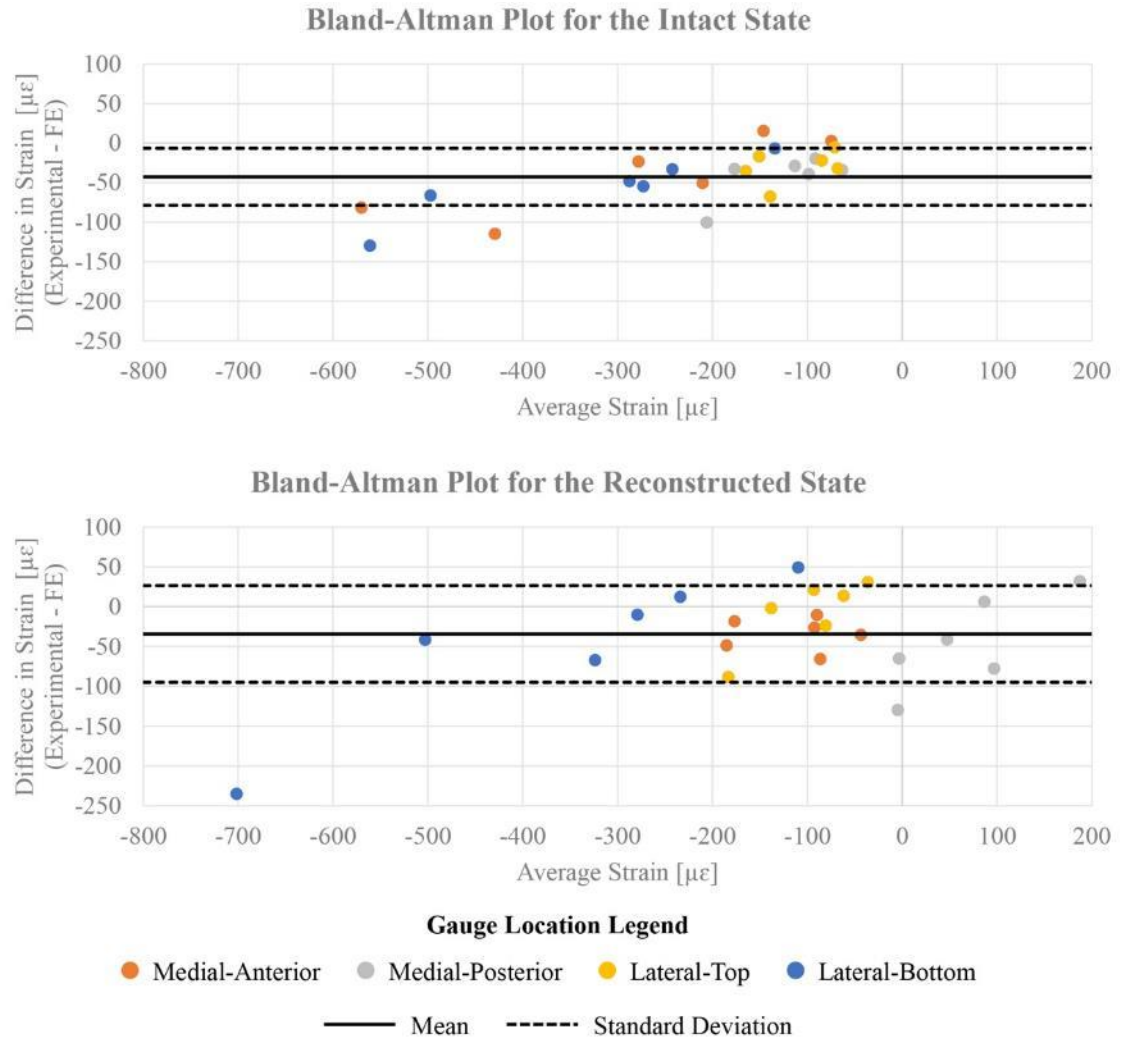


Figure D.5: Bland-Altman Plots for the Intact and Reconstructed States

The absolute error in both intact and reconstructed models was quantified by the RMSE. The overall RMSEs between experimental and FE strains were low, with values of $55.4\mu\epsilon$ and $68.6\mu\epsilon$ for the intact and reconstructed states, respectively. Pooling all gauge locations, the mean percentage error between experimental and FE strains was 18.6% for the intact state, and 6.1% for the reconstructed state. Table D.2 presents the error-values (RMSE and mean percentage error) broken down according to gauge location.

Despite errors associated with the modelling of each bone state, the change in strain comparing the reconstructed and intact states was also found to correlate well, though less so than each state independently, between the experimental and FE models ($R^2 = 0.878$, $P < 0.001$). The corresponding regression was defined by a slope of 1.046 and a vertical intercept of $4.677\mu\epsilon$. The regression and Bland-Altman plots for the change in strain following joint reconstruction are presented in Figure D.6.

D.4 Discussion

The FE method is a strong computational tool for assessing the performance of implants following joint reconstruction. *In-silico* tools such as these can be used for a preliminary assessment of implant performance during the design process. The FE method is particularly good for assessing multiple implant designs or bone states, as each can be directly compared within the same specimen without compromising the underlying bone tissue. While there have been many FE models developed for the humerus [1,6–13], few have attempted to validate their results [6,10,11,13]. Of the humeral models developed to assess implants [1,12,13], only one attempted to validate the reconstructed state of the bone [13], with none validating the intact state as well; and none validated based on the bones strain response. The purpose of the present investigation was to assess the validity of a FE model developed for the humerus both in the intact state and following reconstruction with a stemless implant.

Table D.2: Error Terms for the Intact and Reconstructed States

	Intact State		Reconstructed State	
	RMSE	Mean Error	RMSE	Mean Error
	[$\mu\epsilon$]	[%]	[$\mu\epsilon$]	[%]
Pooled	55.4	18.6	68.6	6.1
Medial-Anterior	62.1	8.6	38.8	30.2
Medial-Posterior	50.1	28.9	70.6	17.1
Lateral-Top	35.7	22.9	40.8	-22.1
Lateral-Bottom	67.9	14.1	103.4	-0.7

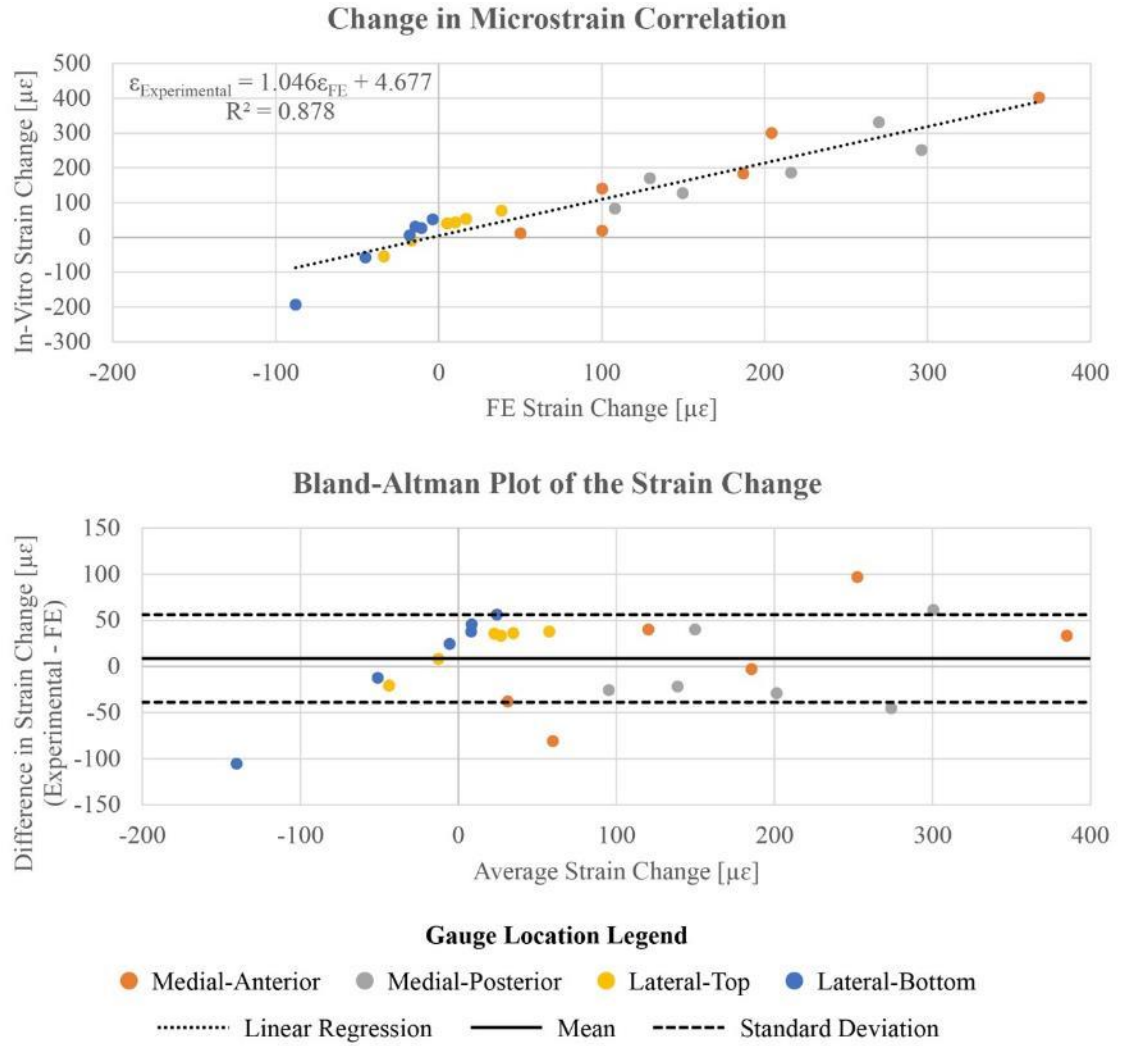


Figure D.6: Linear Regression and Bland-Altman Plots for the Change in Strain Following Humeral Reconstruction

The results of the present investigation provide evidence in support of using the FE method to assess the strain response of bone in both the intact state and following reconstruction with a stemless implant. The experimental and FE strain values correlated well for both the intact and reconstructed models, with R^2 -values exceeding 0.920 for both states. The linear regression terms were also reasonable, with slopes of 1.172 and 1.127 and vertical intercepts of $-9.677\mu\epsilon$ and $-20.428\mu\epsilon$ for the intact and reconstructed states, respectively. In both the intact and reconstructed cases, the FE models tended to underpredict the experimental strain response at high strains (both compression and tension). This variance between the experimental and FE strains is manifested in the deviation of the linear slope term from the unit scalar relationship. Overall, the regression terms reported were not as strong, but compare reasonably well with the intact validation values presented by Dahan *et al*, who reported a slope of 0.917 and a vertical intercept of $90.9\mu\epsilon$ with an R^2 -value of 0.982 [6].

The change in strain attributable to reconstructing the humerus with the stemless implant also presented with a strong correlation between the experimental and FE results ($R^2 = 0.878$). As expected, the correlation was not as strong as the individual intact and reconstructed models, as the errors in each of the individual models were compounded in the calculation of the percentage change. However, the linear relationship (slope: 1.046, vertical intercept: $4.677\mu\epsilon$) between experimental and FE results was better than that of either the intact or reconstructed models independently. The near unit slope and low vertical intercept for the change in strain values are attributed to the use of identical meshing techniques. By using the exact same mesh for both intact and reconstructed models, the node-pairs used for FE strain calculation were identical, as were the approximations that went into the construction of each model. This finding supports the use of identical meshing techniques to construct both intact and reconstructed orthopaedic models in order to present results that focus on the change in FE outcomes as opposed to the strain in either state independently.

A limitation of this study was that the strain response of the proximal humerus was only assessed at four locations. This likely contributed to the lower overall correlation strength found between experimental and FE strains compared to Dahan *et al*, who used 12-

gauges, thereby providing a larger data sample. However, as the focus of the present investigation was stemless reconstruction, which influences strains more proximally than stemmed humeral reconstruction, the proximal bone response was of primary concern for this assessment.

More generally, there are several differences between the experimental and FE configurations that are likely responsible for disparities between the two models. While the humerus was cemented at the same length as the rigid fixation of the FE models, the potting apparatus did undergo some elastic deflection during articular loading, which altered the effective fixation length of the experimental setup. This deflection also affected the orientation of the applied loads. Though the FE models were constructed to mimic orientation changes by maintaining the initial loading vector direction, only deflection from the humerus was accounted for in the FE model, leading to some discrepancy between the two assessments. Similarly, the initial orientation of the applied loads in both tests were based on the humeral head resection plane. While care was taken to align the virtual resection with the experimental one based on several landmarks around the humeral crown, differences in the resection plane tilt could further alter loading orientation between the experimental and FE models. Additionally, the method used to virtually reconstruct the cortical-trabecular boundary *in-silico* relies on maintaining a minimum thickness of 1-voxel (~0.65mm) within the CT scan. In the proximal humerus, the cortex can become thinner than this minimum thickness, which can cause the artificial stiffening of the humeral construct. This explains why FE strains were underpredicted compared to the experimental values. Finally, though the proper frictional coefficients were modelled between the implant and bone, the *in-vitro* tooling produced a press-fit between the fixation-feature and bone, while the FE model was constructed based on a perfect line-to-line fit. This may have produced some discrepancies in implant-bone load transfer between the experimental and FE assessments; though the ease with which the implant was inserted into the bone *in-vitro* was noted qualitatively, suggesting that the press-fit may not have played a major role experimentally.

D.5 Conclusions

In conclusion, the linear elastic response of the proximal humerus correlates very well with FE models for both the intact and reconstructed states. Further, a true strength of the FE method seems to be in the assessment of changes in FE outcome between paired intact and reconstructed models, which in-part correct for the bias of the FE method to underpredict large cortex strains. The strong correlations between experimental and FE strains support the validity of modeling the proximal humerus using identical meshing techniques with 2mm quadratic tetrahedral elements, an inhomogeneous trabecular stiffness (site-pooled regression from Morgan *et al*), a homogeneous cortical stiffness (20GPa), and a frictional implant-bone interface condition.

D.6 References

- [1] Razfar, N., Reeves, J. M., Langohr, D. G., Willing, R., Athwal, G. S., and Johnson, J. A., 2016, “Comparison of proximal humeral bone stresses between stemless, short stem, and standard stem length: a finite element analysis,” *J. Shoulder Elb. Surg.*, **25**(7), pp. 1076–83.
- [2] Nagels, J., Stokdijk, M., and Rozing, P. M., 2003, “Stress shielding and bone resorption in shoulder arthroplasty,” *J. Shoulder Elb. Surg.*, **27**(46)(2), pp. 35–39.
- [3] Denard, P. J., Noyes, M. P., Walker, J. B., Shishani, Y., Gobezie, R., Romeo, A. A., and Lederman, E., 2017, “Proximal stress shielding is decreased with a short stem compared with a traditional-length stem in total shoulder arthroplasty,” *J. Shoulder Elb. Surg.*, **27**(1), pp. 53–58.
- [4] Spormann, C., Durchholz, H., Audigé, L., Flury, M., Schwyzer, H. K., Simmen, B. R., and Kolling, C., 2014, “Patterns of proximal humeral bone resorption after total shoulder arthroplasty with an uncemented rectangular stem,” *J. Shoulder Elb. Surg.*, **23**(7), pp. 1028–1035.
- [5] Inoue, K., Suenaga, N., Oizumi, N., Yamaguchi, H., Miyoshi, N., Taniguchi, N., Munemoto, M., Egawa, T., and Tanaka, Y., 2017, “Humeral bone resorption after anatomic shoulder arthroplasty using an uncemented stem,” *J. Shoulder Elb. Surg.*,

26(11), pp. 1984–1989.

- [6] Dahan, G., Trabelsi, N., Safran, O., and Yosibash, Z., 2016, “Verified and validated finite element analyses of humeri,” *J. Biomech.*, **49**(7), pp. 1094–1102.
- [7] van der Helm, F. C. T., 1994, “A finite element musculoskeletal model of the shoulder mechanism,” *J. Biomech.*, **27**(5), pp. 551–569.
- [8] Büchler, P., Ramaniraka, N. a., Rakotomanana, L. R., Iannotti, J. P., and Farron, a., 2002, “A finite element model of the shoulder: Application to the comparison of normal and osteoarthritic joints,” *Clin. Biomech.*, **17**(9–10), pp. 630–639.
- [9] Kahn, J. F. K. Æ. J. L., 2006, “Finite element analysis of the strain distribution in the humeral head tubercles during abduction : comparison of young and osteoporotic bone,” pp. 581–587.
- [10] Varghese, B., Short, D., Penmetsa, R., Goswami, T., and Hangartner, T., 2011, “Computed-tomography-based finite-element models of long bones can accurately capture strain response to bending and torsion,” *J. Biomech.*, **44**(7), pp. 1374–1379.
- [11] Maldonado, Z. M., Seebeck, J., Heller, M. O. W., Brandt, D., Hepp, P., Lill, H., and Duda, G. N., 2003, “Straining of the intact and fractured proximal humerus under physiological-like loading,” *J. Biomech.*, **36**(12), pp. 1865–1873.
- [12] Schmidutz, F., Agarwal, Y., Müller, P. E., Gueorguiev, B., Richards, R. G., and Sprecher, C. M., 2014, “Stress-shielding induced bone remodeling in cementless shoulder resurfacing arthroplasty: A finite element analysis and in vivo results,” *J. Biomech.*, **47**(14), pp. 3509–3516.
- [13] Favre, P., and Henderson, A. D., 2016, “Prediction of stemless humeral implant micromotion during upper limb activities,” *Clin. Biomech.*, **36**, pp. 46–51.
- [14] Bergmann, G., Graichen, F., Bender, A., Kaab, M., Rohlmann, A., and Westerhoff, P., 2007, “In vivo glenohumeral contact forces-Measurements in the first patient 7 months postoperatively,” *J. Biomech.*, **40**(10), pp. 2139–2149.

- [15] Graichen, F., Arnold, R., Rohlmann, A., and Bergmann, G., 2007, “Implantable 9-Channel Telemetry System for In Vivo Load Measurements With Orthopedic Implants,” *54*(2), pp. 253–261.
- [16] Westerhoff, P., Graichen, F., Bender, a, Halder, a, Beier, a, Rohlmann, a, and Bergmann, G., 2009, “In vivo measurement of shoulder joint loads during activities of daily living.,” *J. Biomech.*, **42**(12), pp. 1840–9.
- [17] Peng, L., Bai, J., Zeng, X., and Zhou, Y., 2006, “Comparison of isotropic and orthotropic material property assignments on femoral finite element models under two loading conditions,” *Med. Eng. Phys.*, **28**(3), pp. 227–233.
- [18] Rho, J. Y., Ashman, R. B., and Turner, C. H., 1993, “Young’s modulus of trabecular and cortical bone material: Ultrasonic and microtensile measurements,” *J. Biomech.*, **26**(2), pp. 111–119.
- [19] Bayraktar, H. H., Morgan, E. F., Niebur, G. L., Morris, G. E., Wong, E. K., and Keaveny, T. M., 2004, “Comparison of the elastic and yield properties of human femoral trabecular and cortical bone tissue,” *J. Biomech.*, **37**(1), pp. 27–35.
- [20] Morgan, E. F., Bayraktar, H. H., and Keaveny, T. M., 2003, “Trabecular bone modulus-density relationships depend on anatomic site,” *J. Biomech.*, **36**, pp. 897–904.
- [21] Staebler, M., Moore, D., Akelman, E., Weiss, A.-P., Fadale, P., and Crisco, J., 1999, “The Effect of Wrist Guards on Bone Strain in the Distal Forearm,” *Am. J. Sports Med.*, **27**(4), pp. 500–506.
- [22] Austman, R. L., Beaton, B. J. B., Quenneville, C. E., King, G. J. W., Gordon, K. D., and Dunning, C. E., 2007, “The effect of distal ulnar implant stem material and length on bone strains,” *J. Hand Surg. Am.*, **32**(6), pp. 848–854.
- [23] Kuiper, J. H., and Huiskes, R., 1996, “Friction and stem stiffness affect dynamic interface motion in total hip replacement.,” *J. Orthop. Res.*, **14**(1), pp. 36–43.

- [24] Zhang, Y., Ahn, P. B., Fitzpatrick, D. C., Heiner, A. D., Poggie, R. A., and Brown, T. D., 1999, "Interfacial Frictional Behavior: Cancellous Bone, Cortical Bone, and a Novel Porous Tantalum Biomaterial," *J. Musculoskelet. Res.*, **3**(4), pp. 245–251.

Appendix E – Ethics Approval



LAWSON FINAL APPROVAL NOTICE

LAWSON APPROVAL NUMBER: R-15-057

PROJECT TITLE: Morphological and finite element analysis of the normal and osteoarthritic glenohumeral joint.

PRINCIPAL INVESTIGATOR: Dr. George Athwal

LAWSON APPROVAL DATE: March 5, 2015

Health Sciences REB#: 105912

Please be advised that the above project was reviewed by the Clinical Research Impact Committee and Lawson Administration and the project:

Was Approved

Please provide your Lawson Approval Number (R#) to the appropriate contact(s) in supporting departments (eg. Lab Services, Diagnostic Imaging, etc.) to inform them that your study is starting. The Lawson Approval Number must be provided each time services are requested.

Dr. David Hill
V.P. Research
Lawson Health Research Institute

All future correspondence concerning this study should include the Lawson Approval Number and should be directed to Sherry Paiva, Research Approval Officer, Lawson Health Research Institute, 750 Baseline Road, East, Suite 300.

cc: Administration

Appendix F – Post-Hoc CT Calibration Methods

A version of this appendix has been accepted for publication [1].

F.1 Introduction

The use of *in-silico* methods (*e.g.*, finite element (FE) modeling) are becoming increasingly popular for the quantification of bone properties. Often, these methods rely on volumetric bone mineral density data acquired from computed tomography (CT) scans to construct models that accurately depict regional changes in bone density [2–14]. While CT scans have been used to aid diagnostics for many years, the use of quantitative CT (qCT) to construct bone models, with realistic bone mineral density, remains a useful quantitative tool. The accuracy of qCT data depends on the calibration of each scan, as the CT attenuation (typically scaled to Hounsfield Units (HU)) is often converted into either ash density (ρ_{ASH} = ash mass/bone volume), apparent density (ρ_{APP} = hydrated bone mass/total specimen volume), or material density (ρ_{MAT} = bone mass/bone volume), all of which are typically reported in g/cm^3 . The calibration relationship between physical density and CT attenuation is linear [15–19], taking the form of $\rho = m \cdot \text{HU} + b$, where ‘ m ’ and ‘ b ’ are the calibration equation slope and vertical intercepts, respectively, which are calculated using a calibration phantom. Schileo *et al* (2008) reported that apparent density can be calculated as a scalar product of ash density, with a common relationship for both cancellous and cortical bone (*i.e.*, $\rho_{\text{APP}} = \rho_{\text{ASH}}/0.6$) [16]. Since 2008, this relationship has been used widely in the literature to convert between ash and apparent density.

The calibration of bone mineral density from CT attenuation for qCT analysis is typically conducted for each scan independently, as the calibration equation varies between CT scanners, and based on CT settings [18]. As such, calibration phantoms formed with materials of known densities, typically either hydroxyapatite (*e.g.*, SB3), or liquid dipotassium phosphate (*i.e.*, K_2HPO_4), are placed within the field of view of the desired scan, and the CT scanner’s response to the regions of known density are quantified and plotted to determine the linear calibration equation terms. Unfortunately, not all CT scans are calibrated in this manner to allow for accurate bone mineral density assessment

between patients, specimens, or samples. As such, when utilizing uncalibrated clinical scans, post-hoc calibration methods are necessary.

One method that has been proposed for such a post-hoc calibration develops the calibration equation terms by scanning a calibration phantom alone post-hoc in the same CT scanner at the same settings [7]; this method will be referred to as the ‘phantom-only’ method. Alternatively, since the calibration equations are documented to change as a function of CT settings, it is hypothesized that a relationship can be found between those settings and the terms of the calibration equation (*i.e.*, slope, m ; and vertical intercept, b) by assessing several qCT calibrated scans at different settings within a single CT scanner. This method can be termed the CT setting ‘regression-based’ post-hoc calibration.

While studies have been conducted to investigate the variance induced in CT density calibration equations due to changes in CT settings and calibration phantom type [18,19], there remains a void in the literature documenting the variation induced by post-hoc calibration methods. In view of the foregoing, the purpose of this study was two-fold: to determine if a post-hoc calibration equation can be quantified based on CT setting variations (*i.e.*, peak tube voltage, kVp; and tube current, mA), and to then compare these calibration equations to those formed by the post-hoc phantom-only method. It was hypothesized (1) that a stepwise linear regression would be able to predict a density calibration equation for qCT based on CT settings, and (2) that the regression equation would better match standard calibration equations than a post-hoc phantom-only calibration at the same settings.

F.2 Materials and Methods

Five ($n = 5$) cadaveric upper limb specimens (scapula through phalanges) with a mean \pm SD age of 72 \pm 8 years were procured. Each specimen was screened for bone related disease and injury. Helical Computed Tomography (CT) scans were taken of each specimen at 11 predetermined clinical settings (Table 1) using a multi-slice GE 750HD Discovery CT scanner (GE Healthcare; Pollards Wood, Buckinghamshire, United Kingdom). CT settings reflected the clinical ranges in both peak tube voltage (80kV – 140kV) and current (100mA – 300mA) typically used for shoulder scans at our

institution. The reconstruction kernel (BONEPLUS), Field of View (300mm), slice thickness (1.25mm) and subsequent pixel size (0.6mm) were consistent for all scans and are also summarized in Table F.1. The CT technician set the table height for each scan to ensure that the subject was central within the scan volume. For each scan, a dipotassium phosphate (K_2HPO_4) calibration phantom (qCT Pro Model 3, Mindways Software, Austin, TX) containing five rods of known density (varying low and high atomic number), calibrated with liquid K_2HPO_4 and water solutions, along with a hydroxyapatite-distilled water (SB3-H₂O) phantom (SB3 model number 450; GAMMEX, Middleton, WI) were present. These phantoms provide linear calibration for high atomic number materials of unknown density over a range of attenuation values and are designed specifically for extracting quantitative bone mineral density information from CT scans.

Specimens were placed centrally on top of the K_2HPO_4 calibration phantom and within the scanner (forearm extended and palm down) and remained static during each scan. The SB3-H₂O calibration phantom was stationed centrally directly alongside the specimen. Following the completion of scanning, the specimens were removed from the CT scanner, and the phantoms were scanned together, without a cadaver present, at the same 11 predetermined settings.

To quantify the relationship between ash density (in g/cm^3) and CT attenuation (HU), the attenuation (HU) in ten centered circular (150 mm^2) regions evenly spaced along the length of the K_2HPO_4 calibration phantom were collected using Mimics software (V.17.0, Materialize, Leuven, BE). These values were then averaged and used to determine the linear correlation coefficients required to convert any measured HU value to calibrated qCT density as outlined by the phantom manufacturer [17,18,20]; this was done for each CT scan independently. Furthermore, the SB3 bone surrogate was virtually divided into quarters using three axial slices, and the average HU within the SB3 and distilled water were determined at these locations. The regions of interest were of the same shape as the SB3 (rectangular) and H₂O (circular) cross-sections, but represented the inner-50% of the cross-sectional area (to avoid partial voxel sampling effects). The known apparent density of SB3 ($1.82g/cm^3$) and distilled water ($0g/cm^3$) were then used to plot these six

Table F.1: CT settings used for all specimen and phantom-only scans.

Peak Tube Voltage (kVp)	Tube Current (mA)	Slice Thickness (mm)	Pixel Size (mm)
80	100	1.25	0.6
80	200	1.25	0.6
80	300	1.25	0.6
100	100	1.25	0.6
100	200	1.25	0.6
100	300	1.25	0.6
120	100	1.25	0.6
120	200	1.25	0.6
120	300	1.25	0.6
140	100	1.25	0.6
140	200	1.25	0.6

points on graphs of ash density (g/cm^3) vs. attenuation (HU) [15]. A linear calibration line of best fit was then determined for each scan independently. Accordingly, two (K_2HPO_4 and SB3- H_2O) calibration equations were determined for each phantom-with-specimen scan, and each phantom-only scan. A flow chart outlining the workflow for the study is presented in Figure F.1.

Using the known CT settings and the slope and vertical intercepts from the standard (*i.e.*, non post-hoc) the regression post-hoc approach quantified the linear calibration equation by performing a forward stepwise multi-variate linear regression analysis for the slope and intercept terms from each of the phantom-with-specimen scans. In the regression analysis, the slope or intercept were chosen as the dependent variables, while the CT scan energy (kV) and the tube current (mA) were the independent variables. In this manner equations were developed to predict the slope and intercept of the linear density calibration equation as a function of the CT settings.

In total, six linear relationships were established for each CT setting (3 calibration methods: standard calibration, phantom-alone, and regression; for each of the 2 calibration phantoms: K_2HPO_4 and SB3- H_2O). The standard phantom-with-specimen calibrated relationships were taken as the gold standard, by which the phantom-only and regression post-hoc equations were judged.

To assess the two post-hoc calibration methods statistically, the slope and vertical intercept terms of the calibration equations were compared across the five specimen scans corresponding to CT settings of 80-140kVp and 100-200mA using a four-way repeated measures ANOVA. The 300mA settings were excluded from the assessment due to the necessity that 300mA be present at all tube voltages when using the repeated measures design (140kVp at 300mA was deemed unrealistic during specimen scans due to the radiation dosage and expected cooling period). As such, the 4-way repeated measures ANOVA quantifies the effect that (1) the type of calibration phantom (K_2HPO_4 vs. SB3- H_2O), (2) the peak tube voltage (80-140kVp), (3) the tube current (100-200mA), and (4) the method by which the calibration equation was formed (standard calibration vs. phantom-only vs. regression) had on the slope (m) and vertical intercept (b) terms. Bland Altman plots were also created to compare the phantom-only and regression calibration

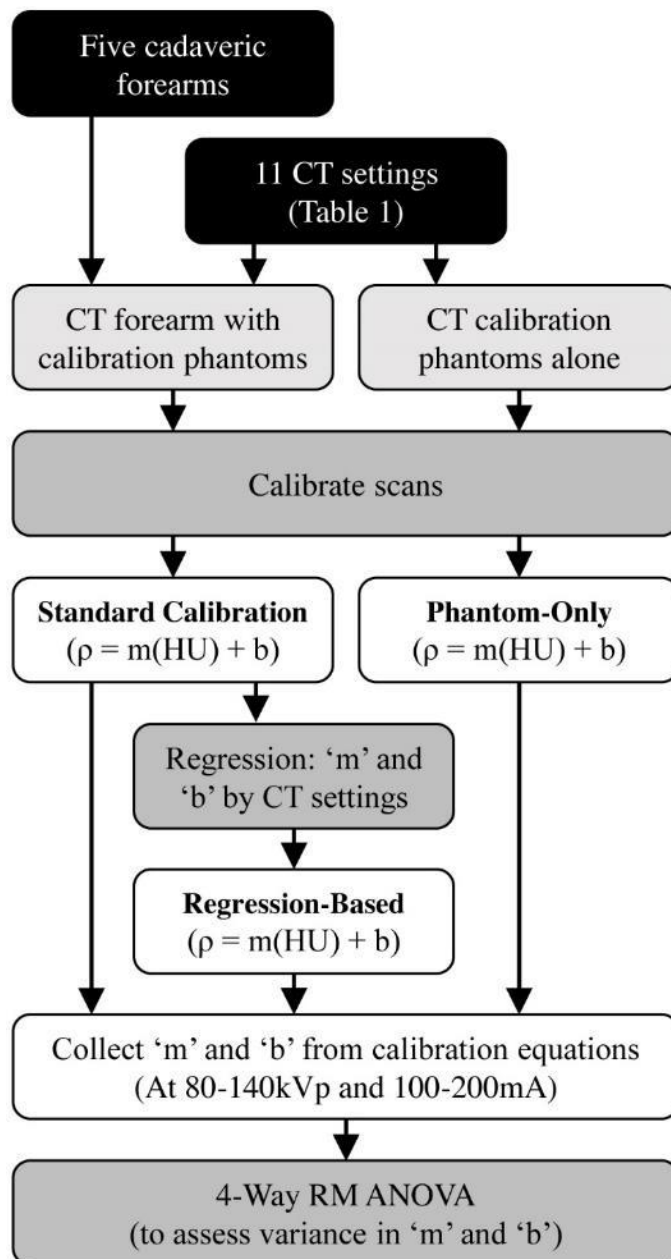


Figure F.1: Process flow diagram, outlining the sequence of events for the phantom-only, regression and standard calibration methods.

methods to the standard calibration method for both slope (m) and vertical intercept (b). Plots of percentage error of predicted ash density were then created for each calibration phantom and peak tube voltage by subtracting the standard calibrated density from the predicted density. The percentage error comparison was conducted over the range of ash density that corresponds to bone (0.06g/cm^3 to 1.2g/cm^3) [21,22]. All statistical tests were performed using SPSS version 23 (IBM, Chicago, Illinois, USA).

F.3 Results

The forward stepwise multi-variate linear regression analysis revealed that peak tube voltage [kVp], but not tube current [mA], was significantly correlated to the slope (m) and vertical intercept (b) calibration terms (Table F.2). The equations to predict slope as a function of peak tube voltage (kVp) demonstrated strong correlation for both the K_2HPO_4 ($R^2 = 0.984$, $p < 0.001$) and the SB3-H₂O ($R^2 = 0.853$, $p < 0.001$) calibration phantoms, while the equations to predict vertical intercept as a function of tube current (mA) demonstrated relatively weaker correlation for both the K_2HPO_4 ($R^2 = 0.472$, $p < 0.001$) and the SB3-H₂O ($R^2 = 0.420$, $p < 0.001$) calibration phantoms.

The four-way repeated measures ANOVA demonstrated that the calibration equation slope was significantly related to the type of phantom chosen ($p < 0.001$; Partial- $\eta^2 = 0.995$, Power = 1.000), the calibration method ($p = 0.026$; Partial- $\eta^2 = 0.749$, Power = 0.735), and the peak tube voltage ($p < 0.001$; Partial- $\eta^2 = 1.000$, Power = 1.000), but not the tube current ($p = 1.000$; Partial- $\eta^2 < 0.001$, Power = 0.050) (Table 3). A Bonferroni post-hoc analysis was performed to further investigate differences in calibration method, and revealed that the phantom-only calibration method produced significantly different slope values than both the standard calibration ($p = 0.005$) and regression ($p < 0.001$) methods. Similarly, the standard calibration equation vertical intercept was significantly related to the type of phantom chosen ($p < 0.001$; Partial- $\eta^2 = 1.000$, Power = 1.000), and the peak tube voltage ($p = 0.006$; Partial- $\eta^2 = 0.996$, Power = 1.000), but not the calibration method ($p = 0.682$; Partial- $\eta^2 = 0.046$, Power = 0.064), or the tube current ($p = 0.822$; Partial- $\eta^2 = 0.014$, Power = 0.054) (Table F.3).

Table F.2: Density calibration equation terms derived from stepwise linear regression analysis.

Calibration Phantom	$\rho_{ASH} = m(HU) + b$			
	Slope (m)	R^2	Vertical Intercept (b)	R^2
K_2HPO_4	$4.225E-6(kV) + 2.07E-4$	0.984	$-9.51E-5(kV) + 5.4E-2$	0.472
SB3- H_2O	$3.326E-6(kV) + 2.36E-4$	0.853	$7.848E-5(kV) - 2E-3$	0.420

Table F.3: 4-way repeated measures ANOVA results.

	$\rho_{ASH} = m(HU) + b$					
	Slope (m)			Vertical Intercept (b)		
	p- Value	Partial η^2	Power	p- Value	Partial η^2	Power
Phantom Type	<0.001	0.995	1.000	<0.001	1.000	1.000
Calibration Method	0.026	0.749	0.735	0.682	0.046	0.064
Peak Tube Voltage	<0.001	1.000	1.000	0.006	0.996	1.000
Tube Current	1.000	<0.001	0.050	0.822	0.014	0.054

The slope and vertical intercepts predicted by standard calibration, phantom-only and regression methods are presented in Table F.4. The regression calibration method produced lower maximum average ash density percent differences (K₂HPO₄: 80kV: 1.6%; 100kV: -1.4%; 120kV: -1.0%; 140kV: 1.3%; SB3-H₂O: 80kV: 3.0%; 100kV: -3.1%; 120kV: -1.0%; 140kV: 1.9%) compared to the phantom-only calibration method (K₂HPO₄: 80kV: -3.9%; 100kV: -4.2%; 120kV: -3.5%; 140kV: -3.2%; SB3-H₂O: 80kV: -13.4%; 100kV: -7.6%; 120kV: -5.3%; 140kV: -4.1%) over the range of ash density corresponding to bone, regardless of peak tube voltage and which calibration phantom was used (Figure F.2). Graphs of percentage difference also showed that the K₂HPO₄ calibration phantom had lower maximum average ash density percent differences than the SB3-H₂O calibration phantom. Bland Altman plots further confirmed that the regression calibration method produced lower differences than the phantom-only calibration method (Figure F.3) for both slope and vertical intercept.

F.4 Discussion

The stepwise linear regression successfully predicted ash density calibration terms using the peak tube voltage [kVp], but tube current [mA] was rejected as a correlating factor. This result is supported by the findings of Giambini *et al* (2015), who determined that peak tube voltage had a significant effect on volumetric bone mineral density measures, but tube current did not [18].

Unfortunately, Giambini *et al* (2015) did not quantify the relationship between peak tube voltage and volumetric bone mineral density, so there exists no equation with which to judge the present result. The slope was found to have a higher correlation than the vertical intercept to the peak tube voltage. While the vertical intercept correlation coefficients are low, it is important to note that when using the calibration equation in the range of expected bone mineral density, it is the slope that has a larger impact on the resultant ash density. The formulation of an acceptable ash density calibration equation using linear regression proves the first hypothesis to be valid.

The regression-based density calibration method better matched the calibration method than the phantom-only method. Accordingly, the second hypothesis was also valid. The repeated measures

Table F.4: Density calibration equation terms derived by calibrated, phantom-only and regression methods.

			$\rho_{ASH} = m(HU) + b$		
Phantom	Evaluation Method	Peak Tube Voltage [kVp]	Slope (m)	Vertical Intercept (b)	
K ₂ HPO ₄	Standard Calibration	80	5.359E-4 (6.433E-6)	4.722E-2 (2.529E-3)	
		100	6.393E-4 (7.470E-6)	4.427E-2 (2.028E-3)	
		120	7.190E-4 (8.094E-6)	4.309E-2 (1.636E-2)	
		140	7.875E-4 (8.742E-6)	4.135E-2 (1.755E-3)	
	Phantom-Only	80	5.139E-4 (9.837E-7)	4.755E-2 (2.110E-4)	
		100	6.115E-4 (1.120E-6)	4.431E-2 (9.563E-5)	
		120	6.937E-4 (2.720E-6)	4.196E-2 (5.496E-4)	
		140	7.619E-4 (7.043E-7)	4.034E-2 (3.860E-5)	
	Regression	80	5.450E-4 (0.000E+0)	4.639E-2 (0.000E+0)	
		100	6.295E-4 (0.000E+0)	4.449E-2 (0.000E+0)	
		120	7.140E-4 (0.000E+0)	4.259E-2 (0.000E+0)	
		140	7.985E-4 (0.000E+0)	4.069E-2 (0.000E+0)	
	SB3-H ₂ O	Standard Calibration	80	4.880E-4 (2.111E-5)	4.792E-3 (1.499E-3)
			100	5.880E-4 (2.484E-5)	5.500E-3 (1.571E-3)
120			6.360E-4 (3.043E-5)	8.020E-3 (2.575E-3)	
140			6.900E-4 (3.162E-5)	9.162E-3 (2.018E-3)	
Phantom-Only		80	4.200E-4 (5.611E-20)	8.820E-3 (2.210E-4)	
		100	5.400E-4 (1.122E-19)	9.780E-3 (5.848E-4)	
		120	6.000E-4 (0.000E+0)	9.700E-3 (4.793E-4)	
		140	6.600E-4 (0.000E+0)	9.510E-3 (9.487E-5)	
Regression		80	5.021E-4 (0.000E+0)	4.278E-3 (0.000E+0)	
		100	5.686E-4 (0.000E+0)	5.848E-3 (0.000E+0)	
		120	6.351E-4 (0.000E+0)	7.418E-3 (0.000E+0)	
		140	7.016E-4 (0.000E+0)	8.987E-3 (0.000E+0)	

*Regression equations do not present with standard deviations, as the regression equations are constant for each peak tube voltage (kVp).

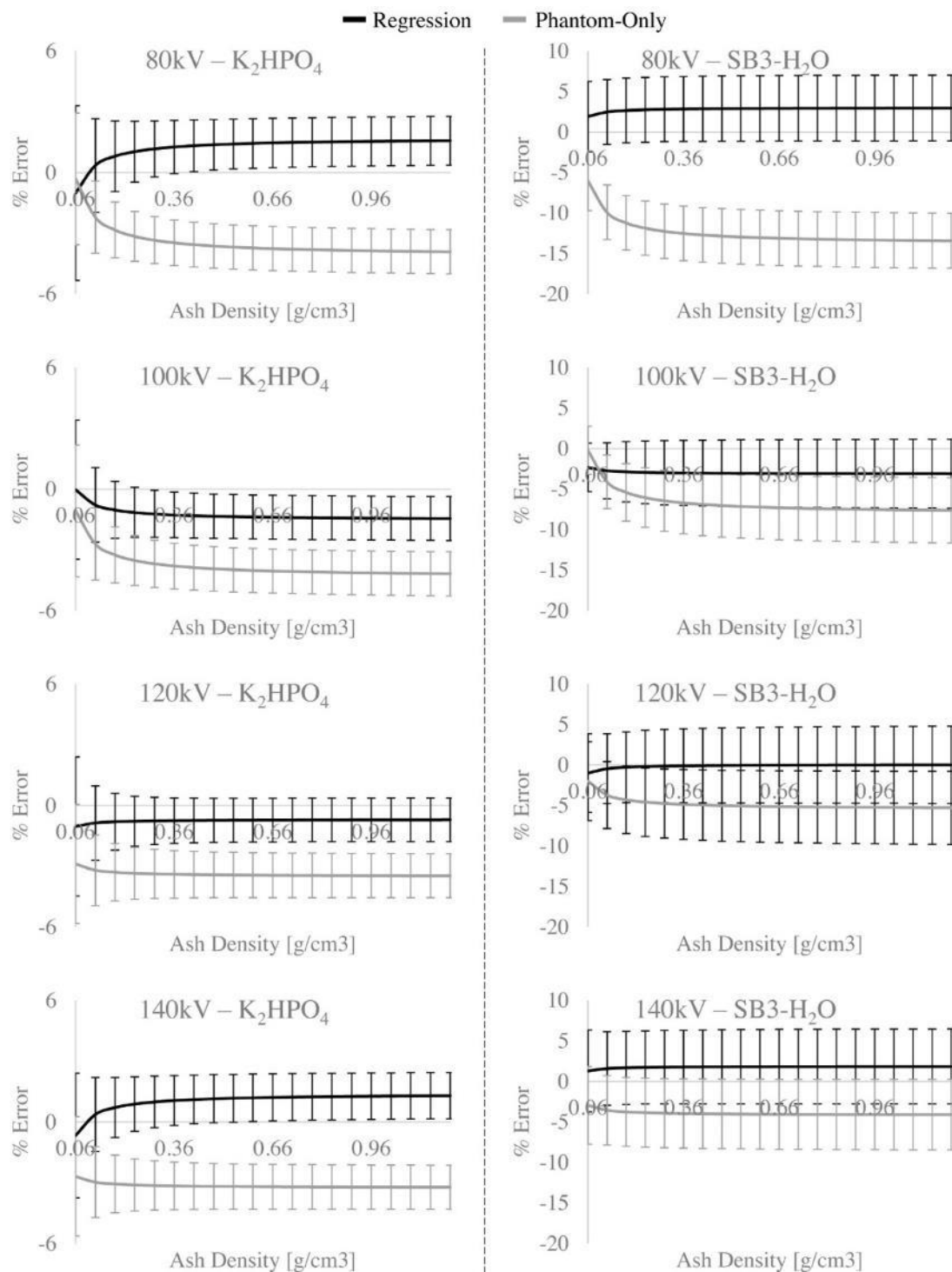


Figure F.2: Plots of mean \pm SD ash density percent difference (relative to proper calibration equation terms) for both phantom-only and regression calibration methods.

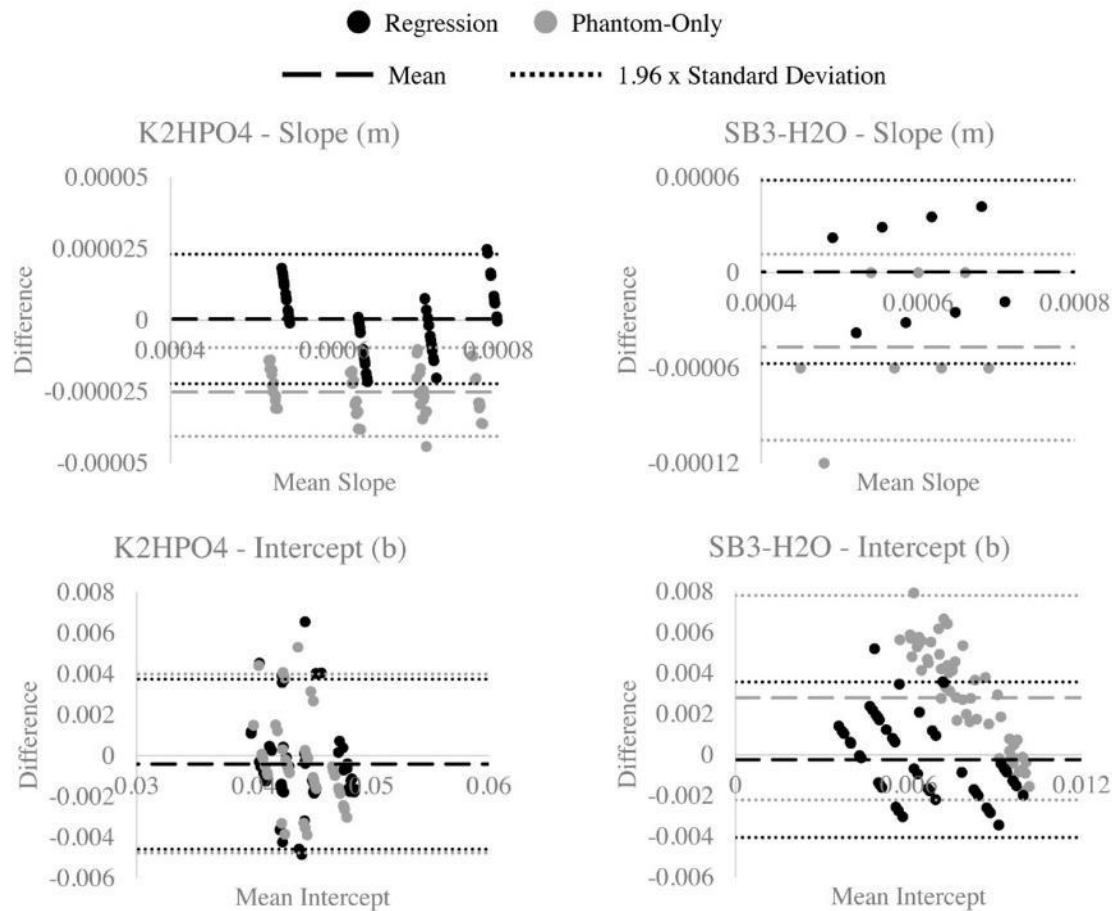


Figure F.3: Bland-Altman plots for density calibration equation slope and vertical intercept terms, comparing phantom-only and regression calibration methods.

ANOVA demonstrated that the calibration method had a significant main effect on the calibration equation slope; and a Bonferroni post-hoc test revealed that the phantom-only calibration method predicted slopes that were significantly different than the calibrated and regression methods.

Bland-Altman and percent difference plots of ash density also revealed that the regression method produced smaller differences relative to the standard calibration method compared to the phantom-only method. An inherent limitation of the phantom-only method of post-hoc calibration is that the volume of solid material present in the scanning chamber changes between the original scan, and the post-hoc scan. The removal of the specimen tissue has an effect on the attenuation that the CT scanner experiences in each scan. While there is variation in tissue volume present between specimens, which should account for some variance in regression and standard calibration terms, there is a far greater change in tissue volume when performing a scan with the phantom only. This variation in attenuation present between phantom-only and regular scans is suggested as a possible cause of some of the differences seen between the proper and phantom-only calibration equation terms. These results suggest that, while the proper calibration method will always be preferred, in the event that post-hoc qCT scan calibration is necessary, the regression method does a better job of replicating calibration compared to the phantom-only method.

The repeated measures ANOVA also indicated that the choice of calibration phantom significantly affects the terms of the calibration equation. K_2HPO_4 was found to significantly increase the predicted density compared to SB3- H_2O . While differences between solid (*i.e.*, calcium hydroxyapatite) and liquid (*i.e.*, dipotassium phosphate) calibration phantoms was also reported in 1993 by Faulkner *et al*, they found the opposite trend, with higher bone mineral densities reported from a solid calibration phantom (Image Analysis solid standard) compared to a liquid one (University of California San Francisco liquid standard) [19]. It should be noted that Faulkner *et al* (1993) used a solid calcium hydroxyapatite phantom that was contained in ‘water-

equivalent⁷ plastic, while the current investigation used actual distilled water as the second reference material for the SB3-H₂O calibration phantom. This difference in calibration phantom may account for the discrepancy in trend between calibration phantom types. Regardless, both results suggest that the type of calibration phantom chosen will impact the calibration equation quantified. Accordingly, the specific type of calibration phantom should be reported in detail for all future qCT studies requiring bone mineral density calibration.

A limitation of this work is that the resulting calibration equations are specific to the CT scanner used in the present study. These equations are expected to change between CT scanners, and should not be applied to uncalibrated scans obtained on different devices. Furthermore, it should be noted that, when applying the regression method of post-hoc calibration, the tissue present in the scans used to construct the regression equations should be similar in volume and density to the subject of the scans to which the calibration would be applied (*i.e.*, cadaveric arms should not be used for living patients who would have greater tissue volume, and *vice-versa*). Having said this, the purposes of the present investigation were to present the regression post-hoc calibration method, and to compare it with phantom-only and standard calibrations, not to develop universal calibration equations for all CT scanners.

Should others seek to replicate the post-hoc regression calibration methods described above, it is important to best match the conditions of the uncalibrated scans (*i.e.*, same scanner, reconstruction kernel, kVp settings, *etc.*), and to conduct scans at CT voltages that capture the full range of the uncalibrated scans to avoid extrapolating results. Mean percentage errors should also be quantified when developing post-hoc calibration scans, so that they can be reported along with qCT results that are determined using the regression method. Once equations are formed, they permit the determination of calibration equations for a database of uncalibrated scans at a variety of known CT peak tube voltages, provided those scans were obtained from the same CT scanner that was used to develop the post-hoc regression equations. Furthermore, though the results of the

present investigation have been presented in terms of ash density only, the scalar relationship developed by Schileo *et al* (2008) suggests that results apply for apparent density as well [16]. Additionally, information regarding the quality assurance scans performed for the CT scanner used in this investigation are not presented directly. As the scanner used is an active clinical CT scanner used for upper limb diagnostic imaging, quality assurance scans are completed by the hospital's imaging physics department at regular intervals for clinical use. To ensure consistency with the quality assurance scans, those performed within this study were completed by the same CT technician who conducts the quality assurance scans. Finally, a related limitation of this work is that the CT scans performed for the regression analysis were not conducted at multiple time points. Documentation of any transient effects on the regression formulation may be of interest for future investigations; however, clinical scans performed since this investigation have yielded consistent density calibration terms.

In conclusion, stepwise linear regression can be used to form correlations between peak tube voltage and the terms of density calibration equations. This form of post-hoc CT scan calibration produced lower percentage errors than post-hoc phantom-only scans, and better replicated the proper calibration terms. While proper CT scan calibration, where a calibration phantom is used at the time of scan acquisition, is always preferable, post-hoc regression seems to be an acceptable calibration method with relatively low mean errors (-3.1% to 3.0%) compared to proper calibration methods.

F.5 References

- [1] Reeves, J. M., Knowles, N. K., Athwal, G. S., and Johnson, J. A., 2018, "Methods for Post-Hoc Quantitative CT Bone Density Calibration: Phantom-only and Regression," *J. Biomech. Eng.*, p. (In Press).
- [2] Cong, A., Buijs, J. O. Den, and Dragomir-Daescu, D., 2011, "In situ parameter identification of optimal density-elastic modulus relationships in subject-specific finite

- element models of the proximal femur,” *Med. Eng. Phys.*, **33**(2), pp. 164–173.
- [3] Keaveny, T. M., McClung, M. R., Wan, X., Kopperdahl, D. L., Mitlak, B. H., and Krohn, K., 2012, “Femoral strength in osteoporotic women treated with teriparatide or alendronate,” *Bone*, **50**(1), pp. 165–170.
- [4] Keyak, J. H., Sigurdsson, S., Karlsdottir, G. S., Oskarsdottir, D., Sigmarsdottir, A., Kornak, J., Harris, T. B., Sigurdsson, G., Jonsson, B. Y., Siggeirsdottir, K., Eiriksdottir, G., Gudnason, V., and Lang, T. F., 2013, “Effect of finite element model loading condition on fracture risk assessment in men and women: The AGES-Reykjavik study,” *Bone*, **57**(1), pp. 18–29.
- [5] Tawara, D., Sakamoto, J., Murakami, H., Kawahara, N., Oda, J., and Tomita, K., 2010, “Mechanical evaluation by patient-specific finite element analyses demonstrates therapeutic effects for osteoporotic vertebrae,” *J. Mech. Behav. Biomed. Mater.*, **3**(1), pp. 31–40.
- [6] Kopperdahl, D. L., Aspelund, T., Hoffmann, P. F., Sigurdsson, S., Siggeirsdottir, K., Harris, T. B., Gudnason, V., and Keaveny, T. M., 2014, “Assessment of incident spine and hip fractures in women and men using finite element analysis of CT scans,” *J. Bone Miner. Res.*, **29**(3), pp. 570–580.
- [7] Razfar, N., Reeves, J. M., Langohr, D. G., Willing, R., Athwal, G. S., and Johnson, J. A., 2016, “Comparison of proximal humeral bone stresses between stemless, short stem, and standard stem length: a finite element analysis,” *J. Shoulder Elb. Surg.*, **25**(7), pp. 1076–83.
- [8] Dragomir-Daescu, D., Op Den Buijs, J., McEligot, S., Dai, Y., Entwistle, R. C., Salas, C., Melton, L. J., Bennet, K. E., Khosla, S., and Amin, S., 2011, “Robust QCT/FEA models of proximal femur stiffness and fracture load during a sideways fall on the hip,” *Ann.*

- Biomed. Eng., **39**(2), pp. 742–755.
- [9] Eberle, S., Göttlinger, M., and Augat, P., 2013, “An investigation to determine if a single validated density-elasticity relationship can be used for subject specific finite element analyses of human long bones,” *Med. Eng. Phys.*, **35**(7), pp. 875–883.
- [10] Eberle, S., Göttlinger, M., and Augat, P., 2013, “Individual density-elasticity relationships improve accuracy of subject-specific finite element models of human femurs,” *J. Biomech.*, **46**(13), pp. 2152–2157.
- [11] Haider, I. T., Speirs, A. D., and Frei, H., 2013, “Effect of boundary conditions, impact loading and hydraulic stiffening on femoral fracture strength,” *J. Biomech.*, **46**(13), pp. 2115–2121.
- [12] Kheirollahi, H., and Luo, Y., 2015, “Assessment of Hip Fracture Risk Using Cross-Section Strain Energy Determined by QCT-Based Finite Element Modeling,” *Biomed Res. Int.*, p. e413839.
- [13] Campoli, G., Bolsterlee, B., van der Helm, F., Weinans, H., and Zadpoor, A. a, 2014, “Effects of densitometry, material mapping and load estimation uncertainties on the accuracy of patient-specific finite-element models of the scapula,” *J. R. Soc. Interface*, **11**(93), p. 20131146.
- [14] Pomwenger, W., Entacher, K., Resch, H., and Schuller-Götzburg, P., 2014, “Need for CT-based bone density modelling in finite element analysis of a shoulder arthroplasty revealed through a novel method for result analysis,” *Biomed. Eng. / Biomed. Tech.*, **59**(5), pp. 421–430.
- [15] Taylor, W. R., Roland, E., Ploeg, H., Hertig, D., Klabunde, R., Warner, M. D., Hobatho, M. C., Rakotomanana, L., and Clift, S. E., 2002, “Determination of orthotropic bone elastic constants using FEA and modal analysis,” *J. Biomech.*, **35**(6), pp. 767–773.

- [16] Schileo, E., Dall'Ara, E., Taddei, F., Malandrino, A., Schotkamp, T., Baleani, M., and Viceconti, M., 2008, "An accurate estimation of bone density improves the accuracy of subject-specific finite element models," *J. Biomech.*, **41**, pp. 2483–2491.
- [17] Keyak, J. H., Lee, I. Y., and Skinner, H. B., 1994, "Correlations between orthogonal mechanical properties and density of trabecular bone : Use of different densitometric measures," *J. Biomed. Mater. Res.*, **28**, pp. 1329–1336.
- [18] Giambini, H., Dragomir-Daescu, D., Huddleston, P. M., Camp, J. J., An, K.-N., and Nassr, A., 2015, "The Effect of Quantitative Computed Tomography Acquisition Protocols on Bone Mineral Density Estimation," *J. Biomech. Eng.*, **137**(November), pp. 1–6.
- [19] Faulkner, K. G., Gluer, C. C., Grampp, S., and Genant, H. K., 1993, "Cross-Calibration of Liquid and Solid QCT Calibration Standards: Corrections to the UCSF Normative Data," *Osteoporos. Int.*, **3**, pp. 36–42.
- [20] Software, M., 2011, "QCT PRO: Bone Mineral Densitometry Software CT Calibration Phantom," pp. 1–10.
- [21] Ashman, R. B., 1989, "Experimental Techniques," *Bone Mechanics*, S.C. Cowin, ed., CRC Press Inc., Boca Raton, p. 76.
- [22] Bonnucci, E., 2000, "Basic Composition and Structure of Bone," *Mechanical Testing of Bone and the Bone-Implant Interface*, Y.H. An, and R.A. Draughn, eds., CRC Press Inc., Boca Raton, pp. 3–21.

Appendix G - Creating Masks and Solid Body Models of Bone

G.1 Introduction

The method described herein attempts to provide a starting point for developing ‘good’ bone masks in Mimics (version 19), then how to use SolidWorks to develop these into separate cortical and trabecular solid models. This approach has been developed through trial and error, using the proximal humerus as a sample. The general approach is to first develop a water-tight and completely-filled overall bone mask, then to develop a mask that estimates the trabecular bone and canal, which is smooth (*i.e.*, avoids fissures of dense cortical bone in the subchondral region). These two masks can then be developed into 3D STL files that can be exported to SolidWorks, where Boolean operations can create a cortical shell.

When developing Finite Element (FE) models, we take apply a constant elastic modulus to the cortical shell (~20GPa), and regionally-varying elastic moduli to the trabecular-canal. A smooth surface that divides the cortical and trabecular-canal regions is desirable to permit meshing. The trabecular-canal elastic modulus is derived from the underlying bone attenuation in Mimics, so while a smooth transition is not completely anatomic, the irregularities in the transition-region are accounted for with higher attenuations experienced near the smooth transition surface.

G.2 Bone Masking Methods

G.2.1 The Proximal Humerus Mask

1. Using the right-side panel, create a new mask using Mimic’s default ‘bone’ settings.
 - a. Name the created mask ‘Bone’.
2. For the proximal humerus, we are not concerned with the distal end, and as such, we can remove this section of the bone. To do so:
 - a. Move to the Mimics pane that best represents the transverse (or axial) view of the humerus.

- b. Move down the shaft of the humerus until you are approximately $\frac{3}{4}$ of the total length (or however far you require for your study).
 - c. Select the 'Bone' mask from the right-side panel. Right-click and select 'Edit Mask'.
 - i. Remove all the 'Bone' mask in this slice.
 - ii. Move to the next-most proximal slice, and using the 'Edit Mask' tool, fill in the humerus canal so that there are no gaps.
 1. This creates a 'water-tight' bottom of the proximal humerus mask.
3. Right-click on the 'Bone' mask, and select 'Region Growing'.
 - a. Click on the humeral shaft portion of the 'Bone' mask to try and isolate it from the surrounding 'Bones' that are also contained in this mask.
 - b. Depending on the 'quality' of the bone and the resolution of the CT scan that you are working with, you may not be able to separate the humerus using region growing on the first try. If this is the case:
 - i. Select the 'Bone' mask in the right-side panel, right-click and select 'Edit Mask'.
 - ii. Remove parts of the 'Bone' mask that are bridging between the separate bone sections. These will most likely present in the joints, between articular surfaces, and must be deleted manually by moving slice-by-slice.
 - c. Name the isolated humerus bone as 'ProxHum'.
 4. Right-click on the 'ProxHum' mask, and select 'Morphology'.
 - a. Select 'Close' from the drop-down menu, and make sure that the mask the operation will be performed on is 'ProxHum'.
 - b. Set the closing distance as 2 pixels (Note: This may have to be adjusted, but I find 2px is a good starting point).
 - c. Apply the operation.
 - d. Name the resulting mask 'ProxHum_Closed'.

5. Use the 'Cavity Fill' feature (looks like a paint can) on the top-panel to fill the empty space outside of the 'ProxHum_Closed' mask. This is done by clicking on the space outside of the 'ProxHum_Closed' mask.
 - a. Make sure you are using the 'ProxHum_Closed' mask as the driving mask, and that the fill will be applied to a new mask.
 - b. This operation should fill all the space around the 'ProxHum_Closed' mask, and should leave the trabecular-canal of the proximal humerus hollow (not filled by the new mask). If the trabecular-canal is filled with the new mask, you must use the 'Edit Mask' tool to fill any gaps that exist in the 'ProxHum_Closed' mask. These gaps typically present around the articular surface. After filling the gaps, try the cavity fill operation again.
 - c. Name the resulting mask 'Space'.
6. Perform another 'Cavity Fill' operation, this time using the 'Space' mask as the driving mask, and mapping to a new mask.
 - a. Click on the void space in the 'Space' mask that corresponds to the proximal humerus.
 - b. This should create a completely solid proximal humerus mask.
 - c. Name the resulting mask 'ProxHum_Filled'.
7. Select 'ProxHum_Filled' from the right-side panel. Right-click and select 'Calculate 3D'.
 - a. This will generate a 3D representation of the 'ProxHum_Filled' mask in the '3D Objects' panel that is beneath where the different masks are located.
8. Select the newly created 3D object. Right-click and select 'Smoothing'.
 - a. Make sure smoothing settings are set as: Iterations = 12, Smooth Factor = 0.3.
 - i. These settings can be varied, but I find these values work well.
9. Now right-click and select 'Wrapping'.
 - a. Make sure the wrapping settings are set as: Smallest Detail = 1mm, Gap Closing Distance = 3mm.

- i. Again, these settings are what I have found work well, but they can be changed.
10. Repeat the 'Smoothing' operation one more time.
 - a. Iterations of 'Smoothing' and 'Wrapping' operations should be done to suit your needs. These are typically what I use, but can be varied.
 - b. Hide all other versions of the proximal humerus 3D object.
11. Rename the final 3D object 'ProxHum'.
12. Export the 'ProxHum' in STL format.

G.2.2 The Trabecular Mask

1. Select the 'ProxHum_Filled' mask from the right-side panel. Right-click and select 'Morphology'.
 - a. Select 'Erode' from the drop-down menu.
 - b. Make sure you are using 'ProxHum_Filled' as the driving mask, and that you are creating a new mask.
 - c. Set the erosion to be 2 pixels.
 - d. Apply.
 - e. Name the resulting mask as 'ProxHum_Filled_Eroded'.
2. Create a new mask and manually set the threshold such that you create a cortical-like mask that maintains the thick cortical shell regions, but that minimizes the cortical infiltration beneath the subchondral surface.
 - a. This is rather subjective, but the idea is that you want to have a good approximation of the cortical shell, without too many (you won't be able to remove them all) of the cortical fissures infiltrating the subchondral trabecular-canal. I find that between 600HU and 800HU is a good place to start.
 - b. Name the resulting mask as 'Cortical'.
3. Select the 'Boolean' operation from the top-panel.
 - a. Select 'Subtract' from the drop-down menu.
 - b. Subtract the 'Cortical' mask from the 'ProxHum_Filled_Eroded' mask.
 - c. Name the resulting mask as 'Trab'.

4. Select the 'Trab' mask from the right-side panel. Right-click and select 'Morphology'.
 - a. Select 'Erode' from the drop-down menu.
 - b. Erode the 'Trab' mask to a new mask by 1 pixel.
 - c. Name the resulting mask as 'Trab_Eroded'.
5. Select the 'Trab_Eroded' mask from the right-side panel. Right-click and select 'Region Growing'.
 - a. Click on the main trabecular body in the 'Trab_Eroded' mask.
 - b. Name the resulting mask as 'Trab_Eroded_RG'.
6. Select the 'Trab_Eroded_RG' mask from the right-side panel. Right-click and select 'Morphology'.
 - a. Select 'Close' from the drop-down menu.
 - b. Close the 'Trab_Eroded_RG' mask to a new mask by 2 pixels.
 - c. Name the resulting mask as 'Trab_Closed'.
7. Select the 'Trab_Closed' mask from the right-side panel. Right-click and select 'Morphology'.
 - a. Select 'Dilate' from the drop-down menu.
 - b. Dilate the 'Trab_Closed' mask to a new mask by 2 pixels.
 - c. Name the resulting mask as 'Trab_Closed_Dilated'.
8. Select the 'Trab_Closed_Dilated' mask from the right-side panel. Right-click and select 'Calculate 3D'.
 - a. This will generate a 3D representation of the 'Trab_Filled_Dilated' mask in the '3D Objects' panel that is beneath where the different masks are located.
9. Select the newly created 3D object. Right-click and select 'Wrapping'.
 - a. Make sure the wrapping settings are set as: Smallest Detail = 1mm, Gap Closing Distance = 3mm.
 - i. Again, these settings are what I have found work well, but they can be changed.
10. Now right-click and select 'Smoothing'.

- a. Make sure smoothing settings are set as: Iterations = 12, Smooth Factor = 0.3.
 - i. These settings can be varied, but I find these values work well.
 - b. Repeat smoothing two more times, or as many times as is necessary to prevent you from seeing the trabecular 3D object through the 'ProxHum' 3D object.
 - i. Note: as you repeat wrapping and smoothing functions, you will be generating 3D objects. To judge your most recent progress, you want to hide the older versions and only view the most recent (perhaps with the 'ProxHum' 3D object shown as well).
11. Rename the final iteration of the proximal humerus' trabecular-canal as 'Trabecular'.
12. Export the 'Trabecular' 3D object in STL format.

G.3 Solid Body Modeling in SolidWorks

1. Launch SolidWorks, and click on the open button.
 - a. Under file type, select STL.
 - b. Click on the options button that appears, and ensure that you are attempting to import the STL as a 'Solid Body', and that 'Translate into positive coordinates' is NOT selected. We need each part to remain positioned the same as it was in the Mimics.
 - c. Select the 'ProxHum' file that was exported in the final step of 'Developing the Proximal Humerus Mask' above, and click OK.
2. The file will take some time to develop a solid model from the STL surfaces, but once it completes, you should see that a solid object has been added to the Part's tree on the left hand side of the screen.
 - a. To check if the object has been imported as a solid, select the cross-section view, and move your cross-section plane through the part to visualize the solid interior.

- b. Occasionally, SolidWorks may take issue with the number of surfaces that it needs to convert into a solid object. If this happens, try to trim the mask before exporting as an STL if possible, or attempt to smooth it further.
3. Once the part has been imported as a solid body properly, save it as a .SLDPRT file.
4. Repeat steps 1-3 for the 'Trabecular' STL file.
5. With both parts created, open the ProxHum.SLDPRT in SolidWorks.
6. Import Trabecular.SLDPRT into ProxHum.SLDPRT.
 - a. In ProxHum.SLDPRT, select 'Insert' then 'Part...'
 - b. From the popup box select 'Trabecular.SLDPRT'.
 - c. The program will give you the option of 'dropping' the part with the window, but you need to ensure that the part remains aligned to the same global coordinate system as the Mimics CT scan and the 'ProxHum', so from the left-side panel, check off 'Solid Bodies', then click on the green 'checkmark'.
 - d. Now, the Trabecular.SLDPRT should be located within the ProxHum.SLDPRT, and they should be aligned according to the Mimics global coordinate system.
7. Subtract the volume of Trabecular.SLDPRT from the ProxHum.SLDPRT.
 - a. Select 'insert', then 'Features', then 'Combine'.
 - b. For Operation Type, choose 'Subtract'.
 - c. Select the ProxHum as the main body, and Trabecular as the Bodies to Subtract.
 - d. Confirm by clicking on the green 'checkmark'.
 - e. Now, you should be left with a hollowed-out version of the proximal humerus whose inner surface directly matches the outer surface of the Trabecular.SLDPRT. This represents the cortical bone of the proximal humerus.
 - f. Save the resulting part as 'Cortical.SLDPRT'.
8. You can now perform any cuts, implant orientation, *etc.* that you wish on these solid body models.

- a. When you are satisfied with your models, and wish to move them to Abaqus for development into Finite Element models, you should save each part as 'STEP AP214' files, as these retain the geometry of the parts best for importing into Abaqus.

G.4 In-Silico Humeral Head Resection and Positioning a Stemless Implant

G.4.1 Humeral Head Resection

To create a surgical resection plane in SolidWorks, I use 3 points. In order to reduce the plane's orientation sensitivity to the points (permitting easier refinement), it is best to place the points far apart. This procedure is best done on the Cortical bone because the boney landmarks are more easily discerned. The trabecular bone will be cut afterwards using the same points.

1. Identify the 'Crown' of the proximal humerus. This is the 'lip' where the articular dome of the humeral head begins to curve back in upon itself to draft down to the rest of the proximal humerus. It should more-or-less resemble a circular curvature on the medial side of the bone.
2. Using the Sketch tab, select the '3D Sketch' option (using the arrow next to the normal 'Sketch' button).
3. Select the 'Point' tool, and select 3 points around the circumference of the humeral crown. Ensure that when you drop the points, they fall on the outer surface of the cortex, and that they do not lock to an edge or vertex; this will permit some movement of the point within the surface that you select. Try to select a point superior-laterally, as well as one somewhat anterior and one somewhat inferior-medially.
4. Once you are satisfied with your points, exit the 3D Sketch, and create a Reference Plane using the Reference Geometry button.
 - a. Select the points and confirm your choice.
5. From the Insert button, select 'Cut', then 'Surface Cut'.
 - a. Use your newly created resection plane as the cutting surface, and select to remove the top (or head) of the humerus.

- b. Confirm your selection.
6. At this point, it is best to review your resection with a clinician.
 - a. In my experience, it takes several iterations of steps 3-5 to get an appropriate surgical resection.
7. Once the proper surgical resection has been formed, make note of the (x,y,z) position of each of the resection plane points (and fix/anchor each point so that it will not move), so that you can use the same ones for the trabecular bone as well.
8. Save your part as 'Cortical_Bottom.SLDPRT'.
9. Reverse the side to retain in the head resection so that you are keeping only the top of the humeral head, and save this as a separate part 'Cortical_Top.SLDPRT'.
10. Repeat for the Trabecular bone, but rather than iterating the point position, when you drop the three points into the display, use the left-side control pane to indicate the exact same (x,y,z) position of each point. In this way, the resection planes should be identical between the cortical and trabecular bones.
11. This should leave you with top and bottom segments for both the cortical and trabecular bone.

G.4.2 Resection Coordinates and Stemless Implant Positioning

To position the humeral head appropriately, we need to form a reproducible resection-based humeral coordinate system.

1. In the Trabecular_Bottom.SLDPRT determine the centroid of the humeral resection plane.
 - a. Select the resection surface.
 - b. Under the Evaluate tab, select 'Section Properties'. This will give you the centroid position (x,y,z).
2. Create a 3D sketch, place a point, and use the left panel to set the point's coordinates to the resection centroid, and fix the point in space.
3. Now, create another 3D sketch and select the most superior-lateral (SL) and the most inferior-medial (IM) points on the resection surface.
4. Connect SL and IM with a reference axis. Call this the SI-Axis.

5. Create a reference plane through the SI-Axis and perpendicular to the resection plane. This will be the coronal plane.

Together the resection plane, resection centroid, SI-axis and the Coronal Plane can be used to position stemless implants repeatably in the proximal humerus.

G.4.3 Stemless Implant Positioning

1. Open a new assembly file in SolidWorks and insert the Trabecular_Bottom.SLDPRT such that it retains its part/mimics coordinate system and is fixed in space (by clicking the checkmark, NOT by dropping it in the display).
2. Add the Stemless implant that you are working with, by dropping it into the display so that it is floating and can move to mate with the bone as required.
3. Select the top surface of the implant (or backside of the articular/head component), and mate this to be coincident with the resection surface.
4. Use implant features (fins, *etc.*) to rotate the implant into alignment with the coronal plane (*e.g.*, the Tornier Simpliciti has a superior-laterally directed fin that is to be parallel with the coronal plane).
5. Create a central axis within the implant part (*i.e.*, this would be the rotational axis of an axisymmetric fixation feature or would be the central axis of the implants head that should be perpendicular to the resection plane), and mate it to be coincident with the resection plane's centroid.

Together, these mates should completely restrict the implant in all six dimensions.

6. Right-click on the Implant's name in the left-side panel, and 'Fix' it in space.
7. Save this file as 'Implant_Positioning.SLDASM'
8. Right-click on the Trabecular_Bottom.SLDPRT and 'Suppress' it.
9. Use Save-as and change the file type to SLDPRT to save the implant positioned in space as a separate part file. Name this 'Implant_Positioned.SLDPRT'.

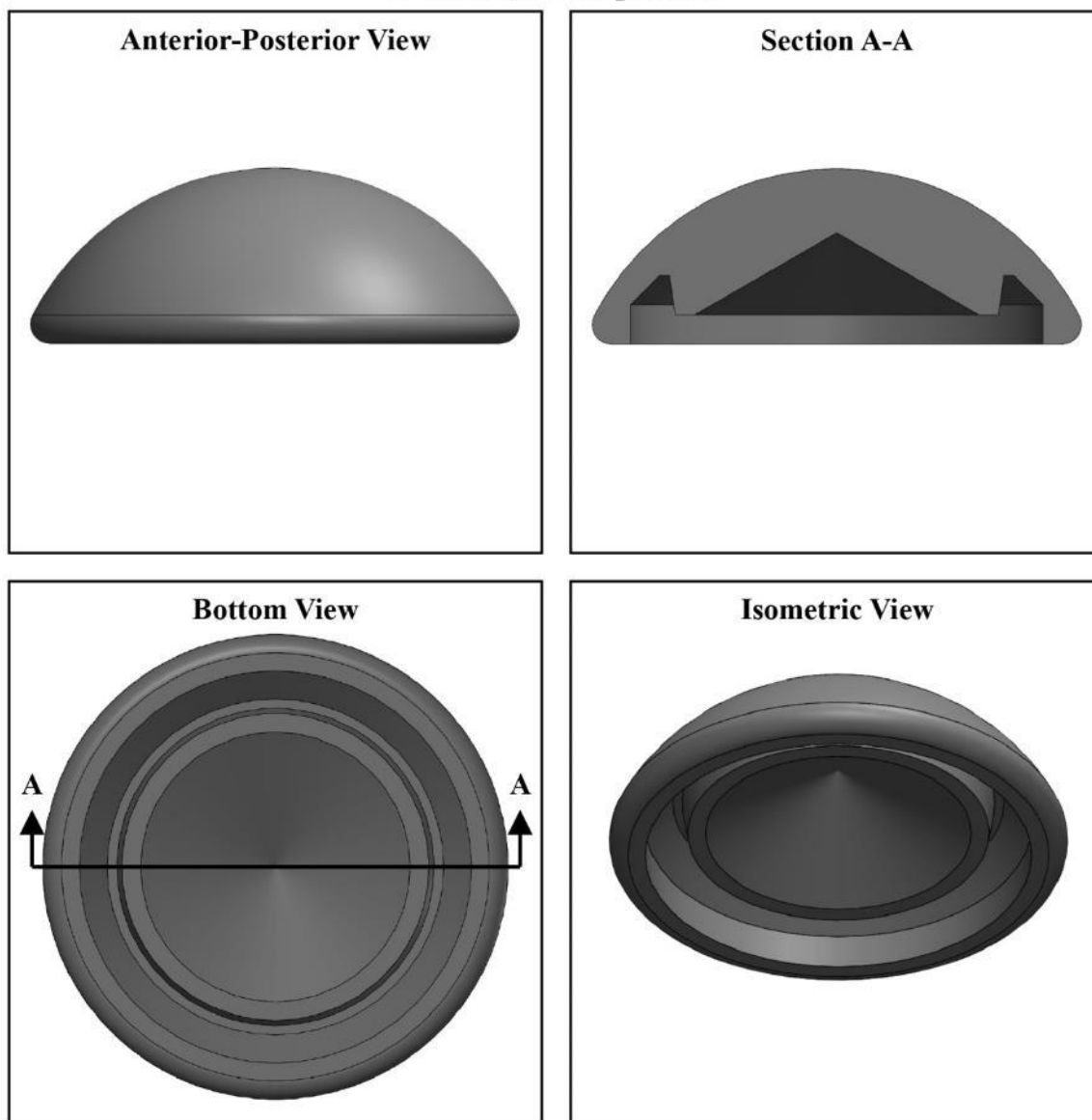
G.4.4 Cutting the Implant's Fixation Features out of the Bone

1. Open the Trabecular_Bottom.SLDPRT in SolidWorks.
2. Click 'Insert', then 'Part...' and select the Implant_Positioned.SLDPRT.

- a. Again, the program will give you the option of ‘dropping’ the part with the window, but we just positioned it relative to the Trabecular_Bottom’s coordinate system, so from the left-side panel, check off ‘Solid Bodies’, then click on the green ‘checkmark’.
3. Subtract the volume of Implant_Positioned.SLDPRT from the Trabecular_Bottom.SLDPRT.
 - a. Select ‘insert’, then ‘Features’, then ‘Combine’.
 - b. For Operation Type, choose ‘Subtract’.
 - c. Select the Trabecular_Bottom as the main body, and Implant_Positioned as the Bodies to Subtract.
 - d. Confirm by clicking on the green ‘checkmark’.
 - e. Now, you should be left with a hollowed-out version of the Trabecular_Bottom whose inner surface directly matches the outer surface of the Implant_Positioned.SLDPRT.
 - f. Save the resulting part as ‘Trabecular_Bottom_Cut.SLDPRT’.
 4. Also save this part as a STEP AP214 file so that it can be easily imported into Abaqus.

Appendix H – Generic Stemless Implant Details

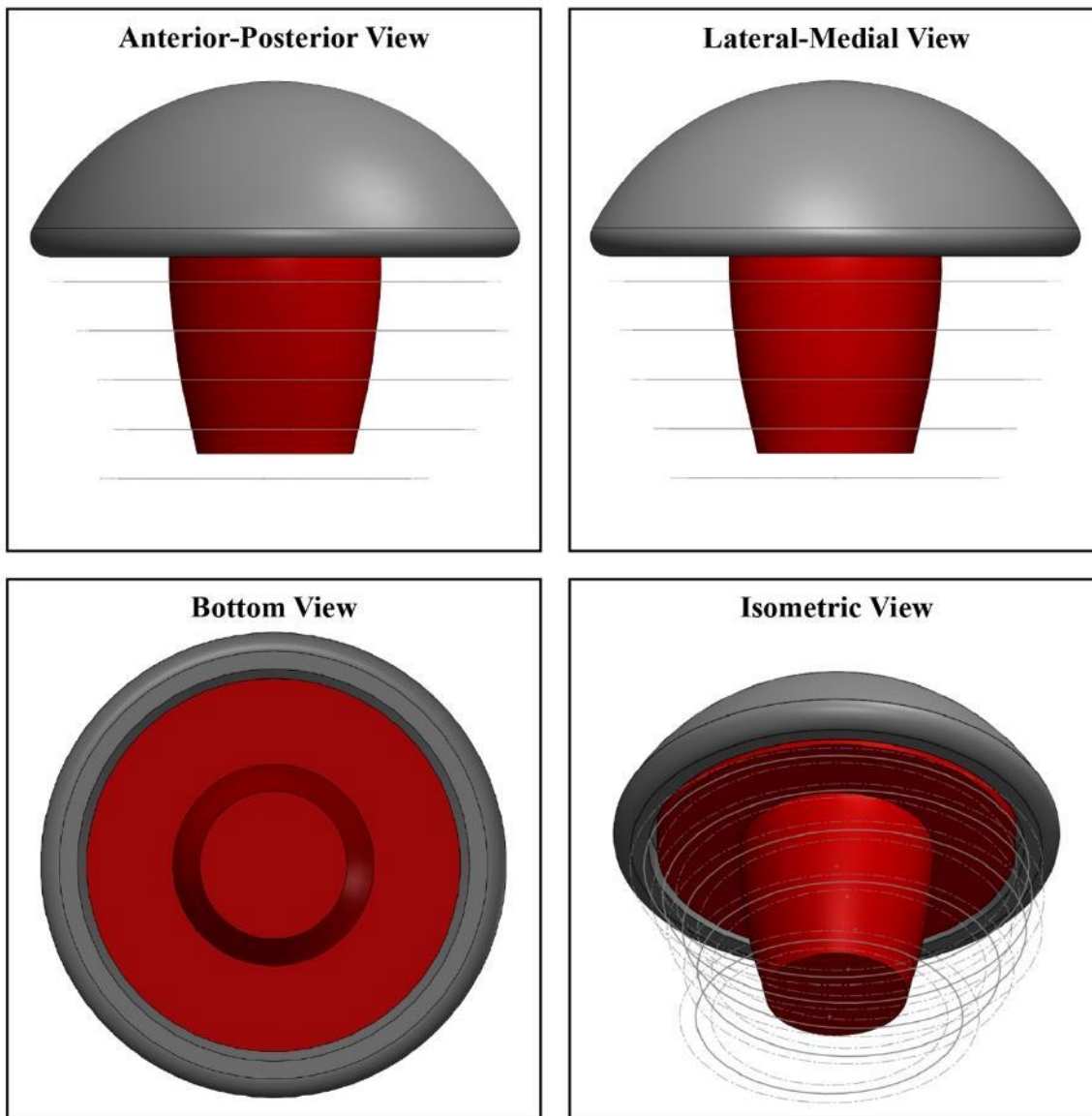
Articular Component



Implant Details: This articular component is designed to mate with the fixation features *via* a Morse taper that is contained within the articular dome to avoid removing additional metaphyseal bone beneath the humeral head resection. The articular dome is defined by an aspect ratio of 2.8:1 (diameter:height) to reflect a realistic curvature, as per Chapter 3 morphological results. A population of articular components exist, each varying in articular diameter in 2mm increments.

Figure H.1: Additional Views of the Stemless Implant Articular Component

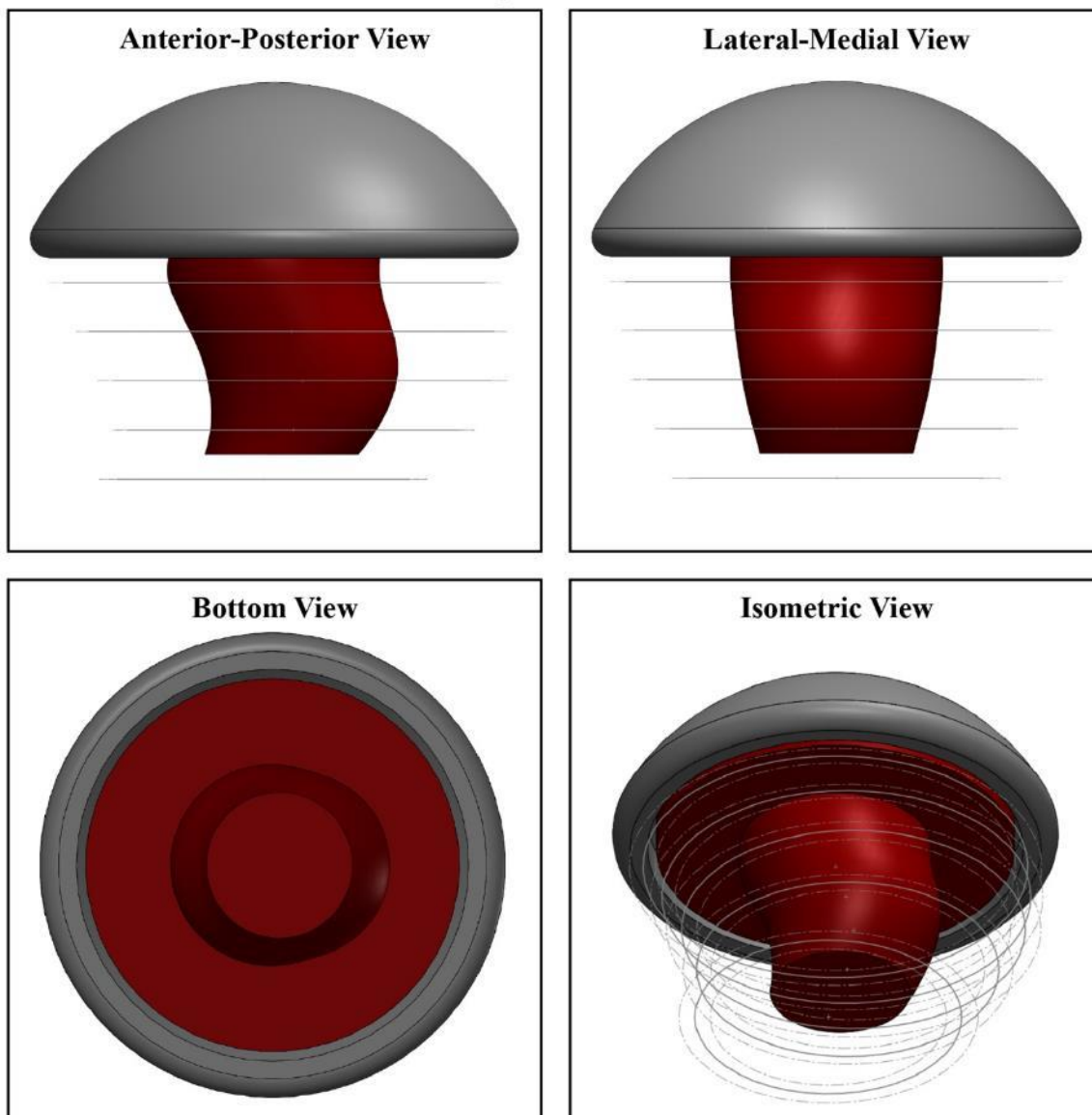
PegStraight



Implant Details: This implant is designed with a central fixation feature that varied as a function of depth, such that the peg diameter is $\frac{1}{2}$ of the pooled canal diameter from the morphological assessment of the humerus described in Chapter 3 (solid grey lines = mean, dashed lines = SD). The fixation feature extends 20mm into the humeral metaphysis, and is structured with a standard axisymmetric curvature.

Figure H.2: Additional Views of the PegStraight Stemless Fixation Feature

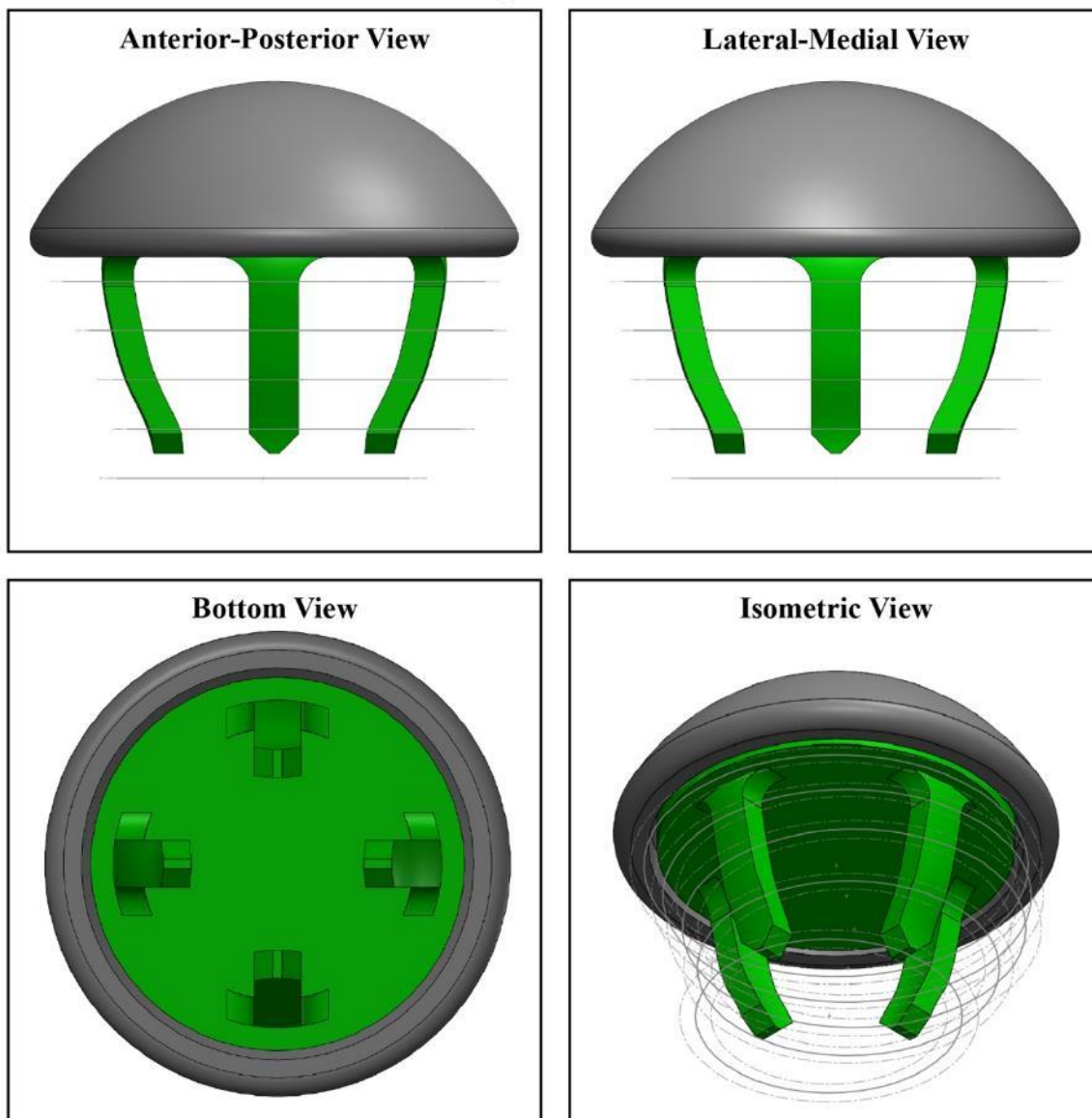
PegAnatomic



Implant Details: This implant is designed with a central fixation feature that varied as a function of depth, such that the peg diameter is $\frac{1}{2}$ of the pooled canal diameter from the morphological assessment of the humerus described in Chapter 3 (solid grey lines = mean, dashed lines = SD). The fixation feature extends 20mm into the humeral metaphysis, and follows the anatomic canal path's medial-lateral curvature (Chapter 3).

Figure H.3: Additional Views of the PegAnatomic Stemless Fixation Feature

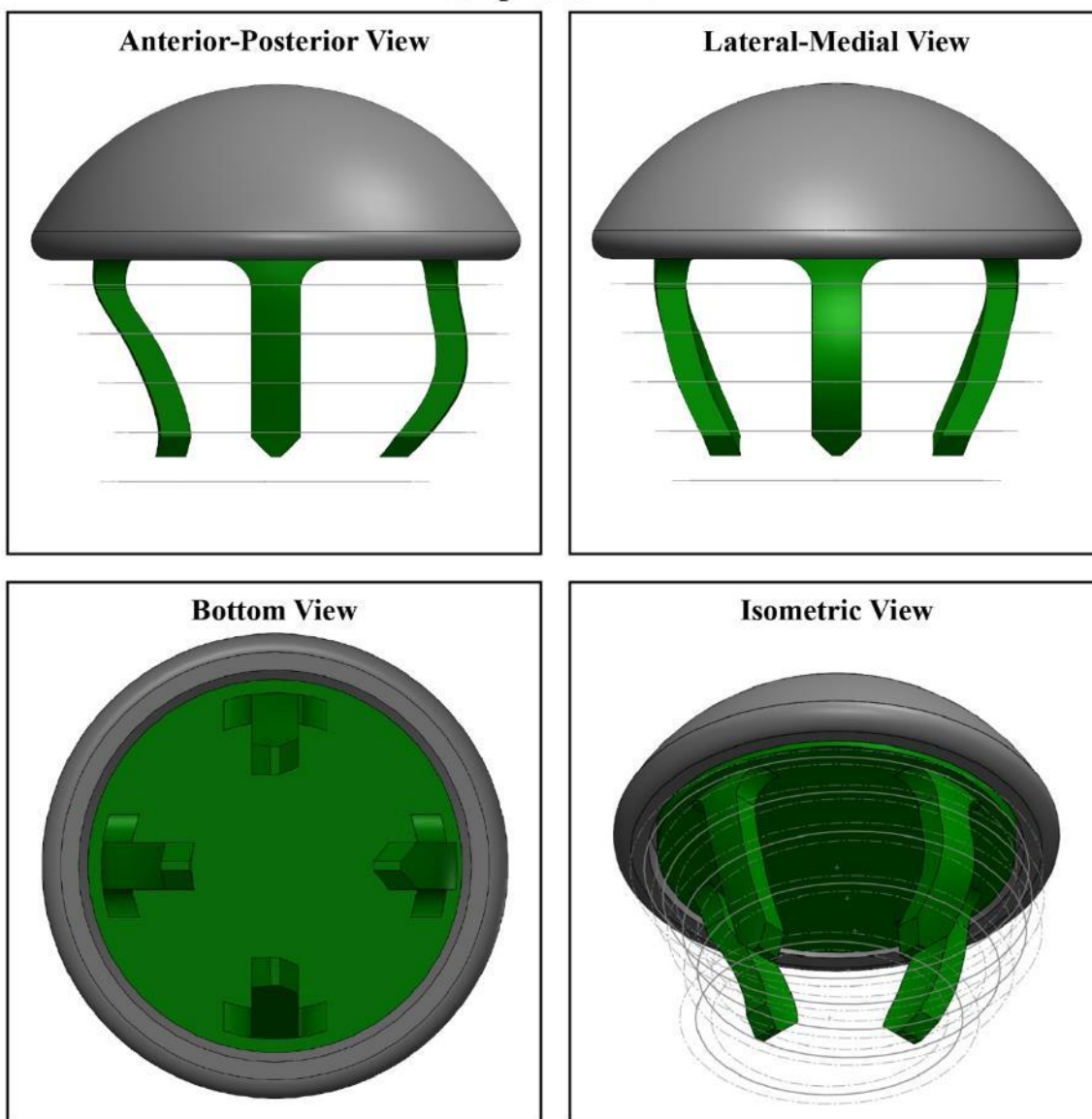
Peripheral4x5S



Implant Details: This implant is designed with a peripheral fixation feature that varied as a function of depth, such that the peg are radially located at $\frac{3}{4}$ of the pooled canal diameter from the morphological assessment of the humerus described in Chapter 3 (solid grey lines = mean, dashed lines = SD). The fixation feature extends 20mm into the humeral metaphysis, and is structured with a standard axisymmetric curvature. Pegs are 5mm wide and 3mm thick.

Figure H.4: Additional Views of the Peripheral4x5S Stemless Fixation Feature

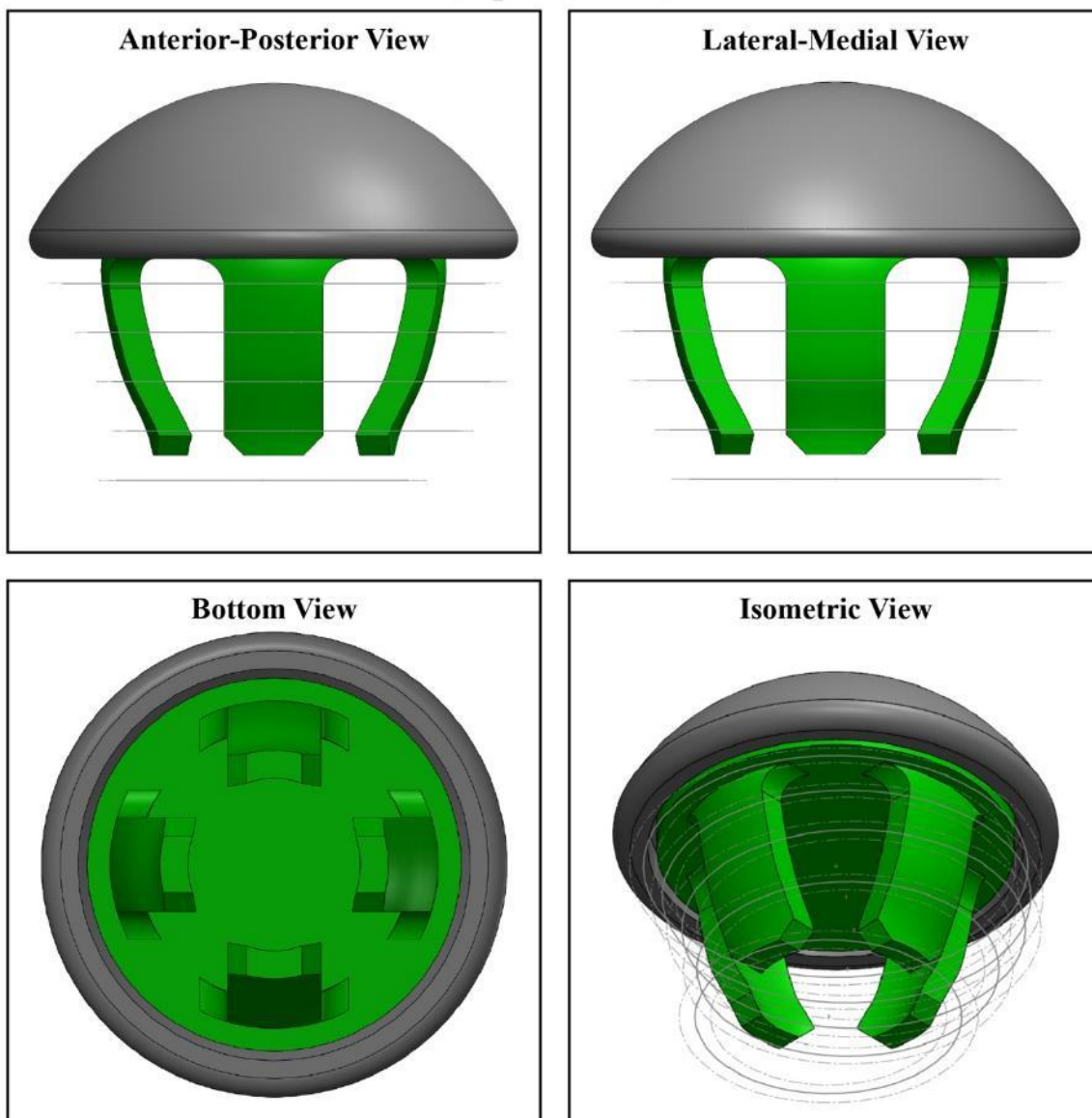
Peripheral4x5A



Implant Details: This implant is designed with a peripheral fixation feature that varied as a function of depth, such that the pegs are radially located at $\frac{3}{4}$ of the pooled canal diameter from the morphological assessment of the humerus described in Chapter 3 (solid grey lines = mean, dashed lines = SD). The fixation feature extends 20mm into the humeral metaphysis, and follows the anatomic canal path's medial-lateral curvature (Chapter 3). Pegs are 5mm wide and 3mm thick.

Figure H.5: Additional Views of the Peripheral4x5A Stemless Fixation Feature

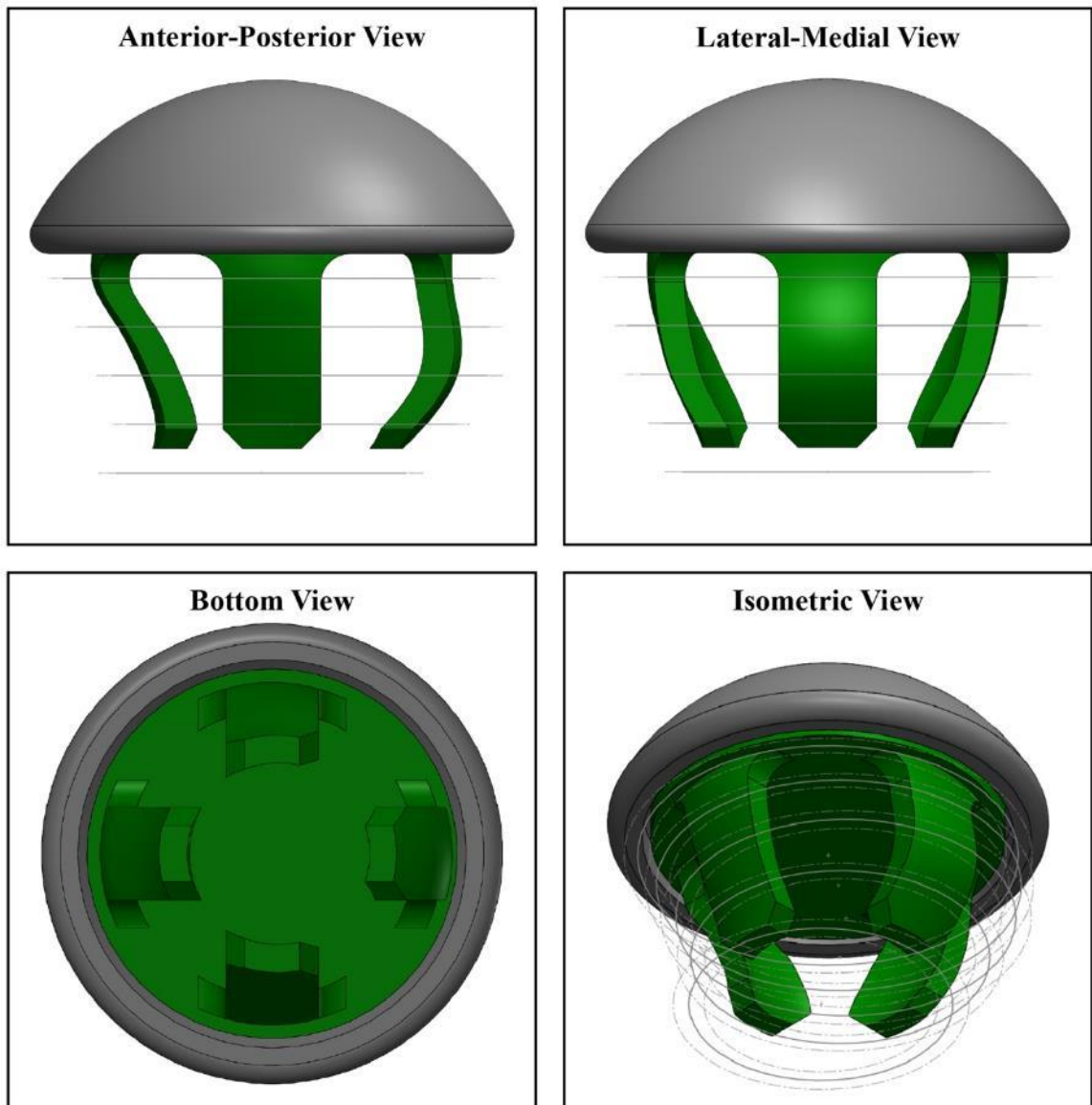
Peripheral4x10S



Implant Details: This implant is designed with a peripheral fixation feature that varied as a function of depth, such that the peg are radially located at $\frac{3}{4}$ of the pooled canal diameter from the morphological assessment of the humerus described in Chapter 3 (solid grey lines = mean, dashed lines = SD). The fixation feature extends 20mm into the humeral metaphysis, and is structured with a standard axisymmetric curvature. Pegs are 10mm wide and 3mm thick.

Figure H.6: Additional Views of the Peripheral4x10S Stemless Fixation Feature

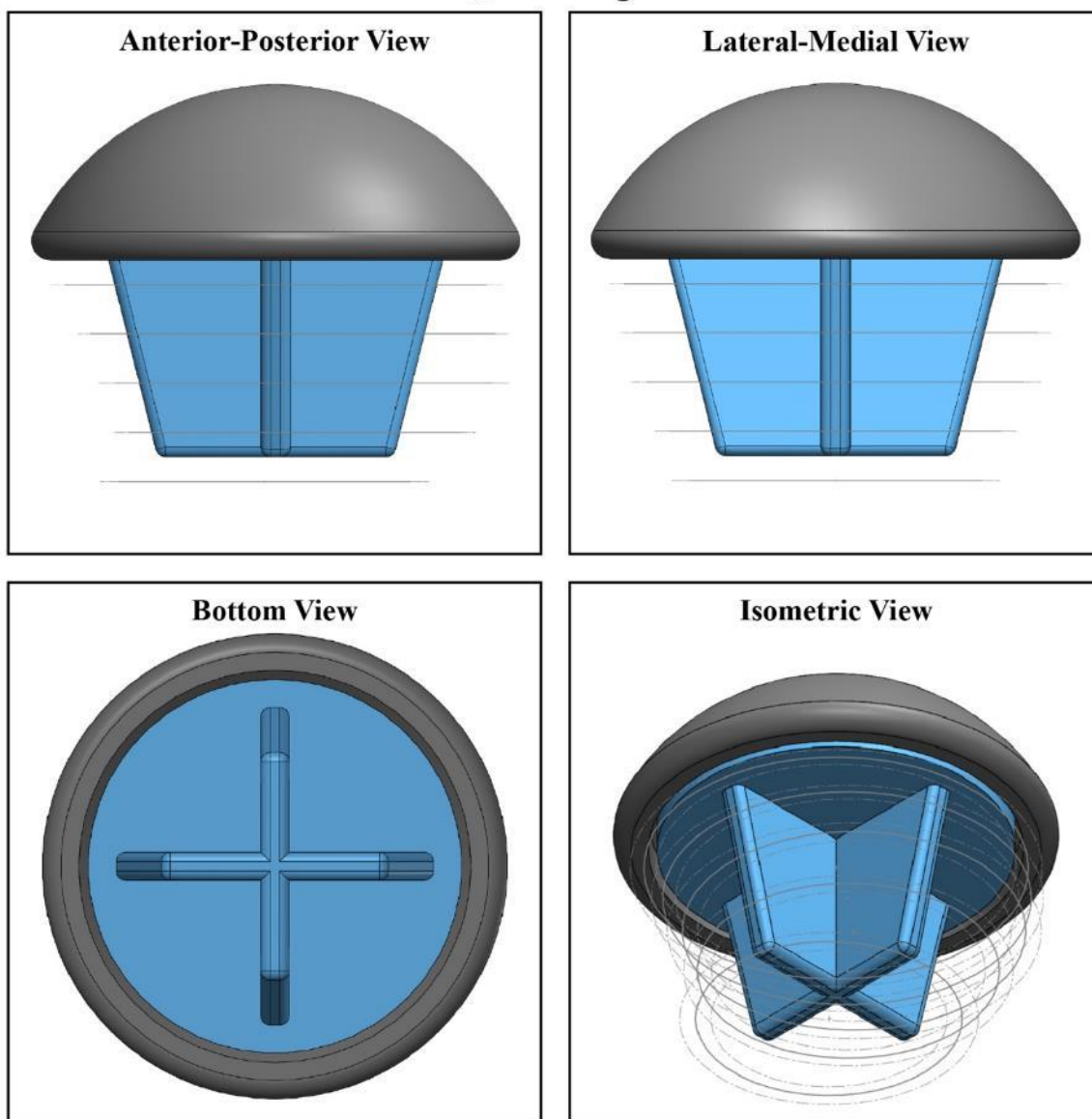
Peripheral4x10A



Implant Details: This implant is designed with a peripheral fixation feature that varied as a function of depth, such that the pegs are radially located at $\frac{3}{4}$ of the pooled canal diameter from the morphological assessment of the humerus described in Chapter 3 (solid grey lines = mean, dashed lines = SD). The fixation feature extends 20mm into the humeral metaphysis, and follows the anatomic canal path's medial-lateral curvature (Chapter 3). Pegs are 10mm wide and 3mm thick.

Figure H.7: Additional Views of the Peripheral4x10A Stemless Fixation Feature

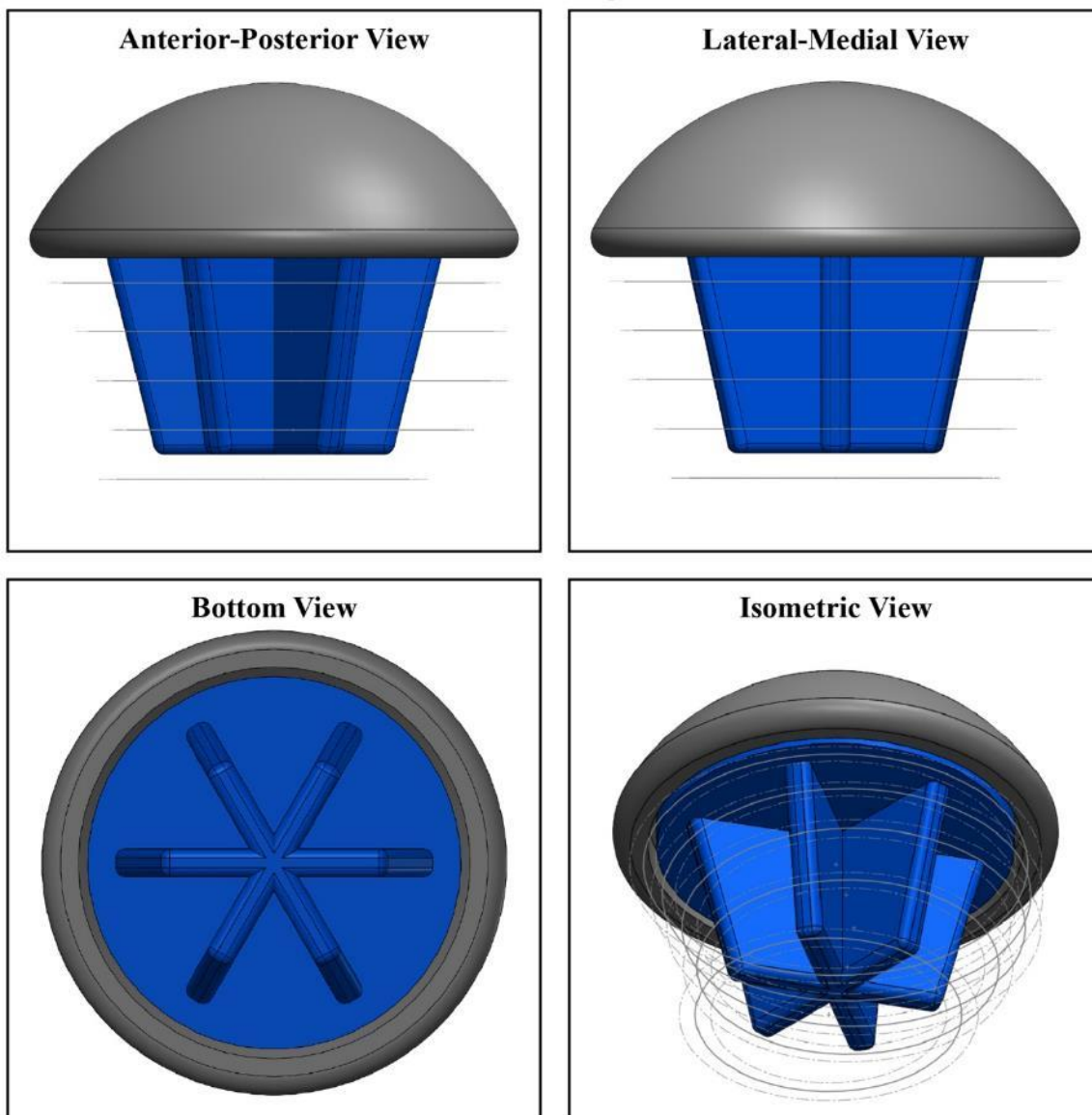
QuadFlange



Implant Details: This implant is designed with a boundary-crossing fixation feature that is composed of four flanges that taper at an angle of 14° to remain within the pooled canal diameters from the morphological assessment of the humerus described in Chapter 3 (solid grey lines = mean, dashed lines = SD). The fixation feature extends 20mm into the humeral metaphysis, and each flange is 3mm thick and 17mm wide at the resection plane.

Figure H.8: Additional Views of the QuadFlange Stemless Fixation Feature

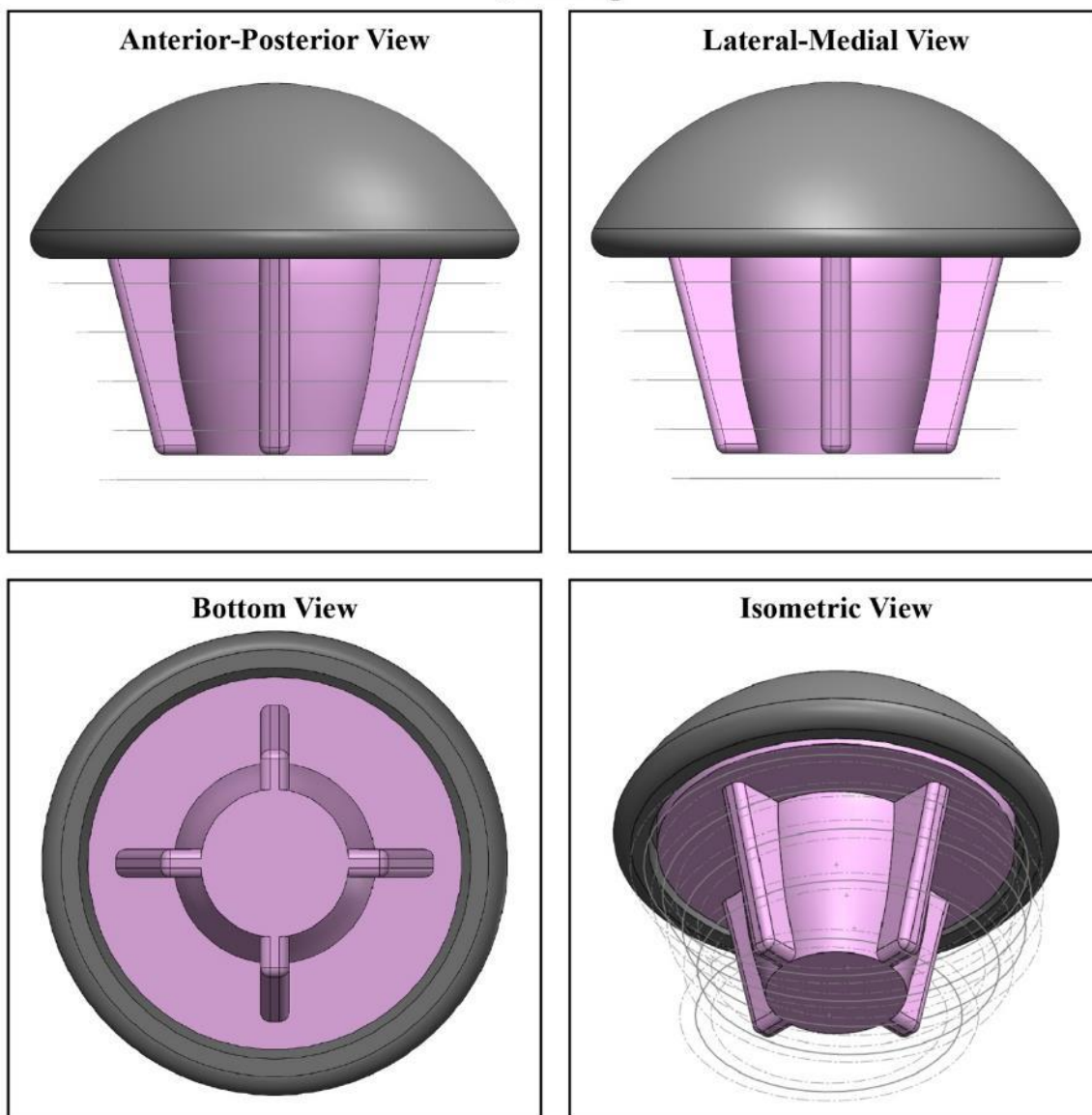
HexFlange



Implant Details: This implant is designed with a boundary-crossing fixation feature that is composed of six flanges that taper at an angle of 14° to remain within the pooled canal diameters from the morphological assessment of the humerus described in Chapter 3 (solid grey lines = mean, dashed lines = SD). The fixation feature extends 20mm into the humeral metaphysis, and each flange is 3mm thick and 17mm wide at the resection plane.

Figure H.9: Additional Views of the HexFlange Stemless Fixation Feature

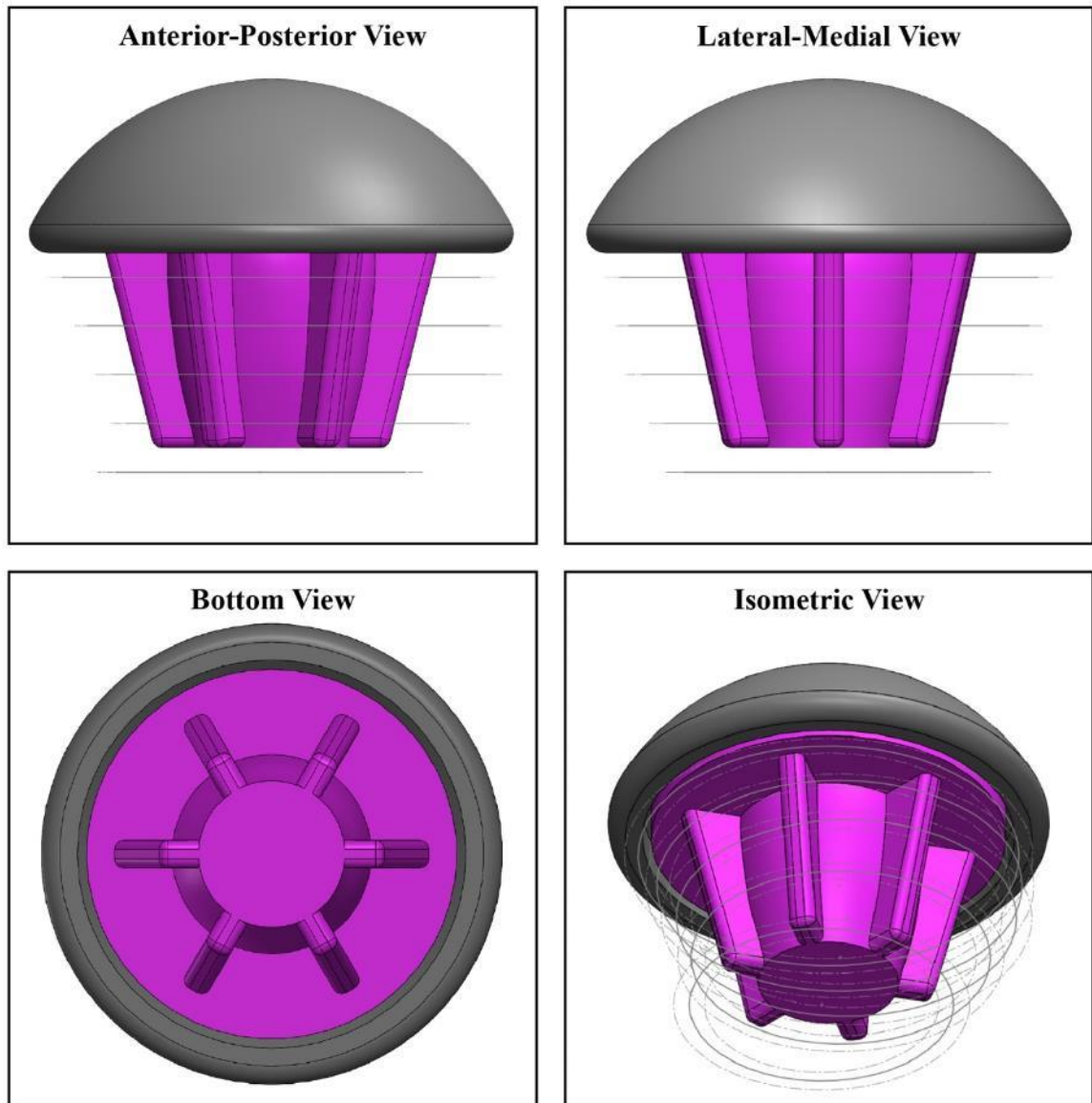
QuadPeg



Implant Details: This implant is designed with a boundary-crossing fixation feature that is composed of four flanges that taper at an angle of 14° . In addition, there is a central peg feature with a diameter that varies as a function of depth to be $\frac{1}{2}$ of the pooled canal diameter from the morphological assessment of the humerus described in Chapter 3 (solid grey lines = mean, dashed lines = SD). The fixation feature extends 20mm into the humeral metaphysis, and each flange is 3mm thick, and 17mm wide at the resection plane.

Figure H.10: Additional Views of the QuadPeg Stemless Fixation Feature

HexPeg



Implant Details: This implant is designed with a boundary-crossing fixation feature that is composed of six flanges that taper at an angle of 14° . In addition, there is a central peg feature with a diameter that varies as a function of depth to be $\frac{1}{2}$ of the pooled canal diameter from the morphological assessment of the humerus described in Chapter 3 (solid grey lines = mean, dashed lines = SD). The fixation feature extends 20mm into the humeral metaphysis, and each flange is 3mm thick, and 17mm wide at the resection plane.

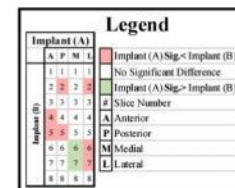
Figure H.11: Additional Views of the HexPeg Stemless Fixation Feature

Appendix I – Supplementary Significance Tables for Stemless Implant Assessment

As a compliment to the tables presented in Chapter 5, Figures I.1 - I.8 are presented to showcase all significant differences between stemless implant types that arose due to the implant-by-slice depth-by-bone quadrant interaction for (1) the change in bone stress (Figures I.1 and I.2) and (2) the time-zero potential bone response (Figures I.3 - I.8) for all slices and quadrants. The huge number of significant differences that presented within these results prevented the classical display of significant differences directly on the figures in Chapter 5 by ‘star-bars’.

Summary of Statistical Differences

Percentage Change in Cortical Bone Stress



		PegStraight					PegAnatomic					QuadPeg					HexPeg					QuadFlange					HexFlange					Peripheral4x5S					Peripheral4x5A					Peripheral4x10S					Peripheral4x10A																																							
		A	P	M	L	S	A	P	M	L	S	A	P	M	L	S	A	P	M	L	S	A	P	M	L	S	A	P	M	L	S	A	P	M	L	S	A	P	M	L	S	A	P	M	L	S	A	P	M	L	S																																			
Peripheral4x10S	Peripheral4x10A	8	8	8	8	8	8	8	8	8	8	8	8	8	8	8	8	8	8	8	8	8	8	8	8	8	8	8	8	8	8	8	8	8	8	8	8	8	8	8	8	8	8	8	8	8	8	8	8	8	8	8	8	8	8	8	8	8	8	8	8	8	8	8	8	8	8	8	8	8	8	8	8	8	8	8	8	8	8	8	8	8	8	8	8	8

Figure I.1: Summary of Statistical Differences for the Change in Cortical Bone Stress Outcome

Summary of Statistical Differences Percentage Change in Trabecular Bone Stress

Implant (A)		Implant (B)	
A	P M L	A	P M L
1	1 1 1	1	1 1 1
2	2 2 2	2	2 2 2
3	3 3 3	3	3 3 3
4	4 4 4	4	4 4 4
5	5 5 5	5	5 5 5
6	6 6 6	6	6 6 6
7	7 7 7	7	7 7 7
8	8 8 8	8	8 8 8

Legend	
A	Implant (A)<Implant (B)
B	Implant (B)>Implant (A)
C	No Significant Difference
P	Posterior
M	Medial
L	Lateral

	PegStraight				PegAnatomic				QuadPeg				HexPeg				QuadFlange				HexFlange				Peripheral4x5S				Peripheral4x5A				Peripheral4x10S				Peripheral4x10A			
	A	P	M	L	A	P	M	L	A	P	M	L	A	P	M	L	A	P	M	L	A	P	M	L	A	P	M	L	A	P	M	L	A	P	M	L	A	P	M	L
	PegStraight				PegAnatomic				QuadPeg				HexPeg				QuadFlange				HexFlange				Peripheral4x5S				Peripheral4x5A				Peripheral4x10S				Peripheral4x10A			

Figure I.2: Summary of Statistical Differences for the Change in Trabecular Bone Stress Outcome

Summary of Statistical Differences

Time-Zero Potential Resorbing Response of Cortical Bone

Implant (A)		Legend		
	A	P	M	L
Implant (B)	1	1	1	1
	2	2	2	2
3	3	3	3	3
4	4	4	4	4
5	5	5	5	5
6	6	6	6	6
7	7	7	7	7
8	8	8	8	8

█	Implant (A) < Implant (B)
█	No Significant Difference
█	Implant (A) > Implant (B)
n	Slice Number
A	Anterior
P	Posterior
M	Medial
L	Lateral

PegStraight			PegAnatomic			QuadPeg			HexPeg			QuadFlange			HexFlange			Peripheral4xSS			Peripheral4x5A			Peripheral4x10S			Peripheral4x10A				
A	P	M	L	A	P	M	L	A	P	M	L	A	P	M	L	A	P	M	L	A	P	M	L	A	P	M	L	A	P	M	L

Figure I.3: Summary of Statistical Differences for the Time-Zero Potential Resorbing Response of Cortical Bone

Summary of Statistical Differences Time-Zero Potential Unchanged Response of Cortical Bone

Legend

Implant (A)		Implant (B)	
A	P	M	L
1	2	3	4
5	6	7	8
9	10	11	12

■ No Significant Difference
 ■ Implant (A)Sig.< Implant (B)
 ■ Implant (A)Sig.> Implant (B)

Slice Number
 A Anterior
 P Posterior
 M Medial
 L Lateral

Implant (A)	PegStraight				PegAnatomic				QuadPeg				HexPeg				QuadFlange				HexFlange				Peripheral4x5S				Peripheral4x5A				Peripheral4x10S				Peripheral4x10A							
	A	P	M	L	A	P	M	L	A	P	M	L	A	P	M	L	A	P	M	L	A	P	M	L	A	P	M	L	A	P	M	L	A	P	M	L	A	P	M	L				
1	1	1	1	1	1	1	1	1	1	1	1	1	1	1	1	1	1	1	1	1	1	1	1	1	1	1	1	1	1	1	1	1	1	1	1	1	1	1	1	1	1	1	1	1

Figure I.4: Summary of Statistical Differences for the Time-Zero Potential Unchanged Response of Cortical Bone

Summary of Statistical Differences

Time-Zero Potential Remodeling Response of Cortical Bone

Implant (A)		Legend			
	A	P	M	L	
Implant (B)	1	1	1	1	No Significant Difference
	2	2	2	2	
	3	3	3	3	
	4	4	4	4	
Implant (A)Sig.<Implant (B)	5	5	5	5	Implant (A)Sig.>Implant (B)
	6	6	6	6	
	7	7	7	7	
	8	8	8	8	
A Anterior P Posterior M Medial L Lateral					

		PegStraight				PegAnatomic				QuadPeg				HexPeg				QuadFlange				HexFlange				Peripheral4x5S				Peripheral4x5A				Peripheral4x10S				Peripheral4x10A			
		A	P	M	L	A	P	M	L	A	P	M	L	A	P	M	L	A	P	M	L	A	P	M	L	A	P	M	L	A	P	M	L	A	P	M	L	A	P	M	L
PegStraight	PegStraight	1	1	1	1	1	1	1	1	1	1	1	1	1	1	1	1	1	1	1	1	1	1	1	1	1	1	1	1	1	1	1	1	1	1	1	1	1	1	1	1
	PegAnatomic	1	1	1	1	1	1	1	1	1	1	1	1	1	1	1	1	1	1	1	1	1	1	1	1	1	1	1	1	1	1	1	1	1	1	1	1	1	1	1	1
	QuadPeg	1	1	1	1	1	1	1	1	1	1	1	1	1	1	1	1	1	1	1	1	1	1	1	1	1	1	1	1	1	1	1	1	1	1	1	1	1	1	1	1
	HexPeg	1	1	1	1	1	1	1	1	1	1	1	1	1	1	1	1	1	1	1	1	1	1	1	1	1	1	1	1	1	1	1	1	1	1	1	1	1	1	1	1
QuadFlange	QuadFlange	1	1	1	1	1	1	1	1	1	1	1	1	1	1	1	1	1	1	1	1	1	1	1	1	1	1	1	1	1	1	1	1	1	1	1	1	1	1	1	1
	HexFlange	1	1	1	1	1	1	1	1	1	1	1	1	1	1	1	1	1	1	1	1	1	1	1	1	1	1	1	1	1	1	1	1	1	1	1	1	1	1	1	1
	Peripheral4x5S	1	1	1	1	1	1	1	1	1	1	1	1	1	1	1	1	1	1	1	1	1	1	1	1	1	1	1	1	1	1	1	1	1	1	1	1	1	1	1	1
	Peripheral4x5A	1	1	1	1	1	1	1	1	1	1	1	1	1	1	1	1	1	1	1	1	1	1	1	1	1	1	1	1	1	1	1	1	1	1	1	1	1	1	1	1
Peripheral4x10S	Peripheral4x10S	1	1	1	1	1	1	1	1	1	1	1	1	1	1	1	1	1	1	1	1	1	1	1	1	1	1	1	1	1	1	1	1	1	1	1	1	1	1	1	1
	Peripheral4x10A	1	1	1	1	1	1	1	1	1	1	1	1	1	1	1	1	1	1	1	1	1	1	1	1	1	1	1	1	1	1	1	1	1	1	1	1	1	1	1	1
	PegStraight	1	1	1	1	1	1	1	1	1	1	1	1	1	1	1	1	1	1	1	1	1	1	1	1	1	1	1	1	1	1	1	1	1	1	1	1	1	1	1	1
	PegAnatomic	1	1	1	1	1	1	1	1	1	1	1	1	1	1	1	1	1	1	1	1	1	1	1	1	1	1	1	1	1	1	1	1	1	1	1	1	1	1	1	1

Figure I.5: Summary of Statistical Differences for the Time-Zero Potential Remodeling Response of Cortical Bone

Summary of Statistical Differences

Time-Zero Potential Resorbing Response of Trabecular Bone

Implant (A)			Implant (B)			Legend			
A	P	M	L	A	P		M	L	
1	1	1	1	1	1	1	1	No Significant Difference	
2	2	2	2	2	2	2	2		
3	3	3	3	3	3	3	3	Implant (A) Sig < Implant (B)	
4	4	4	4	4	4	4	4		
5	5	5	5	5	5	5	5	Implant (A) Sig > Implant (B)	
6	6	6	6	6	6	6	6		
7	7	7	7	7	7	7	7	Slice Number	
8	8	8	8	8	8	8	8		
								A	Anterior
								P	Posterior
								M	Medial
								L	Lateral

		PegStraight				PegAnatomic				QuadPeg				HexPeg				QuadFlange				HexFlange				Peripheral4x5S				Peripheral4x5A				Peripheral4x10S				Peripheral4x10A							
		A	P	M	L	A	P	M	L	A	P	M	L	A	P	M	L	A	P	M	L	A	P	M	L	A	P	M	L	A	P	M	L	A	P	M	L	A	P	M	L	A	P	M	L
Peripheral4x5S	Peripheral4x5S	1	1	1	1	1	1	1	1	1	1	1	1	1	1	1	1	1	1	1	1	1	1	1	1	1	1	1	1	1	1	1	1	1	1	1	1	1	1	1	1	1	1	1	1
	Peripheral4x5A	1	1	1	1	1	1	1	1	1	1	1	1	1	1	1	1	1	1	1	1	1	1	1	1	1	1	1	1	1	1	1	1	1	1	1	1	1	1	1	1	1	1	1	1
Peripheral4x10S	Peripheral4x10S	1	1	1	1	1	1	1	1	1	1	1	1	1	1	1	1	1	1	1	1	1	1	1	1	1	1	1	1	1	1	1	1	1	1	1	1	1	1	1	1	1	1	1	1
	Peripheral4x10A	1	1	1	1	1	1	1	1	1	1	1	1	1	1	1	1	1	1	1	1	1	1	1	1	1	1	1	1	1	1	1	1	1	1	1	1	1	1	1	1	1	1	1	1
PegStraight	PegStraight	1	1	1	1	1	1	1	1	1	1	1	1	1	1	1	1	1	1	1	1	1	1	1	1	1	1	1	1	1	1	1	1	1	1	1	1	1	1	1	1	1	1	1	1
	PegAnatomic	1	1	1	1	1	1	1	1	1	1	1	1	1	1	1	1	1	1	1	1	1	1	1	1	1	1	1	1	1	1	1	1	1	1	1	1	1	1	1	1	1	1	1	1
QuadFlange	QuadFlange	1	1	1	1	1	1	1	1	1	1	1	1	1	1	1	1	1	1	1	1	1	1	1	1	1	1	1	1	1	1	1	1	1	1	1	1	1	1	1	1	1	1	1	1
	HexFlange	1	1	1	1	1	1	1	1	1	1	1	1	1	1	1	1	1	1	1	1	1	1	1	1	1	1	1	1	1	1	1	1	1	1	1	1	1	1	1	1	1	1	1	1

Figure I.6: Summary of Statistical Differences for the Time-Zero Potential Resorbing Response of Trabecular Bone

Summary of Statistical Differences Time-Zero Potential Unchanged Response of Trabecular Bone

Implant (A)		Implant (B)		Legend					
A	P	M	L	A	P	M	L		
1	1	1	1	1	1	1	1	Implant (A)Sig.< Implant (B) No Significant Difference Implant (A)Sig.> Implant (B) Slice Number A Anterior P Posterior M Medial L Lateral	
2	2	2	2	2	2	2	2		
3	3	3	3	3	3	3	3		
4	4	4	4	4	4	4	4		
5	5	5	5	5	5	5	5		
6	6	6	6	6	6	6	6		
7	7	7	7	7	7	7	7		
8	8	8	8	8	8	8	8		

	PegStraight				PegAnatomic				QuadPeg				HexPeg				QuadFlange				HexFlange				Peripheral4x5S				Peripheral4x5A				Peripheral4x10S				Peripheral4x10A							
	A	P	M	L	A	P	M	L	A	P	M	L	A	P	M	L	A	P	M	L	A	P	M	L	A	P	M	L	A	P	M	L	A	P	M	L	A	P	M	L				
PegStraight	1	1	1	1	1	1	1	1	1	1	1	1	1	1	1	1	1	1	1	1	1	1	1	1	1	1	1	1	1	1	1	1	1	1	1	1	1	1	1	1	1	1	1	1
QuadPeg	1	1	1	1	1	1	1	1	1	1	1	1	1	1	1	1	1	1	1	1	1	1	1	1	1	1	1	1	1	1	1	1	1	1	1	1	1	1	1	1	1	1	1	1
HexFlange	1	1	1	1	1	1	1	1	1	1	1	1	1	1	1	1	1	1	1	1	1	1	1	1	1	1	1	1	1	1	1	1	1	1	1	1	1	1	1	1	1	1	1	1
Peripheral4x5S	1	1	1	1	1	1	1	1	1	1	1	1	1	1	1	1	1	1	1	1	1	1	1	1	1	1	1	1	1	1	1	1	1	1	1	1	1	1	1	1	1	1	1	1
Peripheral4x5A	1	1	1	1	1	1	1	1	1	1	1	1	1	1	1	1	1	1	1	1	1	1	1	1	1	1	1	1	1	1	1	1	1	1	1	1	1	1	1	1	1	1	1	1
Peripheral4x10S	1	1	1	1	1	1	1	1	1	1	1	1	1	1	1	1	1	1	1	1	1	1	1	1	1	1	1	1	1	1	1	1	1	1	1	1	1	1	1	1	1	1	1	1
Peripheral4x10A	1	1	1	1	1	1	1	1	1	1	1	1	1	1	1	1	1	1	1	1	1	1	1	1	1	1	1	1	1	1	1	1	1	1	1	1	1	1	1	1	1	1	1	1

Figure I.7: Summary of Statistical Differences for the Time-Zero Potential Unchanged Response of Trabecular Bone

Summary of Statistical Differences

Time-Zero Potential Remodeling Response of Trabecular Bone

Implant (A)				Legend	
A	P	M	L	Color Key	Text Key
1	1	1	1		
2	2	2	2	Light Red	No Significant Difference
3	3	3	3	Light Green	Implant (A)Sig.> Implant (B)
4	4	4	4	Light Purple	Slice Number
5	5	5	5	Light Blue	A: Anterior
6	6	6	6	Light Orange	P: Posterior
7	7	7	7	Light Yellow	M: Medial
8	8	8	8	Light Grey	L: Lateral

Implant (B)	PegStraight				PegAnatomic				QuadPeg				HexPeg				QuadFlange				HexFlange				Peripheral4x5S				Peripheral4x5A				Peripheral4x10S				Peripheral4x10A											
	A	P	M	L	A	P	M	L	A	P	M	L	A	P	M	L	A	P	M	L	A	P	M	L	A	P	M	L	A	P	M	L	A	P	M	L	A	P	M	L	A	P	M	L				
1	1	1	1	1	1	1	1	1	1	1	1	1	1	1	1	1	1	1	1	1	1	1	1	1	1	1	1	1	1	1	1	1	1	1	1	1	1	1	1	1	1	1	1	1	1	1	1	1
2	2	2	2	2	2	2	2	2	2	2	2	2	2	2	2	2	2	2	2	2	2	2	2	2	2	2	2	2	2	2	2	2	2	2	2	2	2	2	2	2	2	2	2	2	2	2	2	2
3	3	3	3	3	3	3	3	3	3	3	3	3	3	3	3	3	3	3	3	3	3	3	3	3	3	3	3	3	3	3	3	3	3	3	3	3	3	3	3	3	3	3	3	3	3	3	3	3
4	4	4	4	4	4	4	4	4	4	4	4	4	4	4	4	4	4	4	4	4	4	4	4	4	4	4	4	4	4	4	4	4	4	4	4	4	4	4	4	4	4	4	4	4	4	4	4	4
5	5	5	5	5	5	5	5	5	5	5	5	5	5	5	5	5	5	5	5	5	5	5	5	5	5	5	5	5	5	5	5	5	5	5	5	5	5	5	5	5	5	5	5	5	5	5	5	5
6	6	6	6	6	6	6	6	6	6	6	6	6	6	6	6	6	6	6	6	6	6	6	6	6	6	6	6	6	6	6	6	6	6	6	6	6	6	6	6	6	6	6	6	6	6	6	6	6
7	7	7	7	7	7	7	7	7	7	7	7	7	7	7	7	7	7	7	7	7	7	7	7	7	7	7	7	7	7	7	7	7	7	7	7	7	7	7	7	7	7	7	7	7	7	7	7	7
8	8	8	8	8	8	8	8	8	8	8	8	8	8	8	8	8	8	8	8	8	8	8	8	8	8	8	8	8	8	8	8	8	8	8	8	8	8	8	8	8	8	8	8	8	8	8	8	8

Figure I.8: Summary of Statistical Differences for the Time-Zero Potential Remodeling Response of Trabecular Bone

Appendix J – von Mises Stress Plots for Chapter 5 FE Models

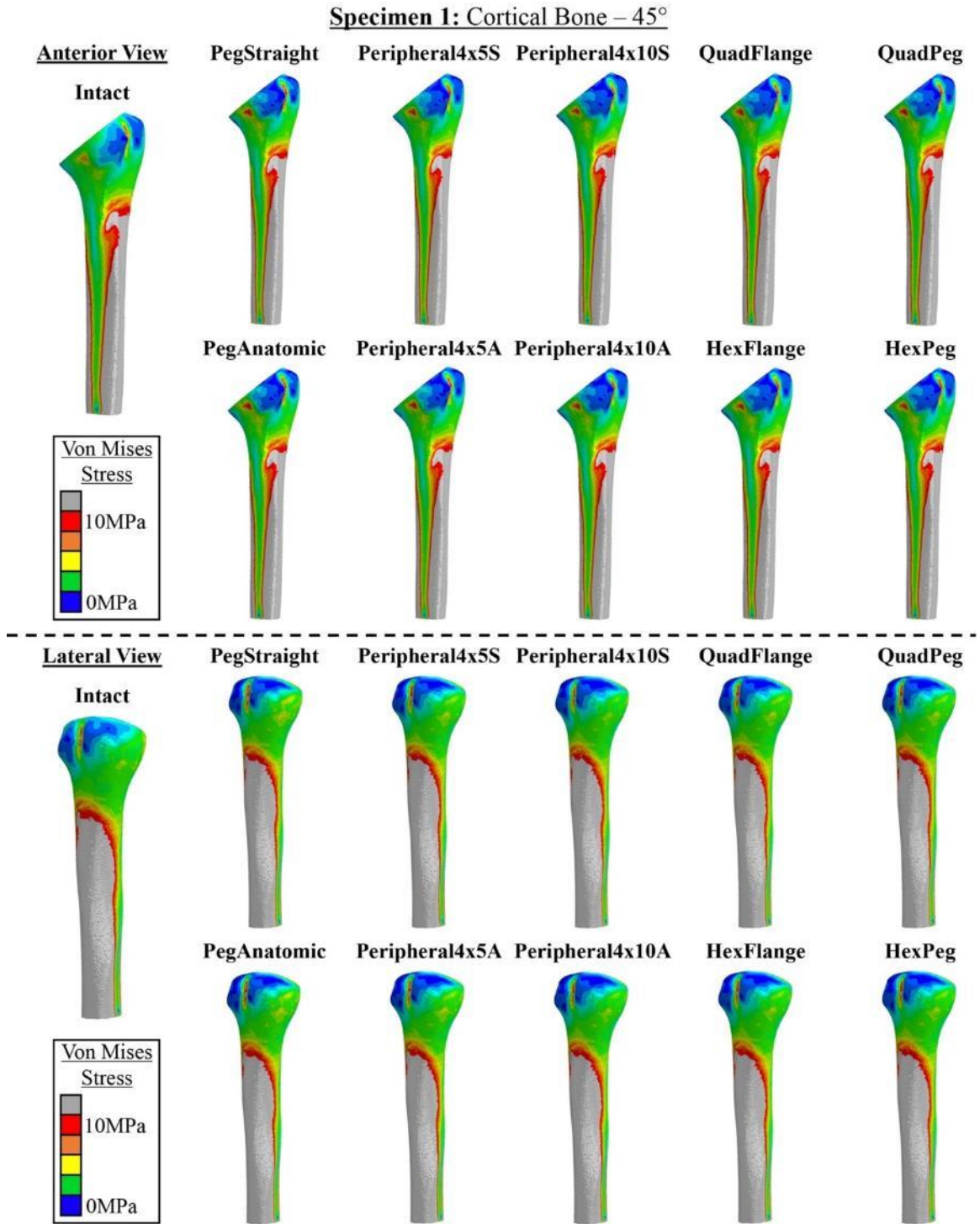


Figure J.1: von Mises Plots of Specimen 1's Cortical Shell for Loading at 45° of Abduction

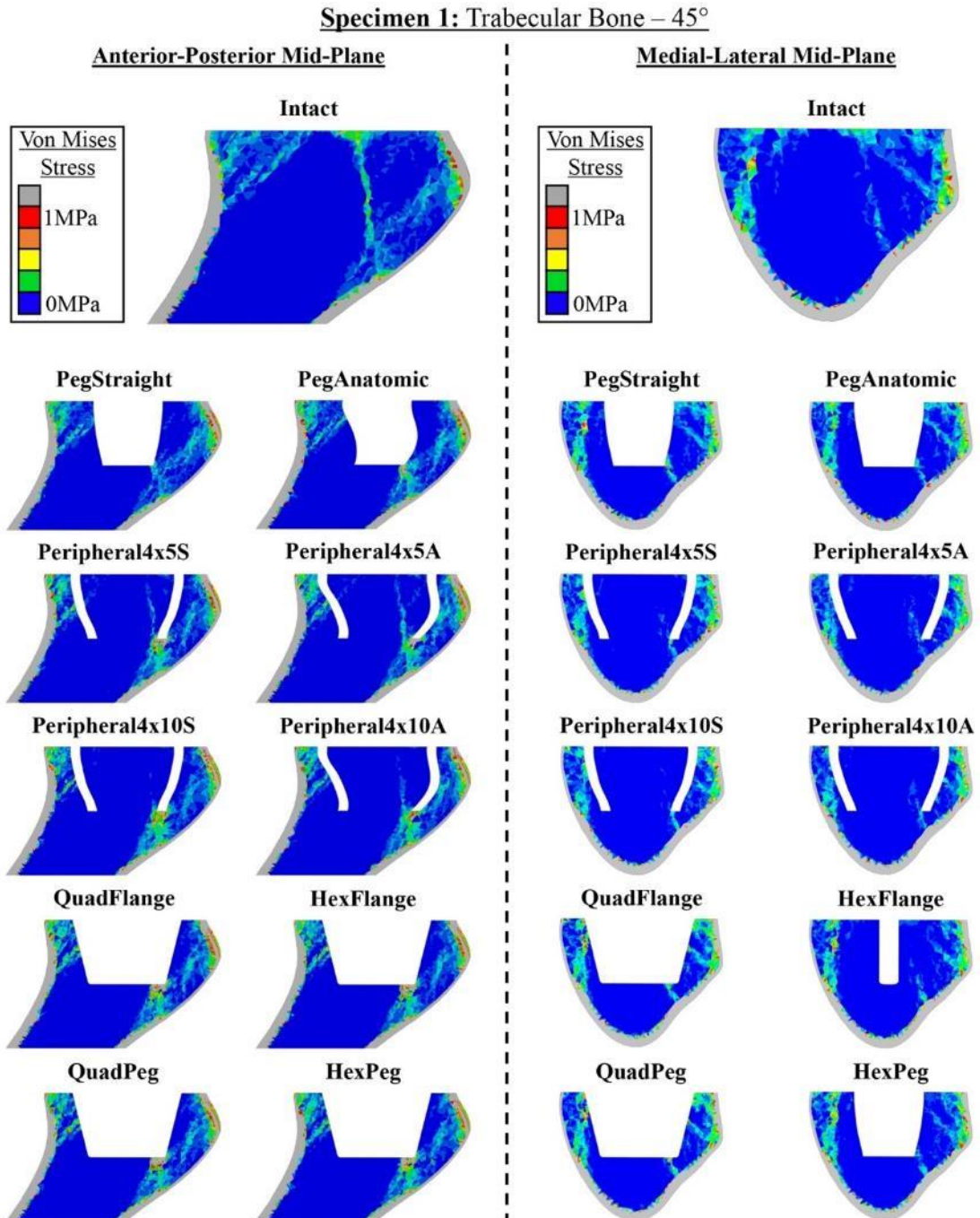


Figure J.2: von Mises Plots of Specimen 1's Trabecular-Canal for Loading at 45° of Abduction

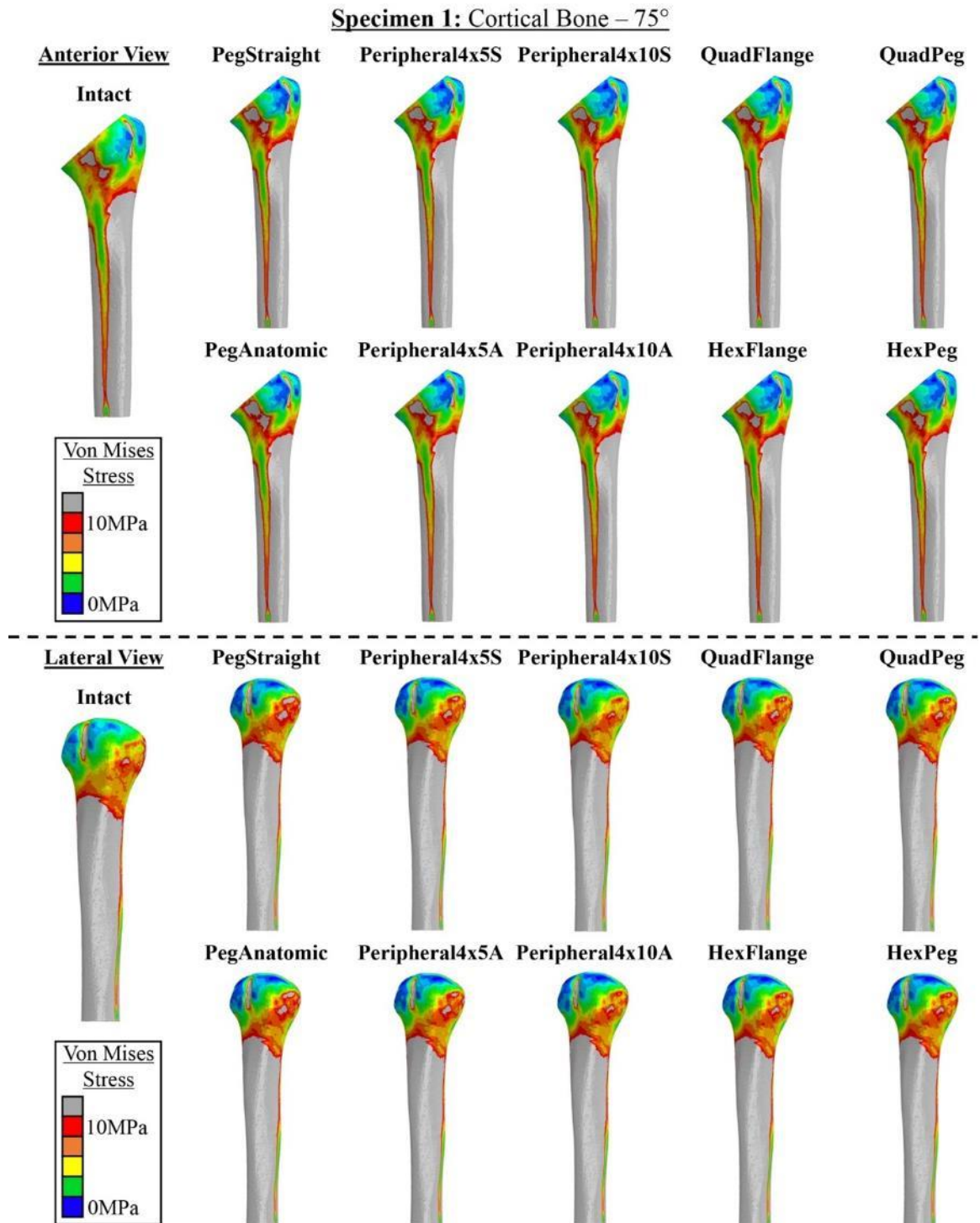


Figure J.3: von Mises Plots of Specimen 1's Cortical Shell for Loading at 75° of Abduction

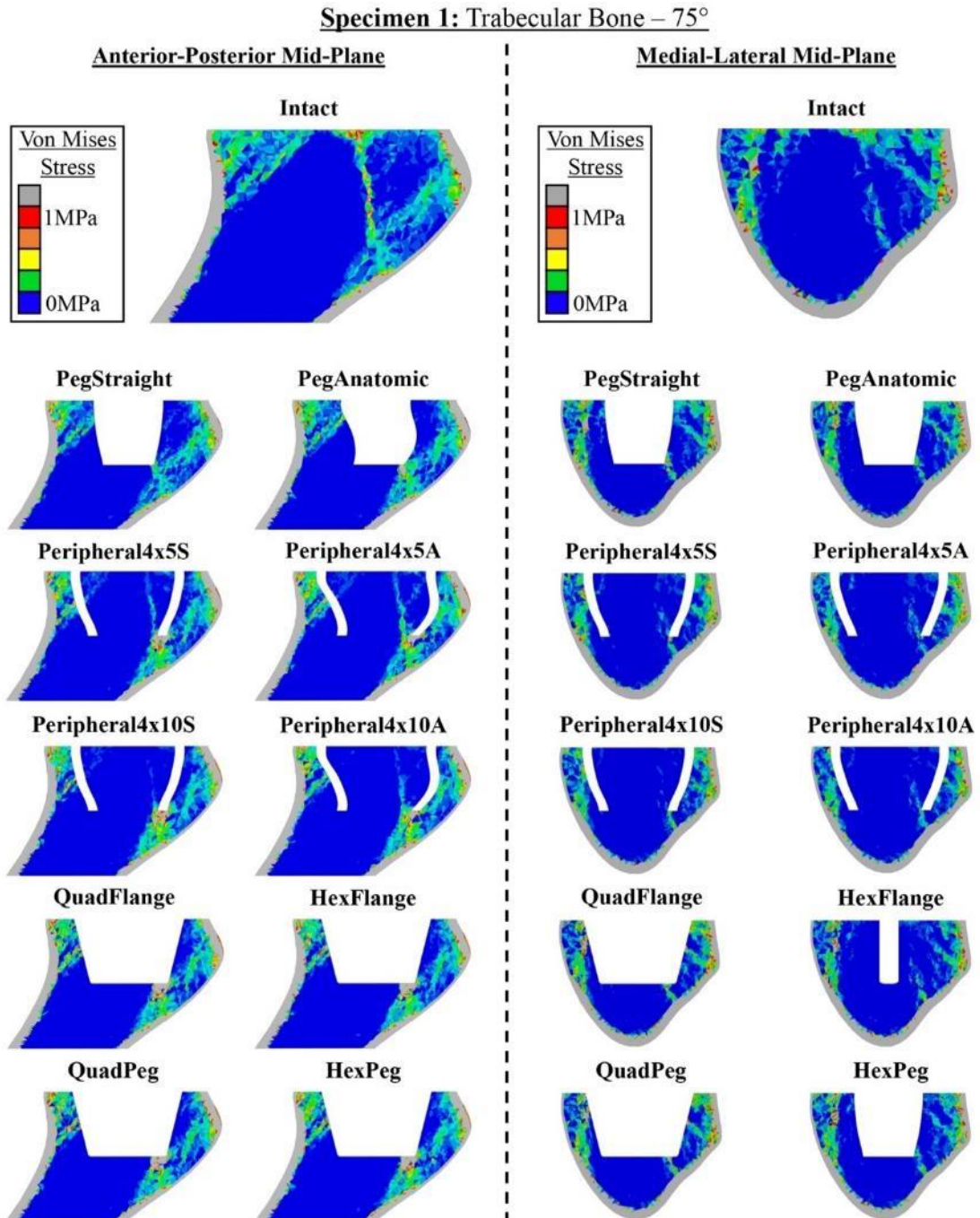


Figure J.4: von Mises Plots of Specimen 1's Trabecular-Canal for Loading at 75° of Abduction

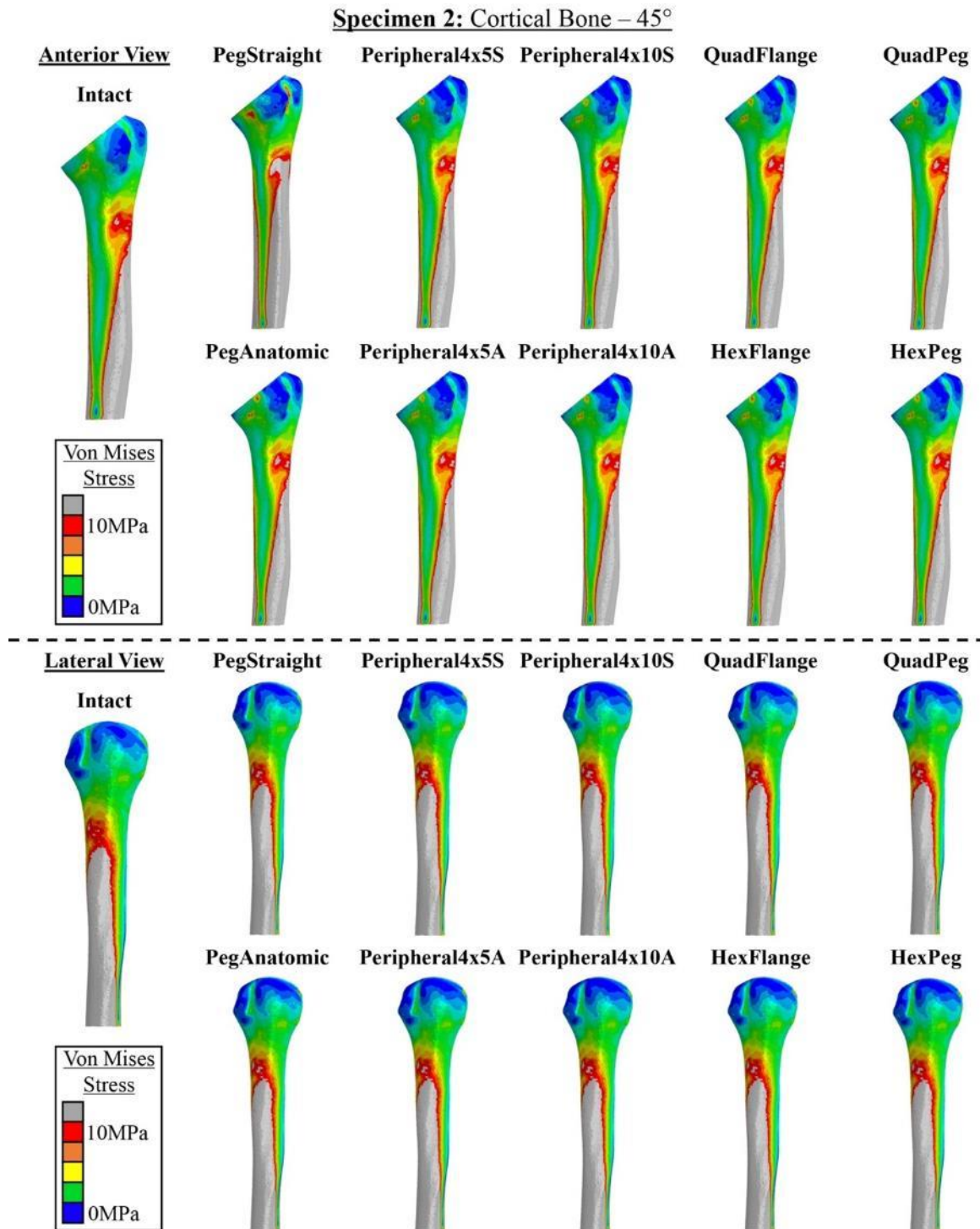


Figure J.5: von Mises Plots of Specimen 2's Cortical Shell for Loading at 45° of Abduction

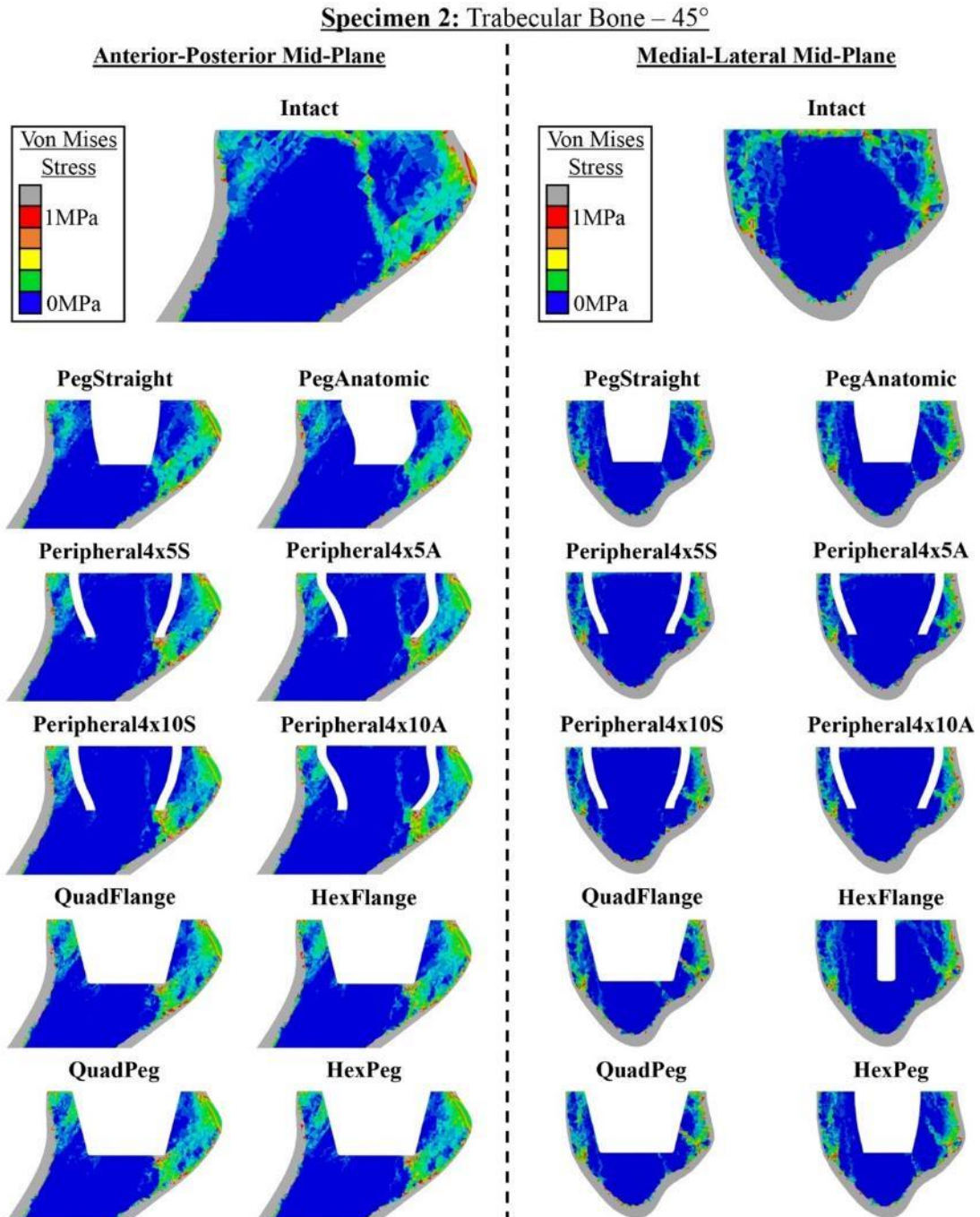


Figure J.6: von Mises Plots of Specimen 2's Trabecular-Canal for Loading at 45° of Abduction

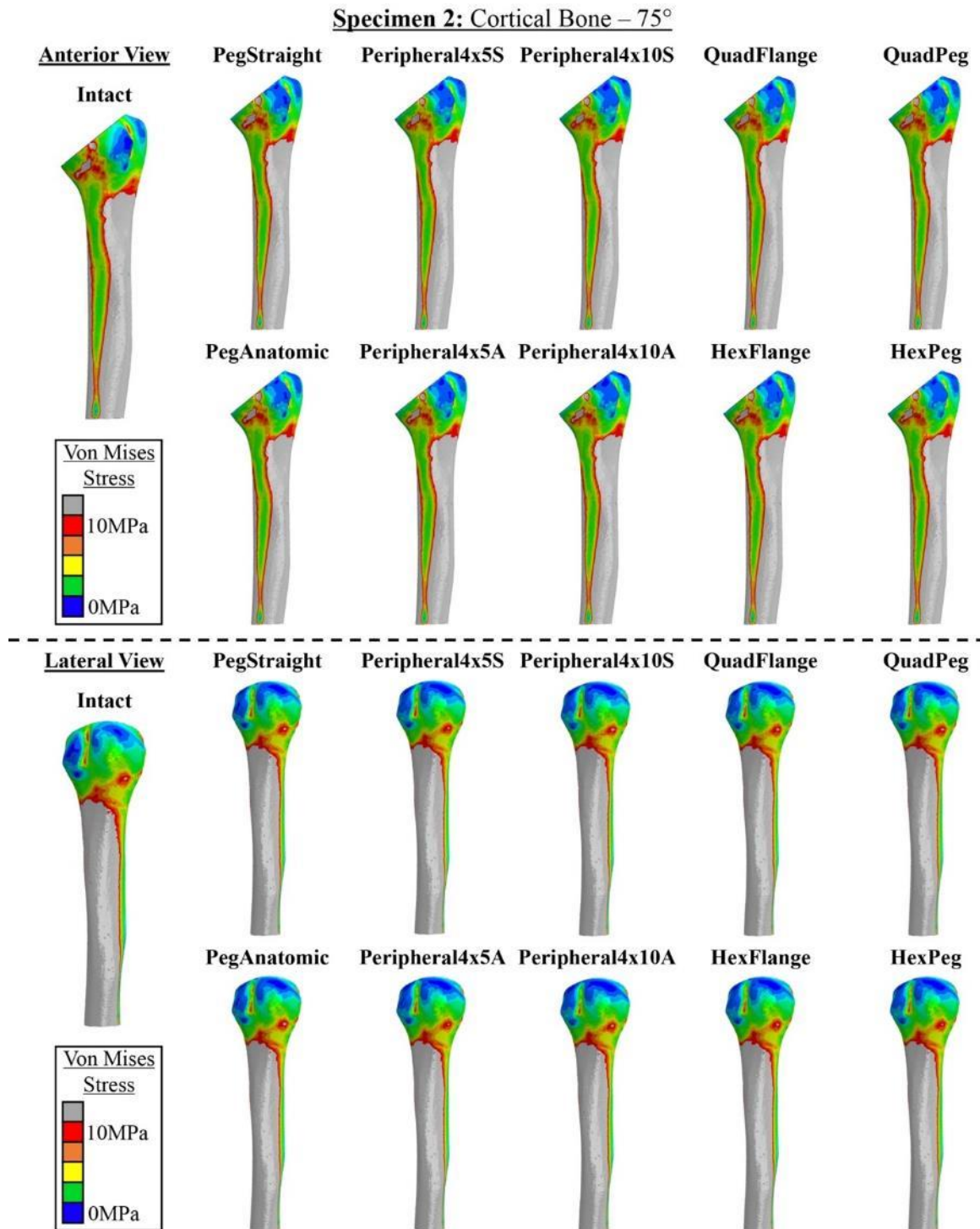


Figure J.7: von Mises Plots of Specimen 2's Cortical Shell for Loading at 75° of Abduction

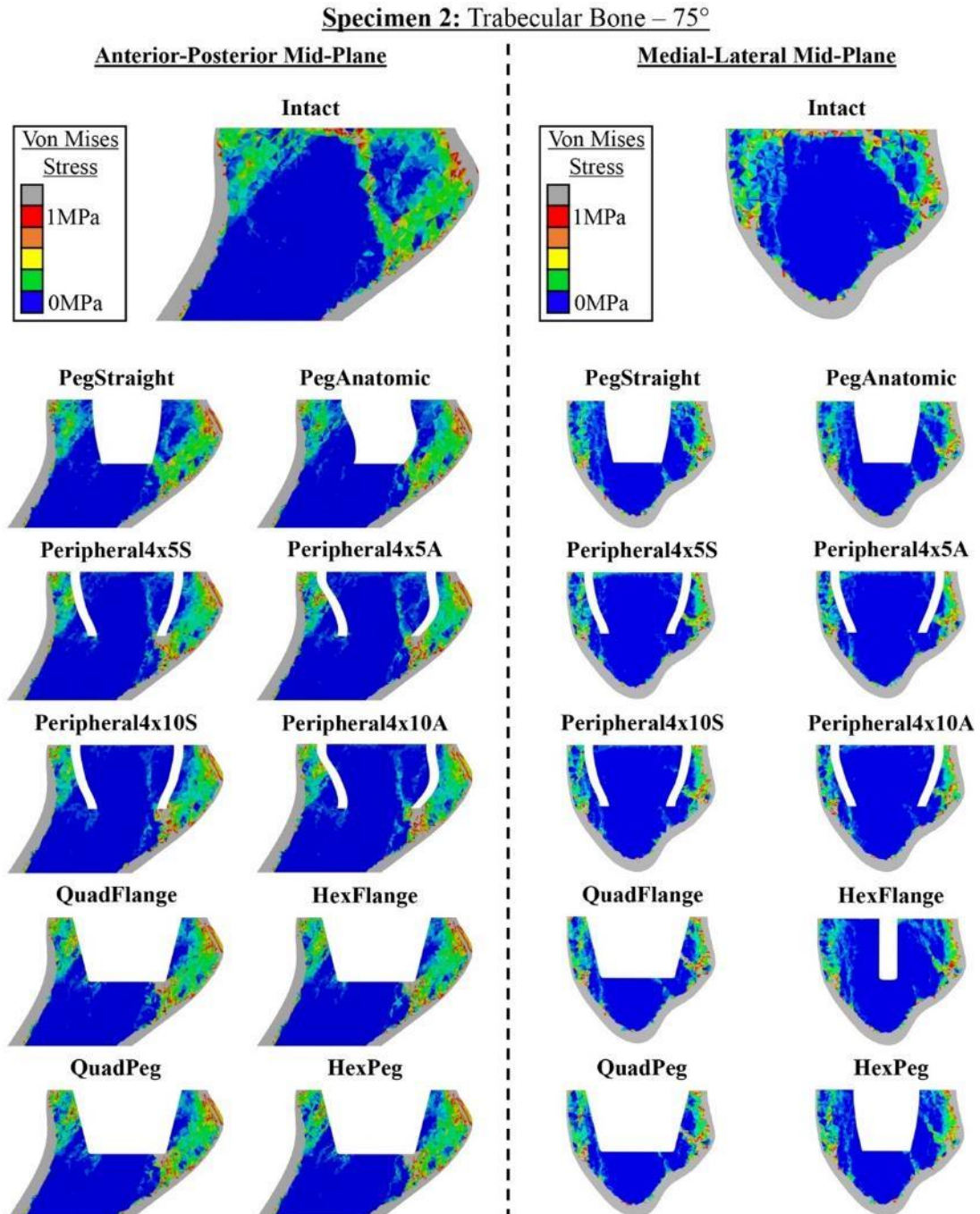


Figure J.8: von Mises Plots of Specimen 2's Trabecular-Canal for Loading at 75° of Abduction

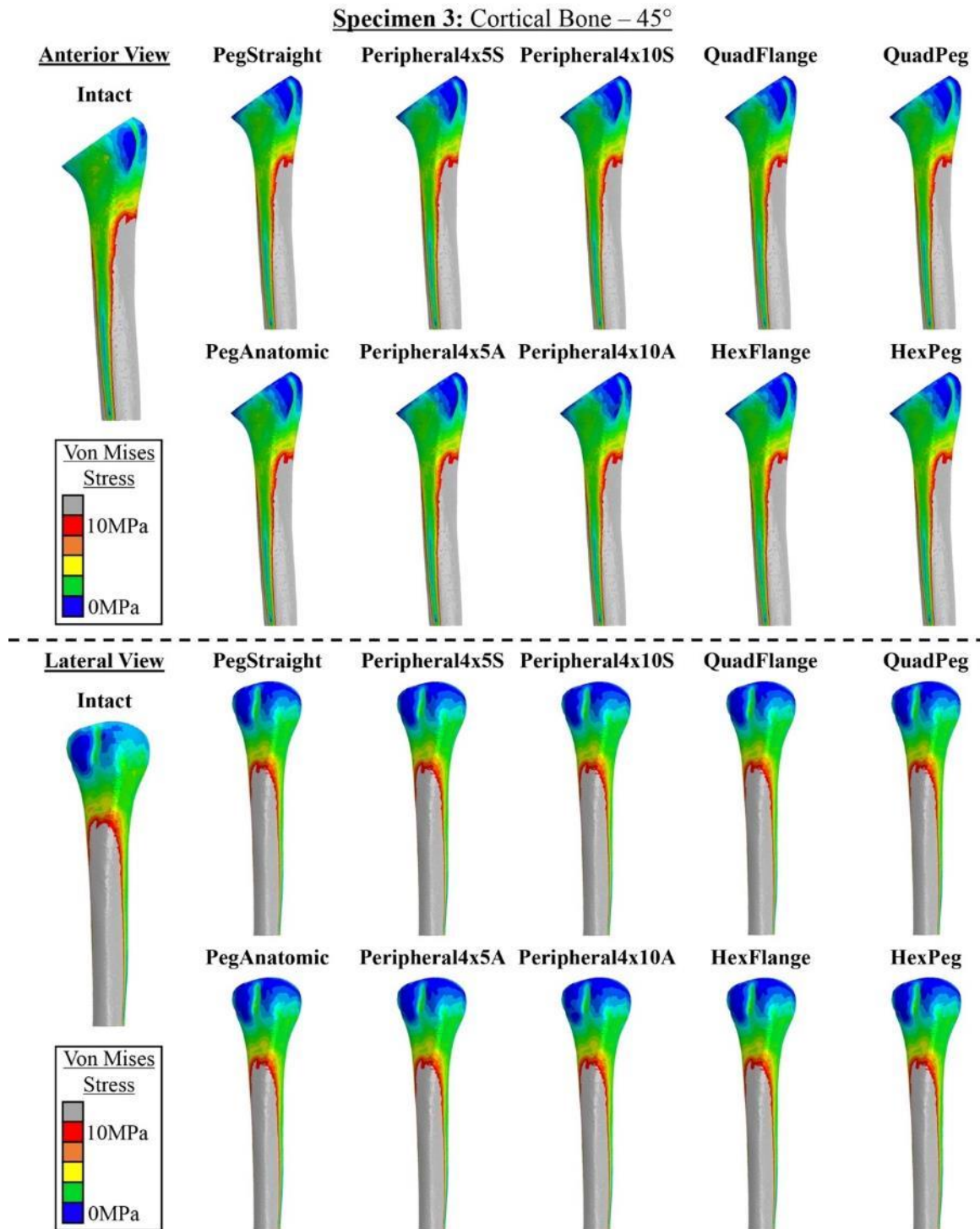


Figure J.9: von Mises Plots of Specimen 3's Cortical Shell for Loading at 45° of Abduction

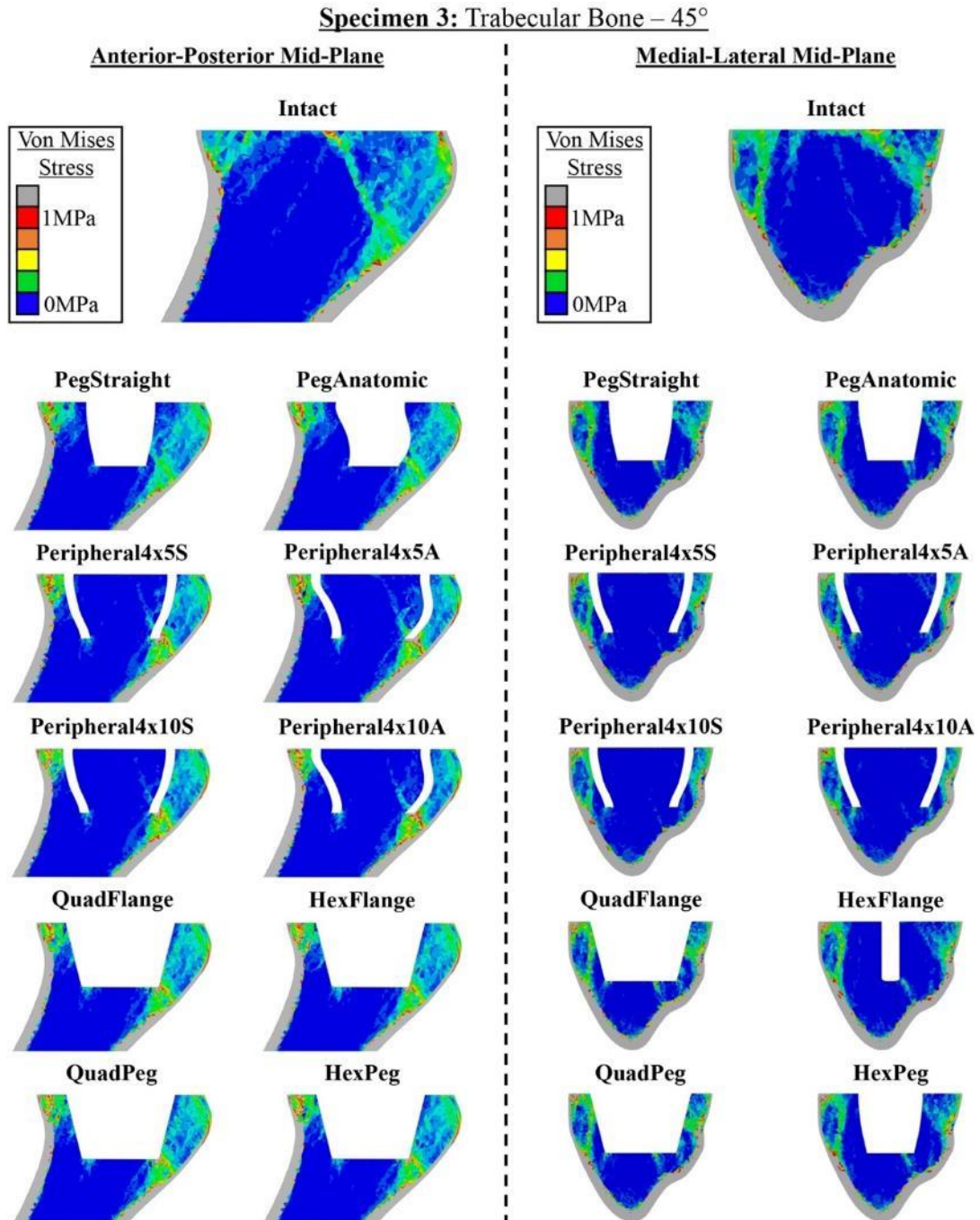


Figure J.10: von Mises Plots of Specimen 3's Trabecular-Canal for Loading at 45° of Abduction

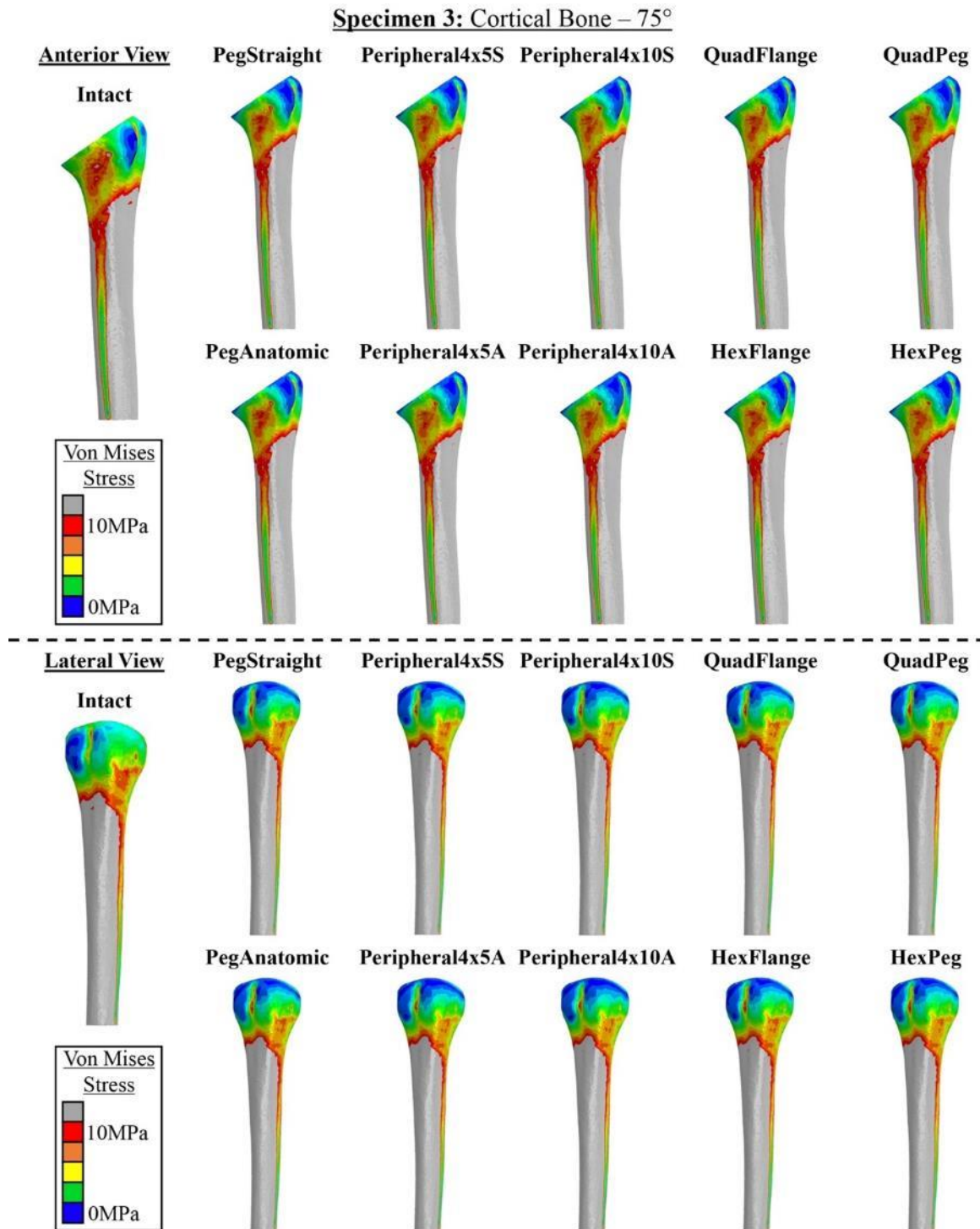


Figure J.11: von Mises Plots of Specimen 3's Cortical Shell for Loading at 75° of Abduction

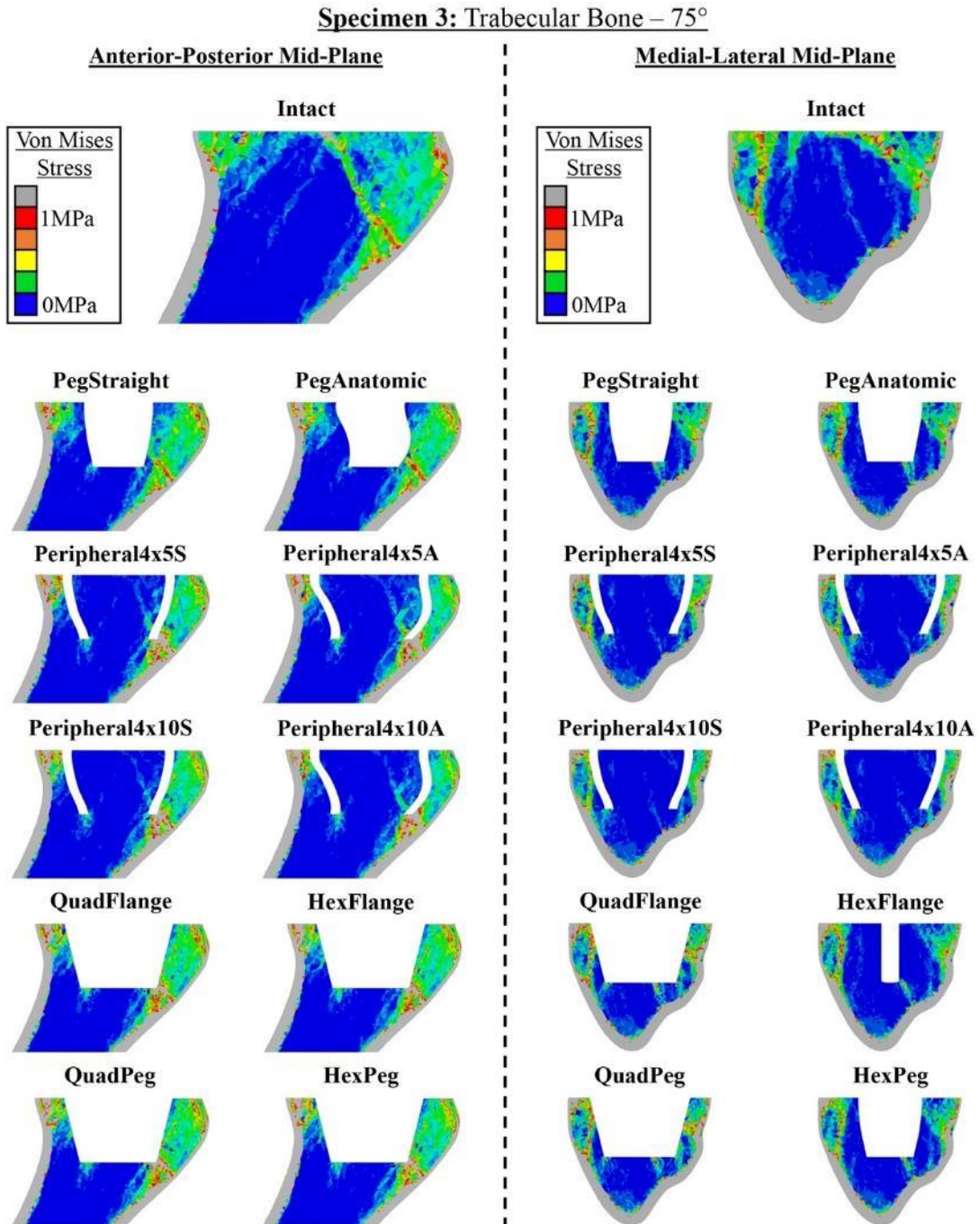


Figure J.12: von Mises Plots of Specimen 3's Trabecular-Canal for Loading at 75° of Abduction

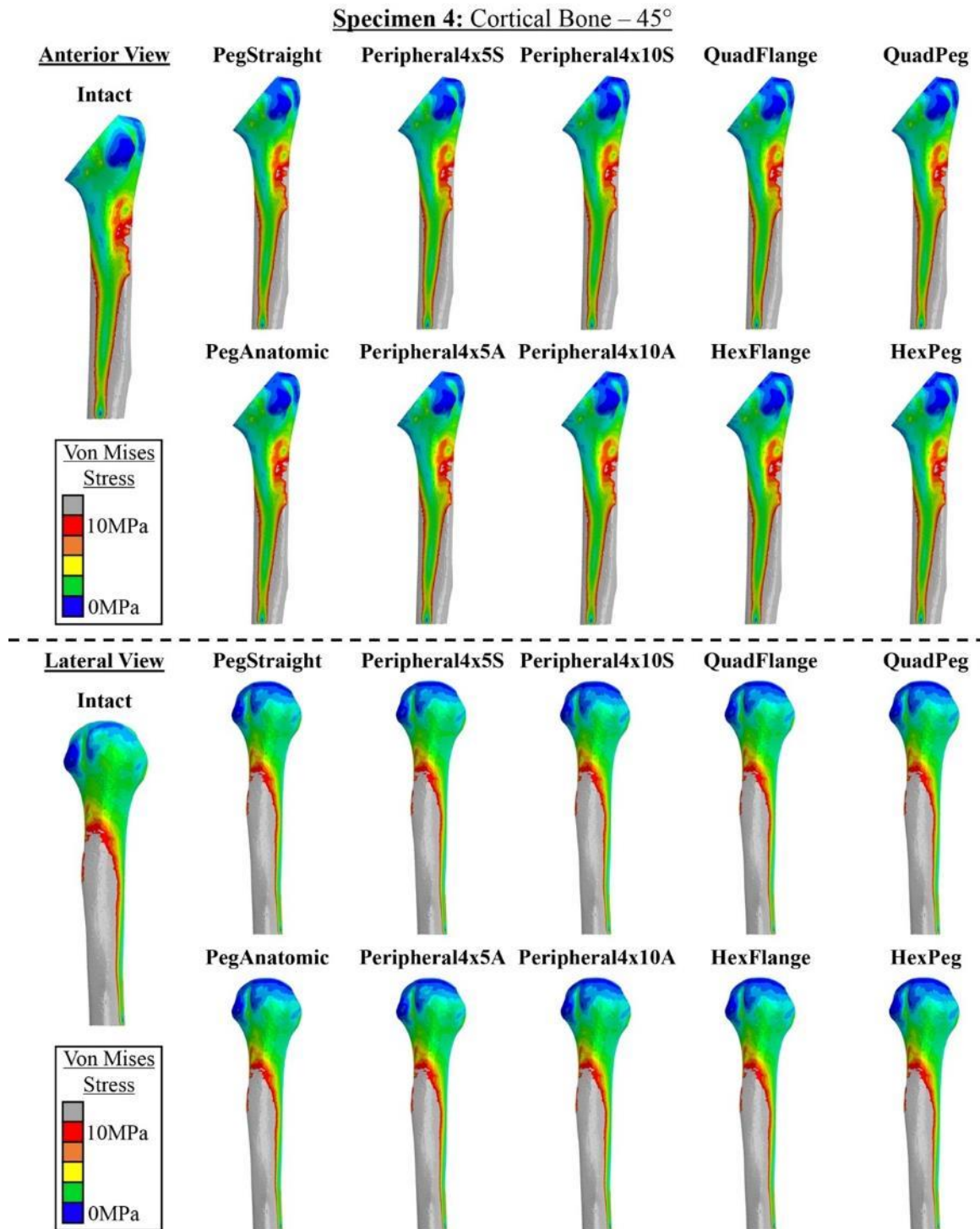
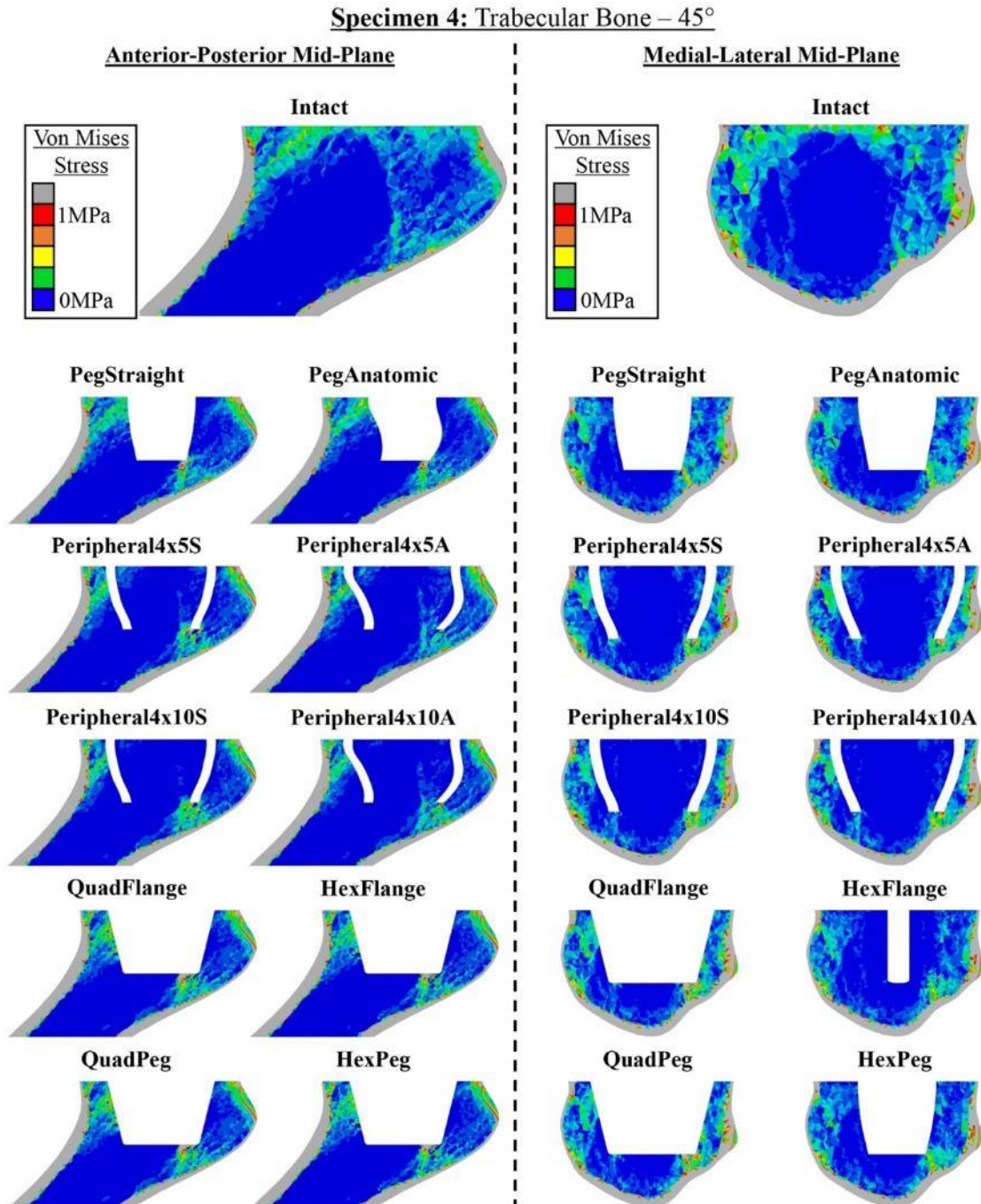


Figure J.13: von Mises Plots of Specimen 4's Cortical Shell for Loading at 45° of Abduction



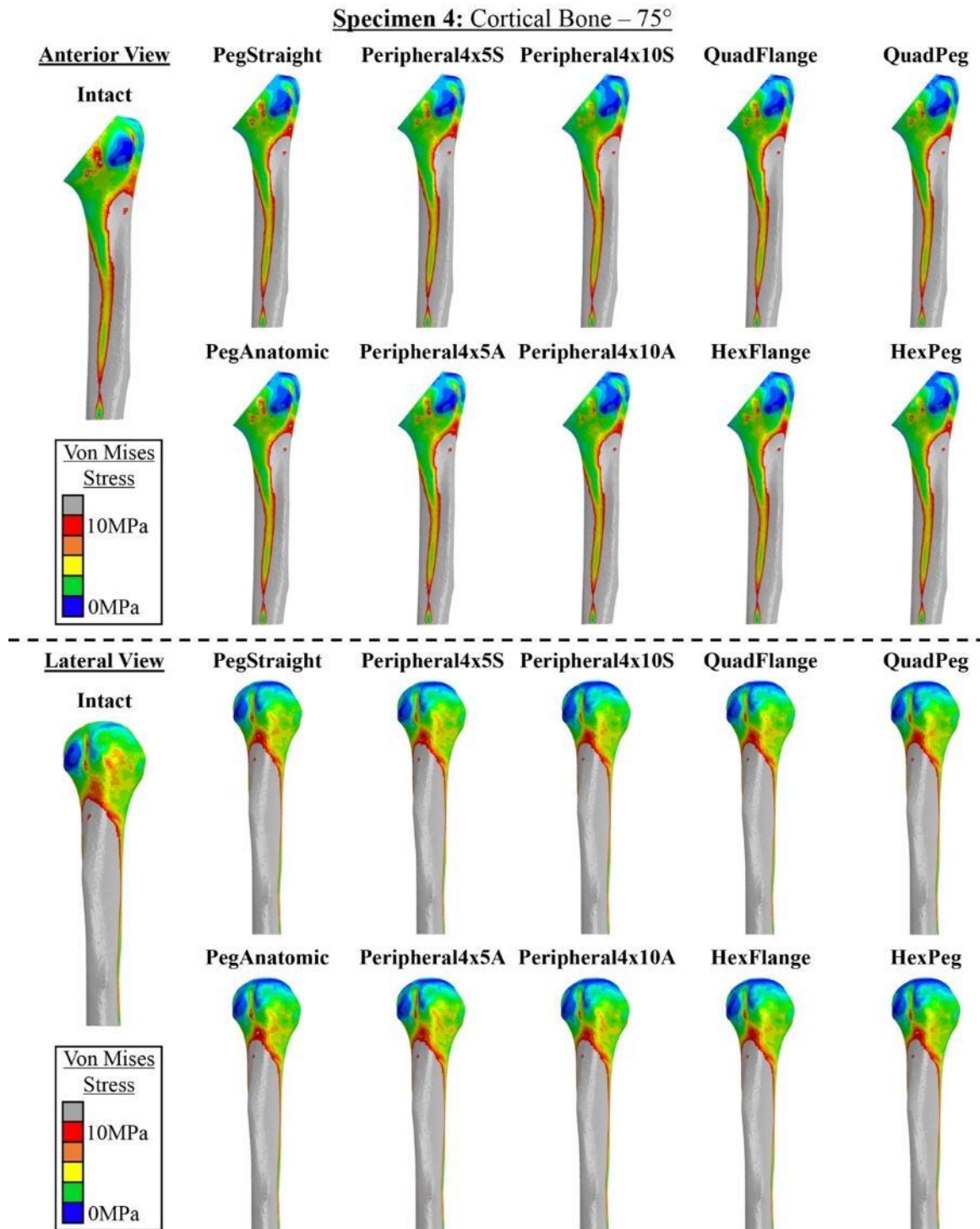


Figure J.15: von Mises Plots of Specimen 4's Cortical Shell for Loading at 75° of Abduction

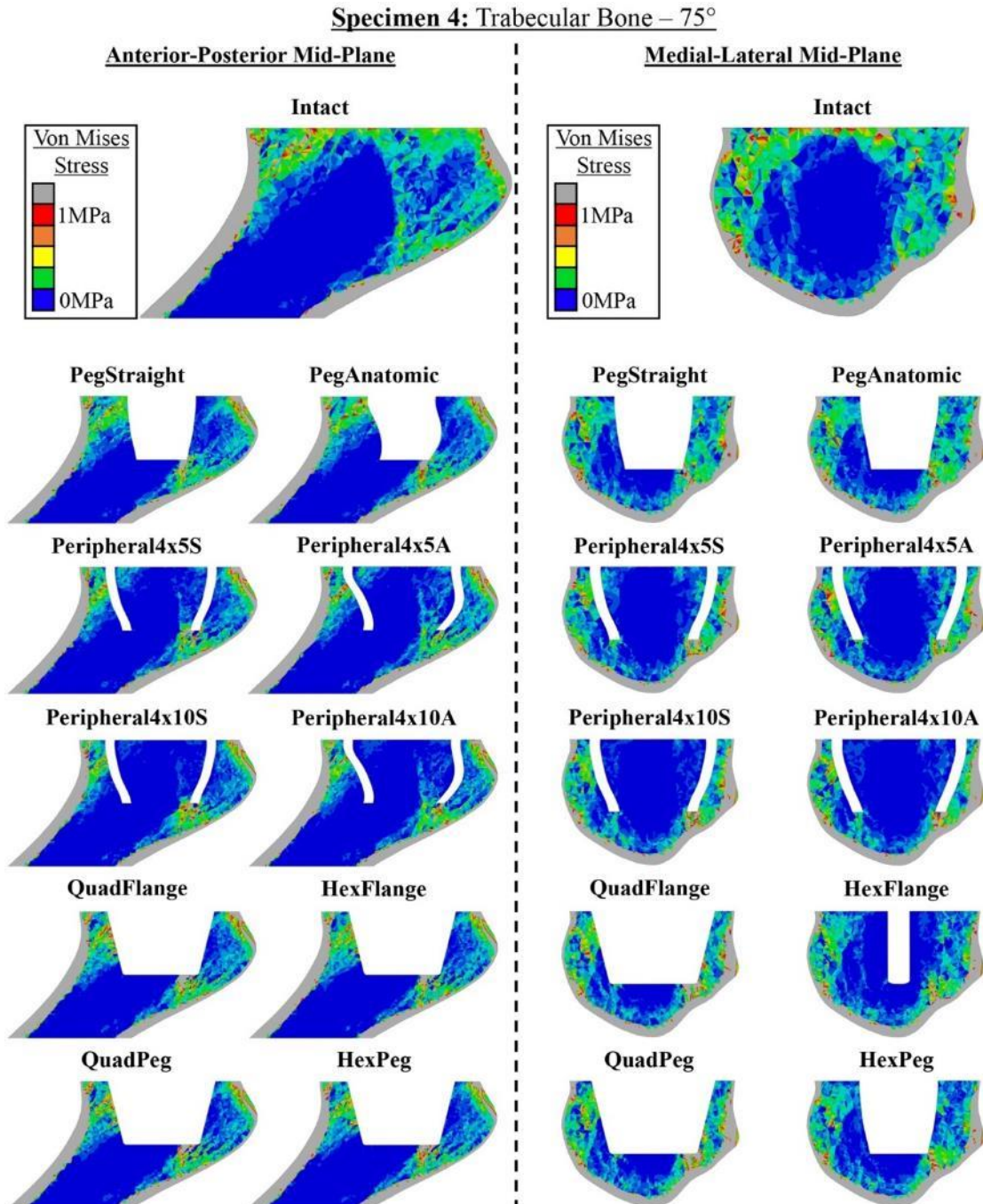


Figure J.16: von Mises Plots of Specimen 4's Trabecular-Canal for Loading at 75° of Abduction

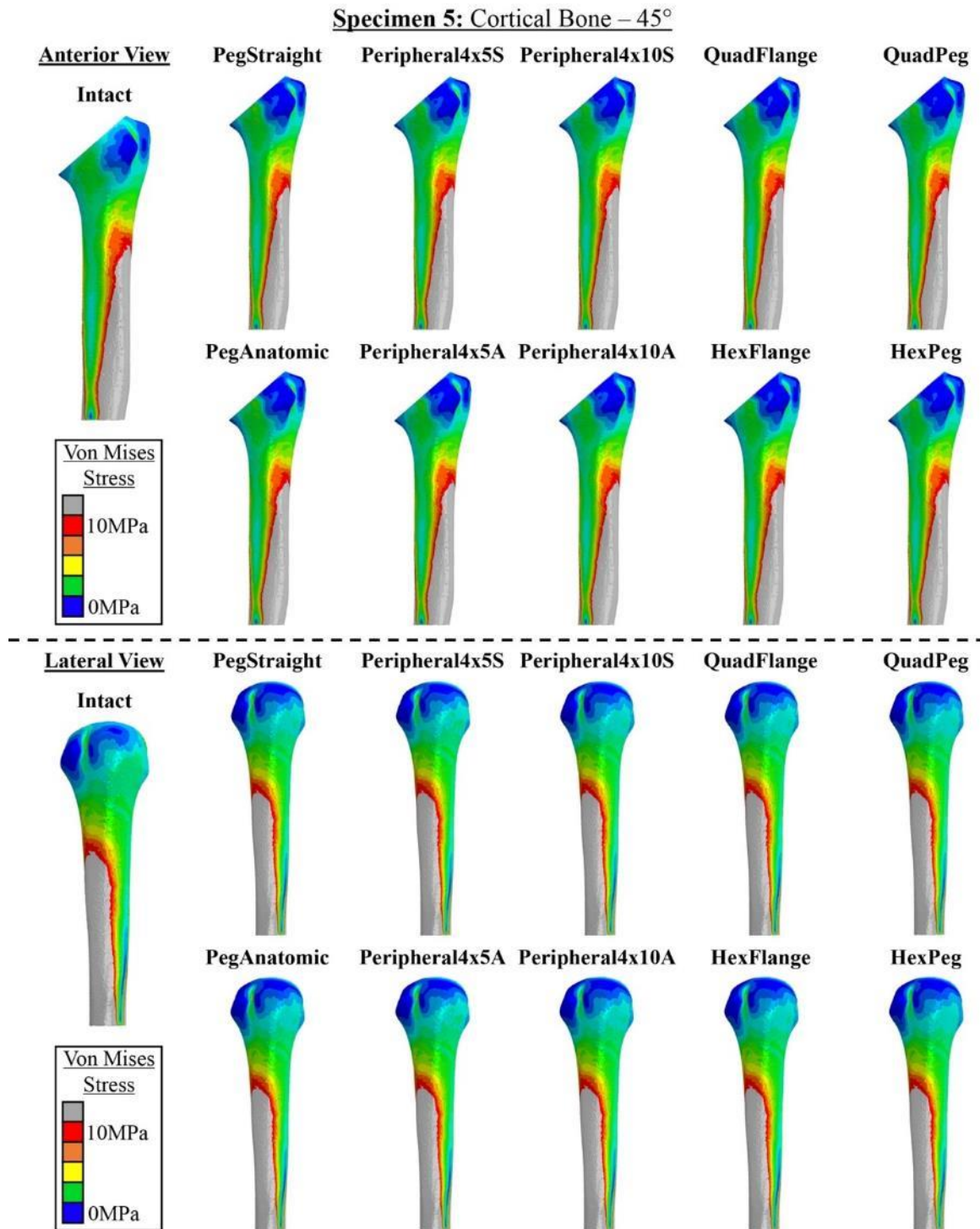
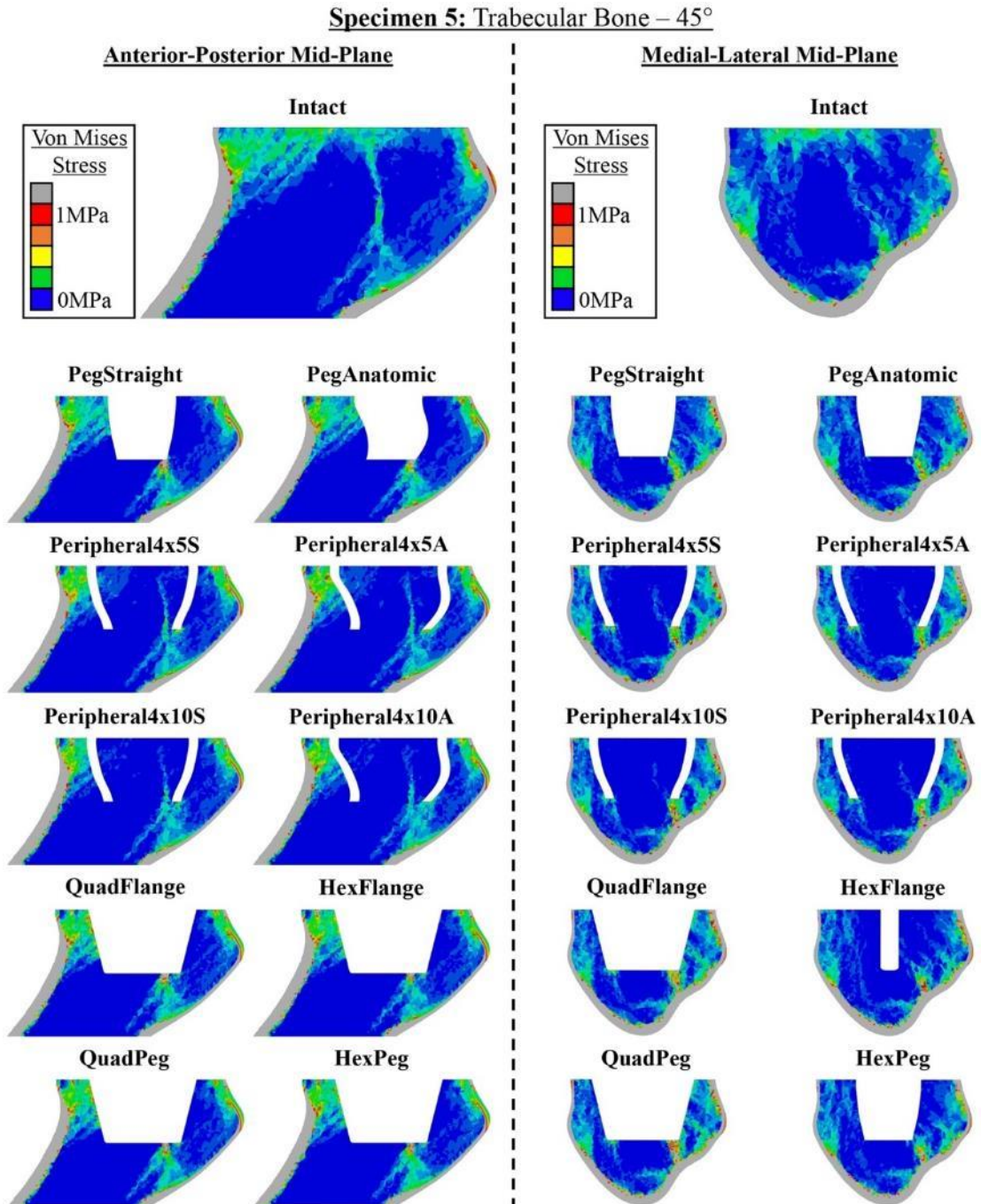


Figure J.17: von Mises Plots of Specimen 5's Cortical Shell for Loading at 45° of Abduction



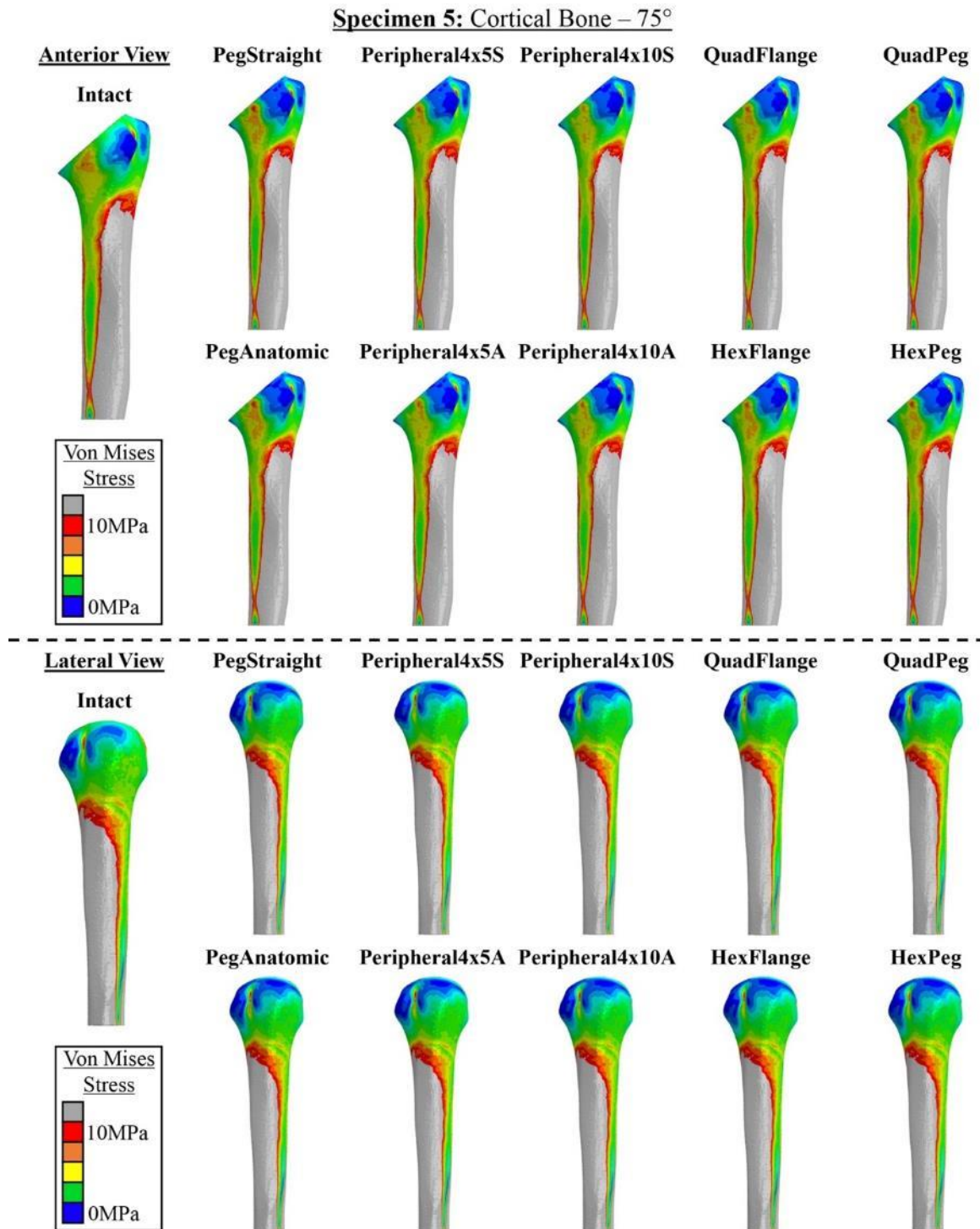


Figure J.19: von Mises Plots of Specimen 5's Cortical Shell for Loading at 75° of Abduction

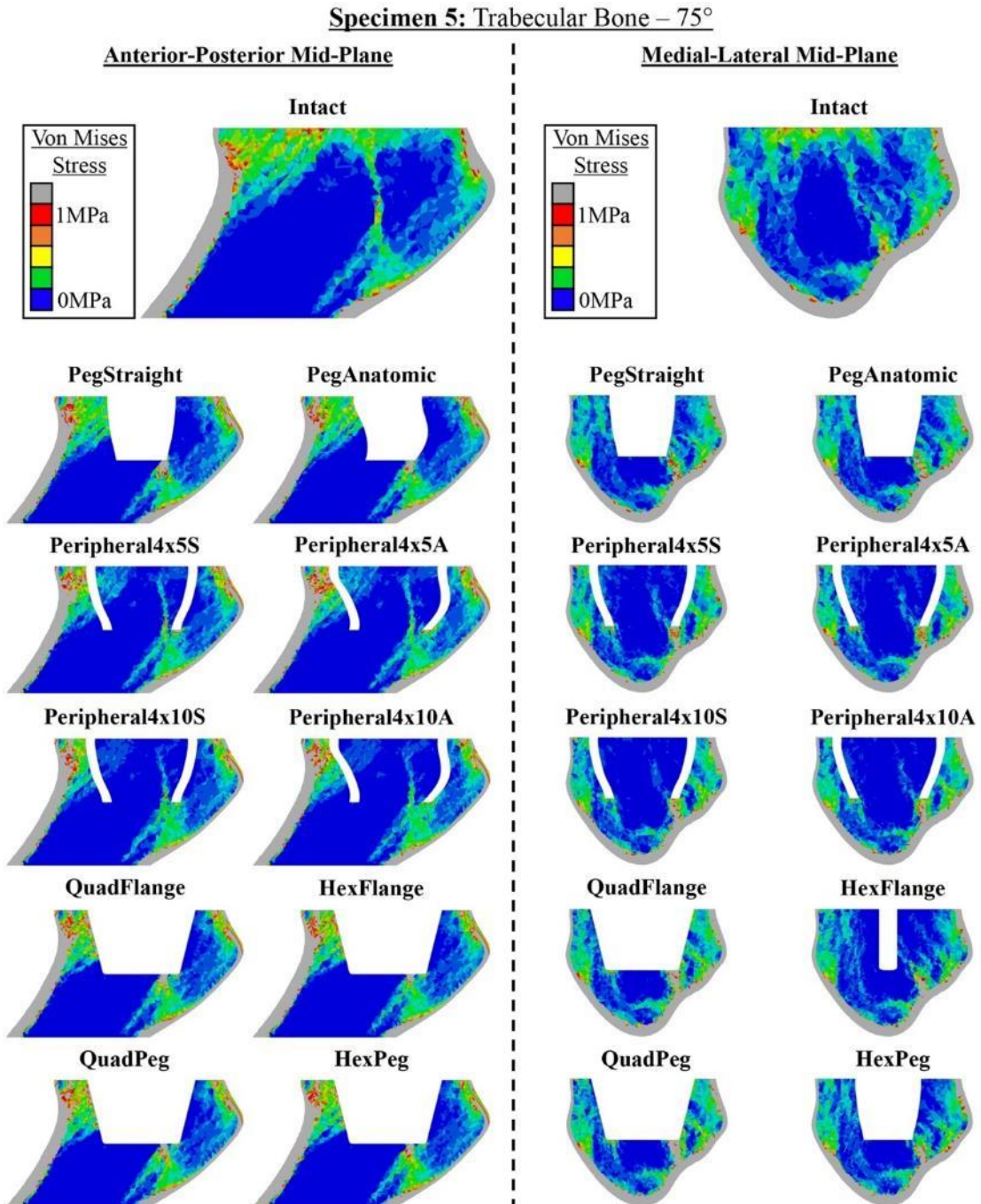


Figure J.20: von Mises Plots of Specimen 5's Trabecular-Canal for Loading at 75° of Abduction

Curriculum Vitae

Jacob M Reeves

PhD Candidate, MEng, BEng, EIT

EDUCATION:

2014 – 2018

Doctor of Philosophy - Mechanical & Materials Engineering

The University of Western Ontario, London, Canada

- Collaborative program with Musculoskeletal Health Research (a CIHR Training Program)

2012 – 2013

Master of Engineering Science - Mechanical & Materials Engineering

The University of Western Ontario, London, Canada

- Accelerated Masters program
- Collaborative program with Musculoskeletal Health Research (a CIHR Training Program)

2008 – 2012

Bachelor of Engineering Science - Mechanical & Materials Engineering

The University of Western Ontario, London, Canada

- John E. K. Foreman Gold Medal Award winner for highest aggregate final marks for 3rd and 4th years in the mechanical engineering program
- The Canadian Society for Mechanical Engineering Award for demonstrating outstanding achievement in mechanical engineering
- Graduated *with Distinction*

THESIS PROJECTS:

2014 – Present (Expected 2018)

Doctoral Thesis

“An In-Silico Assessment of Stemless Shoulder Arthroplasty: from CT to Predicted Bone Response”

Supervisors: Dr. James Johnson and Dr. George Athwal

- Use of finite element methods to quantify the changes in bone stress following joint reconstruction
- Evaluation of humeral implants available in industry today
- Development of new stemless implants to investigate changes in native bone stress in the proximal humerus

2012 – 2013

Master's Thesis

“Development and assessment of an impact apparatus and high-speed camera motion tracking system to quantify the effect of static muscle loads on fracture threshold measures in the distal radius”

Supervisors: Dr. Cynthia Dunning and Dr. James Johnson

- Quantified the effect of muscle loads on wrist fracture thresholds
- Designed a LabVIEW program for tracking bone impact motion from high-speed camera video
- Collected and analyzed strain gauge, load cell and high-speed video data

ACADEMIC AWARDS AND ACHIEVEMENTS:

2017-2018

Ontario Graduate Scholarship - \$15,000

2015 – 2018

Transdisciplinary Bone and Joint Training Award – \$15,000

2014 – 2017

NSERC Post-Graduate Scholarship - \$63,000

2016

Western's Doctoral Excellence Research Award - \$10,000

2014

Top Poster Presentation (Trauma) - \$100

- Bone and Joint Injury and Repair Conference; London, Canada

2013 – 2014

Ontario Graduate Scholarship - \$15,000 (Declined)

2012 – 2013

Ontario Graduate Scholarship - \$15,000

2012 – 2013

Queen Elizabeth II Graduate Scholarship in Science & Technology - \$15,000 (Declined)

2012

John E.K. Foreman Gold Medal Award in Mechanical & Materials Engineering

- Graduated with top marks in the Mechanical Engineering program

2012

The Canadian Society for Mechanical Engineering Award

- Demonstrated outstanding accomplishment in Mechanical Engineering

2011

NSERC Undergraduate Student Research Award - \$6,720

2010

UWO Faculty Association Scholarship - \$800

2008 – 2012

The Walker-Wood Continuing Scholarship in Engineering - \$20,000

2008 – 2012

The University of Western Ontario Continuing Entrance Scholarship - \$10,000

2008 – 2012

Dean's Honor List

PATENT - PCT:

2013

A Novel Expanding Pedicle Screw for Spinal Surgery

(Provisional Patent and PCT Granted)

Dr. Parham Rasoulinejad, **Mr. Jacob Reeves**, Dr. Stewart McLachlin, Dr. Fawaz Siddiqi, Dr. Christopher Bailey, Dr. Kevin Gurr, Dr. Cynthia Dunning

- Designed a pedicle screw that expands to provide additional fixation in the spines of patients with osteoporosis

RESEARCH POSITIONS:

2013 – Present

HULC Research Engineer

Roth|McFarlane Hand and Upper Limb Centre Bioengineering Lab
St. Joseph's Hospital, London, ON

- Conducted finite element analysis of shoulder contact following joint replacement
- Designed novel humeral head partial joint replacements for Hill-Sachs defects
- Developed custom testing equipment on a project-specific basis using SolidWorks CAD
- Assisted with literature review and CIHR grant renewal writing
- Worked collaboratively in a team of graduate students, engineers and surgeons

2011 – 2013

BTL Research Assistant

The University of Western Ontario, London, ON

- Aided in the design of methodology for knee compression tests
- Operated and collected force and displacement data from an Instron materials testing machine
- Designed novel adapters for mechanical testing using SolidWorks CAD
- Used Tekscan pressure cells for load measurement

RESEARCH EXPERIENCE:

2016 – 2017

Subacromial InSpace Balloon Assessment for Major Rotator Cuff Repair – HULC Research Engineer

- Conducted optical tracking to assess humeral head migration following superior capsule repair and InSpace subacromial balloon repair
- Responsible for testing method development and operation: static shoulder simulator, optical tracking, LabVIEW program development and data analysis

2014 – 2015

Latarjet Endobutton Fixation Assessment – HULC Research Engineer

- Conducted optical tracking of coracoid graft displacement following Latarjet repair using endobutton vs. screw fixation methods
- Responsible for testing method development and operation: materials testing machine, optical tracking, LabVIEW program development and data analysis

2013 – 2014

Partial Joint Reconstruction – HULC Research Engineer

- Assessed the effect of varying implant height and stiffness of partial joint reconstruction implants in the humeral head on joint contact mechanics
- Responsible for finite element model development (ABAQUS) and data analysis

2012 – 2016

Expanding Pedicle Screw – Independent Design

- Developed two designs for expanding pedicle screws that provide greater fixation in osteoporotic bone using SolidWorks CAD
- Collaborated with neurosurgeons, spinal surgeons and engineers to ensure customer needs were met
- Oversaw prototype fabrication, including 3D printing and traditional machining

SUPERVISORY EXPERIENCE:

2016 – Present

Stephany Synnott

Master's of Engineering Science

“A finite element comparison of stem dilation in the proximal humerus”

Department of Biomedical Engineering

The University of Western Ontario, London, ON

2016 – 2017

Dr. Supriya Singh

Master's of Surgery

“*The effect of repair technique on humeral head migration following superior capsule repair and InSpace subacromial balloon repair for major rotator cuff tears*”

Department of Surgery

The University of Western Ontario, London, ON

2014 – 2015

Najmeh Razfar

Master's of Engineering Science

“*Finite element modeling of the proximal humerus to compare stemless, short and standard stem humeral components of varying material stiffness for shoulder arthroplasty*”

Department of Biomedical Engineering

The University of Western Ontario, London, ON

PUBLICATIONS:

Peer-reviewed Journal Articles (7):

1. **Reeves JM**, Langohr GDG, Athwal GS, Johnson JA. “The Effect of Stemless Humeral Component Fixation-Feature Design on Bone Stress and Strain Response: A Finite Element Analysis”, *Journal of Shoulder and Elbow Surgery* (2018) (*In Press*).
2. **Reeves JM**, Knowles NK, Athwal GS, Johnson JA. “Methods for Post-Hoc Quantitative CT Bone Scan Calibration: Phantom-Only and Regression”, *ASME: The Journal of Biomechanical Engineering* (2018) 140(9) (*In Press*).
3. **Reeves JM**, Johnson JA, Athwal GS. “An Analysis of Proximal Humerus Morphology with Special Interest in Stemless Shoulder Arthroplasty”, *Journal of Shoulder and Elbow Surgery* (2018) 27(4), 650-658.
4. **Reeves JM**, Athwal GS, Johnson JA. “An Assessment of Proximal Humerus Density with Reference to Stemless Implants”, *Journal of Shoulder and Elbow Surgery* (2018) 27:4, 641-649.
5. Knowles NK, **Reeves JM**, Ferreira LF. “Quantitative Computed Tomography (QCT) Derived Bone Mineral Density (BMD) in Finite Element Studies: A Review of the Literature”, *Journal of Experimental Orthopaedics* (2016) 3:36.
6. Razfar N, **Reeves JM**, Langohr GDG, Willing R, Athwal GS, Johnson JA. “Comparison of Proximal Humeral Bone Stresses Between Stemless, Short and Standard Stem Length: A Finite Element Analysis (Assessment of Humeral Component Stem Length)”, *Journal of Shoulder and Elbow Surgery* (2016) 25:7, 1076-1083.
7. **Reeves JM**, Burkhart TB, Dunning CE. “The Effect of Static Muscle Forces on the Fracture Strength of the Intact Distal Radius *In Vitro* in Response to Forward Fall Impacts”, *Journal of Biomechanics* (2014) 47:11, 2672-2678.

Manuscripts in Submission (5):

1. Burkhart TA, **Reeves JM**, Dunning CE. “Diagnosis of Distal Radius Fractures and Common Secondary Injuries can be improved through the Development of Image Based Three-dimensional Geometric Models”, *Medical Engineering and Physics* (2018).
2. **Reeves JM**, Athwal GS, Johnson JA, Langohr GDG. “The Effect of Trabecular Modulus Anatomic Site Selection on FE Outcomes for Shoulder Arthroplasty”, *Journal of Shoulder and Elbow Surgery* (2018).
3. Singh S, **Reeves JM**, Langohr GDG, Johnson JA, Athwal GS. “The Subacromial Balloon Spacer versus Superior Capsular Reconstruction in the Treatment of Irreparable Rotator Cuff Tears: A Biomechanical Assessment”, *Journal of Arthroscopy* (2018).
4. Leitch KM, Birmingham TB, **Reeves JM**, Giffin JR, Dunning CE. “Walking-Inspired Loading Parameters Change In-vitro Measures of Strain in Medial Opening Wedge High Tibial Osteotomy”, *ASME: The Journal of Biomechanical Engineering* (2018).
5. Razfar N, **Reeves JM**, Langohr GDG, Willing R, Athwal GS, Johnson JA. “Comparison of Proximal Humeral Bone Stress of Standard Stem Implants for Shoulder Arthroplasty with Varying Material Stiffness”, *ASME: Journal of Biomechanical Engineering* (2018).

CONFERENCE PRESENTATIONS:*Oral Presentations at Peer-reviewed Professional Meetings (11):*

1. Singh S, **Reeves JM**, Langohr GDG, Johnson JA, Athwal GS. “The Subacromial Balloon Spacer versus Superior Capsule Reconstruction in the Treatment of Rotator Cuff Tears: A Biomechanical Assessment”, Annual Meeting of the American Academy of Orthopaedic Surgeons, New Orleans, LA, USA, March 6-10, 2018.
2. **Reeves JM**, Knowles NK, Athwal GS, Johnson JA. “Post-Hoc Quantitative CT Methods for Calibrating Bone Scans: Empty Chamber and Regression”, Annual Meeting of the Canadian Orthopaedic Research Society, Ottawa, ON, Canada, June 15-18, 2017.
3. **Reeves JM**, Athwal GS, Johnson JA. “Regional Variation in Bone Density and Volume Fraction in the Proximal Humerus”, Annual Meeting of the Orthopaedic Research Society, San Diego, CA, USA, March 19-22, 2017.
4. **Reeves JM**, Athwal GS, Johnson JA. “A Comparison of Double Screw vs. Quadruple Button Fixation for the Latarjet Procedure”, Annual Meeting of the Canadian Orthopaedic Research Society, Quebec City, QC, Canada, June 16-19, 2016.
5. Razfar N, **Reeves JM**, Langohr GDG, Willing R, Athwal GS, Johnson JA. “The Effect of Shoulder Humeral Component Length and Material on Bone Stresses: A Finite Element Analysis”, Annual Meeting of the American Academy of Orthopaedic Surgeons, Orlando, FL, USA, March 1-5, 2016.
6. **Reeves JM**, Razfar N, Athwal GS, Johnson JA. “The Effect of Orientation of Stemless Implants on Proximal Humerus Bone Stresses: A Finite Element Study”, Annual Meeting of the Canadian Orthopaedic Association, Vancouver, BC, Canada, June 19-20, 2015.
7. **Reeves JM**, Razfar N, Langohr DG, Athwal GS, King GJ, Johnson JA. “The Effect of Positioning of Partial Joint Resurfacing Implants on the Contact Mechanics of the Opposing Intact Cartilage: A Finite Element Study”, Annual Meeting of the Canadian Orthopaedic Research Society, Vancouver, BC, Canada, June 18, 2015.
8. Razfar N, **Reeves JM**, Langohr GDG, Willing R, Athwal GS, Johnson JA. “The Effect of Shoulder Humeral Component Length on Bone Stresses: A Finite Element (FE) Analysis”, 22nd Annual Symposium on Computational Methods in Orthopaedic Biomechanics, New Orleans, LA, USA, March 14, 2014.
9. **Reeves JM**, Razfar N, Langohr DG, Athwal GS, King GJ, Johnson JA. “The Effect of Material Selection of Partial Joint Replacement Prostheses on the Contact Mechanics of the Opposing Native

- Cartilage: A Finite Element Study”, The Bone and Joint Injury and Repair Conference, London, ON, Canada, January 17-18, 2014.
10. **Reeves JM**, Burkhart TA, McLachlin SM, Dunning CE. “A Colour-Thresholding Technique to Quantify High-Speed Planar Motion of Isolated Distal Radii Specimens During Impact”, Ontario Biomechanics Conference, Barrie, ON, Canada, March 15-17, 2013.
 11. Leitch KL, Birmingham TB, **Reeves JM**, Giffin JR, Dunning CE. “Development of a Materials-testing Fixture to Enable Asymmetric Loading of the Lower Limb: An application of in-vivo gait data”, Annual Meeting of the Canadian Orthopaedic Research Society, Ottawa, ON, Canada, June 8-10, 2012.

Posters at Peer-reviewed Professional Meetings (28):

1. **Reeves JM**, Athwal GS, Johnson JA, Langohr GDG. “The Effect of Trabecular Material Model Selection on Finite Element Model Outcome Measures”, Annual Meeting of the Canadian Orthopaedic Research Society, Victoria, BC, June 21, 2018.
2. Langohr GDG, **Reeves JM**, Johnson JA, Faber KJ. “Changes in Humeral Bone Stress for Humeral Stems of Varying Length”, Annual Meeting of the Canadian Orthopaedic Research Society, Victoria, BC, June 21, 2018.
3. **Reeves JM**, Langohr GDG, Singh S, Johnson JA, Athwal GS. “Humeral Head Migration Following Rotator Cuff Tear and Subacromial Balloon Repair”, Annual Meeting of the Canadian Orthopaedic Research Society, Victoria, BC, June 21, 2018.
4. **Reeves JM**, Langohr GDG, Athwal GS, Johnson JA. “Humeral Response Attributable to Stemless Shoulder Implant Design”, Canadian Bone and Joint Conference, London, ON, Canada, May 11-12, 2018.
5. Langohr GDG, **Reeves JM**, Johnson JA, Faber KJ. “Changes in Humeral Bone Stress for Humeral Stems of Varying Length”, Canadian Bone and Joint Conference, London, ON, Canada, May 11-12, 2018.
6. **Reeves JM**, Athwal GS, Johnson JA, Langohr GDG. “The Effect of Trabecular Material Model Selection on Finite Element Model Outcome Measures”, Annual Meeting of the Orthopaedic Research Society, New Orleans, LA, USA, March 10-13, 2018.
7. Langohr GDG, **Reeves JM**, Johnson JA, Faber KJ. “A Finite Element Analysis of Load Transfer Comparing Short and Standard Length Humeral Stems”, Annual Meeting of the Orthopaedic Research Society, New Orleans, LA, USA, March 10-13, 2018.
8. **Reeves JM**, Langohr GDG, Singh S, Johnson JA, Athwal GS. “Humeral Head Migration Following Rotator Cuff Tear and Subacromial Balloon Repair”, Annual Meeting of the Orthopaedic Research Society, New Orleans, LA, USA, March 10-13, 2018.
9. Singh S, **Reeves JM**, Langohr GDG, Johnson JA, Athwal GS. “The Subacromial Balloon Spacer versus Superior Capsule Reconstruction in the Treatment of Rotator Cuff Tears: A Biomechanical Assessment”, Annual Meeting of the Orthopaedic Research Society, New Orleans, LA, USA, March 10-13, 2018.
10. **Reeves JM**, Knowles NK, Athwal GS, Johnson JA. “Post-Hoc Quantitative CT Methods for Calibrating Bone Scans: Empty Chamber and Regression”, Annual Meeting of the Canadian Orthopaedic Research Society, Ottawa, ON, June 18, 2017.
11. **Reeves JM**, Knowles NK, Athwal GS, Johnson JA. “Methods for Post-Hoc Quantitative CT Bone Scan Calibration: Empty Chamber and Regression”, Annual Meeting of the Orthopaedic Research Society, San Diego, CA, USA, March 19-22, 2017.
12. **Reeves JM**, Knowles NK, Ferreira LF, Athwal GS, Johnson JA. “Post-Hoc Calibration Methods for Quantitative Computed Tomography”, Canadian Bone and Joint Conference, London, ON, Canada, April 8-9, 2016.

13. Caranza V, **Reeves JM**, Burkhart TA. “Development and Validation of a Finite Element Model to Simulate the Opening of a High Tibia Osteotomy”, Canadian Bone and Joint Conference, London, ON, Canada, April 8-9, 2016.
14. **Reeves JM**, Athwal GS, Johnson JA. “A Comparison of Double Screw vs. Quadruple Button Fixation for the Latarjet Procedure”, Annual Meeting of the Orthopaedic Research Society, Orlando, FL, USA, March 5-8, 2016.
15. Razfar N, **Reeves JM**, Langohr GDG, Willing R, Athwal GS, Johnson JA. “A Comparison of Proximal Humeral Bone Stresses for Stemless, Short and Standard Stem Humeral Components for Shoulder Arthroplasty - A Finite Element Study”, Annual Meeting of the Canadian Orthopaedic Research Society, Vancouver, BC, June 18, 2015.
16. Razfar N, **Reeves JM**, Langohr GDG, Willing R, Athwal GS, Johnson JA. “Finite Element Modeling of The Proximal Humerus To Compare Humeral Stem Components of Varying Material Stiffness For Shoulder Arthroplasty”, Annual Meeting of the Canadian Orthopaedic Research Society, Vancouver, BC, June 18, 2015.
17. **Reeves JM**, Razfar N, Langohr DG, Athwal GS, King GJ, Johnson JA. “The Effect of Material Selection and Implant Positioning on Cartilage Stresses Following Partial Joint Resurfacing of the Proximal Humerus: A Finite Element Study”, Annual Meeting of the Orthopaedic Research Society, Las Vegas, NV, USA, March 28-31, 2015.
18. Razfar N, **Reeves JM**, Langohr GDG, Willing R, Athwal GS, Johnson JA. “Comparison of Proximal Humeral Bone Stresses Resulting from Varying Shoulder Implant Stem Design”, Annual Meeting of the Orthopaedic Research Society, Las Vegas, NV, USA, March 28-31, 2015.
19. **Reeves JM**, Razfar N, Langohr DG, Athwal GS, King GJ, Johnson JA. “The Effect of Material Selection and Position of Partial Joint Replacement Prostheses on the Contact Mechanics of the Opposing Native Cartilage: A Finite Element Study”, Meeting of the World Congress of Biomechanics, Boston, MA, USA, July 6-11, 2014
20. Razfar N, **Reeves JM**, Langohr GDG, Willing R, Athwal GS, Johnson JA. “Comparison of Proximal Humeral Bone Stresses Resulting from Varying Shoulder Implant Stem Design”, Meeting of the World Congress of Biomechanics, Boston, MA, USA, July 6-11, 2014
21. **Reeves JM**, Razfar N, Langohr DG, Athwal GS, King GJ, Johnson JA. “The Effect of Material Selection of Partial Joint Replacement Prostheses on the Contact Mechanics of the Opposing Native Cartilage: A Finite Element Study”, Annual Meeting of the Canadian Orthopaedic Research Society, Montreal, QC, June 18-21, 2014.
22. **Reeves JM**, Burkhart TA, Dunning CE. “The Effect of Static Forearm Flexor and Extensor Muscle-Loads on the Fracture Threshold of the Distal Radius: A Cadaveric Study”, Annual Meeting of the Canadian Orthopaedic Research Society, Montreal, QC, June 18-21, 2014.
23. Razfar N, **Reeves JM**, Langohr GDG, Willing R, Athwal GS, Johnson JA. “Comparison of Proximal Humeral Bone Stresses Resulting from Varying Shoulder Implant Stem Design”, Annual Meeting of the Canadian Orthopaedic Research Society, Montreal, QC, June 18-21, 2014.
24. Burkhart TA, **Reeves JM**, Dunning CE. “Improving the Diagnosis of Distal Radius Fractures and Common Secondary Injuries Through the Development of Three-Dimensional Solid Models”, Mimics Innovation Conference, Chichago, IL, USA, May 15-16, 2014.
25. **Reeves JM**, Burkhart TA, Dunning CE. “The Effect of Static Forearm Flexor and Extensor Muscle-Loads on the Fracture Threshold of the Distal Radius: A Cadaveric Study”, The Bone and Joint Injury and Repair Conference, London, ON, January 17-18, 2014.
26. Razfar N, Willing RT, **Reeves JM**, Athwal GS, Johnson JA. “Comparison of Proximal Humeral Bone Stresses Resulting from Varying Shoulder Implant Stem Design”, The Bone and Joint Injury and Repair Conference, London, ON, January 17-18, 2014.

27. Leitch KL, Birmingham TB, **Reeves JM**, Giffin JR, Dunning CE. “Development of a Materials-testing Fixture to Enable Asymmetric Loading of the Lower Limb: An application of in-vivo gait data”, OARSI, Barcelona, Spain, April 26-29, 2012.
28. Leitch KL, Birmingham TB, **Reeves J**, Giffin JR, Dunning CE. “Development of a Materials-testing Fixture to Enable Asymmetric Loading of the Lower Limb: An application of in-vivo gait data”, Ontario Biomechanics Conference, Barrie, Ontario, March 16-18, 2012.

PROFESSIONAL CONFERENCES ATTENDED:

2018 – June	The Canadian Orthopaedic Association/Research Society; Victoria, Canada
2018 – May	The Canadian Bone and Joint Conference; London, Canada
2017 – June	The Canadian Orthopaedic Association/Research Society; Ottawa, Canada
2017 – March	The Orthopaedic Research Society’s Annual Meeting; San Diego, USA
2016 – June	The Canadian Orthopaedic Association/Research Society; Quebec City, Canada
2016 – April	The Canadian Bone and Joint Conference; London, Canada
2016 – March	The Orthopaedic Research Society’s Annual Meeting; Orlando, USA
2015 – June	The Canadian Orthopaedic Association/Research Society; Vancouver, Canada
2015 – March	The Orthopaedic Research Society’s Annual Meeting; Las Vegas, USA
2014 – July	The World Congress on Biomechanics; Boston, USA
2014 – June	The Canadian Orthopaedic Association/Research Society; Montreal, Canada
2014 – March	The Orthopaedic Research Society’s Annual Meeting; New Orleans, USA
2014 – January	The Bone and Joint Injury and Repair Conference; London, Canada
2013 – March	The Ontario Biomechanics Conference; Barrie, Canada
2012 – June	The Canadian Orthopedic Association/Research Society; Ottawa, Canada

MEMBERSHIPS and CERTIFICATIONS:

- **Engineer in Training (EIT)** – Professional Engineers Ontario (PEO)
- **Associate Student/Trainee Member** – Orthopaedic Research Society (ORS)
- **Student Member** – Canadian Society of Mechanical Engineers (CSME)
- Certified SolidWorks Associate

SOCIAL and ACADEMIC OUTREACH:

2016 – Present

MMEGS President

Mechanical and Materials Engineering Graduate Society

- Managed and developed the MME graduate society, with a focus on promoting departmental unity, social activities, *etc.*
- Responsible for lobbying on behalf of the MME graduate students at departmental faculty meetings

2015 – 2016

MMEGS Vice President – Social

Mechanical and Materials Engineering Graduate Society

- Managed and developed social activities within the MME department for graduate students to promote departmental unity, including: MME Escape Room, Coffee Hours, *etc.*

2011 – 2012

Student Representative

Western Engineering Annual March Break Open-House & Fall Preview Day

- Led lab demonstrations in dynamic balancing and heat transfer
 - Promoted Western Engineering and answered questions related to the Mechanical Engineering program
- 2011

Guest Speaker

Saint Thomas Aquinas Catholic Secondary School

- Promoted Western Engineering through recruitment presentations for grade 12 Design and Physics classes